Technological Educational Institute of Crete
School of Applied Sciences
Department of Environmental & Natural Resources Engineering

Master of Science Courses
"Geoenvironmental Resources & Risks"

Laboratory scale application of spectral induced polarization (SIP) method for environmental monitoring

Kirmizakis Panagiotis

Chania
2016

Kirmizakis Panagiotis

Submitted in the Department of Environmental and Natural Resources Engineering,
Technological Educational Institute (TEI) of Crete, Chania

Supervising Committee:
Soupios Pantelis, Professor, TEI of Crete
Ntarlagiannis Dimitrios, Associate Research Professor, Rutgers University
Kalderis Dimitrios, Assistant Professor, TEI of Crete

Copying, storage and distribution of this work, in whole or part of it for commercial purposes is not allowed. Reproduction, storage and distribution for non-profit purposes, educational or research nature is permitted provided that the origin source is indicated and to maintain the existing message. Questions concerning the use of labor for profit should be addressed to the author.

The views and conclusions contained in this document reflect the author and should not be interpreted as reflecting official positions of TEI of Crete.

ABSTRACT

Spectral induced polarization (SIP) in the last couple decades has shifted its applicability from mineral exploration to more environmental applications. Such applications included, but not limited, to environmental pollution and definition of pollutants at the subsurface. SIP method allows a more in-depth investigation of the changes at the grain fluid interface that conventional geophysical methods are not able to detect. SIP measurements in laboratory scale were carried out in order to demonstrate the suitability and sensitivity of the method as monitoring tool in olive-mill wastewater (OMW). The cultivation of the olive tree has always been an important part of economic and social life in the Mediterranean countries. However, the production process creates a large volume of waste, which are characterized by a remarkably large organic load. The most common management practices of OMW is the disposal in evaporation ponds that can lead to high susceptibility of contamination of groundwater and soil degradation. The purpose of this thesis is to determine if the remediation of OMW through phytoremediation and biochar is possible and utilize the SIP method to monitor the process. Further geochemical analysis performed to provide additional insight on OMW and on the treatment processes, and their links to SIP responses.

Key words: Spectral Induced Polarization Method (SIP), Biochar, Bioremediation, Olive-mill wastewater, Phytoremediation

ACKNOWLEDGEMENTS

The completion of this study would not have been possible without the contribution of the people listed below.

Initially, I would like to thank my supervisor Prof. Soupios Pantelis for its substantial assistance with problems encountered during my thesis. The encouragement during my under-graduate level was continuous and I thank him especially for the confidence he showed me at the Master. My assessment of the person is not limited to scientific level and in a friendly after I had the full support and sympathy to anything bothered me during all previous years.

I would like to thank Prof. Lee Slater and Asc. Prof. Dimitrios Ntarlagiannis for supporting my research visit to Rutgers University and their willingness to host me at their laboratory and teach me the SIP method.

I would also to thank Assistant Prof. Dimitrios Kalderis for his useful advices. The fervent support, the proposals and remarks throughout this study were particularly important. I should mention that Dr. Kalderis taught me first the academic thinking and academic ethic since I completed my undergraduate thesis with him publishing together my first paper. Thank you Dimitris for your continuous support.

I am grateful to Prof. E. Gidarakos from the Technical University of Crete and the Ph.D. candidate F. Pellera for their help in the chemical analysis during the biochar treatment.

Thanks to Prof. N. Kalogerakis from the Technical University of Crete and the Ph.D. candidate M. Petousi for their willingness and provision of OMW samples from phytoremediation experiment performed on an experimental tank in space of the Technical University of Crete, Chania.

I would like also to thank the company TSAL S.A. (Pantelis Tsalapatas) for constructing and providing without cost the experimental columns made of high performance plexiglass.

I am grateful to Assoc. Prof. Evert Elzinga from Rutgers University for the IR and XRD analysis that are presented in this thesis.

I would like to thank Dr Vassilis Dimitriou (as head of the Manufacturing Laboratory of our Department) and Mr. Theodore Papadoulis (as chief engineer) for their continuous constructional support during the experiment.

Also, I would like to thank my parents, who in their own way contributed to the completion of this work.

CONTENTS

ABSTRACT iii
ACKNOWLEDGEMENTS iv
CONTENTS v
LIST OF FIGURES vii
LIST OF TABLES ix
1. INTRODUCTION 1
1.1 OBJECT – PURPOSE OF THESIS 1
1.2 LITERATURE REVIEW 1
1.3 STRUCTURE OF THE THESIS 3
2. THEORY – METHODOLOGY 5
2.1 INTRODUCTION 5
2.1.1 Electrode Polarization Mechanism 5
2.1.2 Membrane Polarization 7
2.1.3 Maxwell-Wagner polarization 8
2.1.4 Electrical Double Layer (EDL) polarization 8
2.2 APPLICATION OF SPECTRAL INDUCED POLARIZATION 9
2.3 IP MODEL AND RELATION PARAMETERS 10
2.3.1 Theoretical Basis of IP method 10
2.3.2 Normalized Parameters 13
2.3.3 SIP Modeling 14
3. EXPERIMENTAL PREPARATION 18
3.1 WASTEWATER USED 18
3.2 OMW TREATMENT 20
3.2.1 Phytoremediation 21
3.2.2 Biochar 22
4. LABORATORY MEASUREMENTS 24
4.1 COLUMN CONSTRUCTION AND SAMPLING 24
4.1.1 Electrodes' Specifications 24
4.2 SIP INSTRUMENTATION 25
4.3 GEOMETRIC FACTOR MEASUREMENTS 26
4.3.1 Preparation of solutions 27
4.3.2 Geometric Factor 27
4.4 SENSITIVITY IMPACT OF CHANGES IN GRAIN SIZE 28
4.5 RESPONSE AT DIFFERENT FLUID CONCENTRATIONS 28

4.6 PHYTOREMEDIATION 29
4.7 BIOCHAR 30
5. RESULTS 32
5.1 GEOMETRIC FACTOR MEASUREMENTS 32
5.2 SENSITIVITY IMPACT OF CHANGES IN GRAIN SIZE 34
5.3 RESPONSE AT DIFFERENT FLUID CONCENTRATIONS 38
5.4 PHYTOREMEDIATION 39
5.5 BIOCHAR 42
6. SUMMARY – CONCLUSIONS 52
6.1 METHOD 52
6.2 GEOMETRIC FACTOR MEASUREMENTS 52
6.3 SENSITIVITY IMPACT OF CHANGES IN GRAIN SIZE 52
6.4 RESPONSE AT DIFFERNET FLUID CONCENTRATIONS 52
6.5 PHYTOREMEDIATION 53
6.6 BIOCHAR 53
REFERENCES 54
APPENDIX A 59
A.1 Instrumentation 59
APPENDIX B 66
B.1 Calculation of geometric factor 66
B.2 Fluid tests 67
B.3 Grain size analysis 79
B.4 Different Concentrations 85
B.5 Phytoremediation 94
B.6 Biochar 101

LIST OF FIGURES

Figure 1.1 Electrical conductivity of rocks..... 2
Figure 2.1 Illustration of elements of electrode polarization..... 6
Figure 2.2 (a) porosity filled with electrolyte solution and the measured voltage V_1 in conditions of free ionic motion, **(b)** porosity similar with (a) but clogged by mineral particle causing the overvoltage and the measured voltage $V_2>V_1$..... 6
Figure 2.3 Example of ionic alternative path when the porosity is partially filled by grains of sulfur mineral..... 7
Figure 2.4 Membrane polarization in rock containing clay particles, (a) before application of electric current, (b) after application of electric current..... 8
Figure 2.5 (a) Time-domain IP signal and the measured parameters for the calculation of M, **(b)** Square current waveform at low frequency (~ 1 Hz) which shows the continuous change of the polarity..... 11
Figure 2.6 Simple circuit model for low-frequency ($f \leq 1000$ kHz) electrical current flow in nonmetallic rocks and sediments..... 12
Figure 2.7 Dependence of IP parameters and normalized parameters on fluid conductivity (σ_w) for a Berea sandstone core..... 14
Figure 3.1 Average production of olive oil in EU for the harvesting years 1999/2000 – 2002/2003..... 18
Figure 3.2 Evaporation pond in the broader area of Chania, Crete..... 20
Figure 3.3 Processes associated with phytoremediation..... 22
Figure 4.1 – Schematic and photograph of the used plastic column. In the columns, placed 2 Ag-AgCl electrodes for current injection (C1 & C2) and 5 Ag-AgCl electrodes in chambers for the potential measurements (P1-P5) (all the columns that used were identical)..... 24
Figure 4.2 - Portable Field/Lab Spectral Induced Polarization (PSIP) instrument by Ontash company..... 25
Figure 4.3 - Block diagram of the laboratory Spectral Induced Polarization instrument 25
Figure 4.4 Real conductivity for column 1 during fluid tests before and after taking into account the K factor with a solution of know conductivity 296 μS/cm..... 26
Figure 4.5 Calculation of geometric factor for one of the used columns..... 28
Figure 4.6 Phytoremediation tank of the Technical University of Crete..... 29
Figure 4.7 Biochar from blending of paper sludge and wheat husks that used in the measurements..... 30
Figure 4.8 Mixture Biochar with Ottawa sand..... 31
Figure 5.1 Phase response and fluid conductivity (real and imaginary part) for column 1 between potential electrodes P1-P4 (9 cm) during fluid tests after taking into account the K factor..... 33
Figure 5.2 Phase response and fluid conductivity (real and imaginary part) during grain size analysis measurements to 10000-0.01 Hz (distance between potential electrodes 30 mm)..... 35
Figure 5.3 Phase response and fluid conductivity (real and imaginary part) during grain size analysis measurements to 10000-0.01 Hz (distance between potential electrodes 120 mm)..... 36
Figure 5.4 Phase response and fluid conductivity (real and imaginary part) during grain size analysis measurements to 10000-0.01 Hz (distance between potential electrodes 120 mm)..... 37

Figure 5.5 Phase response and fluid conductivity (real and imaginary part) during measurements with sands saturated with OMW to 10000-0.01 Hz (distance between electrodes 30 mm)..... 38
Figure 5.6 Phase response and fluid conductivity (real and imaginary part) during measurements with quartz sand, saturated with different concentration solutions of OMW to 10000-0.01 Hz (distance between electrodes 120 mm)..... 39
Figure 5.7 Phase response and fluid conductivity measurements after phytoremediation treatment to 10000-0.01 Hz..... 40
Figure 5.8 Single frequency graphs after phytoremediation treatment to 10 Hz..... 41
Figure 5.9 Phase response and fluid conductivity measurements during 10 days with 0% w/w biochar to 10000-0.01 Hz…… 43
Figure 5.10 Phase response and fluid conductivity measurements during 10 days' treatment with 5% w/w biochar to 10000-0.01 Hz……. 44
Figure 5.11 Phase response and fluid conductivity measurements during 10 days' treatment with 10% w/w biochar to 10000-0.01 Hz……... 45
Figure 5.12 Phase response and fluid conductivity measurements during 10 days' treatment with 25% w/w biochar to 10000-0.01 Hz……... 46
Figure 5.13 Single frequency graphs during 10 days treatment with biochar to 10 Hz 47
Figure 5.14 XRD diagram for the 4 samples in which the vertical axis is the intensity of the reflected beam and the horizontal, the degrees (angle) moving the goniometer…... 50
Figure 5.15 IR spectra of biochar samples…… 50
Fig. 5.16 SEM images of the biochar samples……... 51

LIST OF TABLES

Table 2.1 Time and frequency domain expressions of some classical transfer functions. 17
Table 4.1 Composition of standard solutions according to ASTM D1125-95 method… 27
Table 4.2 Composition of prepared solutions…….. 27
Table 4.3 Different concentrations in OMW solutions…… 28
Table 4.4 Chemical characteristics of OMW……... 29
Table 4.5 Different concentrations of biochar in the measured columns…….. 30
Table 4.6 Content of polycyclic aromatic hydrocarbons (PAH), elements, and specific surface area (SSA) in the specimen…….. 31
Table 4.7 Chemical characteristics of OMW……... 31
Table 5.1 Percentage errors for Column 1……... 33
Table 5.2 Percentage errors for Column 2……... 33
Table 5.3 Percentage errors for Column 3……... 33
Table 5.4 Percentage errors for Column 4……... 34
Table 5.5 COD results for the phytoremediation treatment……. 41
Table 5.6 Chemical analysis to the initial OMW and the outflows after the 10 days' treatment in the different biochar concentrations……. 48

1. INTRODUCTION

1.1 OBJECT – PURPOSE OF THESIS

Pollution through olive-mill wastewater (OMW) is a very important, and largely overlooked, environmental problem, that has received considerable public attention over the last few years. OMW is characterized by high recalcitrant organic load and high toxicity values. OMW is usually disposed of into unprotected and uncontrolled evaporation ponds nearby the main olive oil production facility, very often close to sensitive environmental systems (rivers, streams, shallow aquifer sites, etc). Disposal of such wastewater may lead to degradation of soil and groundwater and poses a threat to the flora and fauna of the area (Kavvadias, Doula, & Theocharopoulos, 2014). Therefore, a holistic strategic approach for the management or the decontamination of this type of waste is required. Essential to the success of any organic load removal approach is the accurate monitoring of the process.

This work presents the use of spectral induced polarization (SIP) method in a controlled laboratory experiment using phytoremediation and biochar as a tool for countering land degradation (Barrow, 2012). The SIP method has proved to be an important qualitative monitoring and characterization tool in contaminated land (Kemna et al., 2012) and a prime candidate for a monitoring tool in OWM remediation processes. Previous work has already established the sensitivity of induced polarization on OMW (Ntarlagiannis et al., 2016). The results are very promising suggesting that SIP could be utilized to monitor OMW remediation using biochar in almost real time.

1.2 LITERATURE REVIEW

Nowadays the problem of pollution is particularly severe because of the proliferation of contamination processes. The intense environmental problems in recent years and to date impossible definitive treatment of the causes which are responsible for the contamination, imposed at least the practical monitoring of the problem by developing the necessary techniques. In such cases, the aim is to identify the problem, to describe the hazards and the ecological impact and to create the management plan. These techniques include environmental geophysics that is primarily used for the identification of the environmental problem, mapping the presence and transport of the contaminants into the subsurface and the time-lapse monitoring of contaminants decrease (degradation) when a decontamination method is applied to the contaminated land.

Over the years, different geophysical methods are used to monitor subsurface conditions in real time, such as contamination. The most widely used geophysical methods in environmental studies and particular in the monitoring of contaminants in the subsurface are the geoelectrical methods. Initially, these methods were designed based on the study how currents pass through the subsurface. Geolectrical techniques measure the potential difference in the ground caused by the injection of electricity into it. The difference of the potential reflects the difficulty with which the electric current flows in the subsoil, thus giving an indication of the electrical resistance of the soil. Different geological formations have different electrical resistances. The knowledge of geoelectrical structure of the subsoil can be used for indirect finding of the

geological structure and interest structures. Most characteristic property of the geoelectrical structures of the resistance is the reverse that is the conductivity (Fig. 1.1).

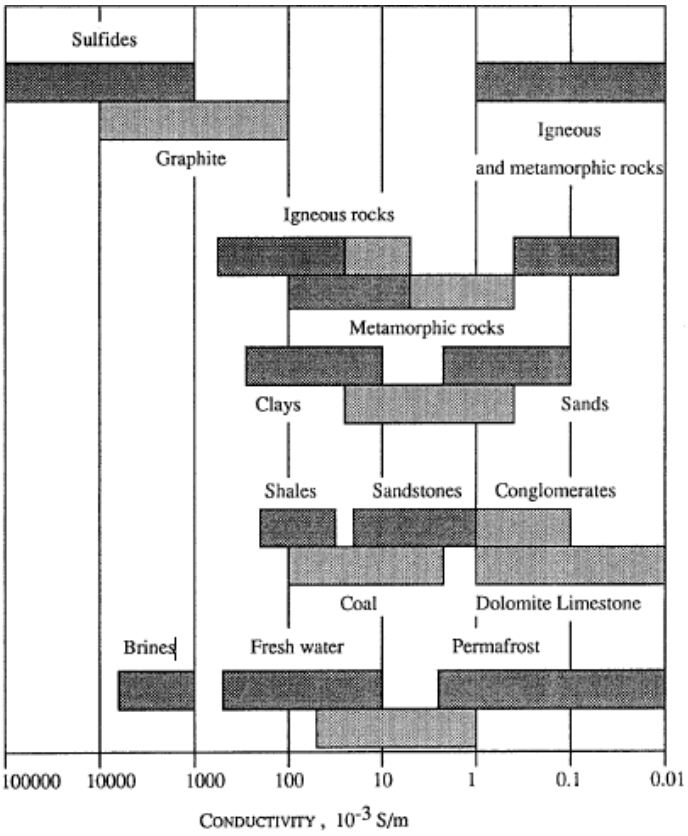

Figure 1.1 Electrical conductivity of rocks (Ruffet, Darot, & Guéguen, 1995).

Electrical methods can be classified into active and passive; in the first category belong the methods using physical fields and the second those that presuppose the existence of artificial fields. The first category includes:

- Self-Potential (SP)

The second category includes:

- Electrical Resistivity Imaging (ERI)
- Induced Polarization (IP)
- Spectral Induced Polarization (SIP)

Self-Potential (SP) is a passive geophysical method that measures naturally occurring electrical field on earth, resulting from multiple processes such as electrokinetic mechanisms, temperature gradients and electrochemical mechanisms (Naudet et al., 2003; Revil et al., 2012; Revil et al., 2003; Reynolds, 2011). Of the most common uses of the method is that in the mineral exploration (Parasnis, 1986) and in environmental applications (Rani et al., 2016; Soupios & Karaoulis, 2015). More recently it has determined that SP method is one promising technique for detecting alteration resulting from microbial processes in the subsurface (Arora et al., 2007; Naudet et al., 2003; Revil et al., 2010a).

Electrical Resistivity Tomography (ERT) is one of the most widespread geophysical methods designed to measure the potential difference caused by injection of electrical current into the earth (Günther & Rücker, 2012) in 2D, 3D or even collecting time lapse (4D) data. Some typical

applications of the ERT method are the mapping of buried wastes and structures (Tsourlos et al, 2014), characterization and monitoring of contaminant plumes (Ntarlagiannis et al., 2016), geological characterization (Andronikidis et al., 2015; Correia & Passos, 2015; Georgescu & Chitea, 2015; Robinson et al., 2016) and especially in the hydrogeological investigations, such as moisture content (Zhou, Shimada, & Sato, 2001), groundwater quality (Ogilvy et al., 2009), groundwater-surface interactions (Cardenas & Markowski, 2011), salt water intrusion (Nguyen et al., 2009) and monitoring rising and falling water levels (Kuras et al., 2009).

The Induced Polarization (IP) method is an extension of the resistivity method. When current is injected into the ground, the ground charges up, or polarizes, like a capacitor. When the current is turned off, the induced charge takes a finite time to dissipate. The time taken for the charge to build up (or dissipate) varies not only with the chargeability of the ground, but also with the frequency of the applied current (Slater & Lesmes, 2002). Induced polarization (IP) methods have repeatedly been shown to provide more diagnostic information on organic contamination than conventional ERT method, including (bio)degradation processes (Atekwana & Slater, 2009; Ntarlagiannis et al., 2016).

Spectral induced polarization (SIP) method improves the time domain induced polarization method by measuring phases and amplitudes at frequencies 10^{-3} to $4 \cdot 10^{3}$ Hz. Although the method of the induced polarization in the frequency domain provides more material discrimination and detailed interpretation, measurements in the time domain remain more attractive because of the less time required to complete the measurements for most practical applications (Dahlin & Leroux, 2012).

This thesis presents an application of the SIP method on a controlled laboratory experiment. We employed different applications to derive the sensitivity and suitability in environmental applications of the method.

1.3 STRUCTURE OF THE THESIS

The structure of the thesis is divided as follows:

Chapter 2: This chapter presents the basic theory and principles governing the method of spectral induced polarization. Indicate the general aspects for the method of induced polarization in the time domain and in the frequency domain.

Chapter 3: This chapter presents the contaminant used for the SIP experiments and the basic theory of the used remediation techniques.

Chapter 4: This chapter presents the main environmental applications and their theoretical background studied in this work with the use of spectral induced polarization method. Also, the equipment used for obtaining the experimental data is presented.

Chapter 5: This chapter presents the most representative results of the measurements described in Chapter 4 aiming to understand the SIP method and the mechanisms of the selected decontamination and capturing technologies that applied in our study.

Chapter 6: This chapter summarizes the conclusions of the total capital, an optimum way of taking measurements proposed in this provision and possible future research suggested based on the knowledge obtained from this thesis.

2. THEORY – METHODOLOGY

2.1 INTRODUCTION

The geoelectrical methods are widespread investigation methods of applied geophysics. The electrical method is carried out through electric current injection of known characteristics in the soil and measuring the developing voltage. In some cases, if we suddenly stop the providing current into the earth, we see that the measured potential does not vanish immediately.

The gradual change of the potential may be due to various reasons that can be attributed either to the influence of the instrumentation or the influence of the geological formations. General the effect of the instrument is very small, but there are geological formations where the time that is required until the measured voltage reaches the final value to be quite high. The manner in which is altered the measured voltage changes from place to place and shape, and the rise time of the voltage curve in function of time can be a diagnostic tool and is the principle of the operation of the induced polarization method (IP).

The phenomenon of induced polarization characterizes the degree to which the subsurface is able to store electrical charge, analogous to a capacitor (Sumner, 1976). This polarization occurs [1] at the interface between a metal and a fluid (electrode polarization), [2] at the interface between a non-metal (e.g. silica or clay minerals) and a fluid (membrane polarization), [3] in the inner dielectric boundary layers on a mesoscopic scale, or at the external electrode-sample interface on a macroscopic scale which leads in both cases to a separation of charges (Maxwell-Wagner polarization), [4] in the inner part of the electrical double layer at the interface between minerals and water (polarization of the Stern layer), and [5] in the outer part of the electrical double layer (polarization of the diffuse layer) (Kemna et al., 2012; Leroy et al., 2008; Lesmes & Morgan, 2001; Marshall & Madden, 1959; Schmutz et al., 2010). This polarization can be observed both in time (IP) and frequency (SIP) domain.

Below are presented the different polarization mechanisms that mentioned above.

2.1.1 Electrode Polarization Mechanism

During of the immersion of an electrode in an ionic solution (electrolyte) of specific ion concentration, we observe a separation-redistribution of the ions and the appearance of a potential leakage between the surfaces of the electrode and the solution (Fig. 2.1).

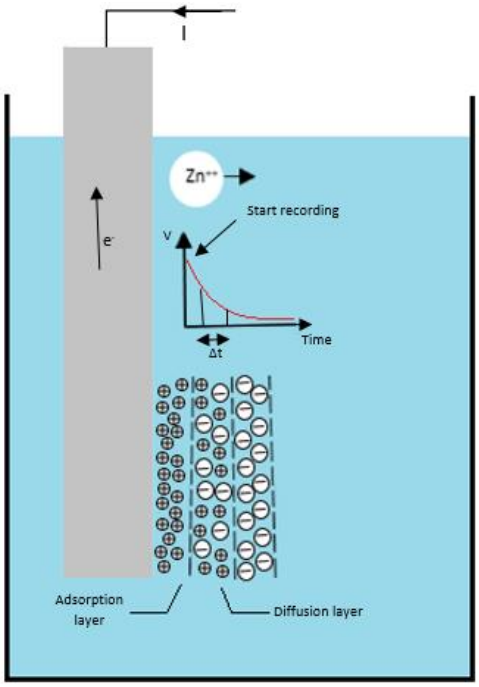

Figure 2.1 Illustration of elements of electrode polarization (modified from Joseph, 2016).

By applying an external voltage to the electrode, the ionic equilibrium is disturbed causing a current flow. The measured potential difference perpendicular to the interface metal-solution change from the initial value. Interrupting the external voltage, causes the gradually return of the voltage to its original value. This distribution has the form of an electrical double layer which consists of an adsorbed and a diffused layer of ions (Fig. 2.1).

Assume geological formation that contains sulfides, which been found to be ideal for the application of the induced polarization method, the conductivity is ionic (through movement of ions in the electrolyte in the porous of the geological formation) and electronic (through metals) (Tselentis & Paraskeuopoulos, 2013) (Fig. 2.2a). Such formulations are considered as a set of metal particles dispersed in the rock that have a specific porosity. If the movement of ions moving through the porous is hindered by a metal particle, then there is a gradual concentration of ionic charges (Fig. 2.2b). Some of the ions can be discharged through oxidation.

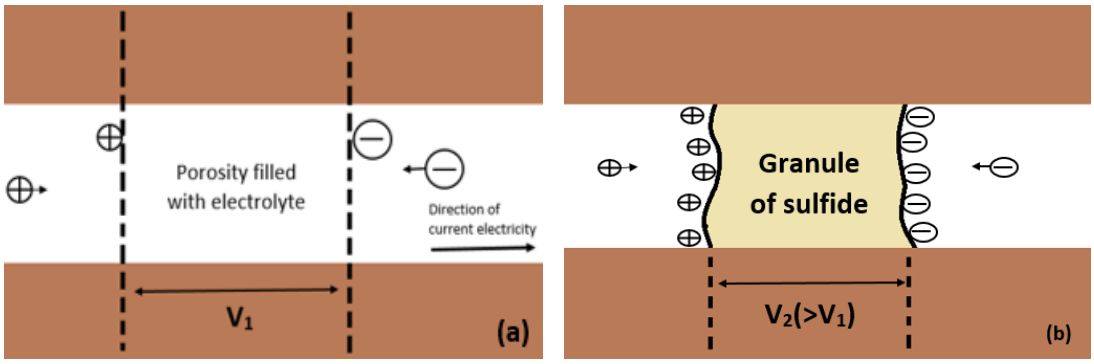

Figure 2.2 (a) porosity filled with electrolyte solution and the measured voltage V_1 in conditions of free ionic motion, **(b)** porosity similar with (a) but clogged by mineral particle causing the overvoltage and the measured voltage $V_2 > V_1$.

The manner in which the loads accumulated causes potential increase on the outer surface of the metal particle (Tselentis & Paraskeuopoulos, 2013). This phenomenon is known as overvoltage and the particles are considered polarized. If the voltage is stopped, there is a gradual dissolution of the accumulated ions through different pathways in the rock (Fig. 2.3). As a result, the metal particles' voltage to be close to zero within a finite time depending on various factors such as the structure of the rock, the porosity, the electrical conductivity of the fluid hosted in the porous, the hydraulic conductivity of the rock, etc.

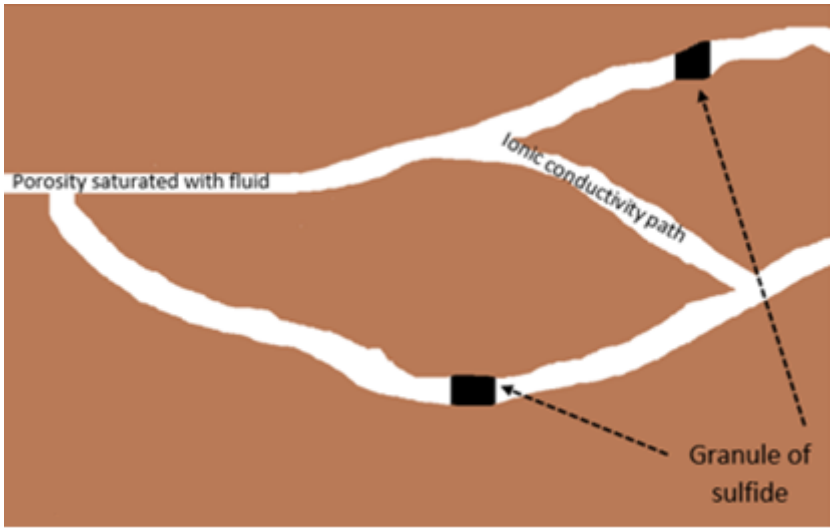

Figure 2.3 Example of ionic alternative path when the porosity is partially filled by grains of sulfur mineral (modified from Tselentis & Paraskeuopoulos, 2013).

2.1.2 Membrane Polarization

The phenomenon of membrane polarization is due to the ion separation because of narrow pore space within boundary layer thicknesses. Charges cannot flow easily, so they accumulate when an electric field is applied. The result is a net charge dipole which adds to any other voltages measured at the surface.

A second form of membrane polarization occurs when there is presence of clay particles which partially block ionic solution paths (Fig. 2.4). If we apply an external potential difference through an electric current injection in the region, we will observe that the positive charges pass easily because of the smaller size, while negative carries which are generally larger than positive accumulate. By cutting off the electric current that we have just injected, the ions will tend to regain their original distribution in space, but as to perform this distribution again it is required some time, and therefore there has been a polarization.

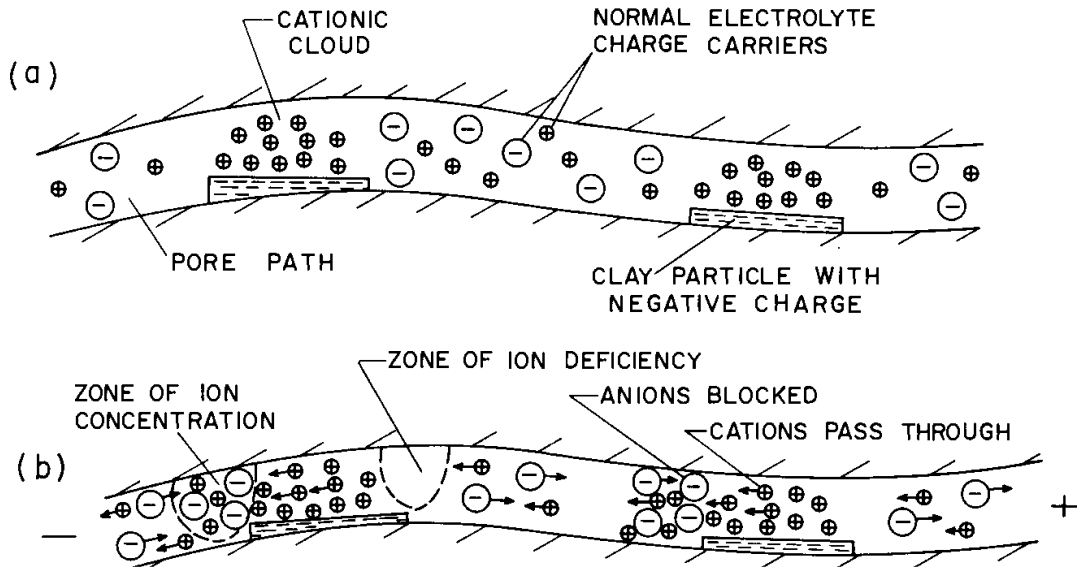

Figure 2.4 Membrane polarization in rock containing clay particles, (a) before application of electric current, (b) after application of electric current (Sumner, 1976).

2.1.3 Maxwell-Wagner polarization

The Maxwell-Wagner polarization is an interfacial polarization due to the discontinuity of displacement currents in a multiphase system with discontinuities of the dielectric permittivity and/or electrical conductivity at the interface between the different phases (Kemna et al., 2012). The Maxwell-Wagner polarization occurs in mixtures composed of segregated constituents with different dielectric permittivity and electrical conductivity (Chen & Or, 2006). The Maxwell-Wagner polarization is mainly responsible for polarization phenomena at the upper end of the considered frequency spectrum, typically above 1 kHz (Kemna et al., 2012).

2.1.4 Electrical Double Layer (EDL) polarization

Electrical double layer (EDL) appears on the surface of an object (solid particle, liquid droplet, gas bubble or porous object) when it is exposed to a fluid. The EDL refers to two parallel layers of charge surrounding the object. Electrical double layer polarization caused by the accumulation of charge carriers in some discontinuities at the porous material in the absence of metallic conductors (Schmutz et al., 2010) and has a significant influence on the behavior of colloids and other surfaces in contact with solutions or solid-state fast ion conductors. EDL describes the electrochemical processes that are responsible to a large extent for the observed SIP responses (Attwa & Günther, 2013).

The first layer, the surface charge (either positive or negative), comprises ions adsorbed onto the object due to chemical interactions. This first layer is called Stern layer and characterizes the interfaces processes in the inner part of EDL. Stern layer polarization contributes to lower frequencies (bellow 100 Hz).

The second layer in EDL is composed of ions attracted to the surface charge via the Coulomb force, electrically screening the first layer. It is loosely associated with the object and it is made of free ions that move in the fluid under the influence of electric attraction and thermal motion rather than being firmly anchored, thus called the diffuse layer.

The presence of an externally applied electric field displaces the electrical diffuse layer. In the far-field, the cations move in the direction of the electric field and the anions move in the opposite direction (Kemna et al., 2012). It is worthy to note that diffuse layer polarization is closely related with membrane polarization in the current conceptualization of the electrochemical IP mechanisms (Kemna et al., 2012; A. Revil & Florsch, 2010).

2.2 APPLICATION OF SPECTRAL INDUCED POLARIZATION

Of the most common uses of the method is that the mining research for the determination of the location and extent of mineralized rocks within a host material (Kemna, 2000; Luo & Zhang, 1998; Marshall & Madden, 1959).

In recent decades, the use of electrical methods has become increasingly preferred to calculate hydraulic parameters over other methods (Attwa & Günther, 2013; Zisser et al., 2010). Many successful efforts have shown the connection of the hydraulic conductivity with the observed electrical properties, but taking into account and other assumptions, like porosity and geometry of the pore space as a unique relationship between electrical properties and hydraulic conductivity does not exist (Attwa & Günther, 2013; Hördt et al., 2007; Mazáč et al., 1985). The method of induced polarization both in the time domain and in the frequency domain (SIP) provides more information about the pore size than other electrical methods, which makes it first choice in hydrogeological applications (Slater & Lesmes, 2002). Several empirical and semi-empirical relationships between IP parameters and hydraulic conductivity have been suggested (Attwa & Günther, 2013; Hördt et al., 2007; L. Slater & Lesmes, 2002b). Slater & Lesmes (2002b) suggested a model between the imaginary component and the grain size which according to them exerts the primary control on SIP response.

Last couple decades there is an extensive use of the method in environmental site characterization, especially with soil contamination with great success. Moreover in case of combined organic and inorganic contaminants, the SIP method can provide additional information for the detection and separation of the two contaminants (Kemna, 2000).

Furthermore, many attempts have been made for the specification of SIP response in hydrocarbon contamination with the results to vary (Borner et al., 1993; Brown et al., 2004; Cassiani et al., 2009; Olhoeft, 1985; Vanhala, 1997). In many cases, the results were similar with the hydrocarbon contamination acted to suppress the SIP response, but in others experiments, it was observed an enhancement of the response.

Over the last decade they have done many promising applications in the field of biogeophysics sector to monitor the biochemical state. It has determined that “SIP response is one of the most promising geophysical techniques for detecting the alteration of mineral-fluid interfaces and pore geometries resulting from microbial growth and biofilm formation” (Kemna et al., 2012; Ntarlagiannis & Ferguson, 2009). The production of organic acids and enhancement of mineral weathering due to microbiological processes, result the alteration of the electrical signatures in the subsurface (Ntarlagiannis, 2006). Even the presence of inactive microbial cells in the porous media can cause an impact in the recorded IP signal (Ntarlagiannis et al., 2005)

2.3 IP MODEL AND RELATION PARAMETERS

2.3.1 Theoretical Basis of IP method

The IP effect appears as a residual voltage following termination of an applied current (time-domain) or as a frequency-dependent resistivity (frequency-domain) (Slater & Lesmes, 2002). Conventional measures of the polarization include the phase angle (f), chargeability (M) and percentage frequency effect (PFE). Chargeability is measured in the time domain, whereas phase angle and PFE are measured in the frequency domain. The most common measurement of the IP effect is the chargeability (M), defined as (Ward, 1990):

$$M = \frac{\int_{t_s}^{t_f} V_s dt}{V_p} \cdot \frac{1}{\Delta t} \tag{2.1}$$

where Vs is a residual voltage integrated over a time window defined between times t_s and t_f after termination of an applied current, Vp is the measured voltage at some time during application of the current, and Δt equals the length of the integrated time window. Units of chargeability are typically quoted as millivolts per volt (mV/V). Figure (2.5) shows the IP waveform and the properties that have used for the calculation of M. An equivalent measurement in the frequency domain is the percentage frequency effect (PFE).

$$PFE = \frac{\sigma(\omega_1) - \sigma(\omega_0)}{\sigma(\omega_0)} \cdot 100 \tag{2.2}$$

where $\sigma(\omega_1)$ and $\sigma(\omega_0)$ are the conductivity measured at frequencies ω_1 and ω_0 ($\omega_1 > \omega_0$). A measure of the method most widely used is the phase angle (ϕ). The phase angle, as in all electrical measurements is related to bulk and surface conduction mechanisms. In non-metallic environments observed small angles, are equal to the ratio of the imaginary conductivity (σ'') to the real conductivity (σ') (Slater & Lesmes, 2002),

$$\phi(\omega) = \tan^{-1}\left(\frac{\sigma''(\omega)}{\sigma'(\omega)}\right) \cong \frac{\sigma''(\omega)}{\sigma'(\omega)} \tag{2.3}$$

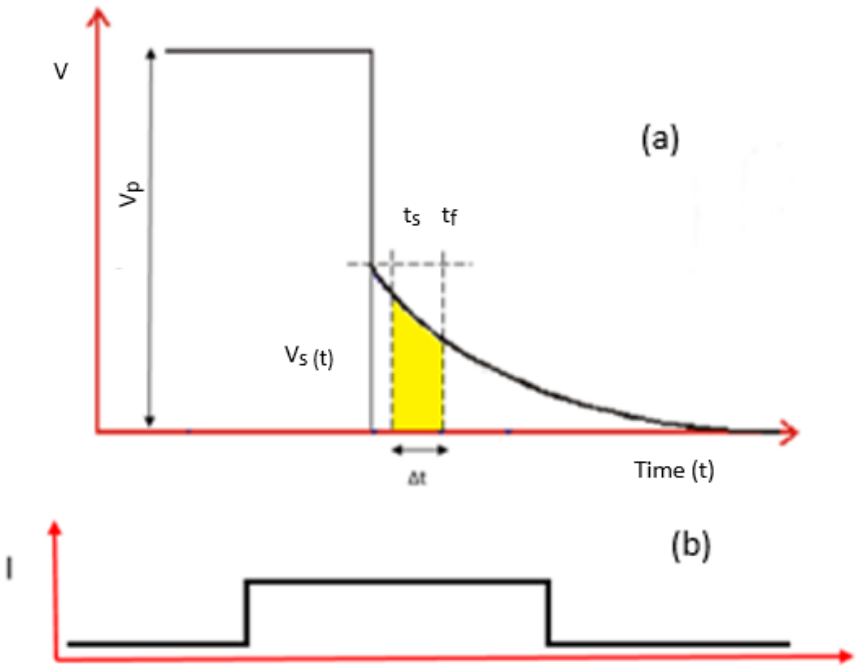

Figure 2.5 (a) Time-domain IP signal and the measured parameters for the calculation of M, **(b)** Square current waveform at low frequency (~ 1 Hz) which shows the continuous change of the polarity.

The non-metal polarization resulting from the diffusion that control polarization processes at the interface between the mineral surfaces and the pore solution (Slater & Lesmes, 2002) can be represented by a complex surface conductivity (σ^*_{surf}),

$$\sigma^*_{surf}(\omega) = \sigma'_{surf}(\omega) + i\sigma''_{surf}(\omega) \tag{2.4}$$

The processes that take place on the surfaces of clay-bearing rocks and their large surface area of clays enhance the magnitude of polarization in sediments and rocks that enclose clays. The polarization effects are also significant and measurable in clay-free unconsolidated material.

As mentioned above the IP phenomenon indicates the capacity of the subsurface. At high frequencies, the intrinsic capacity of the material is determined mainly by the high-frequency dielectric constant (k_∞). The high-frequency imaginary conductivity response is given by $\sigma''_\infty = \omega k_\infty \varepsilon_\infty$, where ε_∞ is the permittivity of vacuum. At low frequencies (f ≤ 1000 kHz), where IP effect is typically measured in the field $\omega k_\infty \varepsilon_\infty \ll \sigma''_{surf}(\omega)$, and the low-frequency SIP response of the sample is given by (L. Slater & Lesmes, 2002),

$$\sigma^* = \left(\sigma_{bulk} + \sigma'_{surf}(\omega)\right) + i\sigma''_{surf}(\omega) = \frac{1}{\rho(\omega)} \tag{2.5}$$

where σ_{bulk} is a bulk conduction term and $\rho(\omega)$ is the complex resistivity. In this frequency range, the imaginary component of the conductivity can be considered as a function of the surface conductivity, whereas the real component of the conductivity is a function of both the bulk and surface conductivity mechanisms (Slater & Lesmes, 2002). In simple terms, the real conductivity (σ′) represents the ohmic conduction (energy loss) and the imaginary conductivity

(σ′′) is a way to express the rate of polarization (energy storage). Below is a simple circuit model (Fig. 2.6), which represents the low frequency electrical properties of a sample under study which represents the low-frequency electrical properties of the sample, contains a purely conductive flow pathway in parallel with a frequency dependent complex conductivity element (σ^*_{surf}).

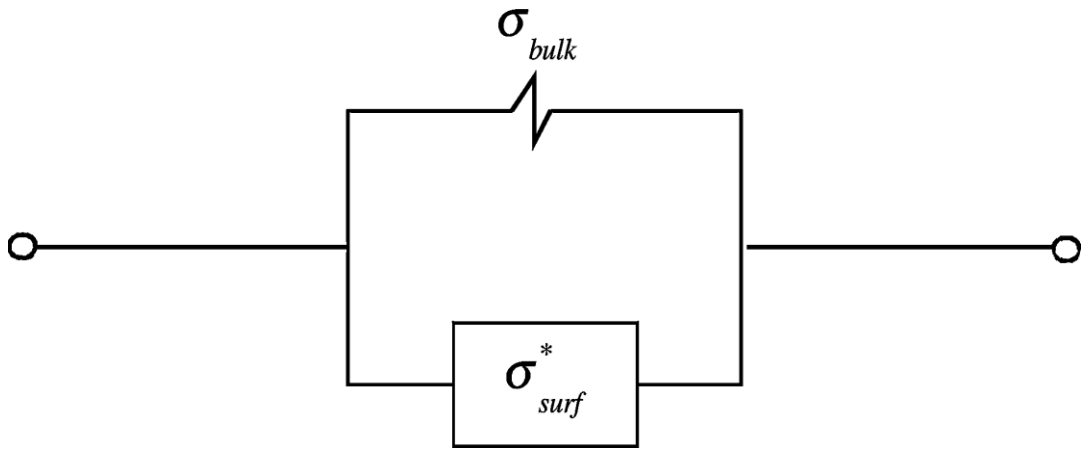

Figure 2.6 Simple circuit model for low-frequency (f ≤ 1000 kHz) electrical current flow in nonmetallic rocks and sediments (Slater & Lesmes, 2002).

The complex surface-conductivity element represents a diffusion-controlled electrochemical polarization pathway at the grain surface–fluid interface. An important aspect of this model is that low-frequency capacitive properties of the sample depends on the electrochemical surface phase, whereas the low-frequency conductive properties of the sample depends on the bulk conduction and surface conduction mechanisms (Slater & Lesmes, 2002):

$$\sigma''_{rock}(\omega) = \sigma''_{surf}(\omega) \tag{2.6}$$

and

$$\sigma'_{rock}(\omega) = \sigma'_{bulk}(\omega) + \sigma'_{surf}(\omega) \tag{2.7}$$

The two parts of the complex surface conductivity (real and imaginary) are related with the specific surface area, the surface charge density, and the surface ionic mobility (Lesmes & Frye, 2001) which directly depend on the concentration and composition of the fluid present in the pores of a formation. The bulk conductivity can be expressed by Archie's Law (Archie, 1942),

$$\sigma'_{bulk}(\omega) = \sigma_w \Phi^m S^n \tag{2.8}$$

where σ_w is the solution conductivity, Φ is the porosity, S is the saturation, and m and n are the cementation and saturation exponents. Based upon the parallel circuit model, the phase response of the rock will be given by,

$$\phi(\omega) = \frac{\sigma''_{surf}(\omega)}{\sigma'_{bulk} + \sigma'_{surf}(\omega)} \tag{2.9}$$

If the bulk conductivity is much greater than the surface conductivity (case of high salinity), then,

$$\phi(\omega) \cong \frac{\sigma''_{surf}(\omega)}{\sigma''_{bulk}(\omega)} \tag{2.10}$$

Equations (8), (9), and (10) show that the field IP parameters ϕ, PFE, and M are relative measures of the surface polarization, which tend to decrease with increasing sample conductivity.

As bulk conduction increases with increasing solution conductivity, porosity, or saturation, the phase response will decrease in magnitude. For convenience in the interpretation, it is better to separate the field data into two different components. The real component will be primarily indicative of conduction processes, which, in the case of low clay content, can be modeled using Archie's Law. The imaginary component will be primarily indicative of the surface polarization mechanisms at the grain-solution interface (Slater & Lesmes, 2002).

Similar to the phase response, PFE and M describe the strength of the polarization process relative to ohmic conduction. The PFE is the ratio of the conductivity dispersion to the formation conductivity, which is primarily determined by the bulk rock properties. Since the low-frequency conductivity dispersion is only a function of the surface properties, the PFE response can be written as,

$$PFE = \frac{\sigma'_{surf}(\omega_1) - \sigma'_{surf}(\omega_0)}{\sigma'_{bulk}} \cdot 100 \tag{2.11}$$

The chargeability can be defined in two parallel conduction paths, which can be thought of as a bulk conductivity (σ'_{bulk}) and a surface conductivity (σ'_{surf}) (Pelton, Ward, Hallof, Sill, & Nelson, 1978). If the surface conductivity is much smaller than the bulk conductivity, the chargeability is proportional to the ratio of the surface conductivity to the bulk conductivity effects (Slater & Lesmes, 2002):

$$M \propto \frac{\sigma'_{surf}}{\sigma'_{bulk} + \sigma'_{surf}} \cong \frac{\sigma'_{surf}}{\sigma'_{bulk}} \tag{2.12}$$

2.3.2 Normalized Parameters

Weighting of the parameters mentioned above, by the measured conductivity (or resistivity) gives the normalized parameters that follow in this subchapter.

One of these normalized parameters is the imaginary conductivity (σ''_{rock}), which is given by,

$$\sigma''_{rock} = \sigma'_{rock} \tan(\phi) \cong \sigma'_{rock}\phi \tag{2.13}$$

The metal factor as defined by Marshall & Madden (1959) is given by,

$$MF = \alpha\sigma(\omega_0)PFE = \alpha\big(\sigma(\omega_1) - \sigma(\omega_0)\big) \qquad (2.14)$$

where α is an arbitrary unit less constant, taken to be equal to 2π x 10^5 (Marshall & Madden, 1959). The normalized chargeability (MN) is given by

$$MN = \sigma'_{rock} M \qquad (2.15)$$

The normalized IP parameters are directly related to the complex surface-conductivity parameter $\sigma^*_{surf}(\omega)$.

The figure (2.7) shows the relationship between the IP parameters and the normalized IP parameters on fluid conductivity for a Berea sandstone (Fig. 2.7). In these experiments which presented in Slater & Lesmes (2002), the salinity of the saturating solution was varied from 24 to 8000 mS/m NaCl. The field IP parameters decrease with increasing solution conductivity and the normalized IP parameters increase with increasing salinity, up to a solution concentration of 1000 mS/m, at which point they then decrease with increasing salinity. The graphs were related with the sensitivity of the normalized IP parameters to the surface chemical properties of porous media.

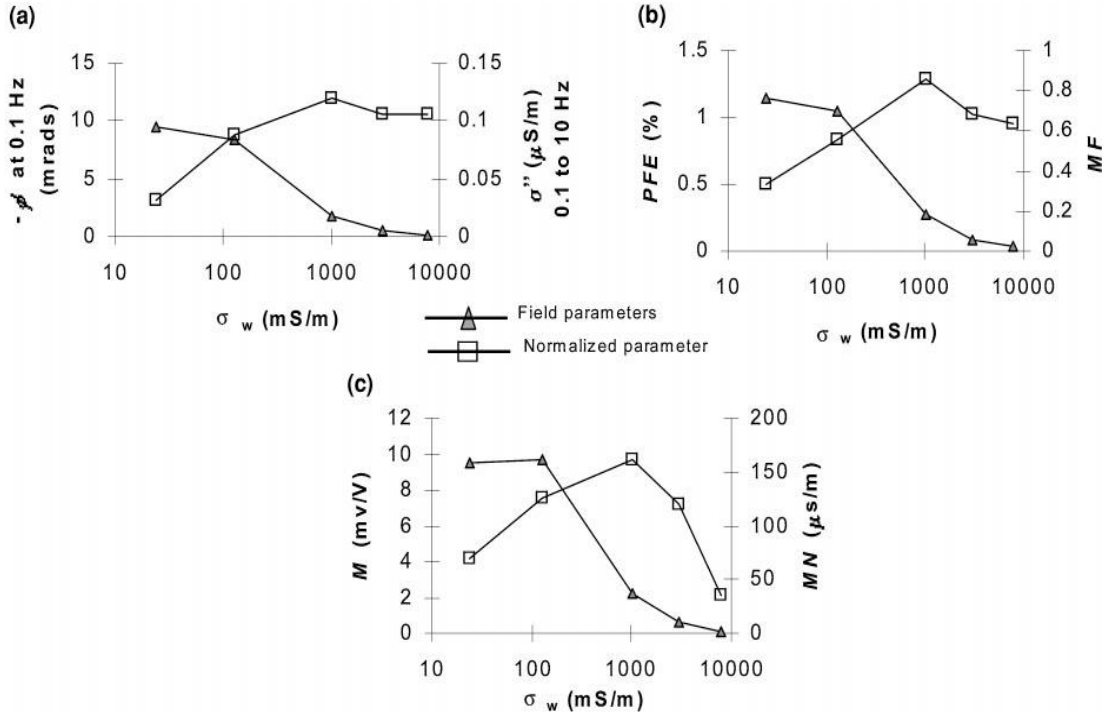

Figure 2.7 Dependence of IP parameters and normalized parameters on fluid conductivity (σ_w) for a Berea sandstone core (Slater & Lesmes, 2002).

2.3.3 SIP Modeling

As part of this thesis, we did not perform any modeling on the data, however if someone wants to apply some modeling to raw SIP data in order to characterize the frequency dependence of electrical properties, a quantitative description of their spectral behavior is needed (Kemna, 2000). There are many mathematical models based on electrochemical theories, petro-physical

parameters, general relaxation theory, etc., to achieve the above requirement. The mathematical relations presented below are described in terms of resistivity because of the similar behavior as dielectric permittivity and in the geophysical society is more common to use the resistivity than conductivity when referred to geoelectrical techniques.

For the purposes of the experimental SIP data have been used from time to time various phenomenological models, such as Debye model, describing orientational dipole polarization in simple, viscous dielectrics. The model is based on the existence of a polarization P due to an applied electric field. Upon termination of the electric field, the decrease of P at a time t is exponential and proportional to the value of P at that instant.

$$\partial_t P = -\frac{1}{\tau} P(t) \tag{2.16}$$

where τ is the relaxation time. Through the Laplace transform, we can get the corresponding permittivity transfer function as

$$\varepsilon(\omega) = \varepsilon_\infty + \frac{\varepsilon_0 - \varepsilon_\infty}{1+(i\omega\tau)} \tag{2.17}$$

where ε_∞ and ε_0 are the asymptotes of permittivity at infinite and zero frequency, respectively and I represents the pure imaginary number. Equation (2.17) extend to

$$\varepsilon(\omega) = \varepsilon_\infty + (\varepsilon_0 - \varepsilon_\infty) \int_0^\infty \frac{g(\tau\prime) d\tau\prime}{1+(i\omega\tau\prime)} \tag{2.18}$$

for any arbitrary continuous distribution of relaxation times $g(\tau')$ due to different physicochemical mechanisms that can take place.

The behavior of most dielectrics deviates from the Debye model that assumes a single settling time characteristic of the material. As extension to Debye model is the Cole-Cole model (Pelton et al., 1978) which is widely prevalent and can be expressed in terms of complex resistivity as

$$\rho(\omega) = \rho_0 \left[1 - M\left(1 - \frac{1}{(1+(i\omega\tau)^c)^a}\right)\right] \tag{2.19}$$

where ρ_0 is the resistivity, M is the chargeability, τ is the relaxation time and α and c are constants describing the shape of the dispersion observed in the phase data (Ustra, Slater, Ntarlagiannis, & Elis, 2012). This generalized model can be reduced to several special cases. In the standard Cole-Cole model, α = 1. When both constants (a and c) are equal to 1, the model is known as Debye model.

A methodology developed to invert broadband dielectric spectra for a distribution of relaxation times that is primarily controlled by the grain-size distribution (Lesmes & Morgan, 2001). Nordsiek & Weller (2008) proposed an alternative approach to fit SIP data, known as Debye Decomposition (DD). In this approach, the SIP measurements are modelled as a superposition of n different Debye spectra. Each Debye spectrum is characterized by a specific chargeability (M_k) and a relaxation time (τ_k) as,

$$\rho(\omega) = \rho_0 \left[1 - \sum_{k=1}^{n} M_k \left(1 - \frac{1}{1+i\omega\tau_k}\right)\right] \quad (2.20)$$

The n pairs of relaxation time (τ_k) and chargeability (M_k), along with the resistivity are the resulting parameters of the model. The integral or total chargeability (M) and mean relaxation time (τ) can be obtained by,

$$M = \sum_{k=1}^{n} M_k \quad (2.21)$$

and

$$\tau = exp\left(\frac{\sum_{k=1}^{n} M_k \cdot ln\, \tau_k}{\sum_{k=1}^{n} M_k}\right) \quad (2.22)$$

The relaxation time is then considered to be proportional to the effective length scale controlling the polarization (Ustra et al., 2012). The normalized chargeability is considered a global direct estimate of the polarizability of the material over the measured frequency range and is thus analogous to σ'' at a single frequency.

$$M_n = \frac{M}{\rho_0} \quad (2.23)$$

Relative to Cole-Cole type models, the DD offers more flexibility in fitting a wider range of shapes of phase spectra (Nordsiek & Weller, 2008). Weller et al. (2010) successfully applied this approach to numerous data sets from SIP measurements on sandstone, sand-clay mixtures and metallic samples. They were able to find a strong linear relationship between m and specific surface area normalized to the pore volume across the multiple data sets (Weller et al., 2010).

Some other pairs of classical transfer functions and their time constant distributions that are widely used are presented in Table (2.1).

Table 2.1 Time and frequency domain expressions of some classical transfer functions (reconstruction from Florsch et. al, 2012).

	$g_\tau(\tau)$	$Z_\omega(\omega) = \int_0^\infty \frac{g_\tau(\tau)}{1+i\omega\tau} d\tau$
1	Debye $g(\tau) = \delta(\tau - \tau_0)$	$\frac{1}{1+i\omega\tau_0}; Re = \frac{1}{1+\omega^2\tau_0^2};$ $Imag = \frac{-\omega\tau_0}{1+\omega^2\tau_0^2}$
2	Cole – Cole $g(\tau) = \frac{1}{2\pi\tau} \frac{\sin \alpha\pi}{\cosh\left[(1-a)\log\left(\frac{\tau}{\tau_0}\right)\right] - \cos\alpha\pi}$	$\frac{1}{1+(i\omega\tau_0)^{1-\alpha}}$ $Re = \frac{1}{2}\left[1 - \frac{\sinh(1-\alpha)\log(\omega\tau_0)}{\cosh[(1-\alpha)\log(\omega\tau_0)] - \cos\alpha\pi}\right]$ $Imag = \frac{1}{2}\frac{\cos(\alpha\pi/2)}{\cosh[(1-\alpha)\log(\omega\tau_0)] + sin(\alpha\pi/2)}$
3	Davidson – Cole $g(\tau) = \frac{\sin\beta\pi}{\pi}\left(\frac{\tau}{\tau_0 - \tau}\right)^\beta \; if\; \tau < \tau_0$ $g(\tau) = 0 \; if \; \tau \geq \tau_0$	$\frac{1}{(1+i\omega\tau_0)^\beta}; with\ y = \mathrm{a}\ \tan(\omega\tau_0)$ $Re = \cos\beta y(\cos y)^\beta;$ $Imag = -\sin\beta y\,(\cos y)^\beta$
4	Constant Phase Element (CPE) $g(\tau) = \frac{\sin\beta\pi}{\pi}\tau^{-\beta}$ Only valid if $0 < \beta \neq 1$	$-\omega^{\beta-1}e^{i\frac{\pi}{2}(1+\beta)}$ $Imag = -\omega^{\beta-1}\sin\left(\frac{\pi}{2}(\beta+1)\right)$
5	$g(\tau) = \frac{1}{\tau}, \tau \in I_{\tau_1,\tau_2}$ $g(\tau) = 0, \tau \notin I_{\tau_1,\tau_2}$	$Re = \ln\left(\frac{\tau_2}{\tau_1}\sqrt{\frac{1+\omega^2\tau_1^2}{1+\omega^2\tau_2^2}}\right) \cdot (1)$ $Imag = \tan^{-1}(\omega\tau_1) - \tan^{-1}(\omega\tau_2)$
6	William & Watt (1970) $\frac{1}{2\sqrt{\pi\tau\tau_0}} exp\left(-\frac{\tau}{4\tau_0}\right)$	$\frac{\sqrt{\pi}}{2\sqrt{\tau_0}} exp\left(\frac{1}{\tau_0}\right) erfc \frac{1}{\sqrt{i\omega\tau_0}}$
7	Kirkwood and Fuoss (1941) $\frac{2}{\pi}\frac{\cos\left(\frac{\alpha\pi}{2}\right)\cosh\left(a\log\left(\frac{\tau}{\tau_0}\right)\right)}{cos^2\left(\frac{\alpha\pi}{2}\right) + sinh^2\left(a\log\left(\frac{\tau}{\tau_0}\right)\right)}$	$Imag = \frac{1}{\cos h\left(\alpha\log\left(\frac{\tau}{\tau_0}\right)\right)}$

3. EXPERIMENTAL PREPARATION

3.1 WASTEWATER USED

The olive-oil industry is one of the most important sectors of the economic development in the Mediterranean countries. Greece is ranked third in olive-oil production worldwide (after Spain and Italy) (Kirmizakis et al., 2015; Niaounakis & Halvadakis, 2006; Paraskeva & Diamadopoulos, 2006). Consequently, olive oil production is an important activity which is vital for both the local and national economy.

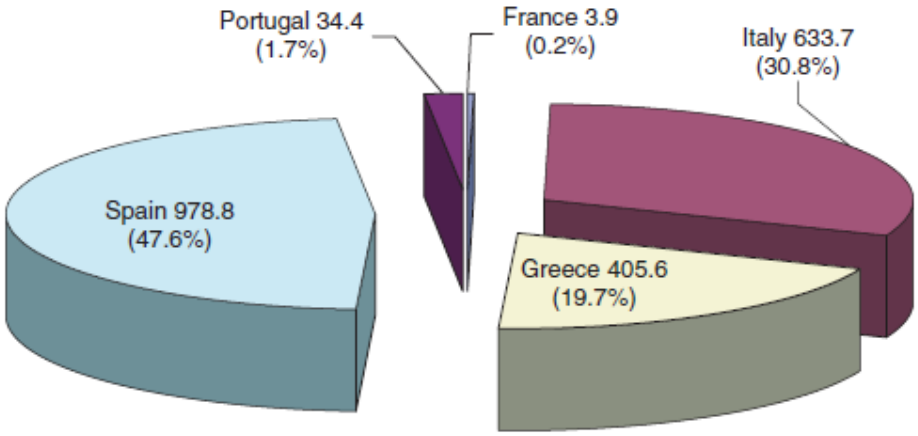

Figure 3.1 Average production of olive oil in EU for the harvesting years 1999/2000 – 2002/2003 (Niaounakis & Halvadakis, 2006)

The basic steps in making olive oil are always the same, no matter what kind of equipment is used. The first step in the oil extraction process is cleaning the olives and removing the stems, leaves, twig and other debris left with olives. The second step is crushing the olives into a paste. The purpose of crushing is to tear the flesh cells to facilitate the release of the olive oil from the vacuoles. Malaxing (mixing) the paste for 20 to 45 minutes allows small oil droplets to combine into bigger ones. It is an indispensable step. The paste can be heated or water added during this process to increase the yield, although this generally results in lowering the quality of olive oil. Longer mixing times increase olive oil yield but allows a longer oxidation period that decreases shelf life. The next step consists in separating the olive oil from the rest of the olive components (wastewaters and solids).

Although the beneficial properties of olive oil on human health, its production procedure generates large volume of wastes. Olive-mill wastewaters are characterized by a dark brown color and unpleasant smell, consisting mainly of water, high organic (mainly phenols and polyphenols) and low inorganic compounds (e.g. potassium and phosphorus). The wastes are acidic (pH = 4 to 5.5), have high conductivity (6000-16000 μS/cm) and exhibit high values BOD and COD.

The components of the waste organic fraction can be separated into three categories (Magalhães et al., 2017; Mulinacci et al., 2001; Rigane et al., 2015):

- compounds directly degradable (e.g., sugars, organic acids, aminoacids)
- biodegradable polymers (e.g. proteins, hemi-cellulose, pectins) and

- hardly degradable components such macromolecular fatty acids, tannins and phenolic compounds.

The last group of organic substances, even that contained a small amount compared to the other two, confers specific properties in the wastewater and substantially is responsible for the difficulties in the management of the wastewater. More specifically, the phenolic compounds in their broadest concept include tannins, are antioxidant substances and their presence inhibit the decomposition of fatty acids, some of which, particularly those of low molecular weight are toxic to lower living beings. Furthermore, certain phenolic compounds (especially in combination with each other or with other organic compounds) are toxic to plants which are at the stage of vegetative growth and to aquatic living organisms (Niaounakis & Halvadakis, 2006). However, we cannot ignore the fact that the presence of phenolic compounds in olive oil increases its antioxidant properties.

In the broader Mediterranean region, there are lots of olive-oil industries, which, most of them, produce olive-oil according to the national legislative frameworks, meaning that waste treatment is including in their activities. However, the majority of mills are small domestic enterprises, scattered throughout the countries, their owners are not well informed on the risks and on the alternative solutions and technologies for waste treatment, while in case that they are informed, they are not willing to adopt new technologies mainly due to their cost. Moreover, the Greek legislation framework on how the olive-oil producers should treat their wastewaters, is not clear. Thus, in the most of the cases, wastewaters are disposed untreated in unprotected evaporation ponds. Local geological conditions (permeable formations, such as porous or fractured/weathered rocks) result in a high vulnerability for groundwater contamination and soil degradation. Organic load, toxic polyphenols and high concentrations of inorganic elements in the OMW can alter dramatically the qualitative characteristics of the subsoil and affect its physical and chemical properties.

Figure 3.2 Evaporation pond in the broader area of Chania, Crete.

It is obvious that the production of olive oil cannot be stopped because of the produced wastes. Since toxic by-products from the olive-oil process will be always produced, emphasis must be given to the control of their pollution effect in the environment and their deposition. The characterization of pollution in public/private lands will facilitate the rehabilitation investments in urban/agricultural environments, minimizing their consequences to the public health.

The objective of this research is to provide an "environmental monitoring tool" to the end-users, by combining the most updated and known geoenvironmental methods (geochemical analysis, geophysical and biogeophysical methods) for studying and understanding of environmental degradation from the disposal of the olive-oil mills and the definition of a strategic framework for addressing this problem.

3.2 OMW TREATMENT

Various physicochemical treatment methods have been successfully implemented to reduce the OMW organic waste load. "Biological processes, aerobic and anaerobic, including anaerobic co-digestion with other effluents and composting, are predominant in the treatment of OMW" (Paraskeva & Diamadopoulos, 2006).

Meanwhile, on pilot scale it has tested the fluid production of compost. It has applied the chemical oxidation and anaerobic digestion of the OMW, with high technical operating and manufacturing costs, respectively. It has also been tested, the co-processing of OMW with sewage in artificial wetlands or in activated sludge plants, a technique that requires prior significant dilution of OMW. Simple physical techniques such as precipitation, have been tested

for the separation of OMW in fractions, but they all require a combination with any of the procedures mentioned above to give a satisfactory degree of the reduction of the organic load and toxicity of the waste.

Over the last years it has been achieved on a laboratory scale, the recovery of the polyphenols from the wastewater using membranes to be used in the perfume industry and medicine.

3.2.1 Phytoremediation

Phytoremediation is a green, effective, inexpensive and non-intrusive technology for the destruction or transformation of the contaminant in the soil (Alkorta & Garbisu, 2001; Singh & Ghosh, 2005). "This technology can be applied to both organic and inorganic pollutants present in soil (solid substrate), water (liquid substrate) or the air" (Singh & Ghosh, 2005). The procedures governing the process of phytoremediation (Fig. 3.3) are described below:

- **Rhizofiltration**. It includes the sorption of contaminants in the plant roots. There have been many attempts by researchers to isolate plants through the rhizofiltration have the ability to absorb significant amounts of heavy metals from soils.
- **Phytostabilization**. It aims to inactivate and isolate the contaminant to prevent the migration from the soil into the ground water or the atmosphere. The phytostabilization based on the ability of plants to secrete substances through their roots, which favor mechanisms such as the humification (commitment of the contaminant in the humic components of the soil), the lignification (commitment on the cell walls of the roots and soil sequestration). However, the major disadvantage is that the contaminant remains on the ground, as it is, and therefore requires regular monitoring or further processing (Singh & Ghosh, 2005).
- **Phytoextraction**. It refers to metal uptake and transport to the aboveground plant parts. This technique is applied in cases of contaminated soils with heavy metals. It relies on the use of plants which have the ability to accumulate high concentrations of metals in their biomass.
- **Phytovolatilization**. It is the transfer of the contaminants from the ground or water and exhaust-release from plant leaves, stems with the evapotranspiration process, after converted into volatile forms (Shah & Braun, 2004).
- **Phytodegradation**. It includes processes which lead to degradation of the contaminant. Degradation is carried out either within the plant, by metabolic processes or externally to the root area through enzyme production. Then takes place the integrating of the decomposed contaminant in the plant tissues.
- **Phytostimulation**. It describes the process of enhancing microbial activity in the rhizosphere by substances secreted by roots, such as sugars, alcohols, and acids that contain organic carbon, which microorganisms use as a food source (Shah & Braun, 2004). This leads to the increased microbial degradation of the contaminants in the soil.

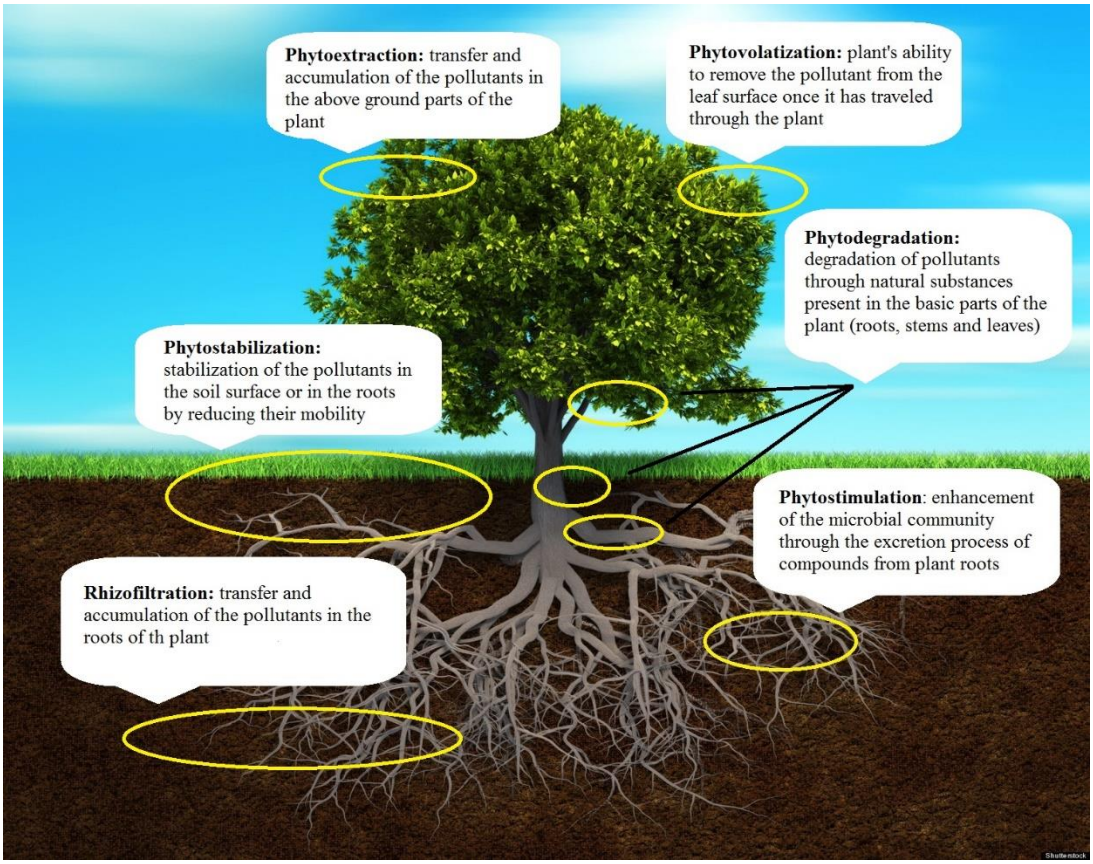

Figure 3.3 Processes associated with phytoremediation.

3.2.2 Biochar

Biochar is a solid residue produced by carbonization processes applied to the soil deliberately to isolate the carbon dioxide as a potentially valuable contribution to agriculture to improve soil fertility, enhancing sustainable production and reduce pollution of streams and groundwater (Barrow, 2012). The biochar may have different physical and chemical properties depending on the raw material and the carbonization technology (torrefaction, slow pyrolysis, intermediate pyrolysis, fast pyrolysis, gasification, hydrothermical carbonization, or flash carbonization) used for its production (Meyer et al., 2011).

In recent years, there is extensive promotion of the use of biochar in the field of countering land degradation. Starting point of this promotion was the rapid agricultural development, which in many cases has been proved environmentally unsustainable. Chronic use of chemical fertilizers can be expensive and constitute pollution hob and aquifer degradation. “Biochar could be a way of disposing of agricultural wastes, human sewage, livestock manure, industrial wastes, refuse, etc., with less greenhouse gas emissions and when applied to the land perhaps even a reduction of pre-existing groundwater and stream contamination (plus some carbon sequestration)” (Barrow, 2012). For example, the slow pyrolysis can minimize the possibility of production and release of toxic substances such as dioxins, and polyaromatic hydrocarbons, which could contaminate the biochar and escape into the environment (Barrow, 2012; Ippolito et al., 2012).

The benefits of biochar do not stop to the improvement of the soil and the commitment of organic substances. Many studies have shown its suitability for plant growth enhancement,

suppress greenhouse gas emissions (which is supported in the United Nations Convention to Combat Desertification), reduce the use of agrochemical products which have the effect of possible contamination of groundwater, reduce soil acidity, suppress methane and nitrous oxide in farmlands, reduce the cost of sewage and animal waste treatment, reduce aluminum toxicity and increase cation exchange capacity (Agrafioti et al., 2014; Bachmann et al., 2016; Manyà, 2012; Meyer et al., 2011).

Many studies have been done on the possible use of biochar to sequester organic and inorganic contaminants (Barrow, 2012; Mohan et al., 2014). Biochar could become a first choice adsorbent material for pollutants treatment, as it is more sustainable and requires less investment than other adsorbents (e.g. activated carbon). With this in mind, the research presented in this section has investigated the possible use of biochar as a mean of reducing the organic load of the OMW.

The ability of biochar adsorbing substances from contaminated aqueous solutions may be related to electrostatic interactions between ions of the solutions and the carbon negative surface charge, to ionic exchange between protons biochar surface and metal cations and acidic oxygen functional groups (e.g. carboxylic and lactone groups), inorganic impurities (e.g., ash and metal oxides) and to basic nitrogen groups present in the solid matrix of carbonaceous materials (Agrafioti et al., 2014).

4. LABORATORY MEASUREMENTS

4.1 COLUMN CONSTRUCTION AND SAMPLING

For the purposes of this thesis, identical acrylic columns were constructed (Fig. 4.1). Each column had a diameter of 50 mm and a length of 250 mm. For the current injection and the potential measuring in the columns, Ag-AgCl electrodes were constructed (Vanhala & Soininen, 1995). The current electrodes are placed at the ends of each column, while five chambers placed along the column for the potential electrodes, resulting the possibility of measuring different distances between the potential electrodes (30, 60, 90 & 120 mm).

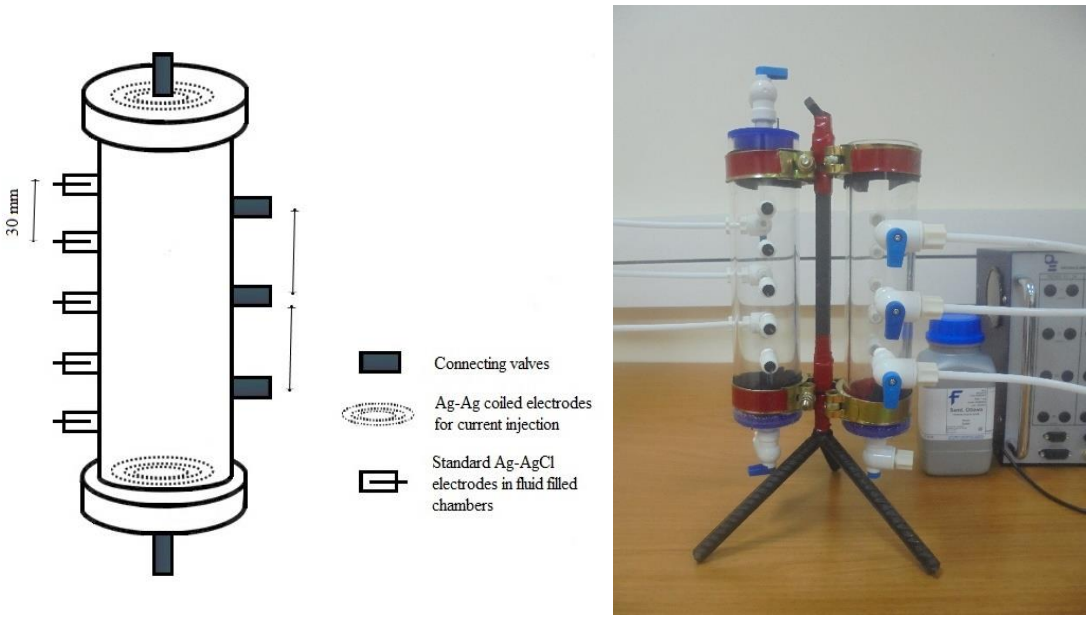

Figure 4.1 – Schematic and photograph of the used plastic column. In the columns, placed 2 Ag-AgCl electrodes for current injection (C1 & C2) and 5 Ag-AgCl electrodes in chambers for the potential measurements (P1-P5) (all the columns that used were identical).

4.1.1 Electrodes' Specifications

For the measurements was used Ag electrodes which had previously been chlorinated, because as has already been demonstrated by other works significance using these electrodes against other (Vanhala & Soininen, 1995). The Ag-AgCl electrodes have advantages over other common metal electrodes due to the more stable nature of the electrodes, which makes them almost non-polarizable, low impedance contact between the sample and measurement apparatus.

The new Ag electrodes before be chlorinated should first be cleaned with ETOH, while previously used electrodes should have removed the old coating chloride. A simple method for removing the coating silver chloride electrode is to quickly pass the electrode through a flame. A properly extinguished wire will be bright silver in color. As with a new wire, clean with ETOH before proceeding to remove finger oils.

4.2 SIP INSTRUMENTATION

A portable field/lab spectral induced polarization (PSIP) instrument (Figure 4.2), was used to determine the spectral response of fluid solutions of known concentrations. The instrument has the capability of simultaneously measuring two columns, as it has two current (C) injection channels, with six potential (P) channels. Detailed information about the SIP instrument are given in Appendix A.

Figure 4.2 - Portable Field/Lab Spectral Induced Polarization (PSIP) instrument by Ontash company.

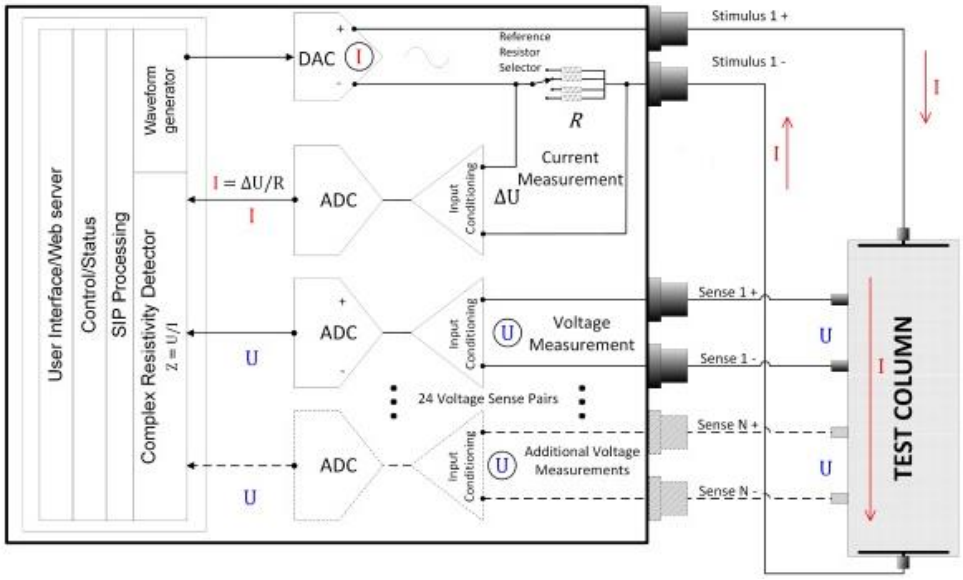

Figure 4.3 - Block diagram of the laboratory Spectral Induced Polarization instrument (http://www.ontash.com/products.htm).

The measured signal is measured as a resistance magnitude (|Z| = Vp/Ip) and phase angle (ϕ) between the injected current and the recorded voltage across the potential electrodes, and through this, we calculate the real and imaginary apparent resistivity or conductivity of the measured signal.

4.3 GEOMETRIC FACTOR MEASUREMENTS

Before any application of the method, it is necessary to estimate the errors and improve the quality of the results of the recorded signal. By measuring known solutions, we have the ability to calculate with greater precision the geometric factor in our measurements, which will help us to arrive at more accurate results during the procedure of the received data and to reduce possible errors.

This can be achieved by the graph of the Fluid Conductivity (μS/cm) to conductance (μS). The conductance in μS is result from:

$$Conductance = \frac{1}{Resistance} \cdot 1.000.000$$

Taking the inverse of the slope (1/slope) of the graph and replacing in the equation that it follows we can calculate the real fluid conductivity in μS/cm for all measurements that we have to do with the under study fluid:

$$Fluid\ conductivity = \frac{1}{Resistance} \cdot K(geometric\ factor) \cdot 1.000.000$$

It is noteworthy that after this process, the real conductivity values of the fluids were much closer to the real one as measured in the laboratory of chemistry both with method ASTM D1125-95, and by the control measurement using a conductivity meter.

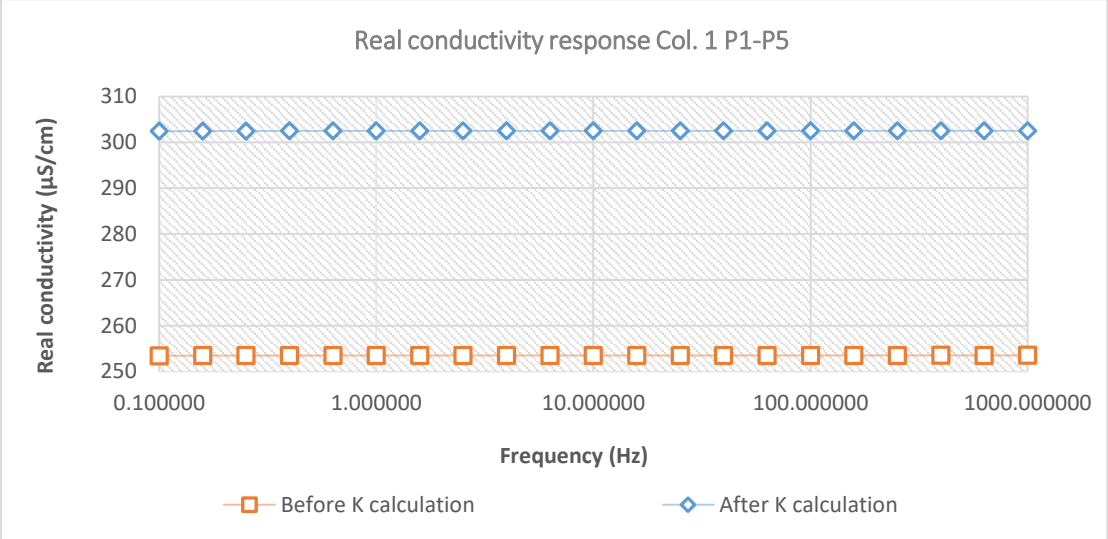

Figure 4.4 Real conductivity for column 1 during fluid tests before and after taking into account the K factor with a solution of know conductivity 296 μS/cm.

4.3.1 Preparation of solutions

The solutions prepared according to the standards of ASTM International and ASTM D1125-95 method. Through the proposed method, which defines precisely the molarity which must have certain standard solutions, we estimated the amount of KCl required for the preparation of the standard conductivity solutions. The following table shows the composition of the standard solutions according to the proposed method. The solutions' shelf life is estimated at two years if stored correctly.

Table 4.1 Composition of standard solutions according to ASTM D1125-95 method.

Conductivity	Molarity	Tolerance (at 25°C)
147 µS/cm	0.001 M	± 5 µS/cm
1413 µS/cm	0.01 M	± 12 µS/cm
12.88 mS/cm	0.1 M	± 0.11 mS/cm

For the purpose of measurements, prepared three solutions of known concentration (70 µS/cm, 300 µS/cm, and 900 µS/cm) using the method ASTM D1125-95, and calculating the exact concentration of the solutions.

Table 4.2 Composition of prepared solutions.

Conductivity	Molarity	Quantity of KCL (gr/L)
70 µS/cm	0.00047 M	0.035 gr/L KCl
300 µS/cm	0.002 M	0.14 gr/L KCl
900 µS/cm	0.0061 M	0.45 gr/L KCl

The solutions were placed into the acrylic tubes. All measurements were performed in controlled laboratory conditions where air temperature was in the range of 20-25 °C.

4.3.2 Geometric Factor

Below, the plot represent the measured conductance vs. the fluid conductivity for one of the three used columns. All the plots are presented in Appendix B.

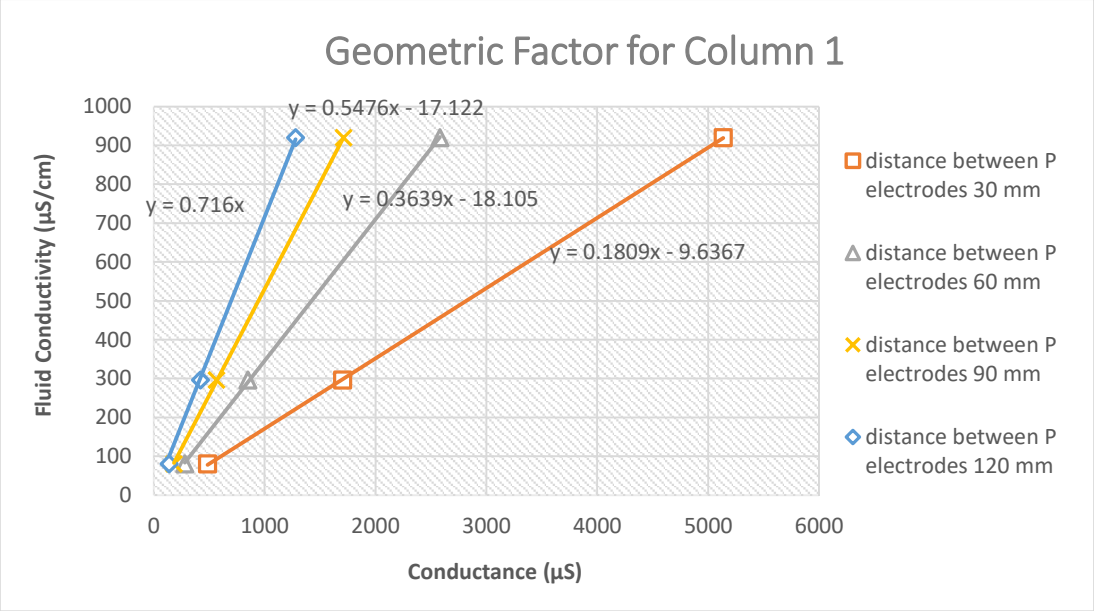

Figure 4.5 Calculation of geometric factor for one of the used columns**.**

4.4 SENSITIVITY IMPACT OF CHANGES IN GRAIN SIZE

The response of the induced polarization dependent on the link of grain size of the porous material that we use and its interfacial chemistry (Weller & Slater, 2015). However, it's not the only parameters determine SIP response (Leroy et al., 2008). As part of the measurements for the SIP sensitivity, we performed SIP measurements at different fractions of quartz sand in a known aqueous solution in order to see the effect of grain size on the SIP signal and the resolution of the method. The grain sizes that we used were quartz sand > 1000 µm, 1000-600 µm, 600-500 µm, 500-125 µm and Ottawa sand 841-595 µm. To prepare the samples, the sands were first moistened with deionized water and before filled in the sample holders, they left and to dry at ambient conditions. All measurements were performed in controlled laboratory conditions where air temperature was in the range of 20-25 °C.

4.5 RESPONSE AT DIFFERENT FLUID CONCENTRATIONS

Taking note of that many times we have diffusion of contaminants in aquifers we did a first approach if we can discretization the existence contaminant in samples diluted with water. For these reasons, SIP measurements were acquired at different experimental columns filled with sand fully saturated with different concentrations OWM (Table 4.3). The contaminant (OMW) used for the experiment was chemically characterized (Table 4.4). The main purpose of this experiment was to see if we can have clear signal of the different OMW concentrations.

Table 4.3 Different concentrations in OMW solutions.

	Dilution	**Conductivity**	**TDS**
OMW Sol. 1	0 %	12090 µS/cm	6.40 ppt
OMW Sol. 2	25 %	10000 µS/cm	5.00 ppt
OMW Sol. 3	50 %	7140 µS/cm	3.57 ppt
OMW Sol. 4	75 %	4000 µS/cm	2.01 ppt

Table 4.4 Chemical characteristics of OMW.

Conductivity	12090 μS/cm
COD	54000 mg O_2/L
NO_3	121 mg/L
PO_4	251.75 mg/L
tN	3930 mg/L
TDS	6.40 ppt

4.6 PHYTOREMEDIATION

As part of this work, measurements were made at OMW samples after treatment in phytoremediation tank (Fig. 4.6), which is installed at the School of Environmental Engineering, Technical University of Crete.

This tank dimensions 1x1x1 m^3 can be divided into three levels. The first, starting from the bottom, contains fine gravel that occupies a height of about 10 cm and the inlet water distribution system. The second level, which is located just above the first, contains medium gravel caliber. These two essential layers help to facilitate the distribution of the inlet water to the remaining part of the tank, which is the largest and represents the saturated zone. The third layer thus reaches the surface of the tank and contains soil and one tamarix plant.

The tamarix is genus of magnoliophyta, magnoliopsida plant belonging to the violales class, in the family of tamaricaceae. It is a tree, native to many coastal areas of Greece and the Mediterranean, close to beaches, river banks and streams in which saturated zone is brackish. The tamarix has a strong root system and roots branch reaching at great depths. It is extremely resistant to drought and salinity of soil. Tamarix is grown along the coasts as an ornamental, for shelterbelts, but also for shadow in the beaches.

Figure 4.6 Phytoremediation tank of the Technical University of Crete.

Just below the surface of the soil is placed a pipe used to drain the stagnant water in the outer container. The recirculation of the contaminant between the outer container and the tank is carried out through an installed pump. This unit operates at ambient conditions 24 hours and the addition of the desired amount of OMW is carried out through an outer container. Sampling was decided to be every three days, as the time of a complete cycle of OMW in the tank.

4.7 BIOCHAR

Three biochar amended columns (5%, 10%, and 25%) and one control were fully saturated with OMW (Table 4.5). The feedstock of the biochar used (Fig. 4.7) was a blending of paper sludge and wheat husks (at 75% dry weight). Pyrolysis took place for 20 min at maximum temperatures of 500 °C. No inert gas was used as flush gas to drive off pyrolytic vapors. The biochar was allowed to gas out for 5 min and was quenched with water to 30% water content (Bachmann et al., 2016) (Table 4.6). With the setup of each column and before the OMW injection therein, the permeability was measured by using the constant-head method (Table 4.5).

Figure 4.7 Biochar from blending of paper sludge and wheat husks that used in the measurements.

Table 4.5 Different concentrations of biochar in the measured columns.

	Different Concentrations of Biochar	**Permeability**
Column 1	Ottawa sand + 0% w/w biochar	$4.27 \cdot 10^{-4}$ m/sec
Column 2	Ottawa sand + 5% w/w biochar	$4.13 \cdot 10^{-4}$ m/sec
Column 3	Ottawa sand + 10% w/w biochar	$3.73 \cdot 10^{-4}$ m/sec
Column 4	Ottawa sand + 25% w/w biochar	$3.04 \cdot 10^{-4}$ m/sec

Table 4.6 Content of polycyclic aromatic hydrocarbons (PAH), elements, and specific surface area (SSA) in the specimen (Bachmann et al., 2016).

CHNOS & Ash		**Main elements**		**PAH**			
C [%]	51.1	P [mg/kg]	6054	SUM [ng/g]	2252	FLA [ng/g]	109
H [%]	1.73	K [mg/kg]	10016	ACE [ng/g]	24	FLU [ng/g]	28
N [%]	1.39	Na [mg/kg]	308	ACY [ng/g]	51	IND [ng/g]	33
O [%]	12.1	Mg [mg/kg]	3234	ANT [ng/g]	65	NAP [ng/g]	896
S [%]	0.116	Mn [mg/kg]	127	BAA [ng/g]	71	PHE [ng/g]	341
S_ICP-OES [%]	0.13	Ca [mg/kg]	62219	BAP [ng/g]	58	PYR [ng/g]	136
Ash [%]	34.78	Fe [mg/kg]	1550	BBF [ng/g]	51		
Heavy metals				BKF [ng/g]	13	**Further parameters**	
Cd [mg/kg]	0.17	Ni [mg/kg]	7.4	BPE [ng/g]	24	pH	9.3
Cr [mg/kg]	8.8	Pb [mg/kg]	17.4	CHR [ng/g]	84	EC [µS/cm]	1054
Cu [mg/kg]	28.7	Zn [mg/kg]	57.4	DBA [ng/g]	6	SSA [m2/g]	97.8

For all experiments, geochemical measurements were performed to support the geophysical observations.

Figure 4.8 Mixture Biochar with Ottawa sand.

Below are the chemical characteristics of the OMW sample (Table 4.7) used for the purposes of carrying out the measurements with different OMW concentrations.

Table 4.7 Chemical characteristics of OMW.

pH	4.88
DO (dissolved oxygen), mg/L	1.47
EC (electrical conductivity), mS/cm	9.4
Phenols, mg/L	2485
Total COD, mg/L	39400
Soluble COD, mg/L	37600
NO_3, mg/L	98
P, mg/L	194
Total Dissolved Solids, ppt	4.8

5. RESULTS

5.1 GEOMETRIC FACTOR MEASUREMENTS

Below are the results of the measurements in various aqueous samples with variable concentrations, made to record the time change of the SIP response over time and to test the sensitivity of the method. The fluid tests were conducted with three different KCl solutions (80.1 µS/cm, 296 µS/cm, 920 µS/cm). We measured the resistance magnitude (Z) and the phase angle between the frequencies 0.1 and 1000 Hz and calculated the real and imaginary conductivities. Some results from the fluid tests in the used columns are presented in the figures below. All the results can be found in Appendix B.

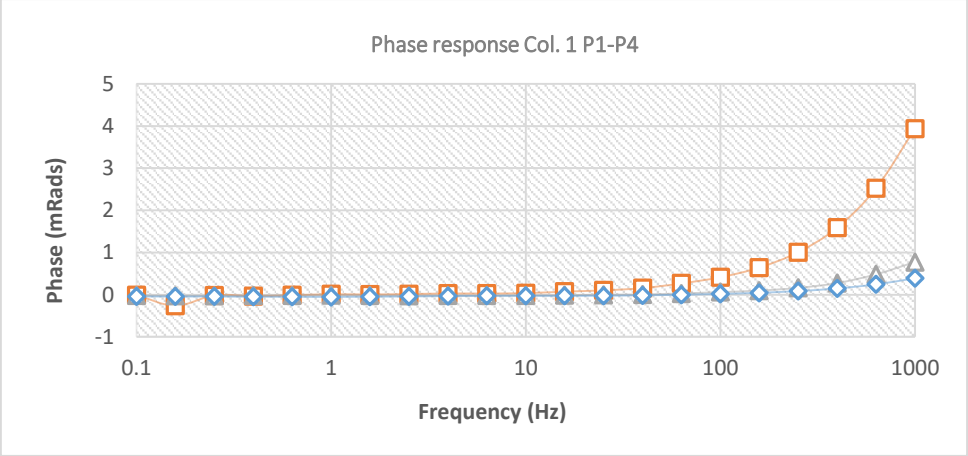

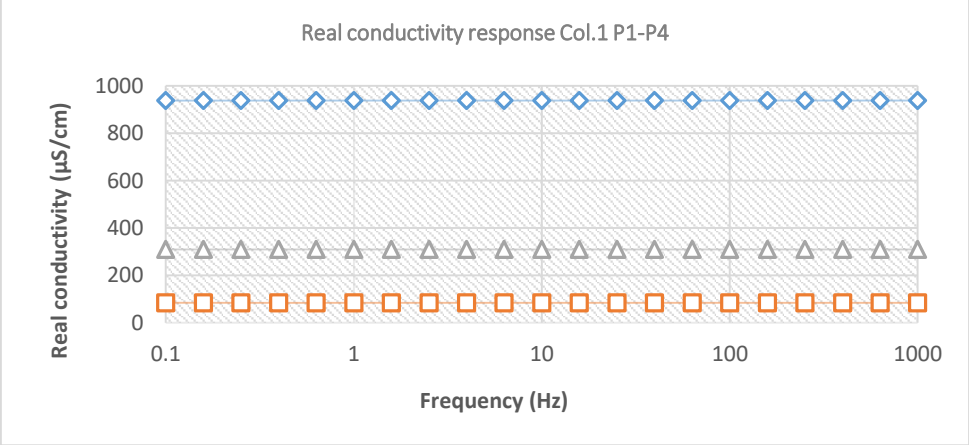

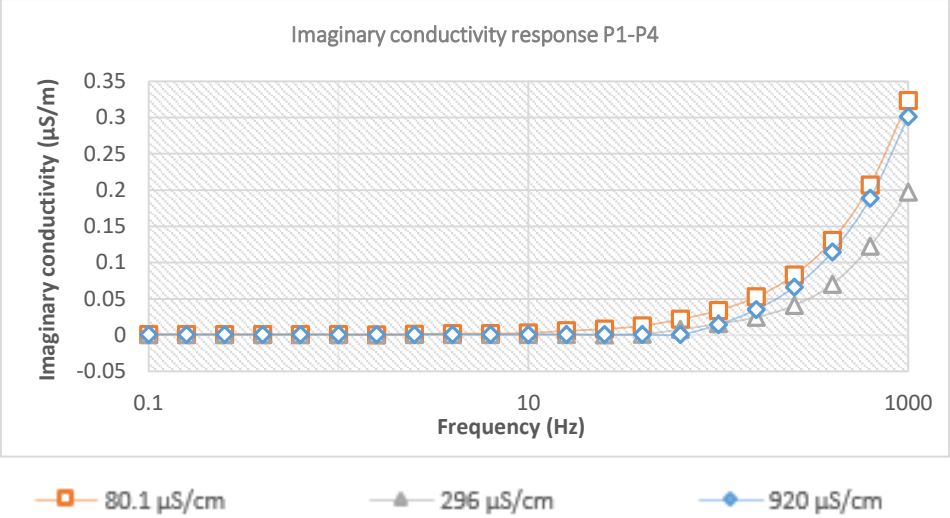

Figure 5.1 Phase response and fluid conductivity (real and imaginary part) for column 1 between potential electrodes P1-P4 (9 cm) during fluid tests after taking into account the K factor.

In order to check the sensitivity and accuracy of the SIP method, we calculate the errors that observed at the four columns used (Table 5.1 to 5.4). We estimated the error between the real conductivity of the buffer solutions that we measured by using a conductivity meter and the average value of the real conductivity that we measured through SIP measurements in the different electrodes combinations (different spacing between potential electrodes).

Table 5.1 Percentage errors for Column 1.

	Inflow Conductivity	Measured Conductivity	Percentage error
1	80.1 µS/cm	83.49 µS/cm	4.23 %
2	296 µS/cm	307.37 µS/cm	3.84 %
3	920 µS/cm	930.52 µS/cm	1.14 %

Table 5.2 Percentage errors for Column 2.

	Inflow Conductivity	Measured Conductivity	Percentage error
1	80.1 µS/cm	80 µS/cm	0.12 %
2	296 µS/cm	302.155 µS/cm	2.07 %
3	920 µS/cm	926.62 µS/cm	0.72 %

Table 5.3 Percentage errors for Column 3.

	Inflow Conductivity	Measured Conductivity	Percentage error
1	80.1 µS/cm	91.82 µS/cm	14.63 %
2	296 µS/cm	305.9 µS/cm	3.34 %
3	920 µS/cm	910.76 µS/cm	1 %

* The high error value in the first solution is due to leakage in the raw measurements resulted a poor contact between the current electrode and the solution.

Table 5.4 Percentage errors for Column 4.

	Inflow Conductivity	Measured Conductivity	Percentage error
1	90.4 µS/cm	100 µS/cm	10.62 %
2	310 µS/cm	322.08 µS/cm	3.89 %
3	930 µS/cm	929.86 µS/cm	0.01 %

SIP method can be successfully used for detailed monitoring of conductive solutions contaminants as the resulting values of the conductivity was stable with small errors relative to the actual values of the solutions.

5.2 SENSITIVITY IMPACT OF CHANGES IN GRAIN SIZE

Below are the results of the SIP measurements collected at different grain size quartzite sand samples fully saturated with aqueous solution of known conductivity, in order to see the sensitivity of the SIP method on grain size variation. The grain sizes were > 1000 µm, 1000-600 µm, 600-500 µm, 500-125 µm and Ottawa sand 595-800 µm. We measured the resistance magnitude (Z) and the phase angle between the frequencies 0.01 and 10000 Hz.

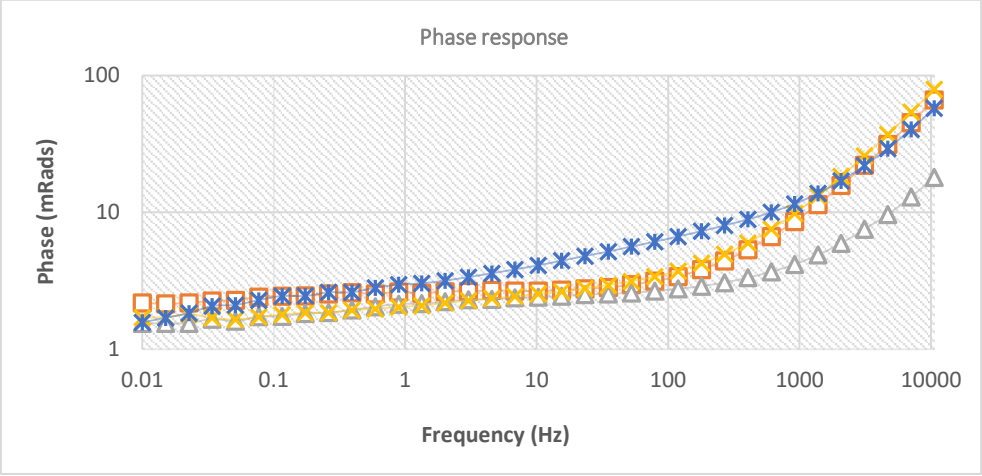

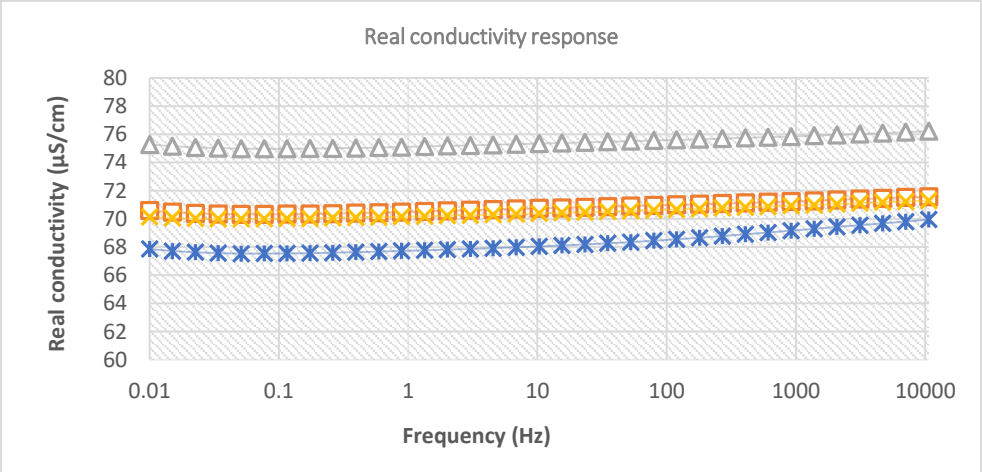

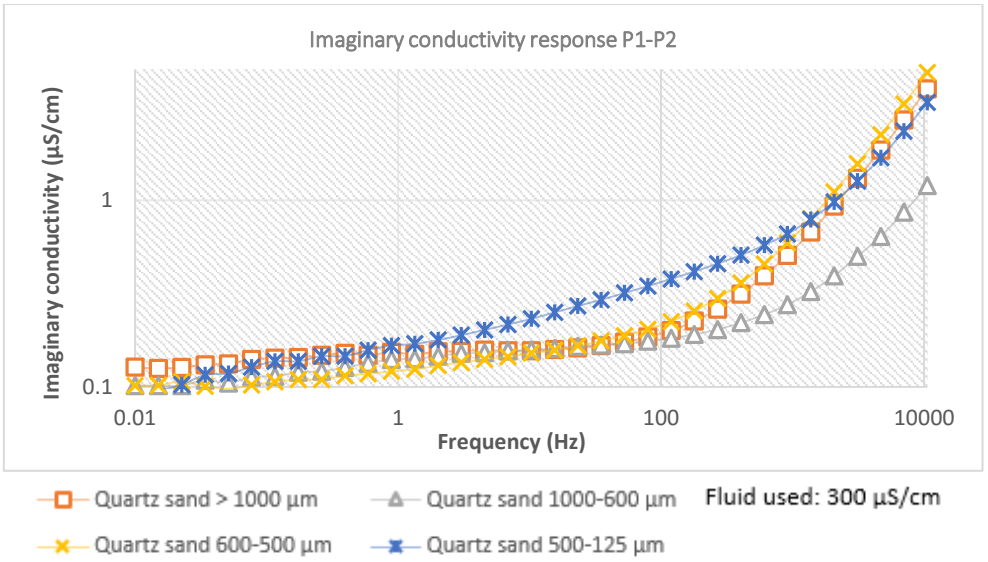

Figure 5.2 Phase response and fluid conductivity (real and imaginary part) during grain size analysis measurements to 10000-0.01 Hz (distance between potential electrodes 30 mm).

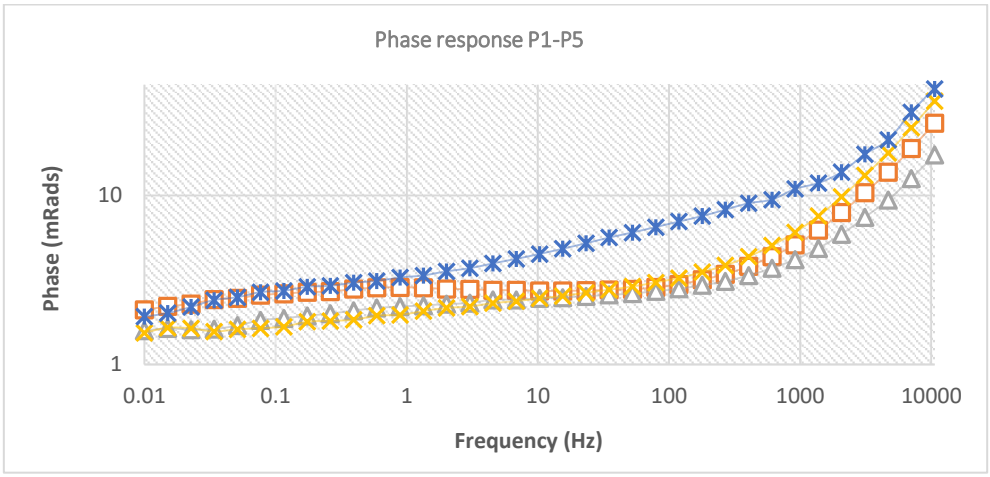

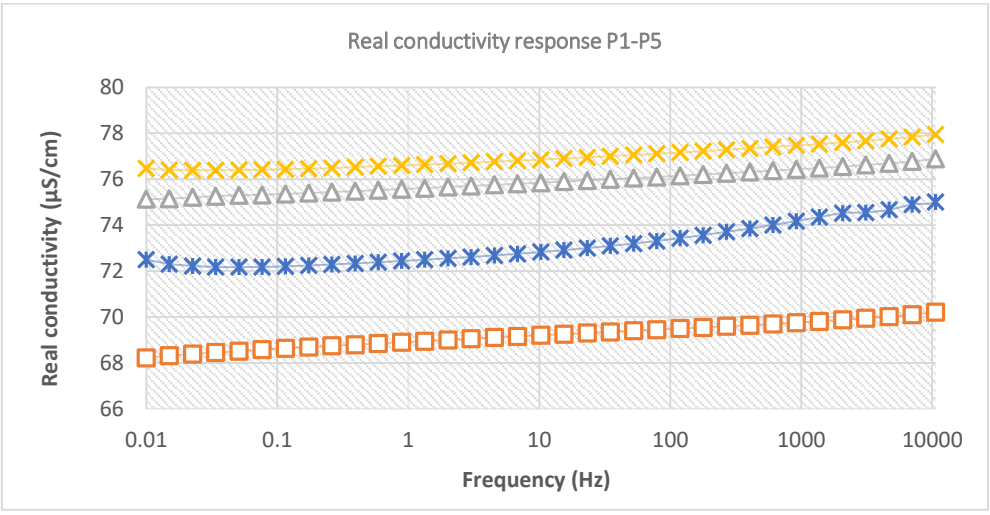

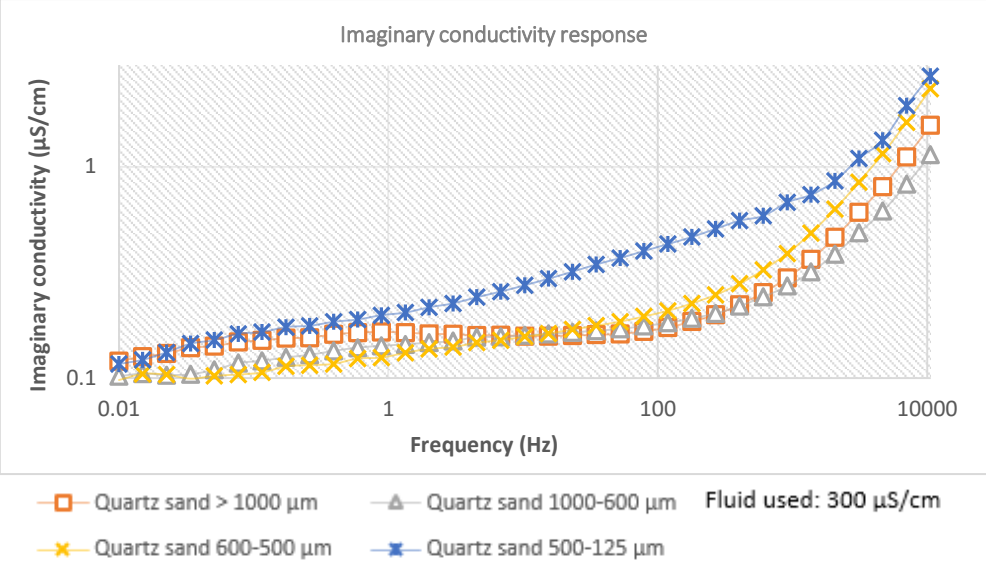

Figure 5.3 Phase response and fluid conductivity (real and imaginary part) during grain size analysis measurements to 10000-0.01 Hz (distance between potential electrodes 120 mm).

The results showed that the SIP response increases as the particle size shrinks. This does not appear if we take into account the smallest particle size (500-125 µm) because before the saturation of the column with our solution, we rinsed the sand with deionized water and left to dry at ambient conditions, and logically it kept even after the cycle of filling with our solution a quantity of deionized water.

We consider as more representative the most distanced potential electrodes (P1-P5) due to the highest sample volume.

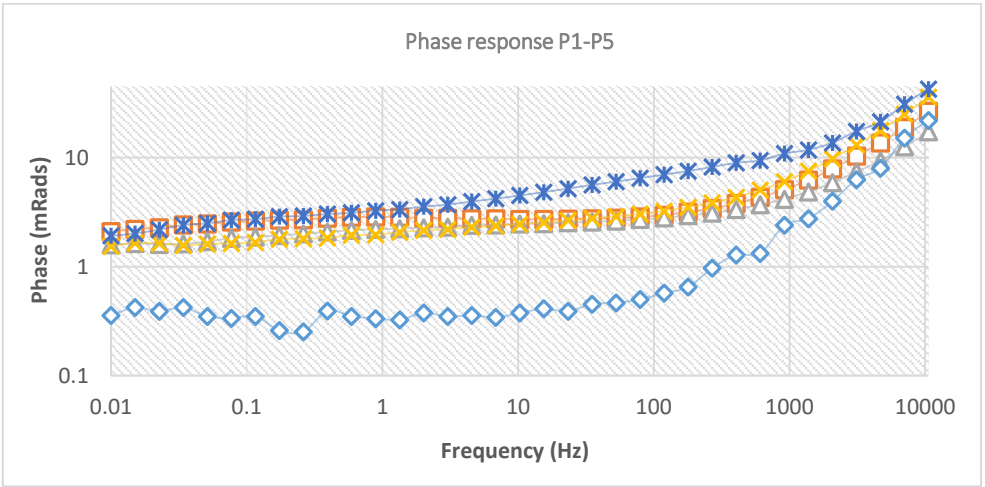

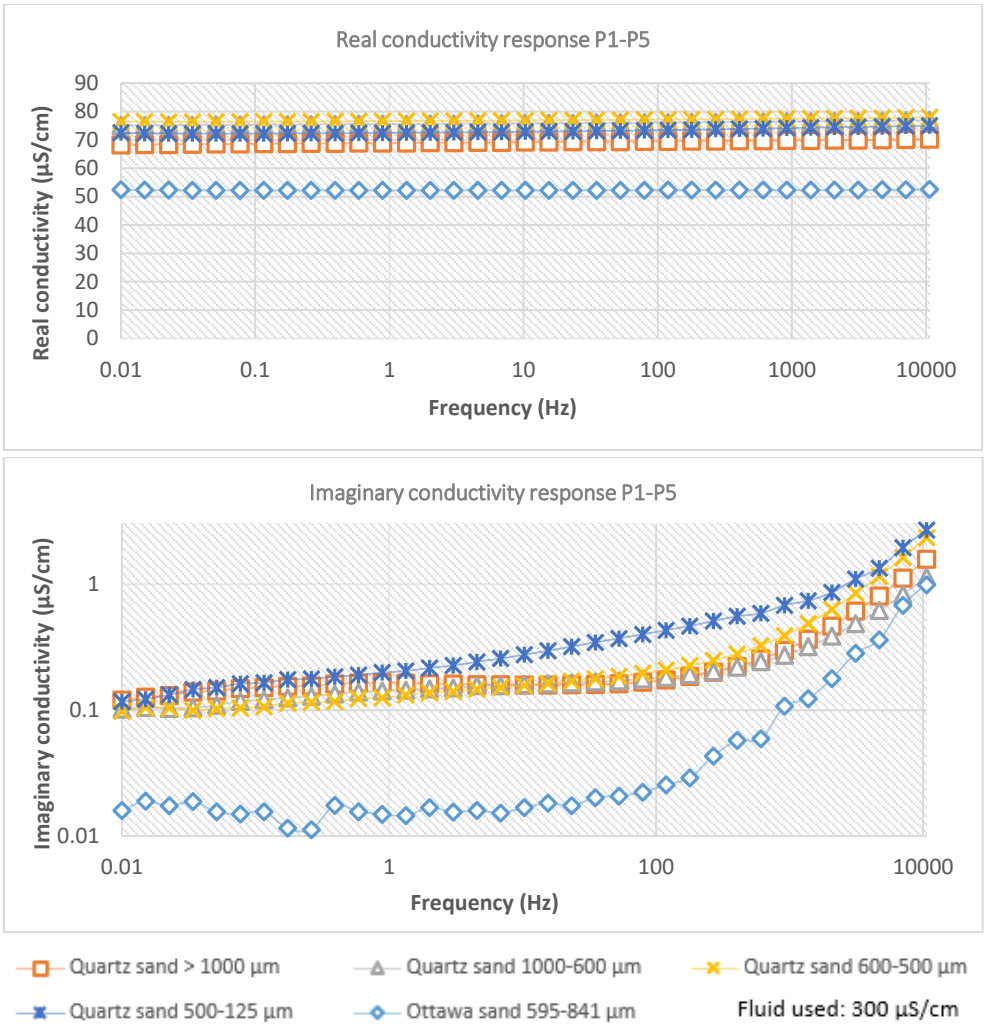

Figure 5.4 Phase response and fluid conductivity (real and imaginary part) during grain size analysis measurements to 10000-0.01 Hz (distance between potential electrodes 120 mm).

The results showed that can be discretization of the grain size in the same material at laboratory scale, but in the case of different materials (Ottawa and Quartz sand) with the same grain size and saturated with the same fluid, we may have different responses.

5.3 RESPONSE AT DIFFERENT FLUID CONCENTRATIONS

Firstly, we collected initial sample of OMW from the phytoremediation tank that described in previous section. We made measurements with three columns, which contained quartz sand 1000-600 μm, > 1000 μm and Ottawa sand 595-840 μm to characterize the initial sample and to see the impact in the different materials.

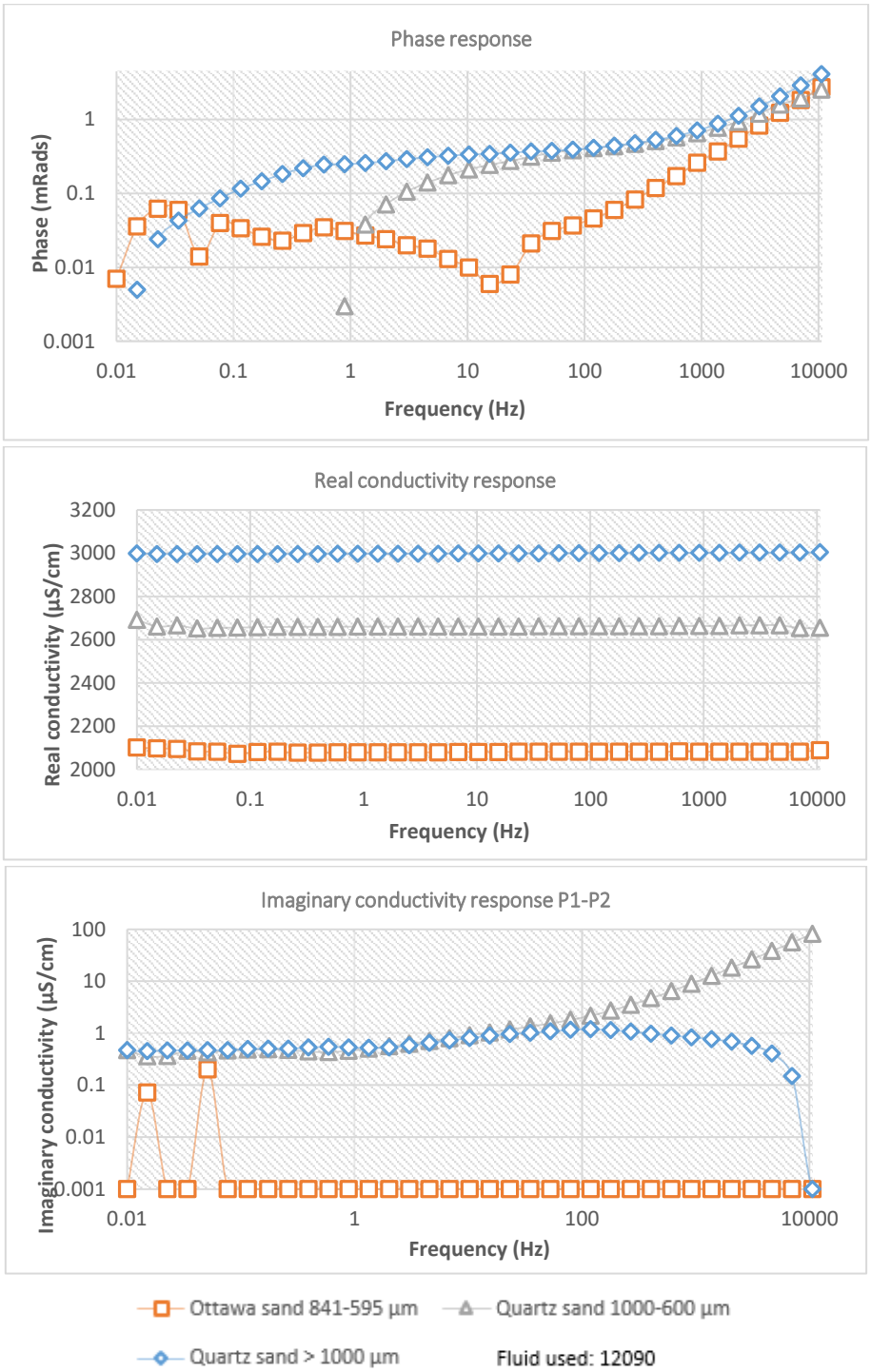

Figure 5.5 Phase response and fluid conductivity (real and imaginary part) during measurements with sands saturated with OMW to 10000-0.01 Hz (distance between electrodes 30 mm).

Below are the results of the measurements in a grain size with OMW diluted samples (Table 4.4) to see if we can have clear signal of different OMW concentration in aqueous solutions.

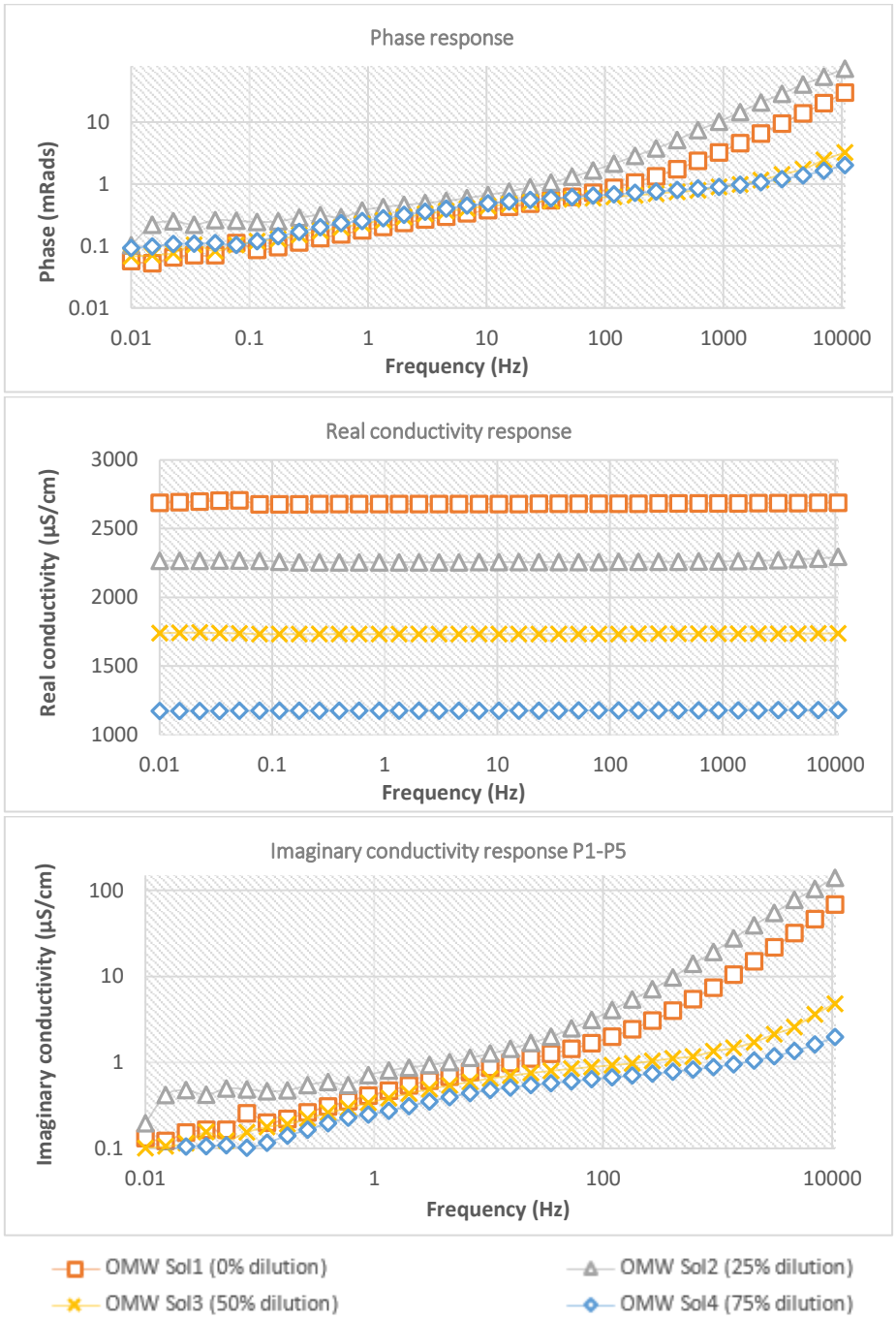

Figure 5.6 Phase response and fluid conductivity (real and imaginary part) during measurements with quartz sand, saturated with different concentration solutions of OMW to 10000-0.01 Hz (distance between electrodes 120 mm).

5.4 PHYTOREMEDIATION

In this section, the SIP measurements from the OMW samples after treatment in phytoremediation tank are presented. The samples collected every 3 days, with starting point

the day 0, before starting pumping the OMW into the tank. The frequency range of the measurements was 0.01 to 10000 Hz.

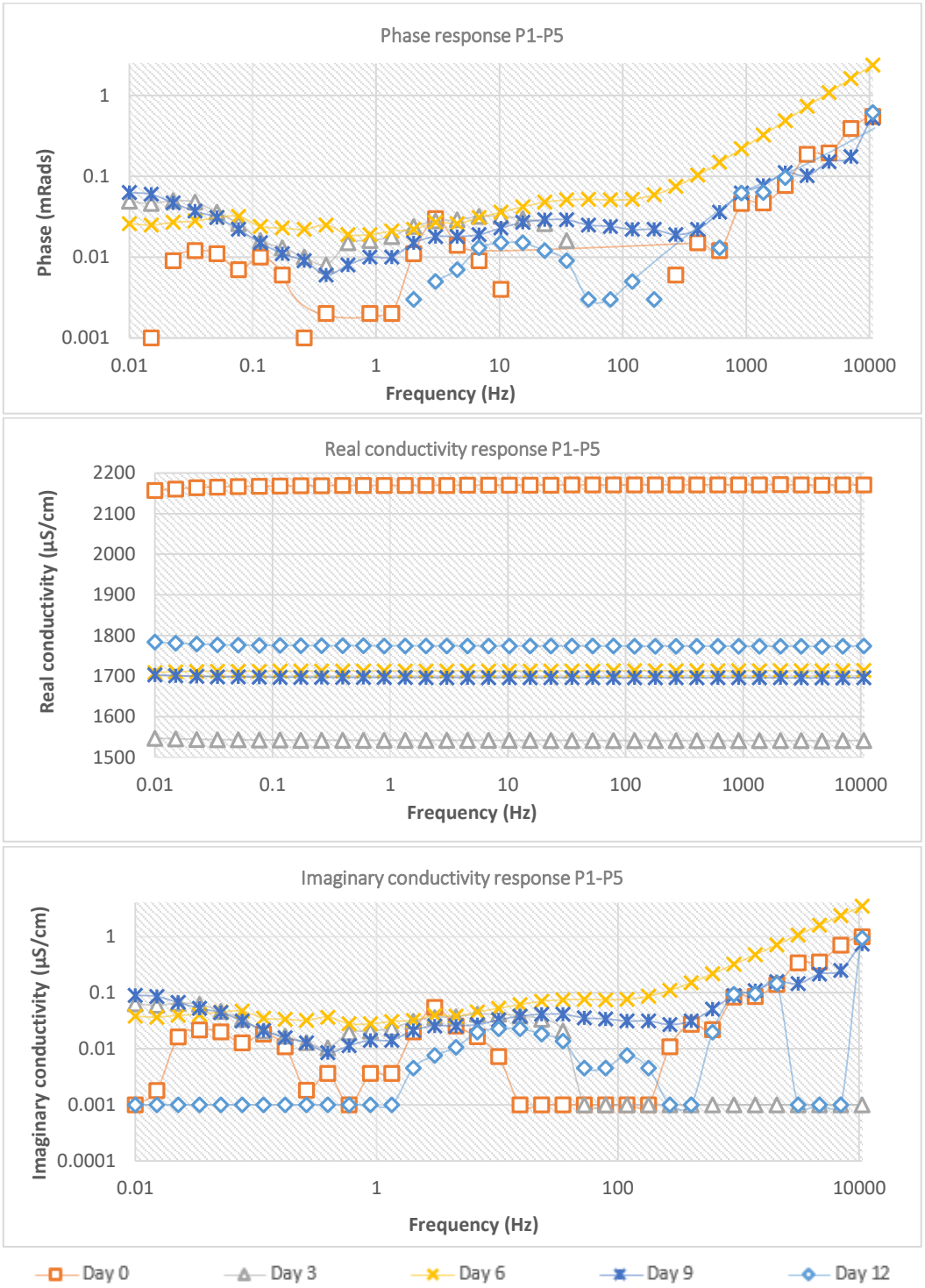

Figure 5.7 Phase response and fluid conductivity measurements after phytoremediation treatment to 10000-0.01 Hz.

Below, the results from the 10 Hz are presented for the easier visualization of any possible change in the different time.

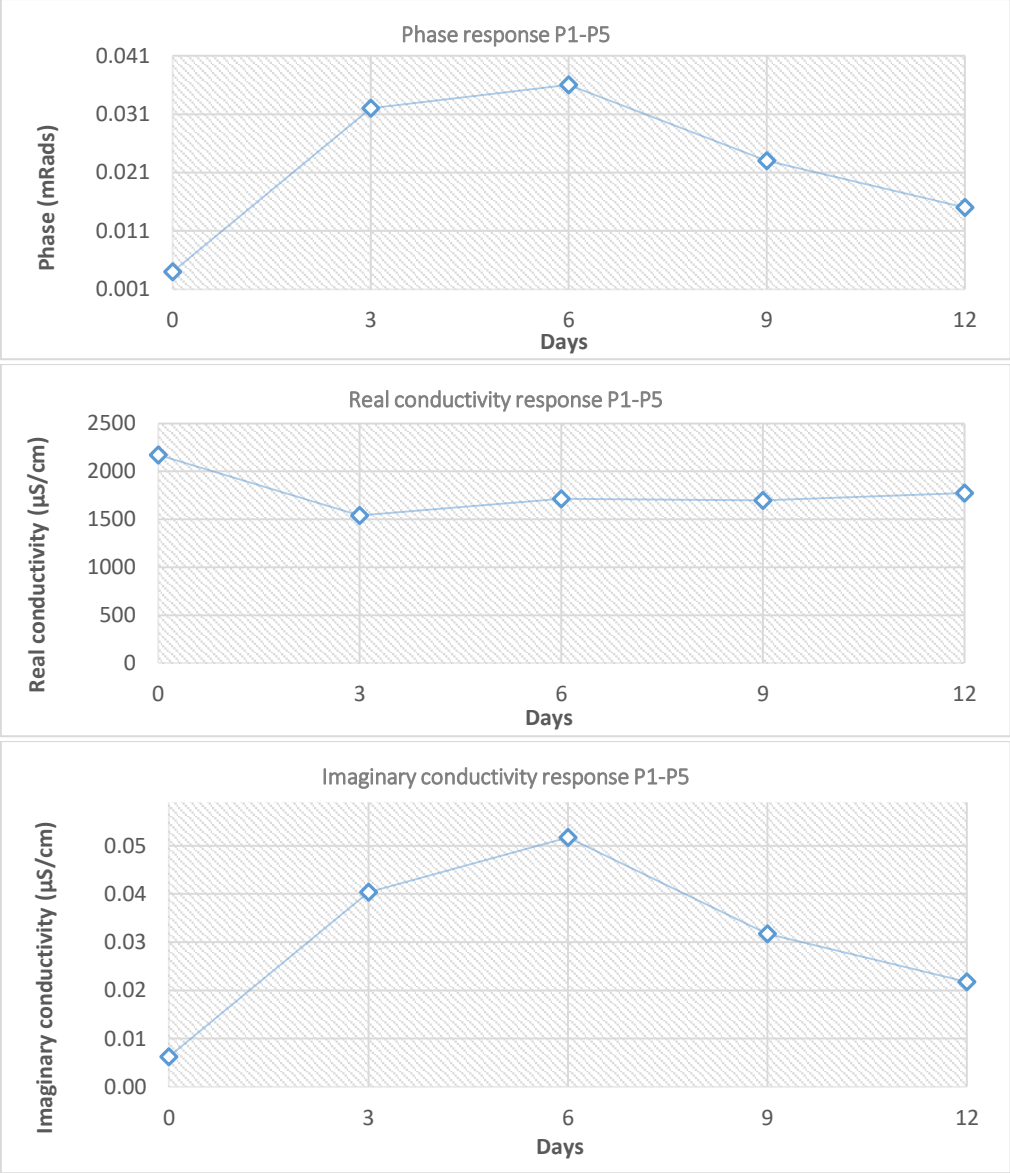

Figure 5.8 Single frequency graphs after phytoremediation treatment to 10 Hz.

Further chemical analysis (Table 5.5) performed to provide additional insight on phytoremediation treatment and OOMW, and their links to SIP responses.

Table 5.5 COD results for the phytoremediation treatment.

Day	TDS	COD (mg/L)	EC (Inflow)
0	6.2	49723	12400 µS/cm
3	3.75	10410	7500 µS/cm
6	4.3	13821	8700 µS/cm
9	3.91	12657	7840 µS/cm
12	3.8	8478	7740 µS/cm

Chemical analyzes showed gradual reduction of the organic load reached COD reduction 83%. SIP responses showed a small drop in the real conductivity after 3 days' treatment. Phase and imaginary part response couldn't give us further information about the phytoremediation processes due to the manner in which the measurements were made. Measurements were not

made directly to the tank or to collected ground core of the root system, but OMW outflow liquids collected and injected in sample holders with clean soil sample.

The real conductivity response (Figure 5.8) shows a sharp decrease after the first 3 days of treatment, followed by approximately stable measurements over the next 9 days. The same trend is observed with the total dissolved solids and COD measurements. The sharp reduction after the first 3 days is followed by stable values for the remaining time of the experiment. As expected, there is a clear connection between the real conductivity response, the TDS and COD, since both TDS and COD are different expressions of the combined content of all anionic/ cationic inorganic and organic substances contained in OMW. This connection is not observed in the imaginary conductivity response (Figure 4.9b), which gradually increases until day 6 and then follows a downward trend until day 12.

5.5 BIOCHAR

In this section, we present the results on the use of SIP method as a monitoring aid in a controlled laboratory experiment with biochar used as a tool for wastewater treatment. Three biochar-modified columns (5%, 10%, 25% biochar in Ottawa sand) and one control (pure Ottawa sand) were saturated with OOMW from one waste pond in Chania. Measurements were obtained every day for a period of 10 days.

Initial, we present the SIP responses for each column during the 10 days' treatment (Fig. 5.9a-c) and after the single frequency results of the columns that helps to determine the optimal concentration of biochar.

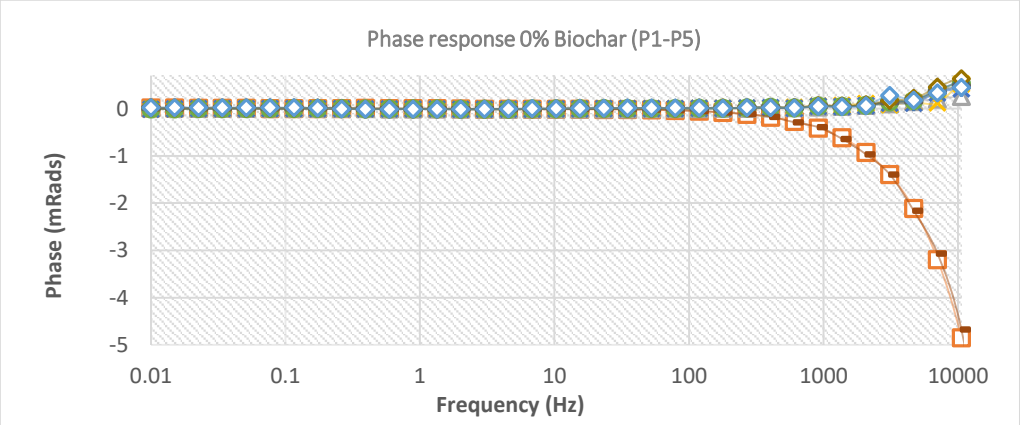

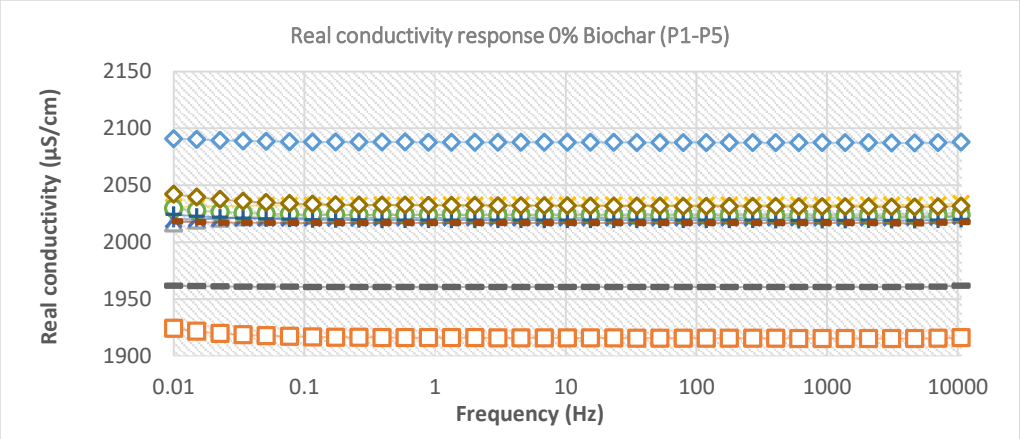

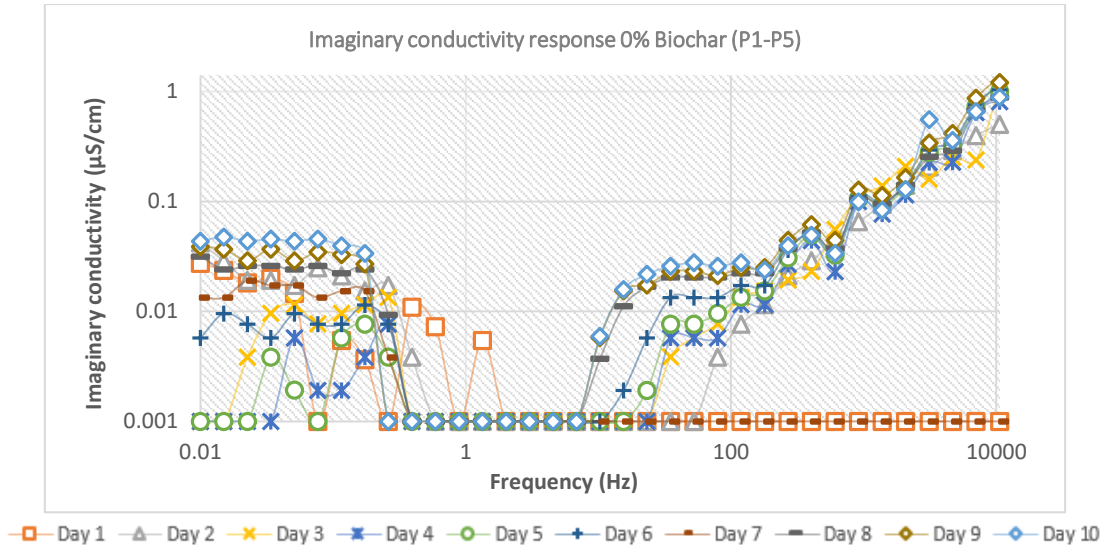

Figure 5.9 Phase response and fluid conductivity measurements during 10 days with 0% w/w biochar to 10000-0.01 Hz.

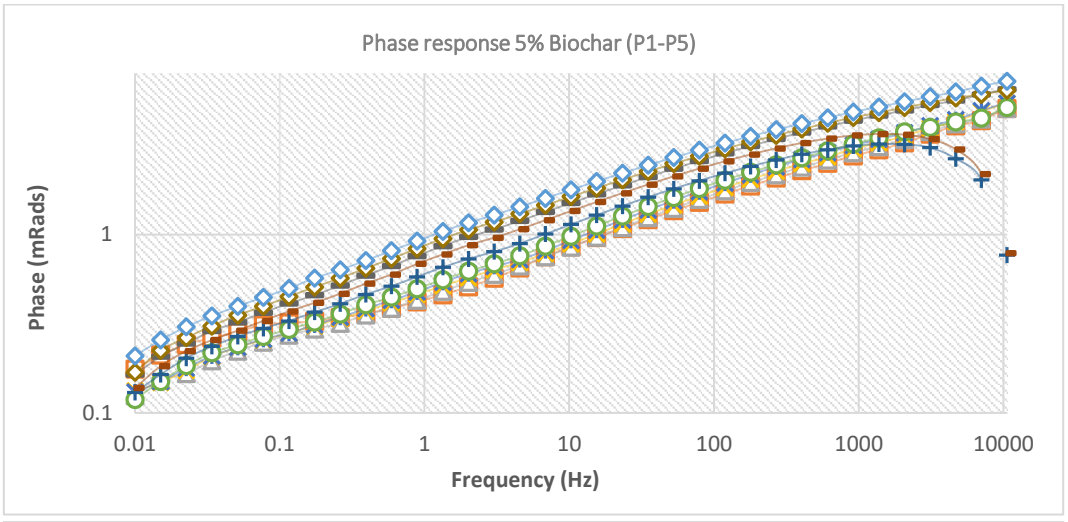

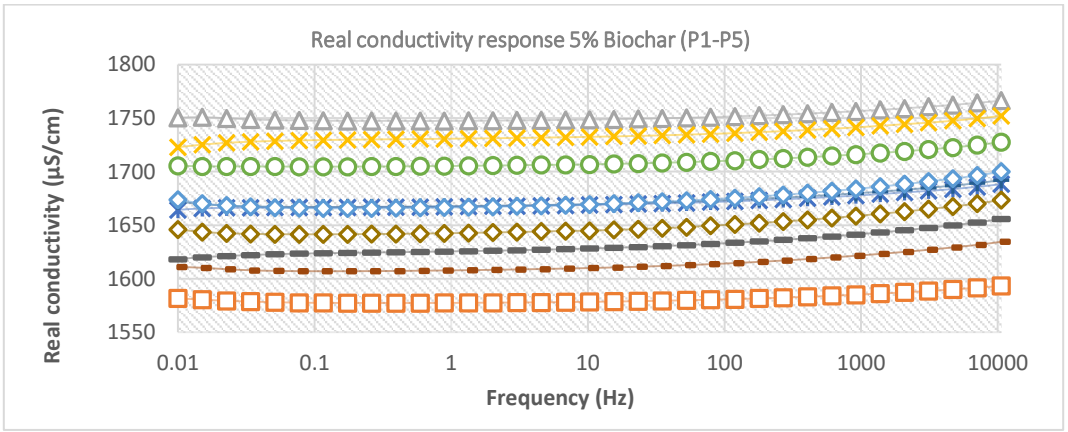

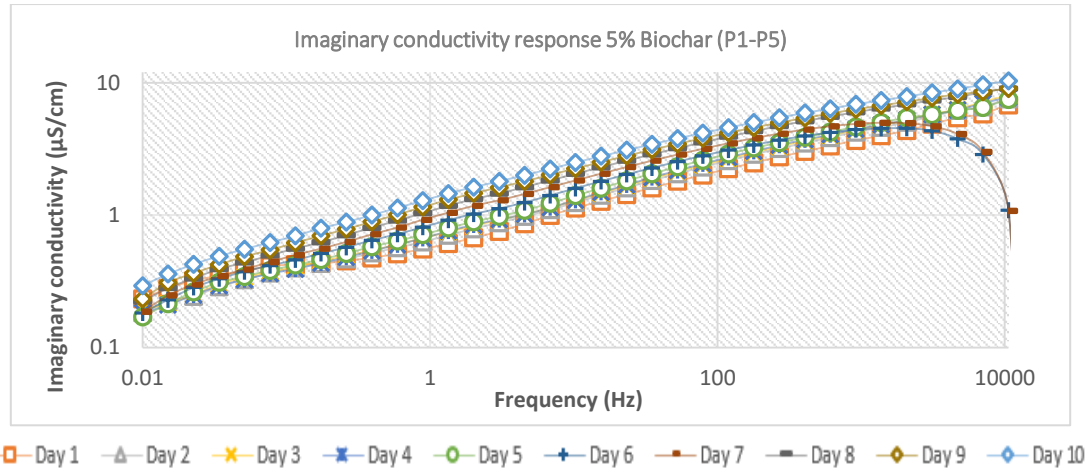

Figure 5.10 Phase response and fluid conductivity measurements during 10 days' treatment with 5% w/w biochar to 10000-0.01 Hz.

On the second day there is a rise of the conductivity values due to the nature of biochar (good electronic conductor, like graphite) which enhances the signal.

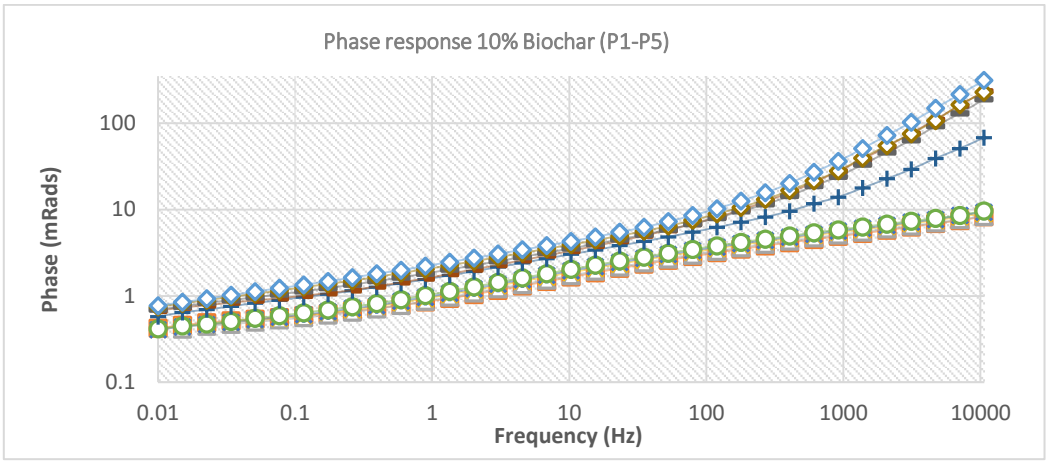

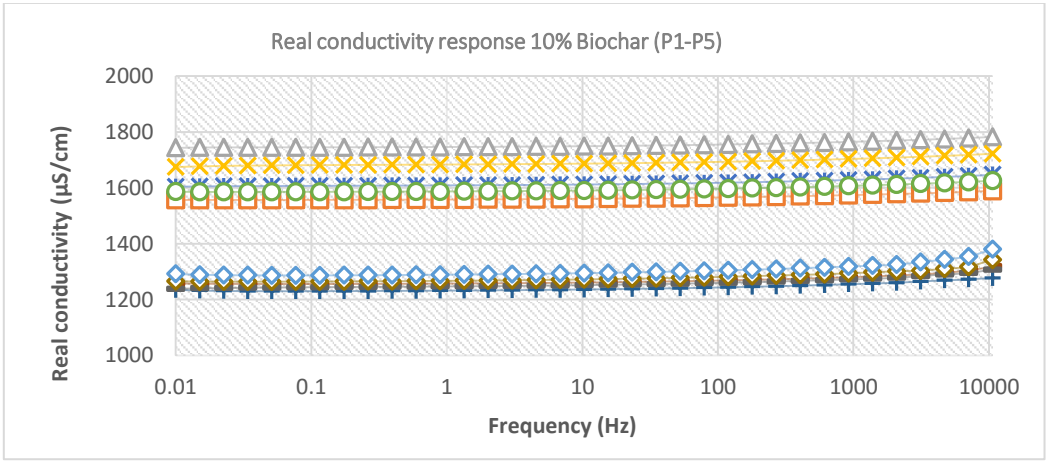

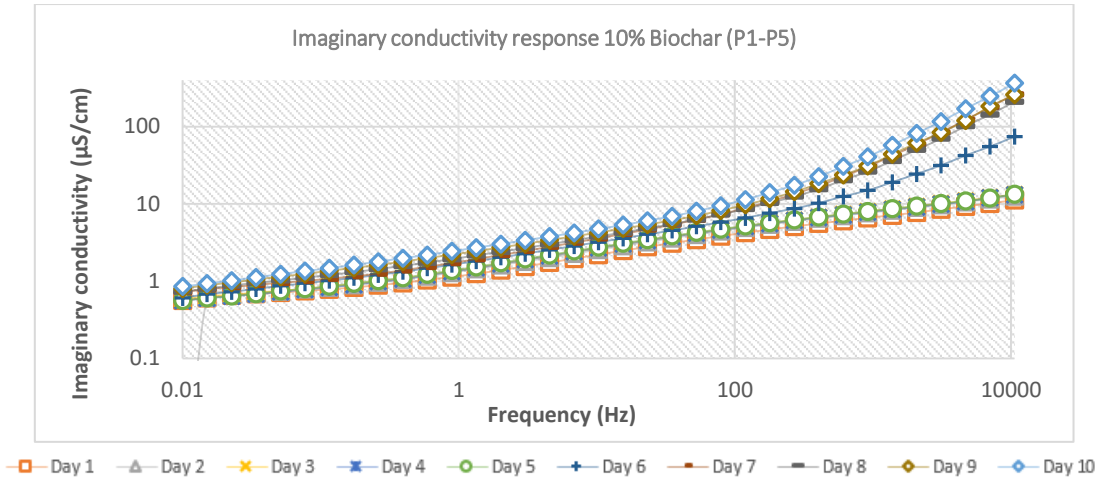

Figure 5.11 Phase response and fluid conductivity measurements during 10 days' treatment with 10% w/w biochar to 10000-0.01 Hz.

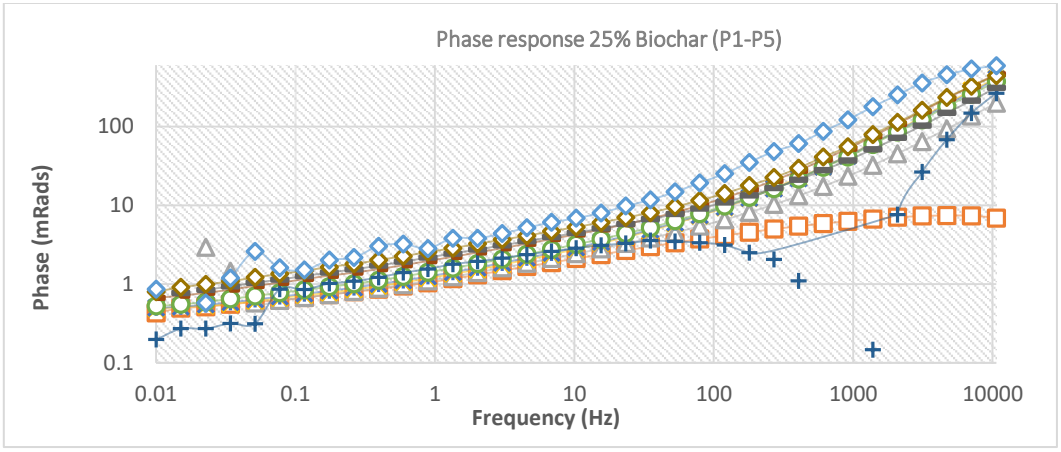

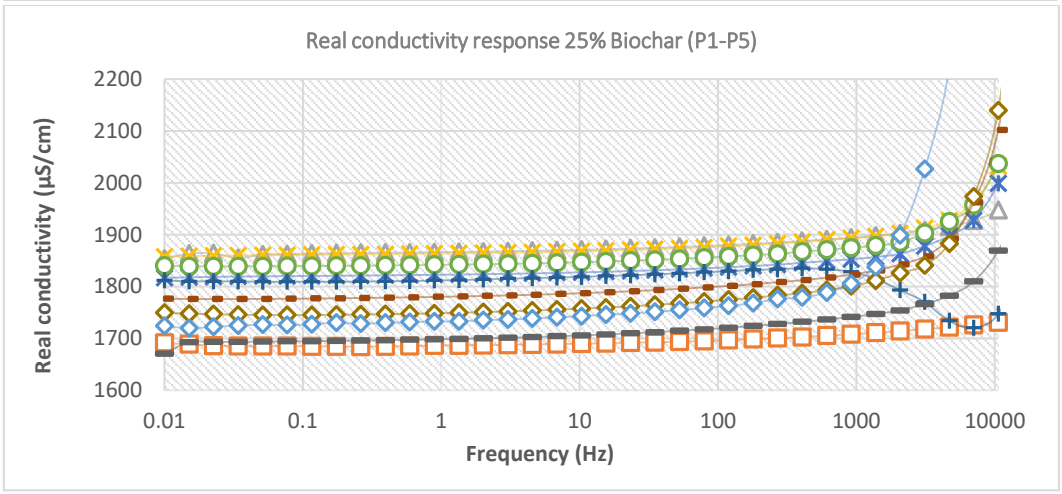

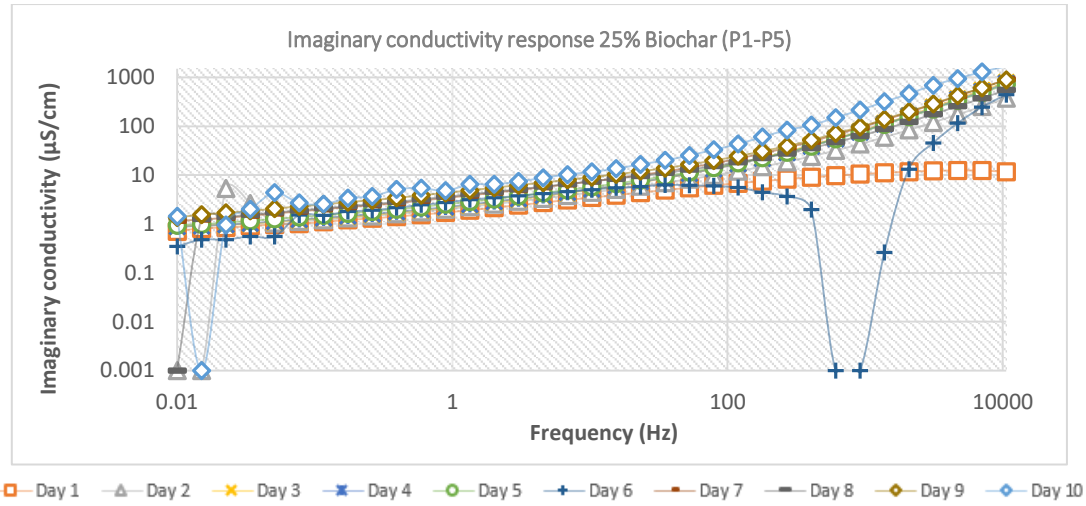

Figure 5.12 Phase response and fluid conductivity measurements during 10 days' treatment with 25% w/w biochar to 10000-0.01 Hz.

Below, the results from the 10 Hz are presented for the easier visualization of any possible change in the 10 days' treatment.

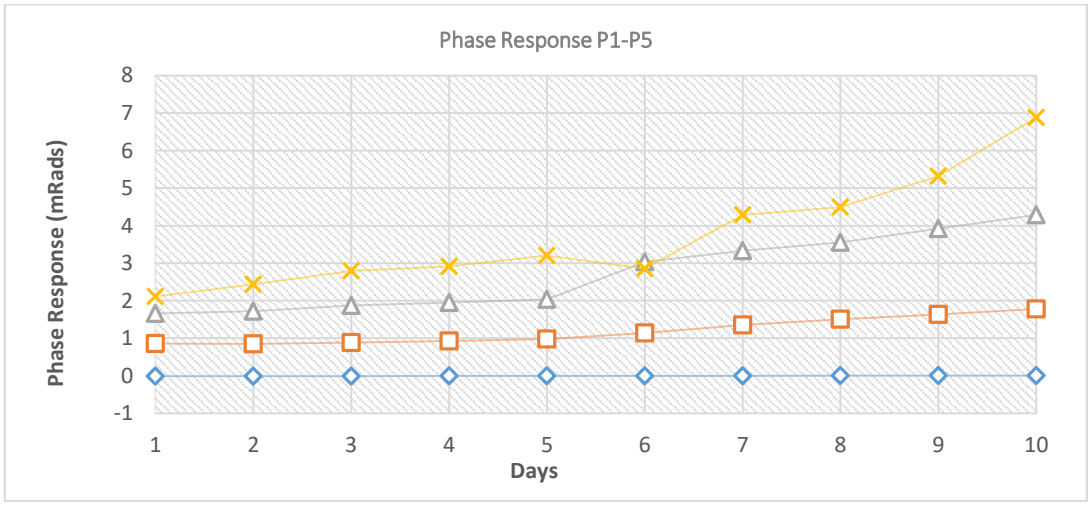

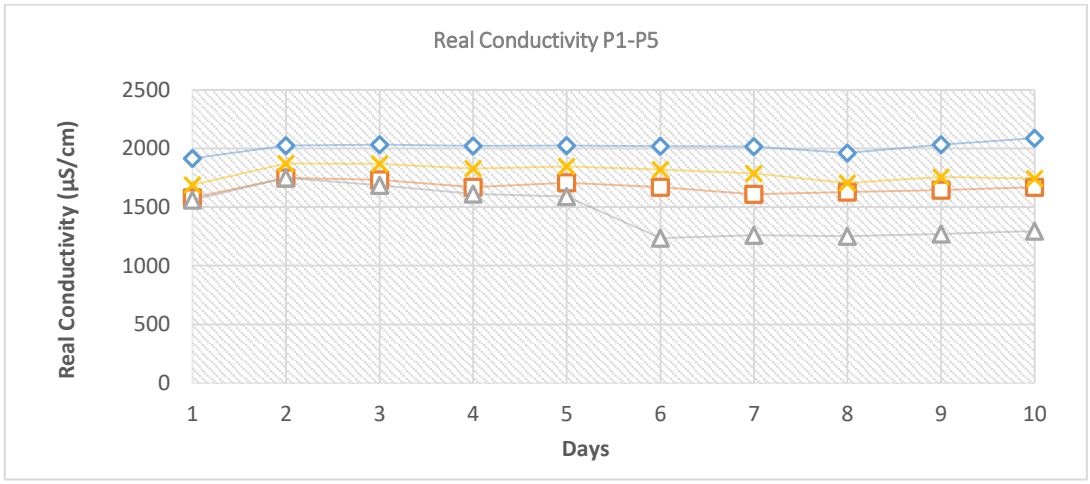

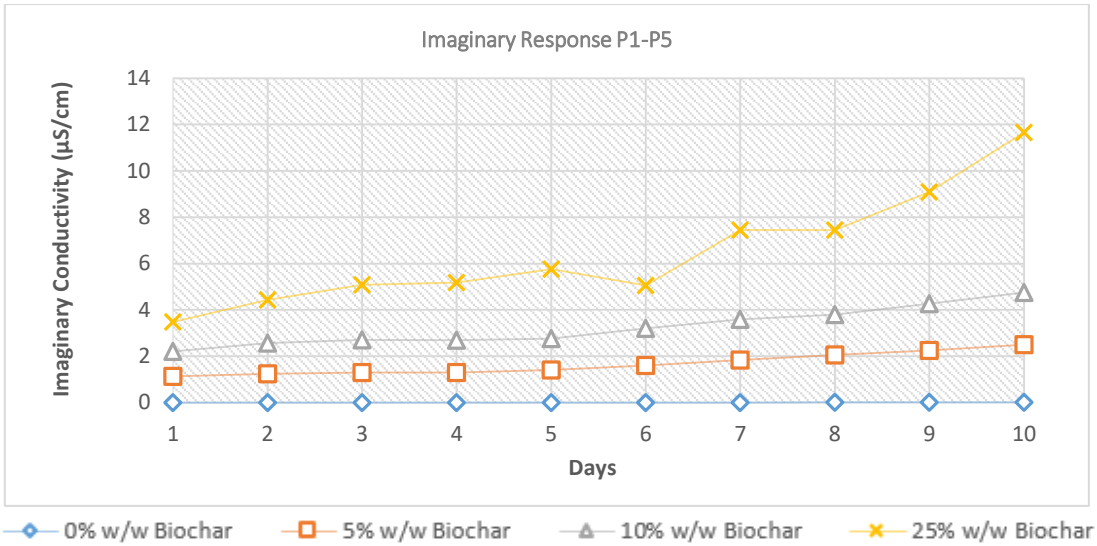

Figure 5.13 Single frequency graphs during 10 days treatment with biochar to 10 Hz.

The real conductivity appears to decrease significantly only for the 10% biochar column. Imaginary conductivity appears to increase with time in all biochar columns, and it seems to be affected by the amount of biochar present.

Li et al. used nuclear magnetic resonance (NMR) to investigate the development of functional groups in biochars and establish their relationship with properties such as pH and conductivity (Li et al., 2013). The regression analysis between functional groups and biochar properties demonstrated that the electrical conductivity of rice straw derived biochars were mainly determined by fused-ring aromatic structures and anomeric O-C-O carbons. These functional groups are the result of dehydroxylation/dehydrogenation and aromatization reactions during the pyrolysis process. Therefore, the electrical conductivity of biochar may depend less on the initial biomass and more on the pyrolysis conditions. These conclusions are also supported by Haegel et al., who used SIP to measure the electrical conductivity of 5 different biochar samples (Haegel et al., 2013). Their results showed that biochars with a larger degree of carbonization (increased C content) showed higher electronic conductivity and yielded higher polarization. The frequency dependence of the polarization further depended on the amount and the size of the biochar particles, which in turn largely depend on pyrolysis conditions.

Further geochemical analysis performed to provide additional insight on OMW and biochar processes, and their links to SIP responses.

Table 5.6 Chemical analysis to the initial OMW and the outflows after the 10 days' treatment in the different biochar concentrations.

	Initial OMW	**0% w/w Biochar**	**5% w/w Biochar**	**10% w/w Biochar**	**25% w/w Biochar**
		After 10 days			
pH	4.88	4.92	6.57	**8**	5.9
DO (dissolved oxygen), mg/L	1.47	4.1	4.3	**3.5**	4.6
EC (electrical conductivity), mS/cm	9.4	9.6	10.9	**9.1**	12.5
Phenols, mg/L	2485	1921.6	850.7	**310.9**	1059.6
Total COD, mg/L	39400	-	-	**-**	-
Soluble COD, mg/L	37600	36500	27100	**16500**	30600
NO3, mg/L	98	37	28	**14**	33
P, mg/L	194	164	106	**29.5**	120
Total Dissolved Solids	4.8	4.84	5.5	**4.57**	6.26

After 10 days of treatment, it was clear that the column with 100% Ottawa sand (0% biochar) did not have any significant effect on the pH, electrical conductivity, COD and total dissolved solids. The sand appeared to retain about RRR% of phenols, FF% of nitrates and TT% of phosphorus. The OMW pH gradually increased to 6.57 and 8, in the columns with 5% and 10% w/w biochar, respectively. This indicates some degree of mineralization (degradation to CO_2 and H_2O) for the organic substances present in the wastewater but the alkaline pH of biochar itself (9.3) also played a significant role. In the 25% w/w biochar column, pH was found reduced in the acidic region at the end of the treatment. This indicates the production of volatile fatty acids, which is a characteristic step in anaerobic treatment of wastewaters, called acidogenesis. Therefore, since the columns had limited air trapped in them as headspace, it is possible that the OMW was initially processed by aerobic microorganisms (bacteria) which consumed the available oxygen and gradually the conditions turned anaerobic. This conclusion is also supported by the increased COD value in the 25% w/w compared to the 5 and 10% w/w biochar columns. It is interesting to note that this phenomenon only appeared in the 25% w/w biochar and not in the pure Ottawa, 5 or 10% w/w biochar columns. This may be due to the decreased total porosity in the 25 w/w % biochar column, which means that this column was loaded with less OMW (approximately 1/3 of the volume the other columns received) but also had less air space available (reduced aeration).

The anaerobic digestion process begins with bacterial hydrolysis of the input materials. Insoluble organic polymers, such as carbohydrates, are broken down to soluble derivatives that become available for other bacteria. Acidogenic bacteria then convert the sugars and amino acids into carbon dioxide, hydrogen, ammonia, and organic acids. These bacteria convert these resulting organic acids into acetic acid, along with additional ammonia, hydrogen, and carbon dioxide. Finally, methanogens convert these products to methane and carbon dioxide. The methanogenic archaea populations play an indispensable role in anaerobic wastewater treatments (Tabatabaei et al., 2010). It has been reported that the addition of biochar in anaerobic treatment reactors increased the maximum production rates of hydrogen and methane, improved hydrogen and methane yield and shortened the lag period between the different anaerobic processes. Biochar addition also enhanced volatile fatty acid generation during hydrogen production (Cooney, Lewis, Harris, Zhang, & Yan, 2016; Mumme, Srocke, Heeg, & Werner, 2014; Sunyoto, Zhu, Zhang, & Zhang, 2016). Biochar provided temporary

substrates to support microbial metabolism and growth and promoted the methanogenic biofilm formation in the methane production stage. In addition to the explanation provided earlier (less available air space), it appears that a 25% w/w biochar sample promoted acidogenesis and catalyzed the overall anaerobic treatment process considerably more than the other samples, within the 10-day experimental framework. Taken into account that anaerobic digestion of wastewaters typically lasts between 15-40 days, we can assume that the other samples (5 and 10% w/w biochar) would also show evidence of anaerobic processes if our experiment had lasted longer.

Mantzavinos et al. reviewed the organic matter degradation of OMW by chemical and biological processes (Mantzavinos & Kalogerakis, 2005). They concluded that an aerobic pretreatment stage may be favorable in reducing the amount of total phenolic compounds and associated toxicity and found out that the rate of anaerobic degradation was about 2.5–4.5 times greater than that of the anaerobic degradation without pretreatment. Therefore, in the experimental set-up used in this study, it may worth adjusting the initial volume of air in the column (headspace), in order to ensure a successful aerobic pre-treatment stage, before the anaerobic process.

The dissolved oxygen values remained stable throughout, although there is probably a significant experimental error involved due to the time taken for the samples to be measured after they exited each column. With respect to the electrical conductivity, all values are comparable except the one corresponding to the 25% w/w column. If the anaerobic degradation hypothesis is correct, then an increased amount of ionic species became solubilized at these conditions.

The highest COD, total phenol, nitrates and phosphorus removal was achieved in the 10% w/w biochar column (56, 87, 85 and 84%, respectively). Therefore, this is the optimum biochar concentration in the Ottawa sand-biochar mixture. The total dissolved solids values were practically the same as the initial OMW, with the exception of the 25% w/w biochar column, where a 23% raise was observed. This indicates that there were significant quantities of leachable inorganic compounds (such as metal salts and/or oxides). The high ash content of this particular type of biochar (34.78%) and the long treatment period of 10 days (well beyond the optimum leaching time of 24 h) support this conclusion (Lokeshappa & Dikshit, 2012). Additionally, the fatty acids generated during the acidogenesis step, promoted the acidic dissolution of metal oxides from the carbon structure, thus increasing the total dissolved solids.

After the treatment of OMW, X-ray diffraction (XRD) analysis were performed to all biochar samples and to the original pure biochar sample to examine any change in their structure (Fig. 5.14).

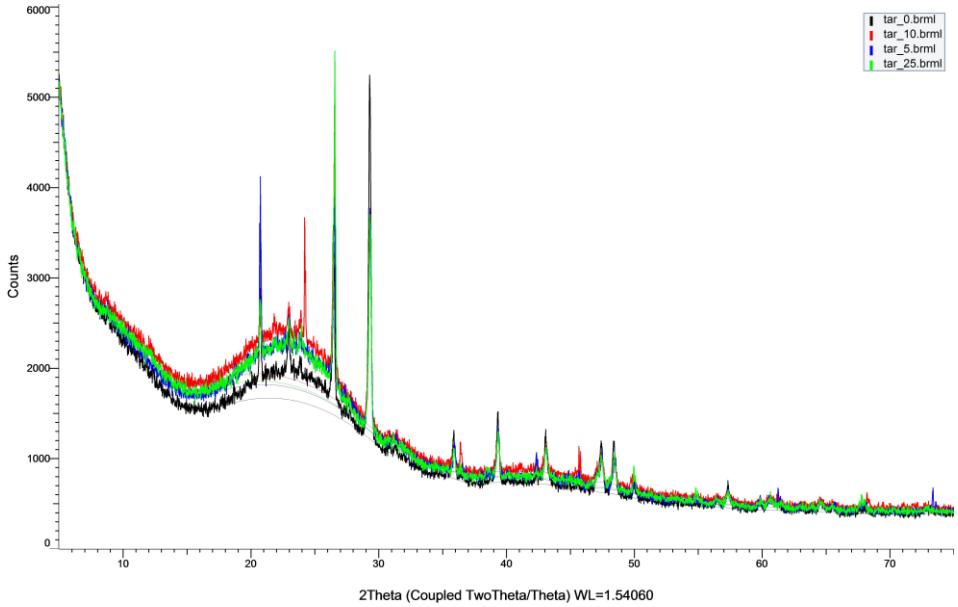

Figure 5.14 XRD diagram for the 4 samples in which the vertical axis is the intensity of the reflected beam and the horizontal, the degrees (angle) moving the goniometer.

From the XRD analysis we cannot do any quantitative interpretation, but we see that there is a change of the crystalline phase from the untreated sample and everything else. The change of the peaks as to the initial sample implies that the grain size increased, which confirms the presence of adsorption during the experiment.

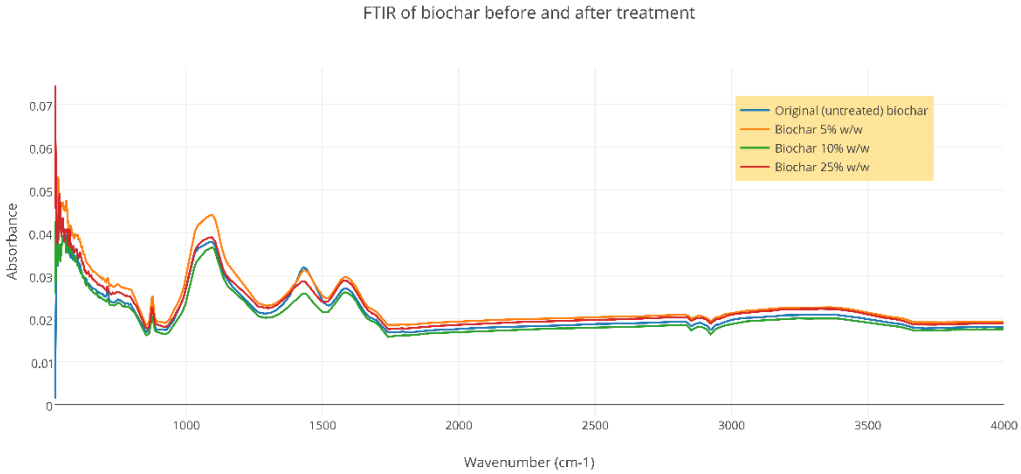

Figure 5.15 IR spectra of biochar samples.

The FTIR spectra of original (untreated), 5, 10 and 25% w/w biochar samples are shown in Figure 5.15 Analysis of the FTIR peaks indicate the biochar surface moieties responsible for interacting with the substances present in OMW. Since we are dealing with a multi-component wastewater, it is practically impossible to allocate spectra changes to individual compounds. Therefore, what we observe is the sum interaction of various contaminants or classes of contaminants (such as phenols) with biochar. Comparing the four spectra, no disappearance of certain bands and appearance of others can be observed. This indicates that breaking of chemical bonds and the formation of new ones did not occur between substances in the OMW and surface groups present on biochar. It is highly likely that biochar reduced the organic and

inorganic load of OMW through a combination of the following mechanisms: electrostatic interactions, physical sorption in the pores and aerobic/anaerobic microbial transformations.

The broad band at 3300 cm^{-1} is due to the presence of hydroxyl groups (–OH). The aromatic –C=C- or the –COO- group is attributed to the peak at 1625 cm^{-1}. The absorbance band at ~1450 cm-1 indicates the –C=O (carbonyl) stretching vibration. The carbonyl and hydroxyl groups are responsible for the basic and anionic properties, respectively. Therefore, potentially both anionic and cationic substances can be adsorbed onto the biochar's surface (Nautiyal, Subramanian, & Dastidar, 2016). The intense absorbance peak at ~1100 cm^{-1} (due to the stretching of ether linkage –C-O-C-) shows the largest variation among the 4 samples. This indicates the participation of the –C-O-C- linkage in adsorption. Oxygen containing functional groups often play a significant role in the adsorption or binding process (Fan et al., 2016). The bands below 800 cm^{-1} correspond to Fe–O bond deformations.

In addition, scanning electron microscope (SEM) measurements were made to examine the case of change between the initial biochar sample and the biochar samples after 10 days' treatment. More specifically, after the ten days of treatment, biochar samples were obtained and rinsed with deionized water and dried in air and then separated from any Ottawa sand residues.

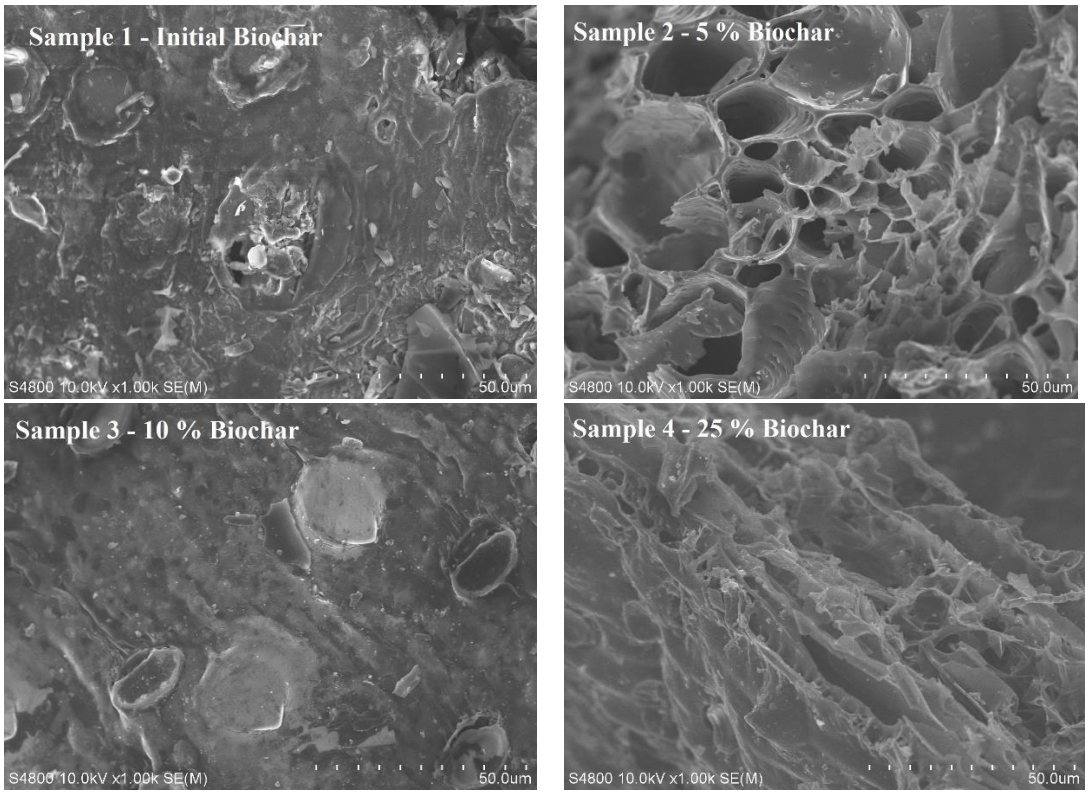

Fig. 5.16 SEM images of the biochar samples.

The results did not reveal any differences between the initial biochar and the treatment ones. The use of the material in the column is not brought change in its physical characteristics, so the material is not changed or destroyed, so it can be reused for further treatment applications.

6. SUMMARY – CONCLUSIONS

This chapter summarizes the conclusions of the total capital, an optimum way of taking measurements proposed in this provision and possible future research suggested based on the knowledge obtained from this thesis.

6.1 METHOD

Despite SIP method is not widely used as other electrical methods (e.g. electrical resistivity tomography), SIP method is a versatile and powerful experimental tool that can be used as a non-destructive way to indirectly reveal significant electric processes leading not only in dielectric characterization of materials, but also in understanding basic fundamental physical behaviors under specific experimental conditions.

The ability to control and change the measurement conditions and taking measurements in a very wide frequency range makes it possible to study different processes and polarization mechanisms. The advantages over other physicochemical study techniques (relatively easy sample preparation, controlled measurement conditions, a large frequency range of measurement), making it an indispensable study tool in a wide range of applications, materials science, hydrogeology, hydrocarbon contamination etc.

6.2 GEOMETRIC FACTOR MEASUREMENTS

SIP method can be successfully used for detailed monitoring of conductive or resistive solutions (e.g. conductive or resistive contaminants) as the resulting values of the conductivity from the columns containing fluid media showed little deviation from the theoretical values, indicating that the steps taken to reduce error were effective.

6.3 SENSITIVITY IMPACT OF CHANGES IN GRAIN SIZE

Individual structural aspects, such as, grain size (Leroy et al., 2008) are not the only parameters determining SIP response. Koch et al., 2011 noted that the SIP response of granular sandy media is an important topic for research in this domain (Koch et al., 2011). For these reasons, measurements were made at different fractions of quartz sand in a known aqueous solution in order to determine the SIP sensitivity in the different grain sizes.

6.4 RESPONSE AT DIFFERNET FLUID CONCENTRATIONS

OMW show a remarkably large load of organic matter compared to the typical municipal wastewater. The discharge of untreated or partially treated OMW in water systems (e.g. aquifers) may lead to a rapid increase in BOD and COD resulting balance disorders of entire ecosystems. This is not immediately apparent as there is no a grounded monitoring process of these water systems to identify pollution beyond laboratory chemical analyses. The SIP responses show that the SIP method is able to distinguish different concentrations of OMW in aqueous solutions.

6.5 PHYTOREMEDIATION

The phytoremediation method based on the SIP and chemical results is an effective degradation method. However, the manner in which the measurements were made wasn't the proper one. Measurements were not made directly to the tank or to collected ground core of the root system, but OMW outflow liquids collected and injected in sample holders with clean soil sample. This probably was the reason that we couldn't collect further information. A challenge in the near future could be the in-situ SIP measurements in the phytoremediation tank that could give us information about the interface changes during the different phytoremediation processes.

6.6 BIOCHAR

During the measurements using biochar we have moved from aerobic to anaerobic treatment. Initially, there was a small amount of oxygen within the columns helped to partial degradation of the OMW and the reduction of phenols, so it was more amenable to subsequent processing.

The biochar production could be an important tool in the prevention and rehabilitation of degraded soils. Notably, each organic material may be a raw material for producing biochar (agricultural and industrial waste, sewage, etc.) which makes the production of biochar a viable waste management technology. However, before making large-scale applications, further research should be performed to understand the biochar and developing protocols, quantify the capacity of biochar and understanding of the contaminant sorption and mechanisms and kinetics.

REFERENCES

Agrafioti, E., Kalderis, D., & Diamadopoulos, E. (2014). Ca and Fe modified biochars as adsorbents of arsenic and chromium in aqueous solutions. *Journal of Environmental Management*, *146*, 444–450. http://doi.org/10.1016/j.jenvman.2014.07.029

Alkorta, I., & Garbisu, C. (2001). Phytoremediation of organic contaminants in soils. *Bioresource Technology*, *79*(3), 273–276. http://doi.org/10.1016/S0960-8524(01)00016-5

Andronikidis, N., Kritikakis, G. S., Agioutantis, Z., Vafidis, A., Steiakakis, C., Papageorgiou, C., … Vargemezis, G. (2015). Mapping the Bedrock Using ERT for Slope Stability Studies at Mavropigi Lignite Open Pit Mine , Northern Greece. In *8th Congress of the Balkan Geophysical Society*.

Arora, T., Linde, N., Revil, A., & Castermant, J. (2007). Non-intrusive characterization of the redox potential of landfill leachate plumes from self-potential data. *Journal of Contaminant Hydrology*, *92*(3-4), 274–292. http://doi.org/10.1016/j.jconhyd.2007.01.018

Atekwana, E. A., & Slater, L. (2009). Biogeophysics: A new frontier in Earth science research. *Reviews of Geophysics*, *47*. http://doi.org/http://dx.doi.org/10.1029/2009JG001159

Attwa, M., & Günther, T. (2013). Spectral induced polarization measurements for predicting the hydraulic conductivity in sandy aquifers. *Hydrology and Earth System Sciences*, *17*(10), 4079–4094. http://doi.org/10.5194/hess-17-4079-2013

Bachmann, H. J., Bucheli, T. D., Dieguez-Alonso, A., Fabbri, D., Knicker, H., Schmidt, H. P., … Zehetner, F. (2016). Toward the Standardization of Biochar Analysis: The COST Action TD1107 Interlaboratory Comparison. *Journal of Agricultural and Food Chemistry*, *64*(2), 513–527. http://doi.org/10.1021/acs.jafc.5b05055

Barrow, C. J. (2012). Biochar: Potential for countering land degradation and for improving agriculture. *Applied Geography*, *34*, 21–28. http://doi.org/10.1016/j.apgeog.2011.09.008

Borner, F., Gruhne, M., & Schoen, J. (1993). Contamination indications derived from electrical properties in the low frequency range. *Geophysical Prospecting*, *41*(1), 83–98.

Brown, S. R., Sorenson, J. R., & Brown, T. I. (2004). A Laboratory Study of the Complex Electrical Resistivity Response of Soils. In *Symposium on the Application of Geophysics to Engineering and Environmental Problems 2004* (pp. 528–539). Environment and Engineering Geophysical Society. http://doi.org/10.4133/1.2923366

Cardenas, M. B., & Markowski, M. S. (2011). Geoelectrical Imaging of Hyporheic Exchange and Mixing of River Water and Groundwater in a Large Regulated River. *Environmental Science & Technology*, *45*(4), 1407–1411. http://doi.org/10.1021/es103438a

Cassiani, G., Kemna, A., Villa, A., & Zimmermann, E. (2009). Spectral induced polarization for the characterization of free-phase hydrocarbon contamination of sediments with low clay content. *Near Surface Geophysics*, *7*(5-6), 547–562.

Chen, Y., & Or, D. (2006). Effects of Maxwell-Wagner polarization on soil complex dielectric permittivity under variable temperature and electrical conductivity. *Water Resources Research*, *42*(6), 1–14. http://doi.org/10.1029/2005WR004590

Cooney, M. J., Lewis, K., Harris, K., Zhang, Q., & Yan, T. (2016). Start up performance of biochar packed bed anaerobic digesters. *Journal of Water Process Engineering*, *9*, e7–e13. http://doi.org/10.1016/j.jwpe.2014.12.004

Correia, A. M., & Passos, J. (2015). Preliminary Results of an ERT in a Vineyard in Estremoz , Portugal. In *8th Congress of the Balkan Geophysical Society*.

Dahlin, T., & Leroux, V. (2012). Improvement in time-domain induced polarization data quality with multi-electrode systems by separating current and potential cables. *Near Surface Geophysics*, *10*(6), 545–565. http://doi.org/10.3997/1873-0604.2012028

Fan, S., Tang, J., Wang, Y., Li, H., Zhang, H., Tang, J., … Li, X. (2016). Biochar prepared from co-

pyrolysis of municipal sewage sludge and tea waste for the adsorption of methylene blue from aqueous solutions : Kinetics , isotherm , thermodynamic and mechanism. *Journal of Molecular Liquids*, *220*, 432–441. http://doi.org/10.1016/j.molliq.2016.04.107

Georgescu, P., & Chitea, F. (2015). Geoelectrical Exploration of Mineral Deposits Using Gradient Array. In *8th Congress of the Balkan Geophysical Society*.

Günther, T., & Rücker, C. (2012). Electrical Resistivity Tomography (ERT) in geophysical applications - state of the art and future challenges. *Schlumberger Symposium -- 100 Years of Electrical Imaging, Paris*, (January).

Haegel, F., Esser, O., Jablonowski, N. D., & Zimmermann, E. (2013). Characterization , monitoring and imaging of biochar by geoelectrical measurements. In *EGU General Assembly* (Vol. 15).

Hördt, A., Blaschek, R., Kemna, A., & Zisser, N. (2007). Hydraulic conductivity estimation from induced polarisation data at the field scale — the Krauthausen case history. *Journal of Applied Geophysics*, *62*(1), 33–46. http://doi.org/10.1016/j.jappgeo.2006.08.001

Ippolito, J. A., Laird, D. A., & Busscher, W. J. (2012). Environmental benefits of biochar. *Journal of Environmental Quality*, *41*(4), 967–972. http://doi.org/10.2134/jeq2012.0151

Joseph, S. (2016). *The Application of Spectral Induced Polarization to Determination of Hydraulic Conductivity*. Victoria University of Wellington.

Kavvadias, V., Doula, M., & Theocharopoulos, S. (2014). Long-Term Effects on Soil of the Disposal of Olive Mill Waste Waters (OMW). *Environmental Forensics*, *15*(1), 37–51. http://doi.org/10.1080/15275922.2013.872713

Kemna, A. (2000). *Tomographic Inversion od Complex Resistivity*. Ruhr - University of Bochum.

Kemna, A., Binley, A., Cassiani, G., Niederleithinger, E., Revil, A., Slater, L., … Zimmermann, E. (2012). An overview of the spectral induced polarization method for near-surface applications. *Near Surface Geophysics*, *10*(6), 453–468. http://doi.org/10.3997/1873-0604.2012027

Kirmizakis, P., Soupios, P., Simyrdanis, K., Kirkou, S., Papadopoulos, N., Tsourlos, P., … Kim, J.-H. (2015). Geoelectrical characterization of an olive oil mill waste (OOMW) site. In *28th Symposium on the Application of Geophysics to Engineering and Environmental Problems 2015, SAGEEP 2015* (pp. 626–629).

Koch, K., Kemna, A., Irving, J., & Holliger, K. (2011). Impact of changes in grain size and pore space on the hydraulic conductivity and spectral induced polarization response of sand. *Hydrology and Earth System Sciences*, *15*(6), 1785–1794. http://doi.org/10.5194/hess-15-1785-2011

Kuras, O., Pritchard, J. D., Meldrum, P. I., Chambers, J. E., Wilkinson, P. B., Ogilvy, R. D., & Wealthall, G. P. (2009). Monitoring hydraulic processes with automated time-lapse electrical resistivity tomography (ALERT). *Comptes Rendus Geoscience*, *341*(10), 868–885. http://doi.org/10.1016/j.crte.2009.07.010

Leroy, P., Revil, A., Kemna, A., Cosenza, P., & Ghorbani, A. (2008). Complex conductivity of water-saturated packs of glass beads. *Journal of Colloid and Interface Science*, *321*(1), 103–117. http://doi.org/10.1016/j.jcis.2007.12.031

Lesmes, D. P., & Frye, K. . K. M. (2001). Influence of pore fluid chemistry on the complex conductivity and induced polarization responses of Berea sandstone. *Journal of Geophysical Research*, *106*(B3), 4079–4090. http://doi.org/10.1029/2000JB900392

Lesmes, D. P., & Morgan, F. D. (2001). Dielectric spectroscopy of sedimentary rocks. *Journal of Geophysical Research: Solid Earth*, *106*(B7), 13329–13346.

Li, X., Shen, Q., Zhang, D., Mei, X., Ran, W., Xu, Y., & Yu, G. (2013). Functional Groups Determine Biochar Properties (pH and EC) as Studied by Two-Dimensional 13C NMR Correlation Spectroscopy. *PLOS ONE*, *8*(6). http://doi.org/10.1371/journal.pone.0065949

Lokeshappa, B., & Dikshit, A. K. (2012). Single Step Extractions of Metals in Coal Fly Ash. *Resources and Environment*, *2*(2), 1–8. http://doi.org/10.5923/j.re.20120202.01

Luo, Y., & Zhang, G. (1998). *Theory and application of spectral induced polarization*. g. Retrieved from http://library.seg.org/doi/pdf/10.1190/1.9781560801856.fm

Magalhães, S. C. Q., Taveira, M., Cabrita, A. R. J., Fonseca, A. J. M., Valentão, P., & Andrade, P. B. (2017). European marketable grain legume seeds: Further insight into phenolic compounds profiles. *Food Chemistry*, *215*, 177–184. http://doi.org/10.1016/j.foodchem.2016.07.152

Mantzavinos, D., & Kalogerakis, N. (2005). Treatment of olive mill effluents: Part I. Organic matter degradation by chemical and biological processes - An overview. *Environment International*, *31*(2), 289–295. http://doi.org/10.1016/j.envint.2004.10.005

Manyà, J. J. (2012). Pyrolysis for Biochar Purposes: A Review to Establish Current Knowledge Gaps and Research Needs. *Environ. Sci. Technologies*, *46*(1539-7954), 7939–7954. http://doi.org/10.1021/es301029g

Marshall, D. J., & Madden, T. R. (1959). Induced Polarization, A Study of its Causes. *Geophysics*, *24*(4), 790–816. http://doi.org/10.1190/1.1438659

Mazáč, O., Kelly, W. E., & Landa, I. (1985). A hydrogeophysical model for relations between electrical and hydraulic properties of aquifers. *Journal of Hydrology*, *79*(1-2), 1–19. http://doi.org/10.1016/0022-1694(85)90178-7

Meyer, S., Glaser, B., & Quicker, P. (2011). Technical, economical and climate related aspects of biochar production technologies: A literature review. *Environmental Science & Technology*, *45*(22), 110930141845009. http://doi.org/10.1021/es201792c

Mohan, D., Sarswat, A., Ok, Y. S., & Pittman, C. U. (2014). Organic and inorganic contaminants removal from water with biochar, a renewable, low cost and sustainable adsorbent - A critical review. *Bioresource Technology*, *160*, 191–202. http://doi.org/10.1016/j.biortech.2014.01.120

Mulinacci, N., Romani, A., Galardi, C., Pinelli, P., Giaccherini, C., & Vincieri, F. F. (2001). Polyphenolic content in olive oil waste waters and related olive samples. *Journal of Agricultural and Food Chemistry*, *49*(8), 3509–3514. http://doi.org/10.1021/jf000972q

Mumme, J., Srocke, F., Heeg, K., & Werner, M. (2014). Use of biochars in anaerobic digestion. *Bioresource Technology*, *164*, 189–197. http://doi.org/10.1016/j.biortech.2014.05.008

Naudet, V., Revil, A., Bottero, J.-Y., & Bégassat, P. (2003). Relationship between self-potential (SP) signals and redox conditions in contaminated groundwater. *Geophysical Research Letters*, *30*(21), 1–4. http://doi.org/10.1029/2003GL018096

Nautiyal, P., Subramanian, K. A., & Dastidar, M. G. (2016). Adsorptive removal of dye using biochar derived from residual algae after in-situ transesterification: Alternate use of waste of biodiesel industry. *Journal of Environmental Management*, *182*, 187–197. http://doi.org/10.1016/j.jenvman.2016.07.063

Nguyen, F., Kemna, A., Antonsson, A., Engesgaard, P., Kuras, O., Ogilvy, R., … Pulido-Bosch, A. (2009). Characterization of seawater intrusion using 2D electrical imaging. *Near Surface Geophysics*, *7*(5-6), 377–390. http://doi.org/10.3997/1873-0604.2009025

Niaounakis, M., & Halvadakis, C. P. (2006). *Olive Processing Waste Management. Literature Review and Patent Survey*. *Waste Management Series 5* (2nd ed., Vol. 2nd editio). Elsevier Ltd.

Nordsiek, S., & Weller, A. (2008). A new approach to fitting induced-polarization spectra. *Geophysics*, *73*(6), F235–F245. Retrieved from http://www.scopus.com/inward/record.url?eid=2-s2.0-57149091136&partnerID=tZOtx3y1

Ntarlagiannis, D. (2006). *Investigating Geophysical Signatures of Microbial Cells, Processes, ad Degradation: Implications for the Geophysical Monitoring of Microbial Activity and Degradation in the Subsurface*. Rutgers Univesity (State University of New Jersey), USA.

Ntarlagiannis, D., & Ferguson, A. (2009). SIP response of artificial biofilms. *Geophysics*, *74*(1), 1–5. http://doi.org/10.1190/1.3031514

Ntarlagiannis, D., Robinson, J., Soupios, P., & Slater, L. (2016). Field-scale electrical geophysics over

an olive oil mill waste deposition site: Evaluating the information content of resistivity versus induced polarization (IP) images for delineating the spatial extent of organic contamination. *Journal of Applied Geophysics*. http://doi.org/10.1016/j.jappgeo.2016.01.017

Ntarlagiannis, D., Yee, N., & Slater, L. (2005). On the low-frequency electrical polarization of bacterial cells in sands. *Geophysical Research Letters*, *32*(24), 1–4. http://doi.org/10.1029/2005GL024751

Ogilvy, R. D., Meldrum, P. I., Kuras, O., Wilkinson, P. B., Chambers, J. E., Sen, M., … Tsourlos, P. (2009). Automated Monitoring of Coastal Aquifers with Electrical Resistivity Tomography. *Near Surface Geophysics*, *7*(5-6), 367–375. http://doi.org/10.1007/s13398-014-0173-7.2

Olhoeft, G. R. (1985). Low-frequency electrical properties. *Geophysics*. Retrieved from http://www.scopus.com/inward/record.url?eid=2-s2.0-0022264798&partnerID=tZOtx3y1

Paraskeva, P., & Diamadopoulos, E. (2006). Technologies for olive mill wastewater (OMW) treatment: A review. *Journal of Chemical Technology and Biotechnology*, *81*(9), 1475–1485. http://doi.org/10.1002/jctb.1553

Parasnis, D. S. (1986). *Principles of Applied Geophysics* (4rth Editi). 29 West 35th Street. New York. NY 10001: Chapman and Hall. http://doi.org/10.1007/978-94-009-4113-7

Pelton, W. H., Ward, S. H., Hallof, P. G., Sill, W. R., & Nelson, P. H. (1978). Mineral discrimination and removal of inductive coupling with multifrequency IP. *GEOPHYSICS*, *43*(3), 588–609.

Rani, P., Di Maio, R., Piegari, E., Simyrdanis, K., Papadopoulos, N., & Soupios, P. (2016). Application of self-potential method for monitoring the contamination from Olive oil mills ' waste (OOMW). In *43rd IAH Conference*. Corum, Montpellier, France.

Revil, a., Mendonça, C. A., Atekwana, E. a., Kulessa, B., Hubbard, S. S., & Bohlen, K. J. (2010). Understanding biogeobatteries: Where geophysics meets microbiology. *Journal of Geophysical Research*, *115*, 1–22. http://doi.org/10.1029/2009JG001065

Revil, A., & Florsch, N. (2010). Determination of permeability from spectral induced polarization in granular media. *Geophysical Journal International*, *181*(3), 1480–1498. http://doi.org/10.1111/j.1365-246X.2010.04573.x

Revil, A., Karaoulis, M., Johnson, T., & Kemna, A. (2012). Review: Some low-frequency electrical methods for subsurface characterization and monitoring in hydrogeology. *Hydrogeology Journal*, *20*(4), 617–658. http://doi.org/10.1007/s10040-011-0819-x

Revil, A., Naudet, V., Nouzaret, J., & Pessel, M. (2003). Principles of electrography applied to self-potential electrokinetic sources and hydrogeological applications. *Water Resources Research*, *39*(5), 1–15. http://doi.org/10.1029/2001WR000916

Reynolds, J. M. (2011). *An Introduction to Applied and Environmental Geophysics. Geophysics* (2nd Editio, Vol. 1). http://doi.org/10.1017/CBO9781107415324.004

Rigane, H., Chtourou, M., Ben Mahmoud, I., Medhioub, K., & Ammar, E. (2015). Polyphenolic compounds progress during olive mill wastewater sludge and poultry manure co-composting, and humic substances building (Southeastern Tunisia). *Waste Management & Research : The Journal of the International Solid Wastes and Public Cleansing Association, ISWA*, *33*(1), 73–80. http://doi.org/10.1177/0734242X14559594

Robinson, J., Slater, L., Johnson, T., Shapiro, A., Tiedeman, C., Ntarlagiannis, D., … Lane, J. (2016). Imaging Pathways in Fractured Rock Using Three-Dimensional Electrical Resistivity Tomography. *Groundwater*, *54*(2), 186–201. http://doi.org/10.1111/gwat.12356

Ruffet, C., Darot, M., & Guéguen, Y. (1995). Surface conductivity in rocks: a review. *Surveys in Geophysics*, *16*(1), 83–105. http://doi.org/10.1007/BF00682714

Schmutz, M., Revil, A., Vaudelet, P., Batzle, M., Viñao, P. F., & Werkema, D. D. (2010). Influence of oil saturation upon spectral induced polarization of oil-bearing sands. *Geophysical Journal International*, *183*(1), 211–224. http://doi.org/10.1111/j.1365-246X.2010.04751.x

Shah, S. D., & Braun, C. L. (2004). Demonstration-Site Development and Phytoremediation Processes

Associated With Trichloroethene (TCE) in Ground Water , Naval Air Station-Joint Reserve Base Carswell Field , Fort Worth , Texas. *U.S. Geological Survey Fact Sheet 2004*, *3087*(August), 1–4.

Singh, S. P., & Ghosh, M. (2005). A Review on Phytoremediation of Heavy Metals and Utilization of It ' s by Products, *6*(04), 214–231.

Slater, L., & Lesmes, D. (2002). IP interpretation in environmental investigations. *Geophysics*, *67*(1), 77. http://doi.org/10.1190/1.1451353

Slater, L., & Lesmes, D. P. (2002). Electrical-hydraulic relationships observed for unconsolidated sediments. *Water Resources Research*, *38*(10), 33–46. http://doi.org/10.1029/2001WR001075

Soupios, P., & Karaoulis, M. (2015). Application of Self-Potantial (SP) Method for Monitoring Contaminants Movement. In *8th Congress of the Balkan Geophysical Society*. Chania, Greece.

Sumner, J. S. (1976). *Principles of induced polarization for geophysical exploration*. *Elsevier Scientific, Amsterdam*. Amsterdam.

Sunyoto, N. M. S., Zhu, M., Zhang, Z., & Zhang, D. (2016). Effect of biochar addition on hydrogen and methane production in two-phase anaerobic digestion of aqueous carbohydrates food waste. *Bioresource Technology*, *219*, 29–36. http://doi.org/10.1016/j.biortech.2016.07.089

Tabatabaei, M., Rahim, R. A., Abdullah, N., Wright, A.-D. G., Shirai, Y., Sakai, K., … Hassan, M. A. (2010). Importance of the methanogenic archaea populations in anaerobic wastewater treatments. *Process Biochemistry*, *45*(8), 1214–1225. http://doi.org/10.1016/j.procbio.2010.05.017

Tselentis, A., & Paraskeuopoulos, P. (2013). *Applied Geophysics*. Athens, Greece: Literal Books.

Tsourlos, P., Vargemezis, G. N., Fikos, I., & Tsokas, G. N. (2014). DC geoelectrical methods applied to landfill investigation: Case studies from Greece. *First Break*, *32*(8), 81–89.

Ustra, A., Slater, L., Ntarlagiannis, D., & Elis, V. (2012). Spectral Induced Polarization (SIP) signatures of clayey soils containing toluene. *Near Surface Geophysics*, *10*(6), 503–515. http://doi.org/10.3997/1873-0604.2012015

Vanhala, H. (1997). Mapping oil-contaminated sand and till with the spectral induced polarization (SIP) method. *Geophysical Prospecting*, *45*(2), 303–326. http://doi.org/10.1046/j.1365-2478.1997.00338.x

Vanhala, H., & Soininen, H. (1995). Laboratory technique for measurement of spectral induced polarization response of soil samples. *Geophysical Prospecting*, *43*, 655–676.

Ward, S. H. (1990). Resistivity and Induced Polarization Methods. *Geotechnical and Environmental Geophysics*, *I*(Review and tutorial), 147–190.

Weller, A., & Slater, L. D. (2015). Induced polarization dependence on pore space geometry: Empirical observations and mechanistic predictions. *Journal of Applied Geophysics*, *123*, 310–315. http://doi.org/10.1016/j.jappgeo.2015.09.002

Weller, A., Slater, L., Nordsiek, S., & Ntarlagiannis, D. (2010). On the estimation of specific surface per unit pore volume from induced polarization: A robust empirical relation fits multiple data sets. *Geophysics*, *75*(4), WA105–WA112.

Zhou, Q. Y., Shimada, J., & Sato, A. (2001). Three-dimensional spatial and temporal monitoring of soil water content using electrical tomography. *Water Resources Research*, *37*(2), 273–285. http://doi.org/http://dx.doi.org/10.1029/2000WR900284; doi:10.102

Zisser, N., Kemna, A., & Nover, G. (2010). Dependence of spectral-induced polarization response of sandstone on temperature and its relevance to permeability estimation. *Journal of Geophysical Research: Solid Earth*, *115*(9), 1–15. http://doi.org/10.1029/2010JB007526

APPENDIX A

A.1 Instrumentation

A portable field/lab spectral induced polarization (PSIP) instrument (Fig. A.1), was used to determine the spectral response. The instrument has the capability of simultaneously measuring more than one column, as it can be delivered with multiple, independent current channels. It should be mentioned that attention should be taken to the cable connection to the column (both C+ and P+ electrodes should be connected to the upper part of the column) during measurement (Fig. A.2).

Figure A.1 Portable Field/Lab Spectral Induced Polarization (PSIP) instrument

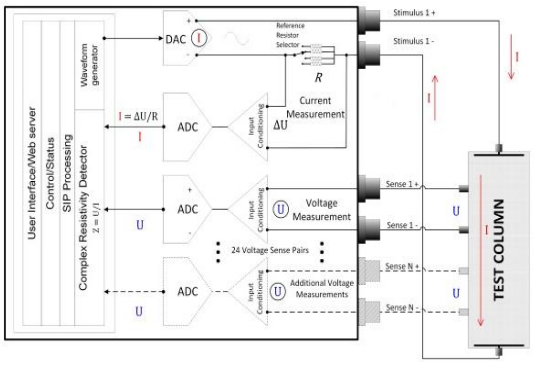

Figure A.2 Block diagram of the laboratory Spectral Induced Polarization (http://www.ontash.com/products.htm)

The PSIP instrument is user-friendly, as all it requires is the instrument's network connection through an Ethernet cable and it will automatically configure itself for network access. All you need for this connection is the instrument connect to a monitor through the PSIP VGA port, and to a keyboard and a mouse through the PSIP USB port.

To start taking measurements, just open a web browser and type the right network address and you have access to the interface (http://PSIP_IP_adress, the address that you have specified before). Theoretically, you can follow the progress of the measurements anywhere, as all that is needed is to connect to a network.

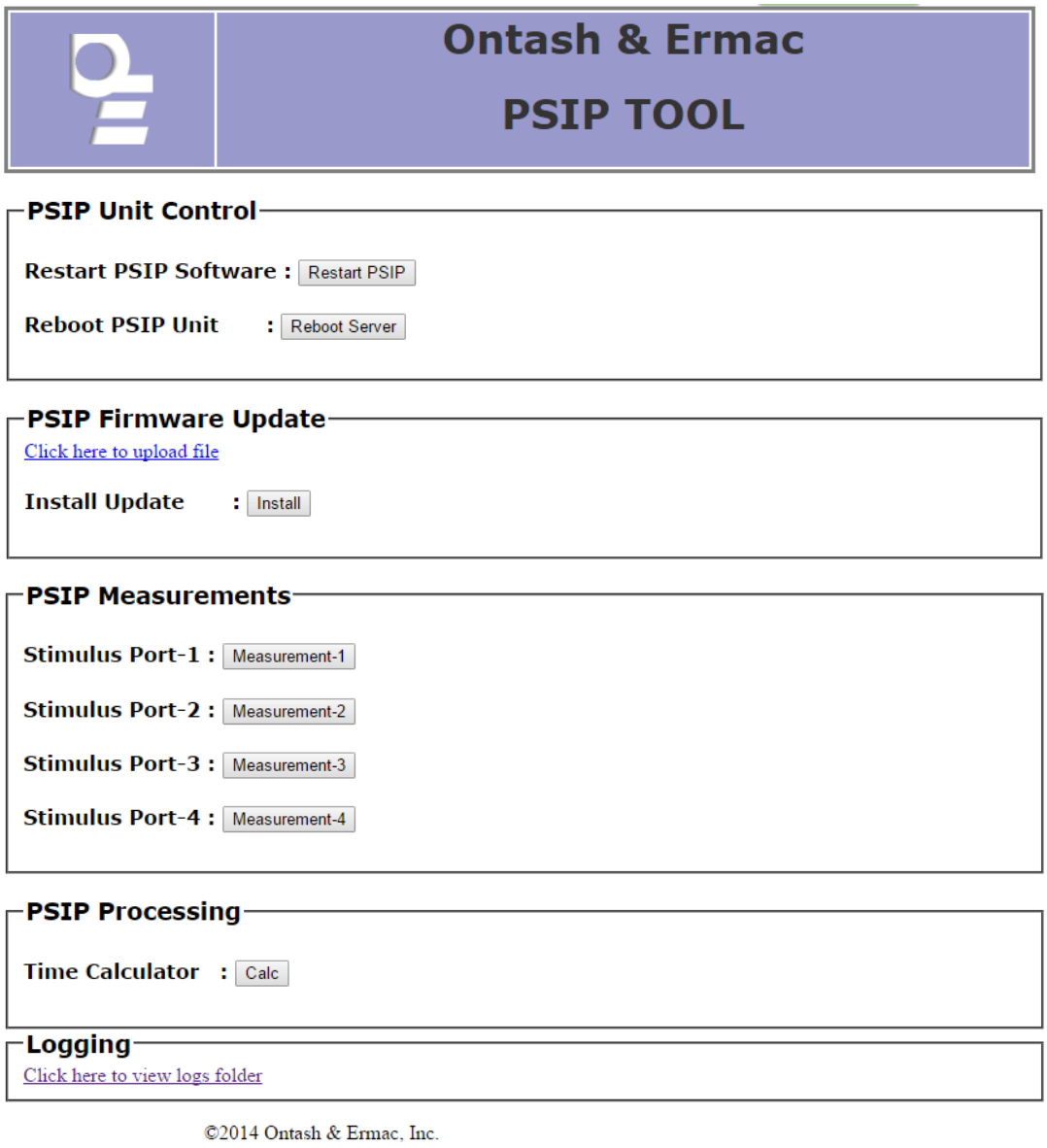

Figure A.3 Starting options menu of the instrument, from which it can be selected which current channel will be used for the measurement or you can make the necessary upgrades.

After selecting the stimulus port, it transferred to a window for the observation of the recording of the measurement and for the adjustment of the settings such as the frequency range, density of the sampling etc. The PSIP interface allows very easily setting the range of the frequencies as well as the number of frequency points per decade.

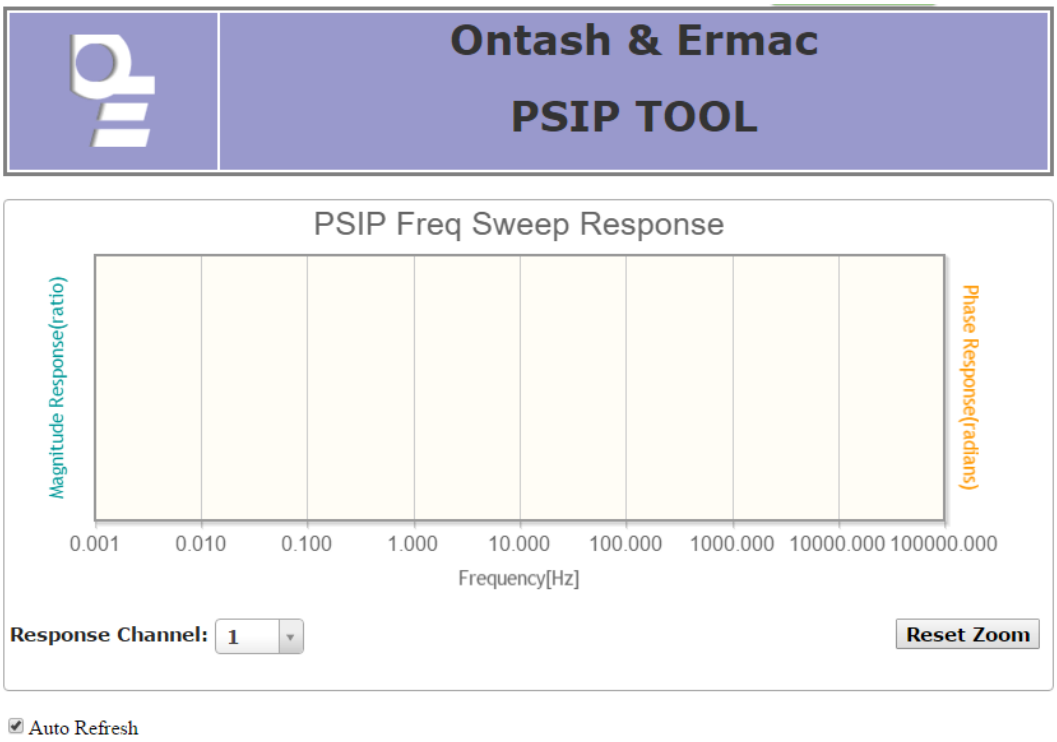

Figure A.4 Recording window of the magnitude and phase response (x axis shows frequency [Hz] in log scale, y axis shows magnitude [ratio] and phase response [radians]).

Use the default settings as follows. At this point it is worth noting that when we changed the "Integration cycles" to 1, we observed a low frequency error. Also, current densities used in SIP measurements should be sufficiently low to avoid non-linear effects (Kemna et al., 2012).

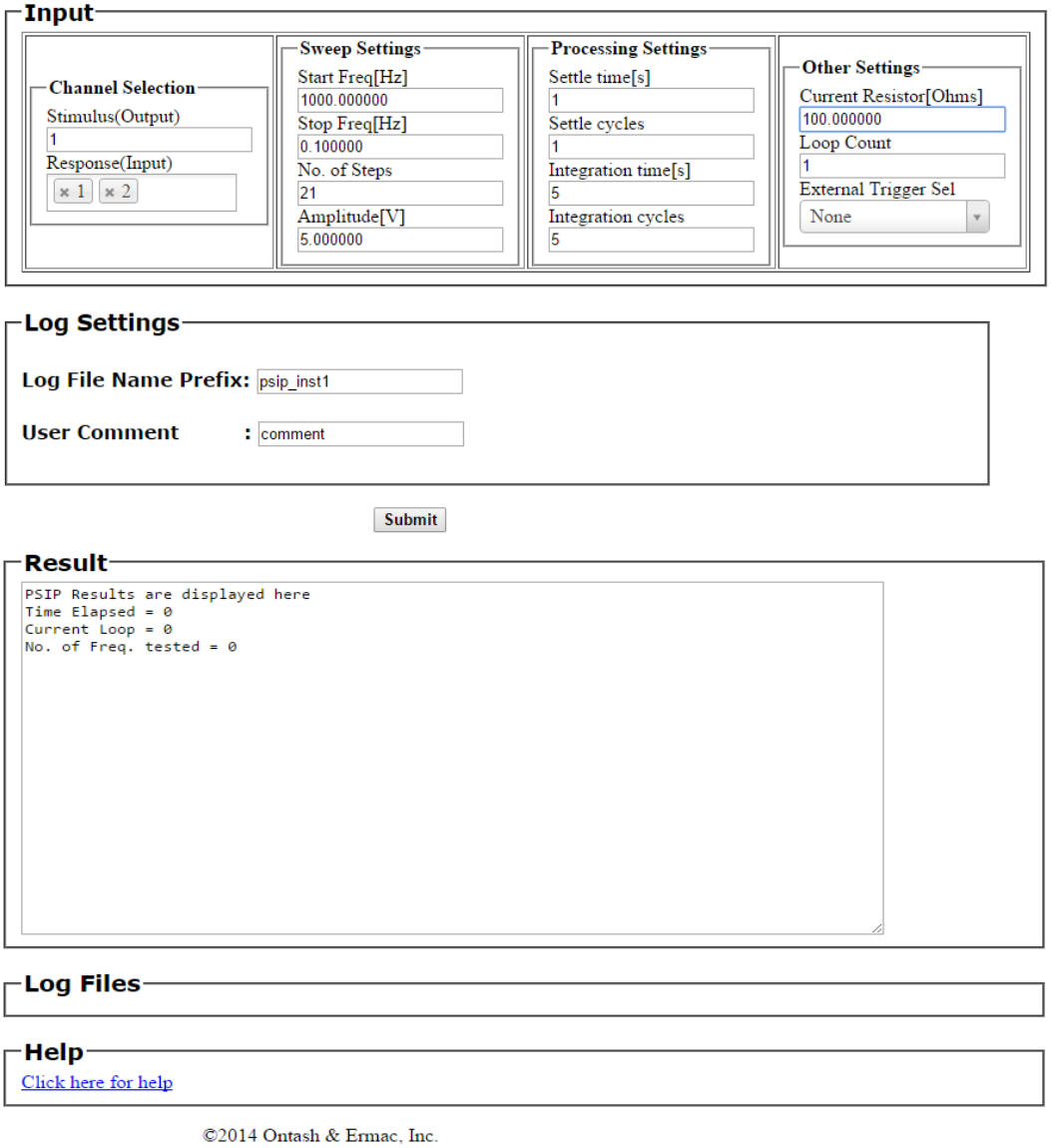

Figure A.5 Snapshot of the default settings.

Then click the submit button to start measurements.

The measured signal is measured as a resistance magnitude (|Z| = Vp/Ip) and phase angle (ϕ) between the injected current and the recorded voltage across the potential electrodes. All results below are from the measurements made with known concentration solutions in the framework of the geometric factor calculation.

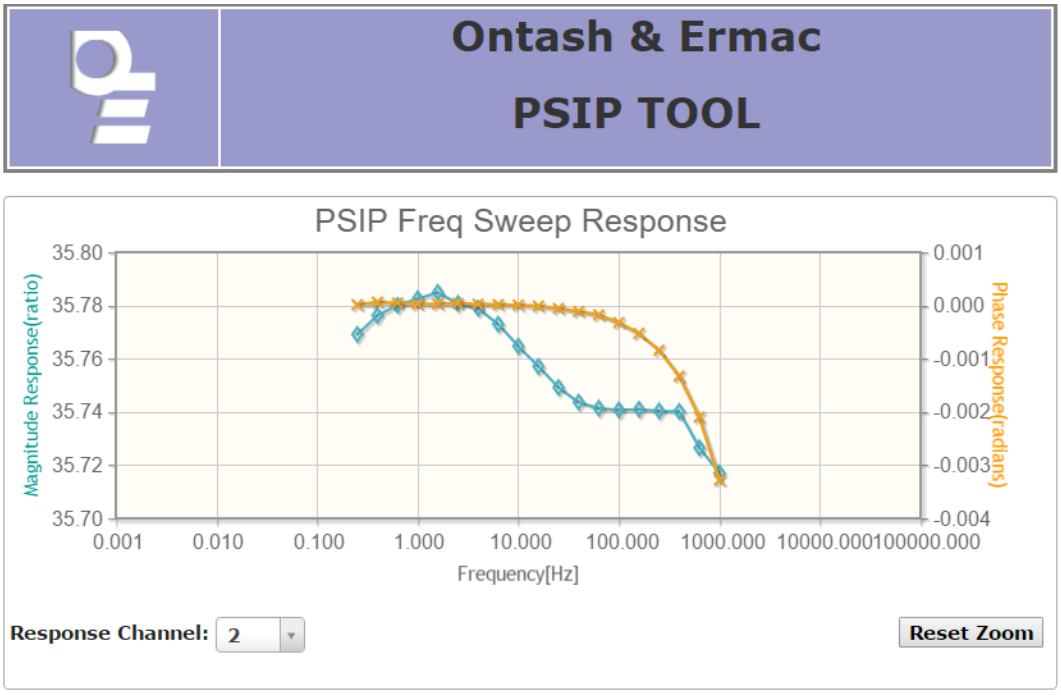

Figure A.6 Snapshot of the recording phase and magnitude response during the fluid tests with KCl solutions.

You can check the results in the "Results" text area.

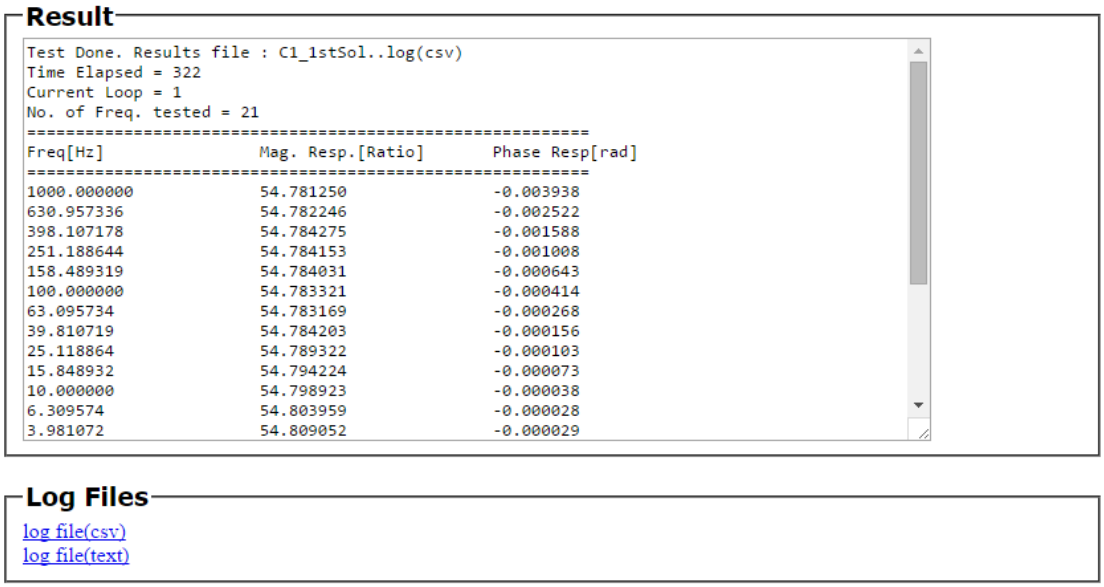

Figure A.7 Results area.

You can also click on the links under "Log Files" to obtain the log files in txt and csv formats from the selected browser to a directory. If you forgot to change the name of the new measurement, you can still download it and change the name afterwards without erasing any data, but if you forgot to download your measurement, it would be lost.

OE	PSIP	Measurement		
PSIP_Version	0.8.0			
Seperator	Comma			
Operator	psip_user			
Description	O&E	PSIP	Measurement	File.
Date	10/3/2016			
Time	11:01:48			
Instance	1			
End_Of_Header				
User_Comment	80.1	Ms/cm		
Current	Resistor[Ohms]	100		
Stimulus	Channel	Num	1	
Response	Channel	Nums	1	
Date	10/3/2016			
Time	11:01:48			
Y_Unit_Label	Hz	Db	rad	
X_Dimension	Time	Time	Time	
End_Of_Header				

X_Value	**AO_sampling_rate**	**Frequency[Hz]**	**Chan-1 Magnitude[ratio]**	**Chan-1 Phase_Shift[rad]**	**Time Stamp[Sec]**	**Loop**	**Com.**
	100000	1000	54.781251	-0.003938	9	1	
	100000	630.957345	54.782247	-0.002522	17	1	
	100000	398.107171	54.784275	-0.001588	27	1	
	100000	251.188644	54.784152	-0.001008	37	1	
	100000	158.48932	54.784029	-0.000643	45	1	
	100000	100	54.78332	-0.000414	55	1	
	100000	63.095735	54.78317	-0.000268	64	1	
	100000	39.810717	54.784203	-0.000156	73	1	
	100000	25.118864	54.789323	-0.000103	82	1	
	100000	15.848932	54.794224	-0.000073	90	1	
	100000	10	54.798924	-0.000038	99	1	
	100000	6.309573	54.80396	-0.000028	109	1	
	100000	3.981072	54.809052	-0.000029	119	1	
	100000	2.511886	54.814804	-0.000015	128	1	
	100000	1.584893	54.818229	-0.000005	137	1	
	100000	1	54.821994	-0.00001	147	1	
	100000	0.630957	54.827609	0.000011	160	1	
	100000	0.398107	54.828507	0.000032	180	1	
	100000	0.251189	54.816117	0.000015	209	1	
	100000	0.158489	54.710749	0.000262	253	1	
	100000	0.1	54.641175	0.000011	321	1	

Figure A.8 Resulting CSV file upon completion of the measurement.

Sample name				resistance(Ohm)	100				
Length:	0.09	m							
Area:	0.002	m2		0.001405305					
freq (Hz)	Phase (Rads)	mag(dB)	resistance	resistivity (Ohm-m)	Fluid C (uS/cm)	Phase (mRads)	Imag cond (S/m)	Real cond (S/m)	New K
1000.000000	-0.000775	17.693445	1769.3445	39.31876667	254.331477	0.775	1.97107E-05	0.02543314	309.493148
630.957345	-0.000483	17.694184	1769.4184	39.32040889	254.3208548	0.483	1.22837E-05	0.025432083	309.480222
398.107171	-0.000276	17.693572	1769.3572	39.31904889	254.3296515	0.276	7.0195E-06	0.025432964	309.490927
251.188644	-0.000162	17.694344	1769.4344	39.32076444	254.3185551	0.162	4.11996E-06	0.025431855	309.477424
158.489320	-0.000097	17.694307	1769.4307	39.32068222	254.3190869	0.097	2.4669E-06	0.025431909	309.478071
100.000000	-0.000062	17.694525	1769.4525	39.32116667	254.3159537	0.062	1.57676E-06	0.025431595	309.474258
63.095735	-0.000031	17.694463	1769.4463	39.32102889	254.3168448	0.031	7.88382E-07	0.025431684	309.475343
39.810717	-0.000005	17.694586	1769.4586	39.32130222	254.3150769	0.005	1.27158E-07	0.025431508	309.473191
25.118864	-0.000001	17.694669	1769.4669	39.32148667	254.313884	0.001	2.54314E-08	0.025431388	309.47174
15.848932	0.000014	17.69475	1769.475	39.32166667	254.3127199	-0.014	-3.56038E-07	0.025431272	309.470323
10.000000	0.000016	17.694726	1769.4726	39.32161333	254.3130648	-0.016	-4.06901E-07	0.025431306	309.470743
6.309573	0.000021	17.694661	1769.4661	39.32146889	254.313999	-0.021	-5.34059E-07	0.0254314	309.47188
3.981072	0.000021	17.694578	1769.4578	39.32128444	254.3151919	-0.021	-5.34062E-07	0.025431519	309.473331
2.511886	0.000022	17.694678	1769.4678	39.32150667	254.3137547	-0.022	-5.5949E-07	0.025431375	309.471582
1.584893	0.000018	17.694632	1769.4632	39.32140444	254.3144158	-0.018	-4.57766E-07	0.025431442	309.472387
1.000000	0.000011	17.694723	1769.4723	39.32160667	254.3131079	-0.011	-2.79744E-07	0.025431311	309.470795
0.630957	0.000017	17.694778	1769.4778	39.32172889	254.3123175	-0.017	-4.32331E-07	0.025431232	309.469833
0.398107	0.00002	17.694984	1769.4984	39.32218667	254.3093568	-0.02	-5.08619E-07	0.025430936	309.466231
0.251189	0.000026	17.695345	1769.5345	39.32298889	254.3041687	-0.026	-6.61191E-07	0.025430417	309.459917
0.158489	0.000023	17.696036	1769.6036	39.32452444	254.2942386	-0.023	-5.84877E-07	0.025429424	309.447833
0.1	0.00002	17.697728	1769.7728	39.32828444	254.2699266	-0.02	-5.0854E-07	0.025426993	309.418248
			1769.4748	39.32166286	254.3127445		AVE	0.025431274	309.470354

Current Density Calculation			
Source voltage (V)	*Voltage or Current (A*	*Current density (A/m²)*	
5	0.267473	0.002675	1.337367

Room Temperature in degrees Celsius	Notes
23.5 - 24.5	
Sample Conductivity (µS/cm)	
296	

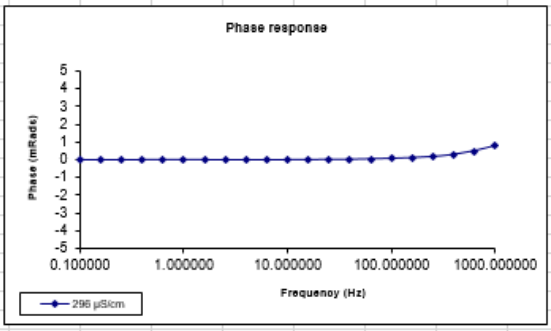

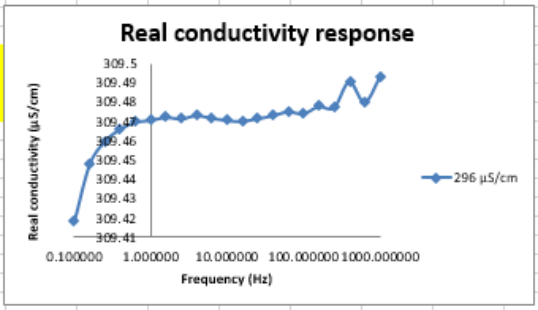

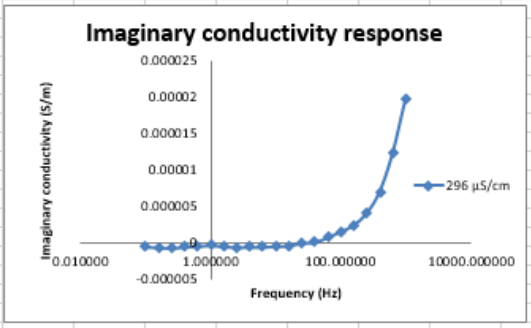

Figure A.9 Resulting file after processing of the primary results.

APPENDIX B

B.1 Calculation of geometric factor

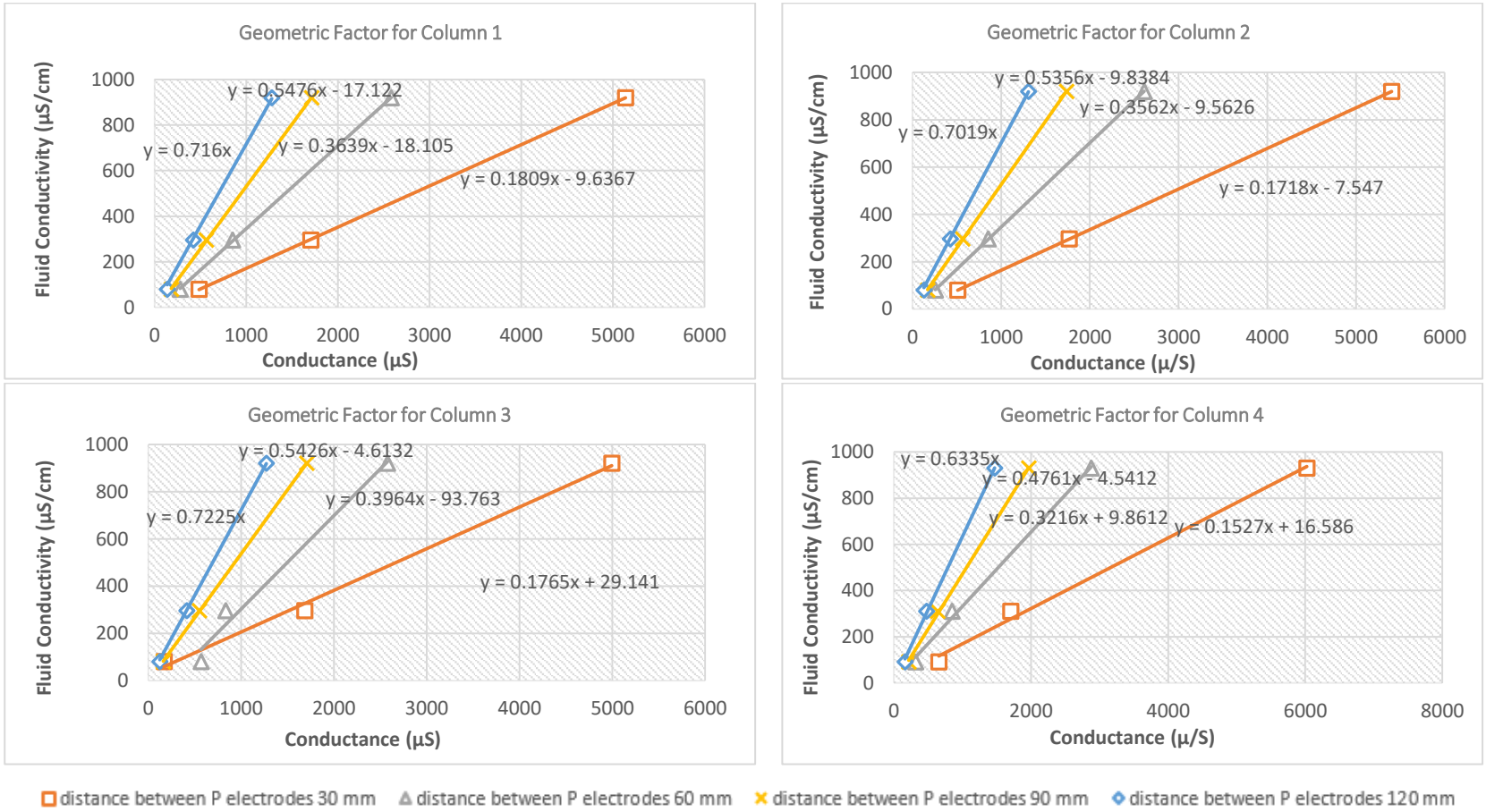

Figure B.1 Calculation of geometric factors for the used columns.

B.2 Fluid tests

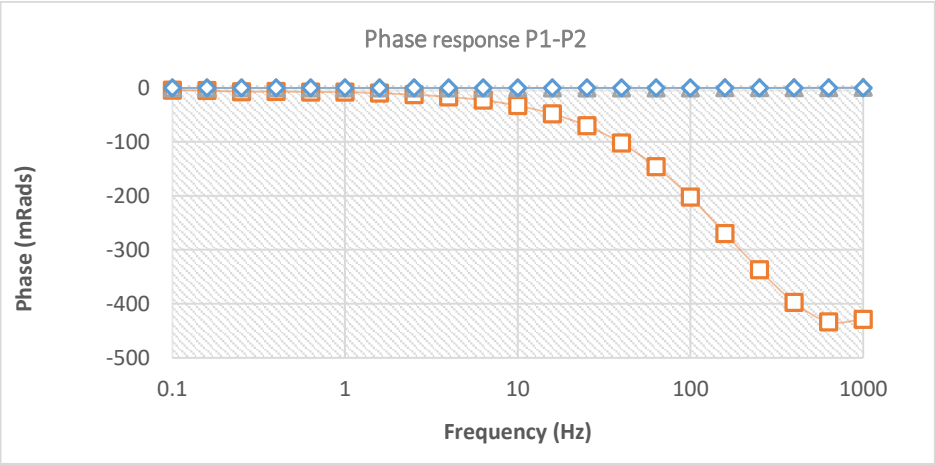

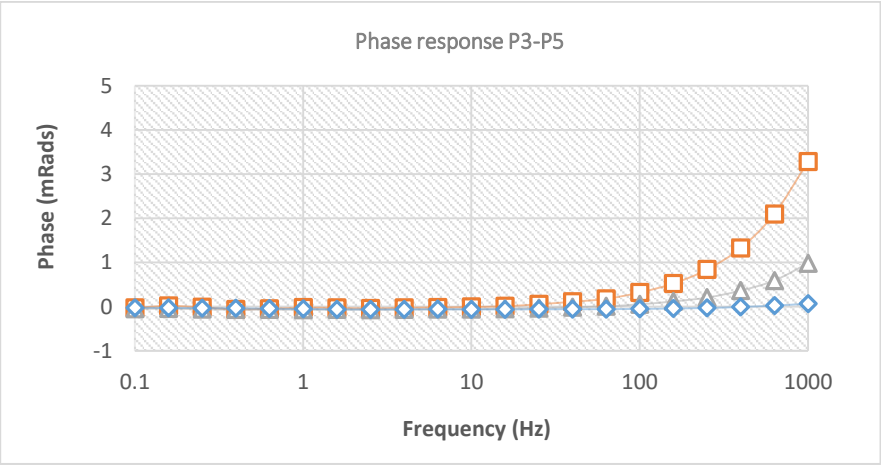

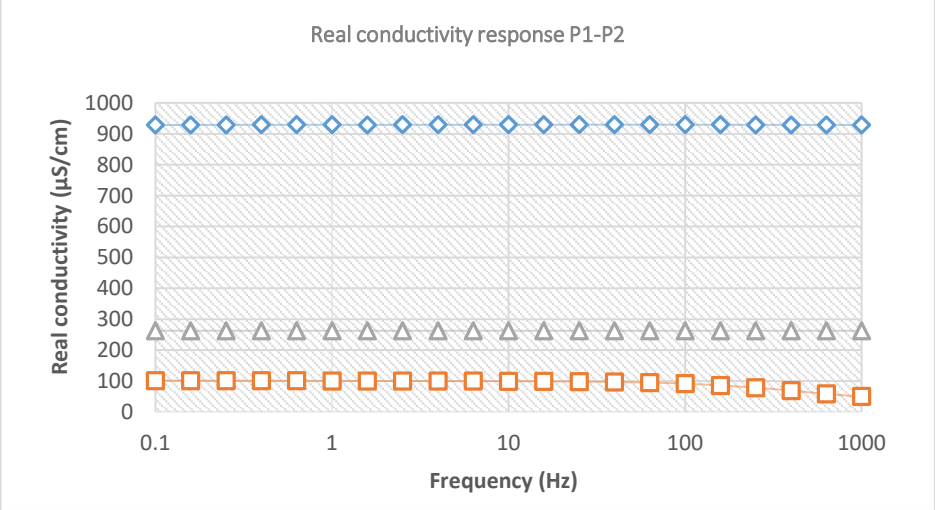

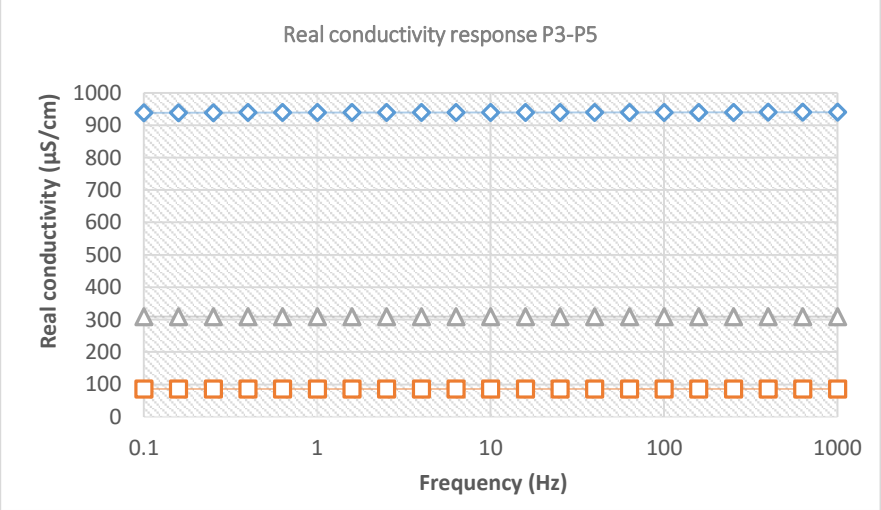

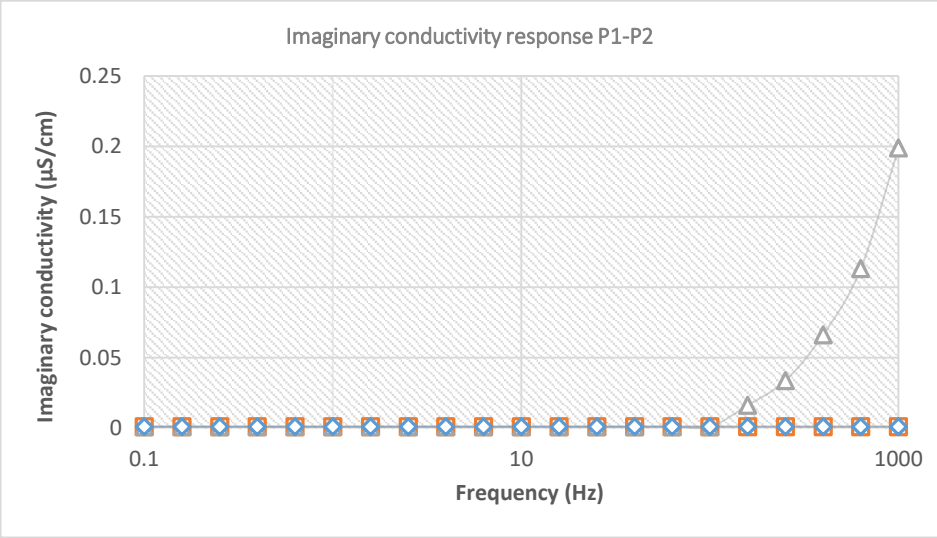
Imaginary conductivity response P1-P2
Imaginary conductivity (µS/cm)
0.25
0.2
0.15
0.1
0.05
0
0.1
10
1000
Frequency (Hz)

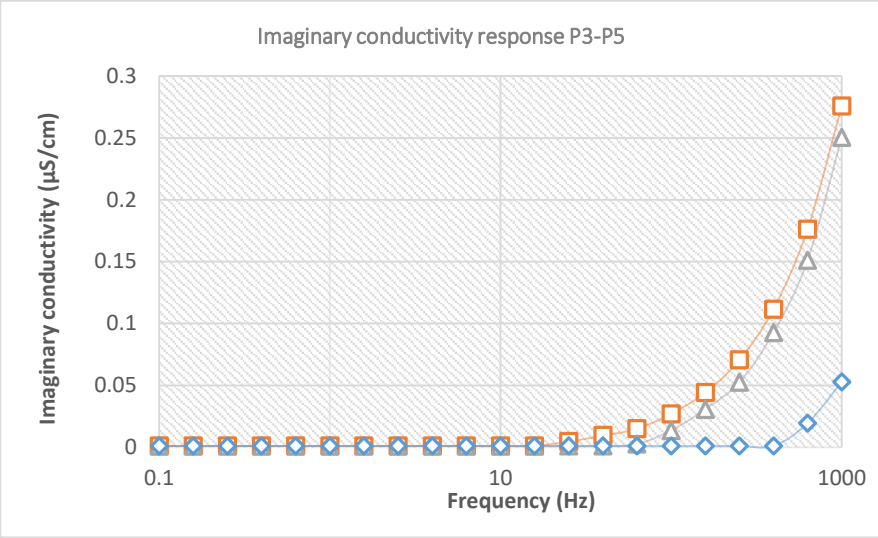
Imaginary conductivity response P3-P5
Imaginary conductivity (µS/cm)
0.3
0.25
0.2
0.15
0.1
0.05
0
0.1
10
1000
Frequency (Hz)

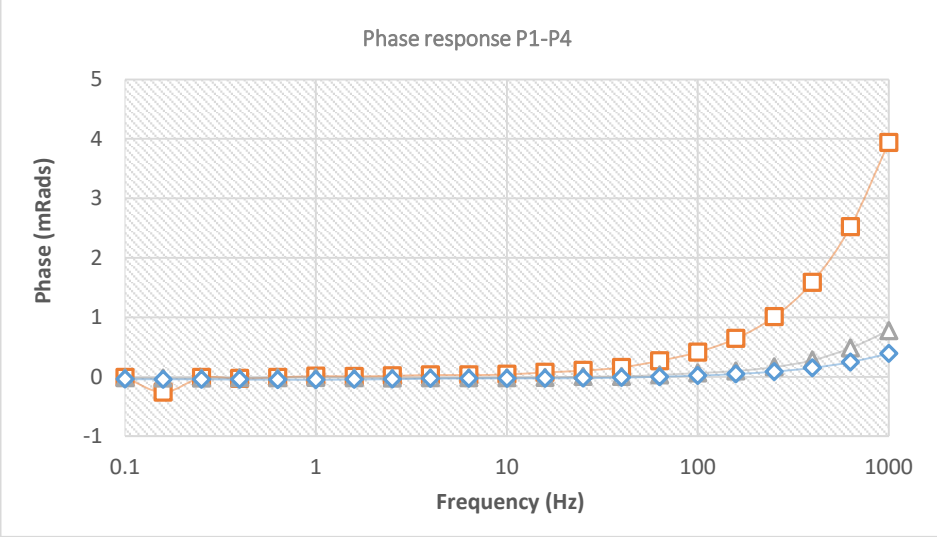
Phase response P1-P4
Phase (mRads)
5
4
3
2
1
0
-1
0.1
1
10
100
1000
Frequency (Hz)

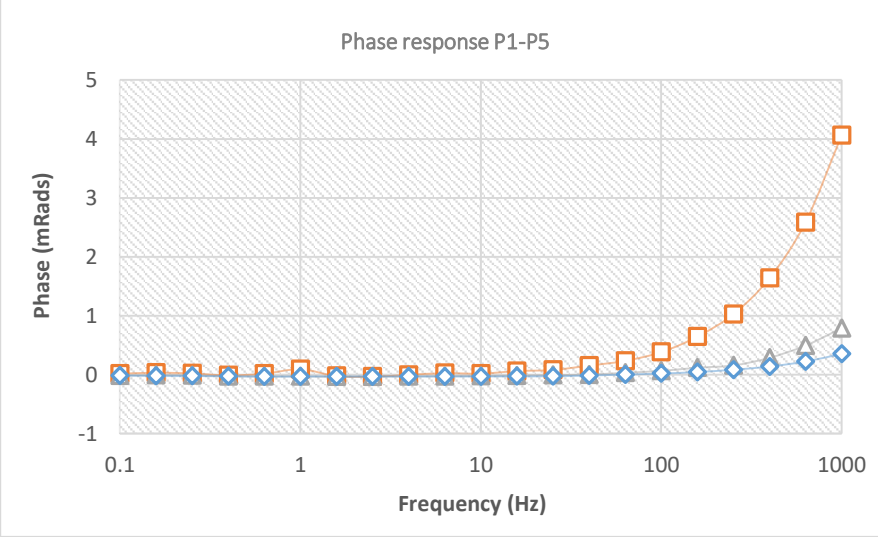
Phase response P1-P5
Phase (mRads)
5
4
3
2
1
0
-1
0.1
1
10
100
1000
Frequency (Hz)

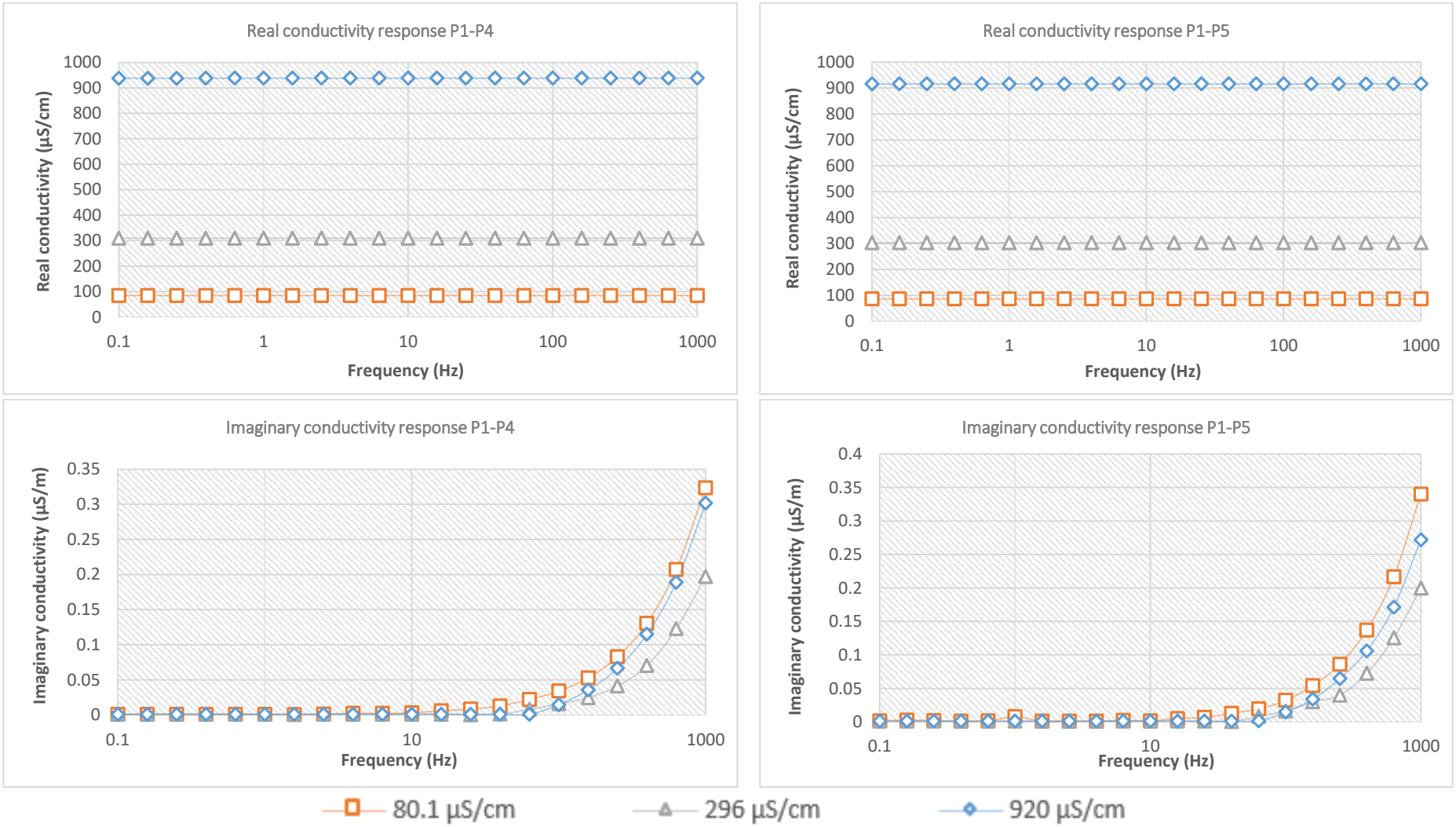

Figure B.2 Phase response and fluid conductivity (real and imaginary part) for column 1 during fluid tests after taking into account the K factor.

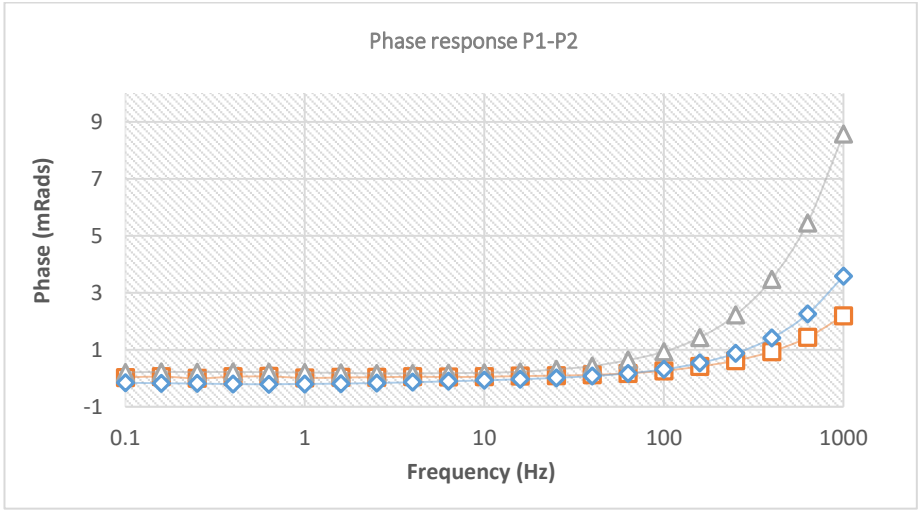
Phase response P1-P2
Phase (mRads)
9
7
5
3
1
-1
0.1
1
10
100
1000
Frequency (Hz)

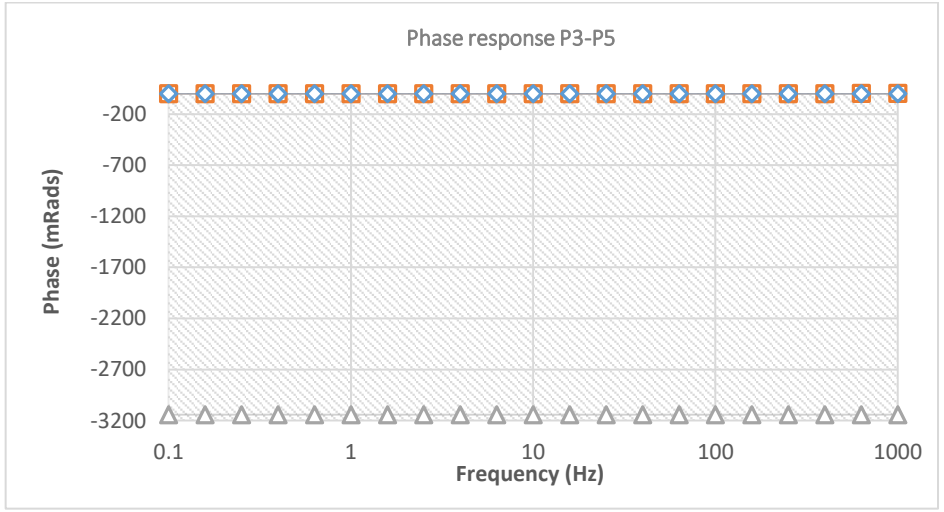
Phase response P3-P5
Phase (mRads)
-200
-700
-1200
-1700
-2200
-2700
-3200
0.1
1
10
100
1000
Frequency (Hz)

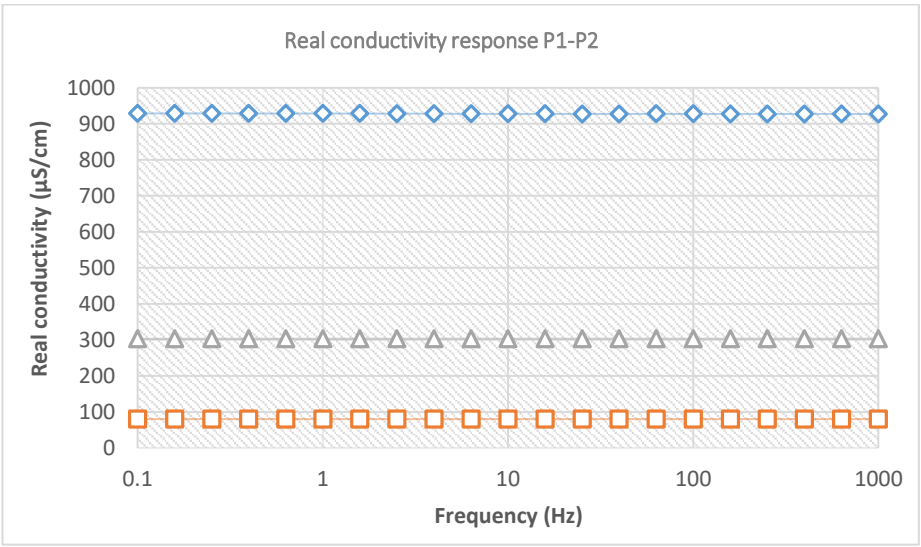
Real conductivity response P1-P2
Real conductivity (µS/cm)
1000
900
800
700
600
500
400
300
200
100
0
0.1
1
10
100
1000
Frequency (Hz)

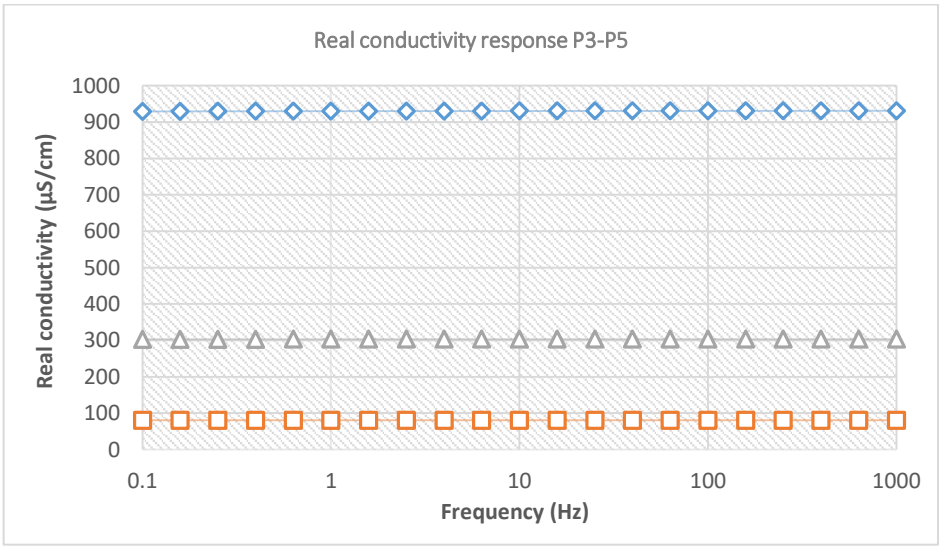
Real conductivity response P3-P5
Real conductivity (µS/cm)
1000
900
800
700
600
500
400
300
200
100
0
0.1
1
10
100
1000
Frequency (Hz)

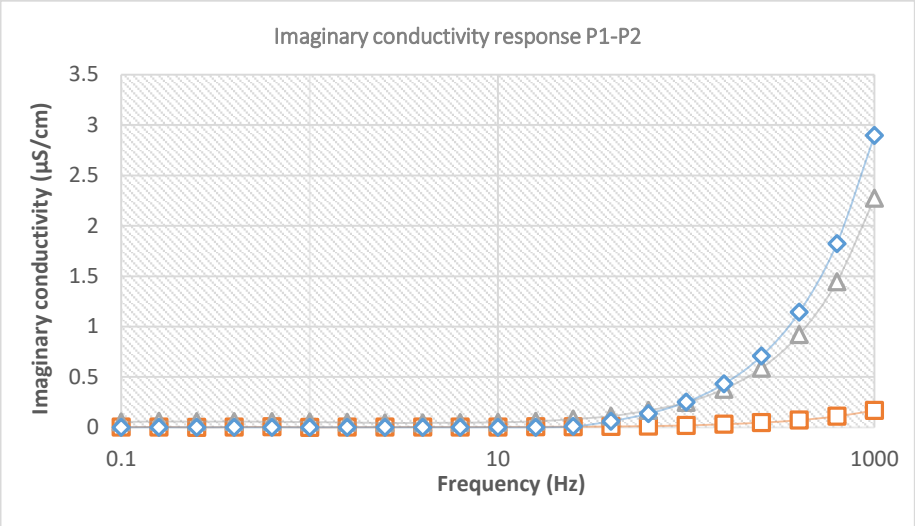
Imaginary conductivity response P1-P2
Imaginary conductivity (µS/cm)
3.5
3
2.5
2
1.5
1
0.5
0
0.1
10
1000
Frequency (Hz)

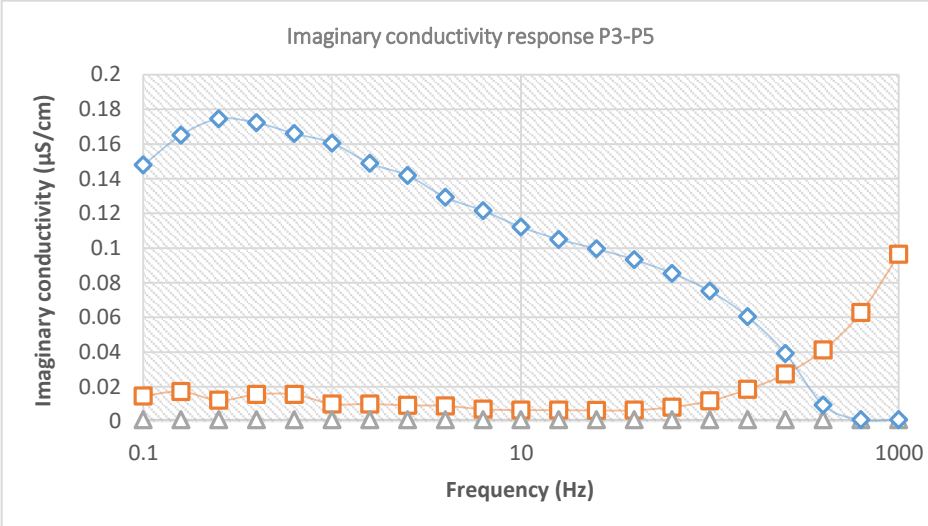
Imaginary conductivity response P3-P5
Imaginary conductivity (µS/cm)
0.2
0.18
0.16
0.14
0.12
0.1
0.08
0.06
0.04
0.02
0
0.1
10
1000
Frequency (Hz)

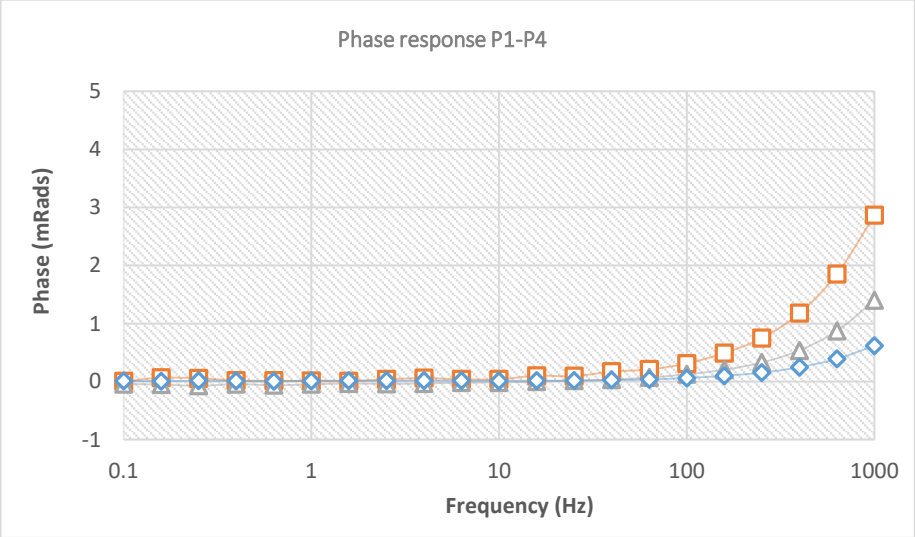
Phase response P1-P4
Phase (mRads)
5
4
3
2
1
0
-1
0.1
1
10
100
1000
Frequency (Hz)

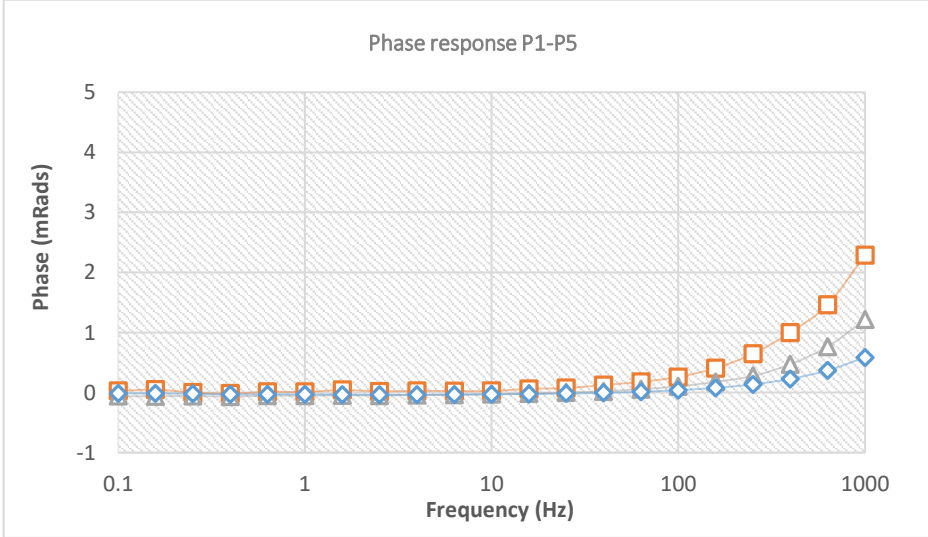
Phase response P1-P5
Phase (mRads)
5
4
3
2
1
0
-1
0.1
1
10
100
1000
Frequency (Hz)

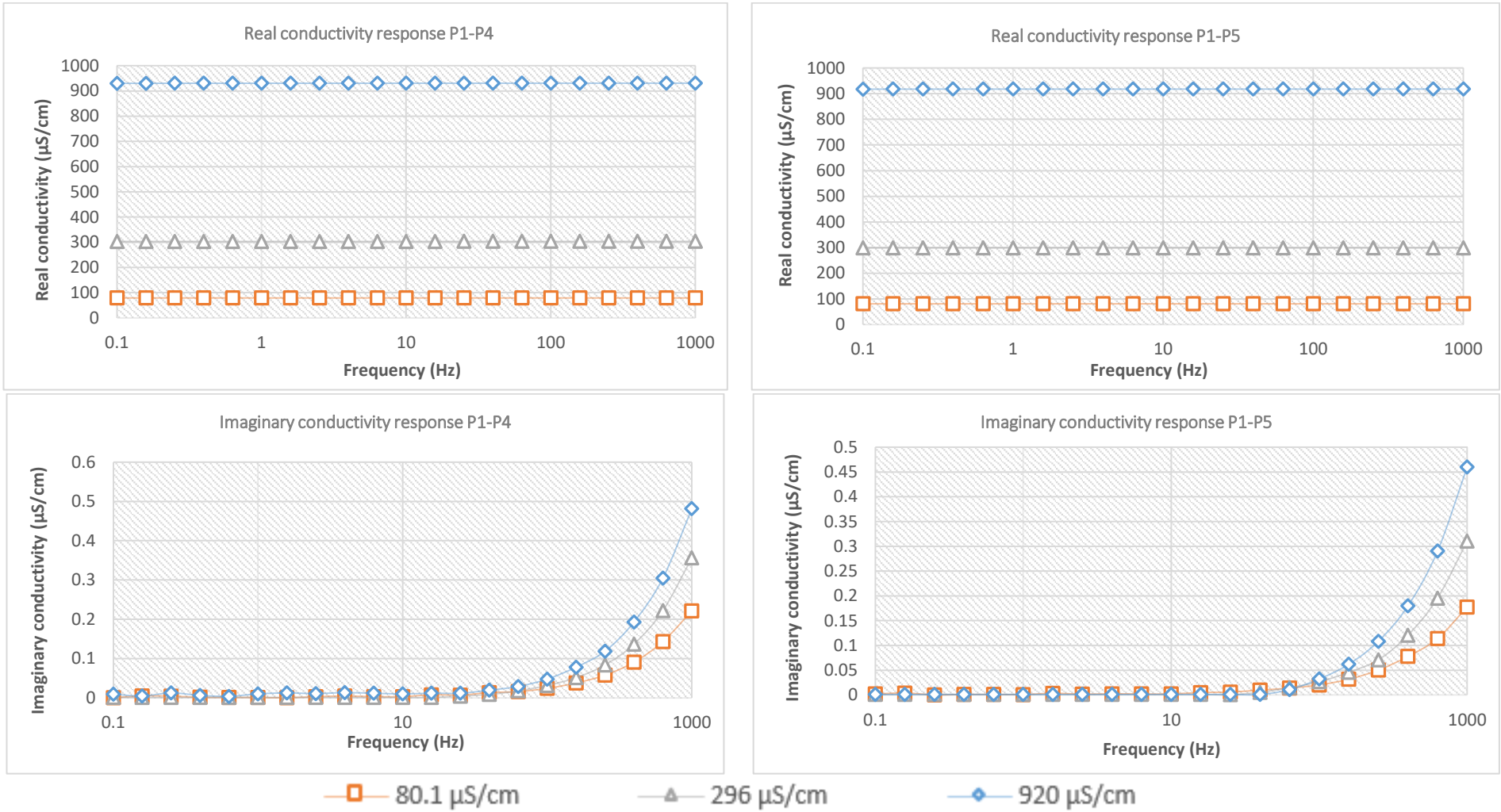

Figure B.3 Phase response and fluid conductivity (real and imaginary part) for column 2 during fluid tests after taking into account the K factor.

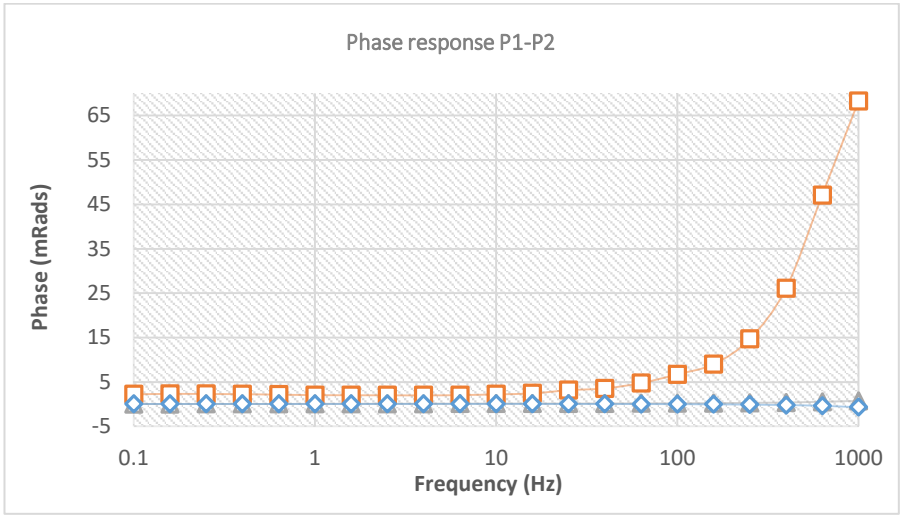
Phase response P1-P2
Phase (mRads)
65
55
45
35
25
15
5
-5
0.1
1
10
100
1000
Frequency (Hz)

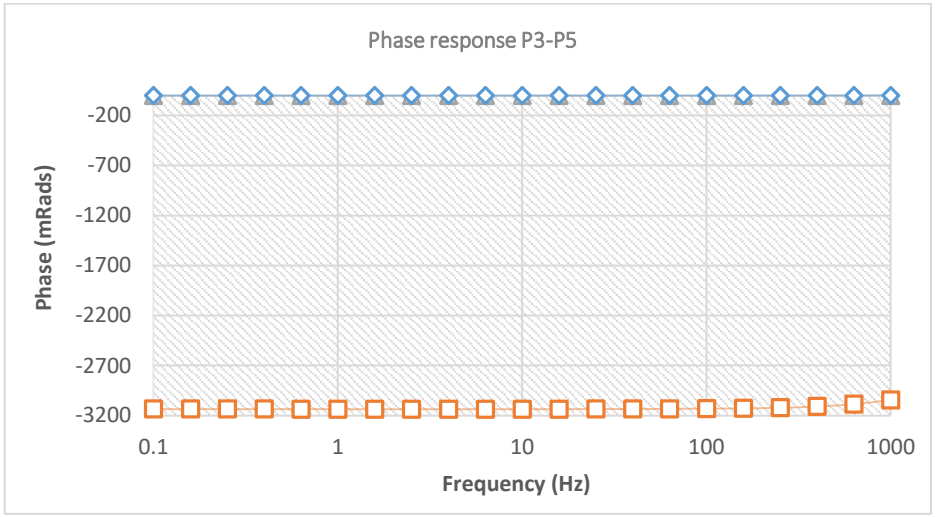
Phase response P3-P5
Phase (mRads)
-200
-700
-1200
-1700
-2200
-2700
-3200
0.1
1
10
100
1000
Frequency (Hz)

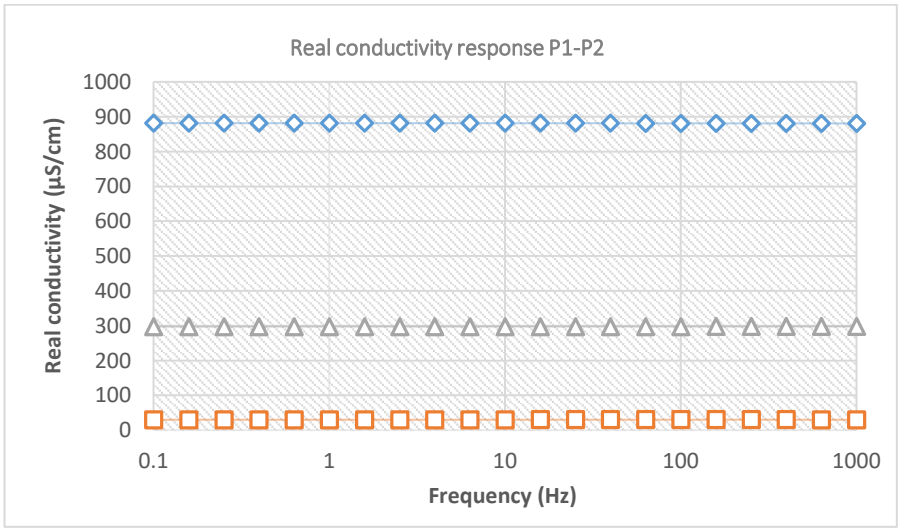
Real conductivity response P1-P2
Real conductivity (µS/cm)
1000
900
800
700
600
500
400
300
200
100
0
0.1
1
10
100
1000
Frequency (Hz)

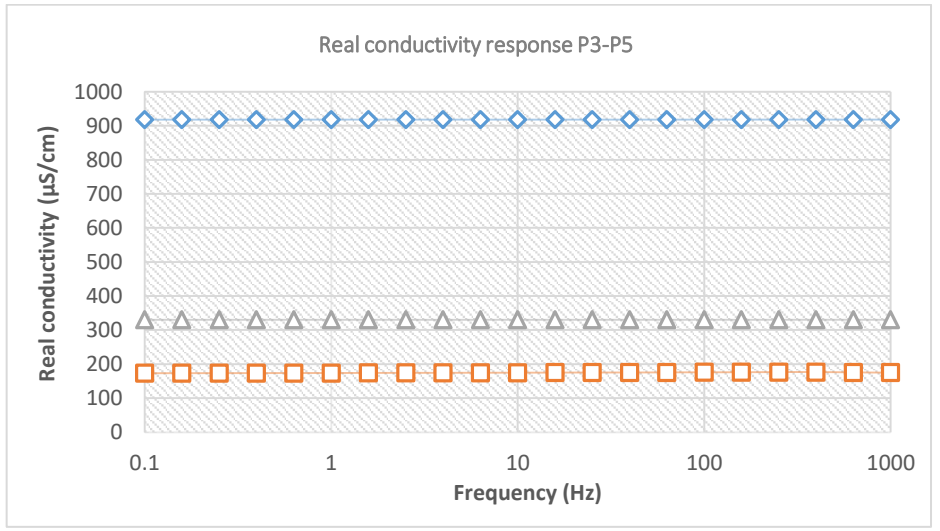
Real conductivity response P3-P5
Real conductivity (µS/cm)
1000
900
800
700
600
500
400
300
200
100
0
0.1
1
10
100
1000
Frequency (Hz)

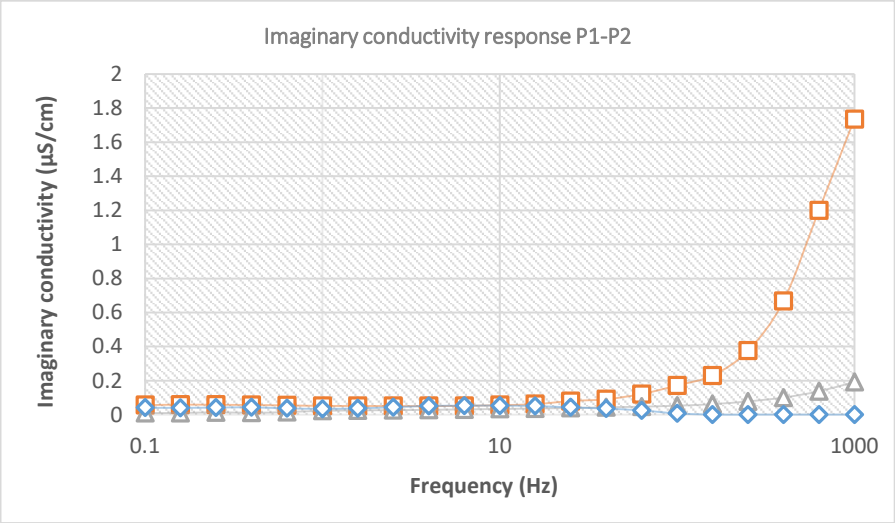
Imaginary conductivity response P1-P2
Imaginary conductivity (µS/cm)
2
1.8
1.6
1.4
1.2
1
0.8
0.6
0.4
0.2
0
0.1
10
1000
Frequency (Hz)

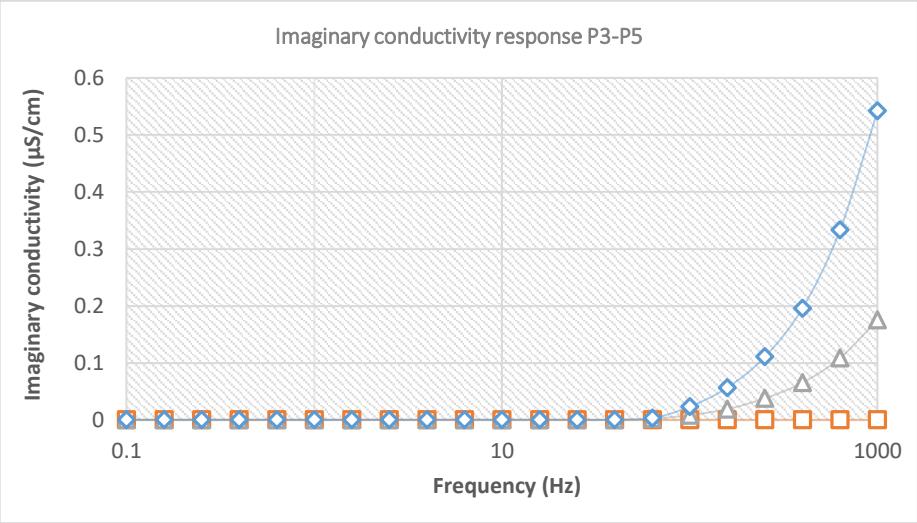
Imaginary conductivity response P3-P5
Imaginary conductivity (µS/cm)
0.6
0.5
0.4
0.3
0.2
0.1
0
0.1
10
1000
Frequency (Hz)

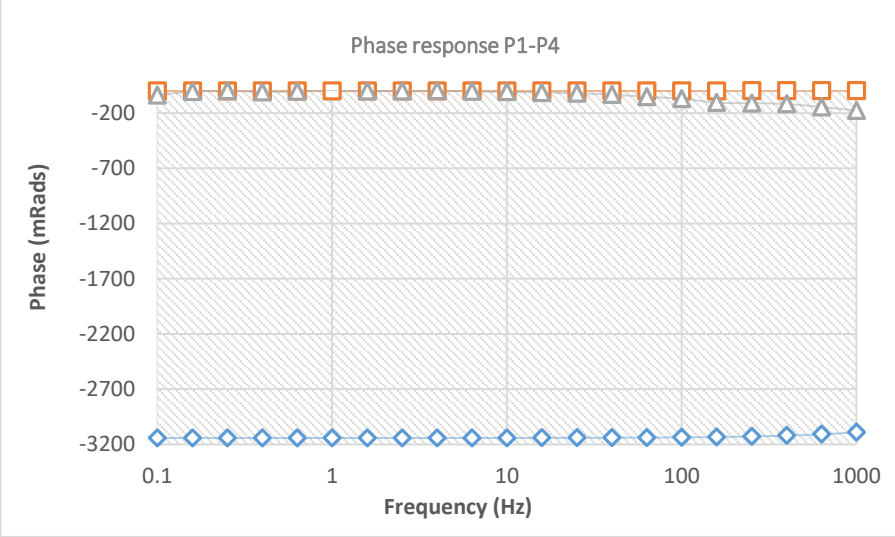
Phase response P1-P4
Phase (mRads)
-200
-700
-1200
-1700
-2200
-2700
-3200
0.1
1
10
100
1000
Frequency (Hz)

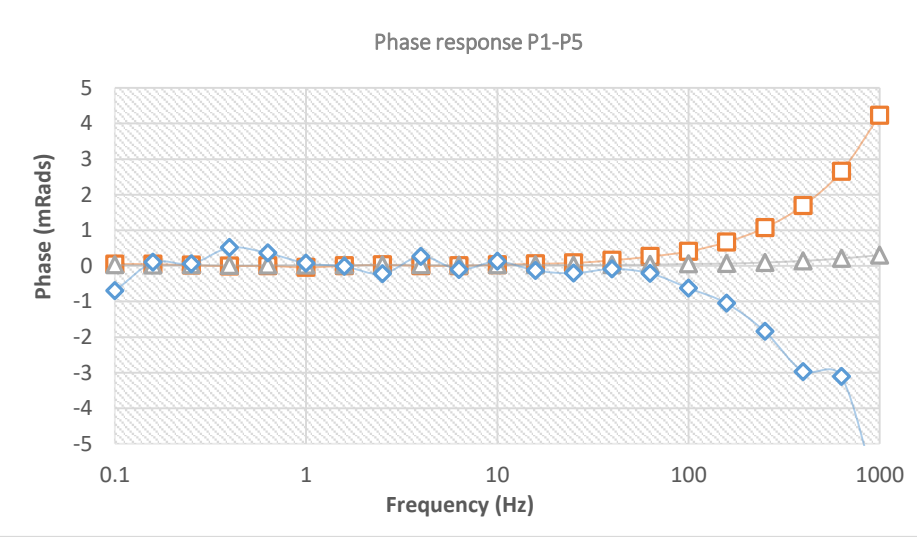
Phase response P1-P5
Phase (mRads)
5
4
3
2
1
0
-1
-2
-3
-4
-5
0.1
1
10
100
1000
Frequency (Hz)

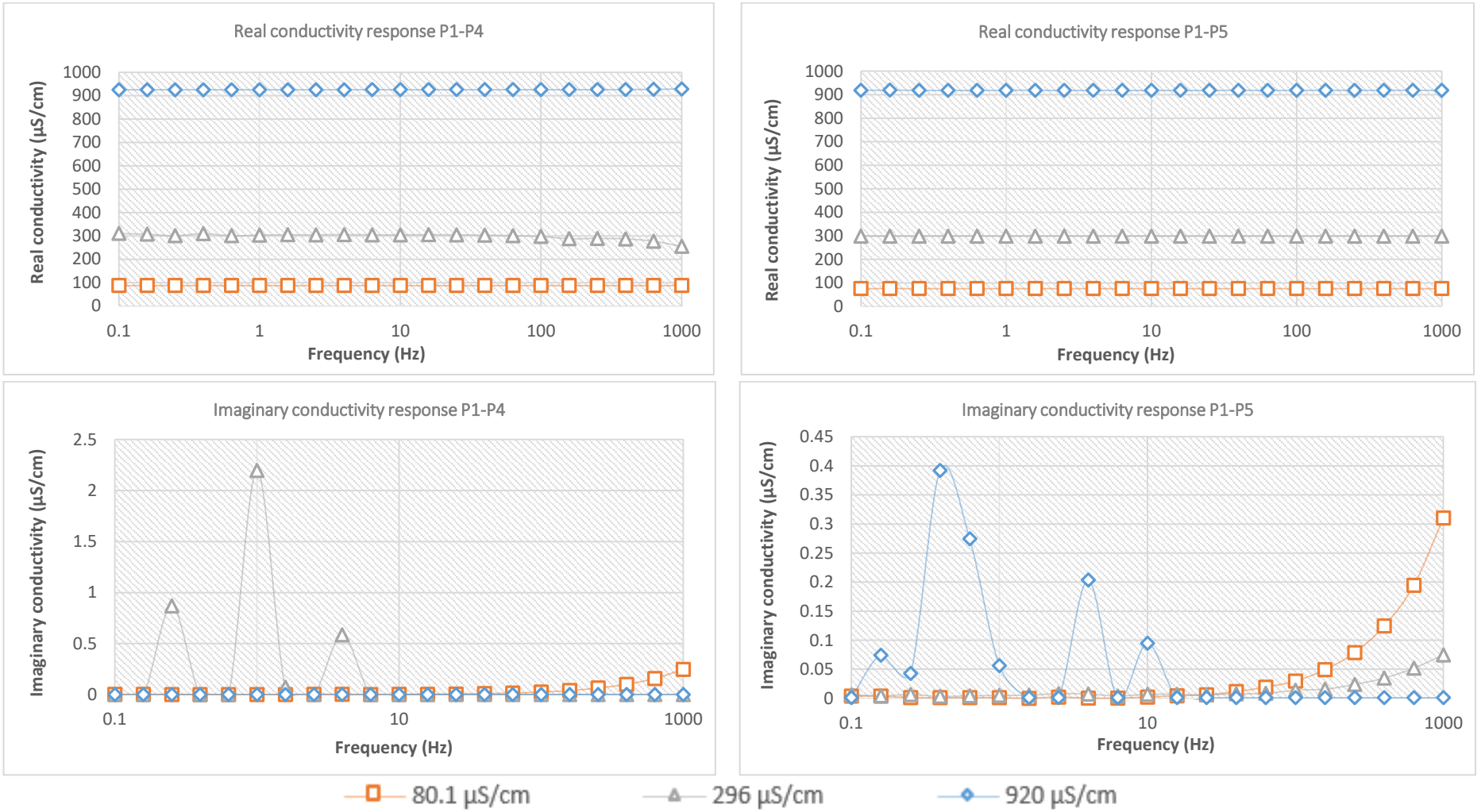

Figure B.4 Phase response and fluid conductivity (real and imaginary part) for column 3 during fluid tests after taking into account the K factor.

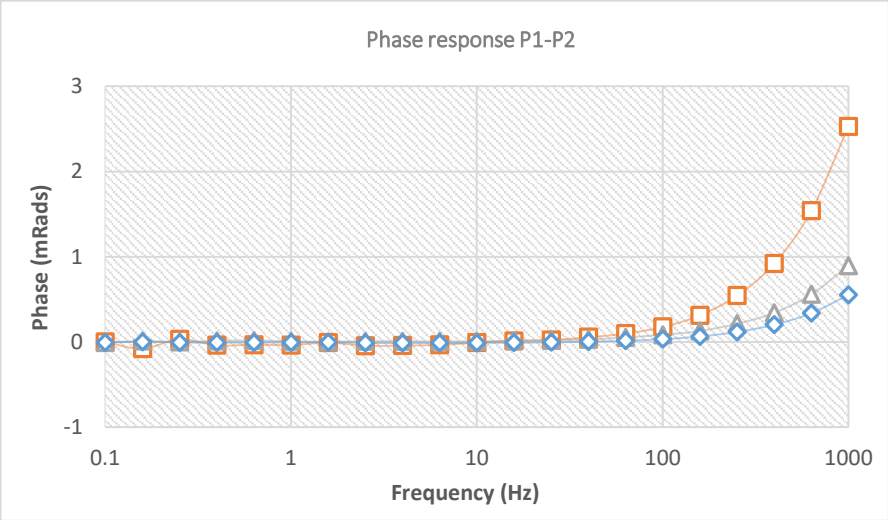
Phase response P1-P2
Phase (mRads)
3
2
1
0
-1
0.1
1
10
100
1000
Frequency (Hz)

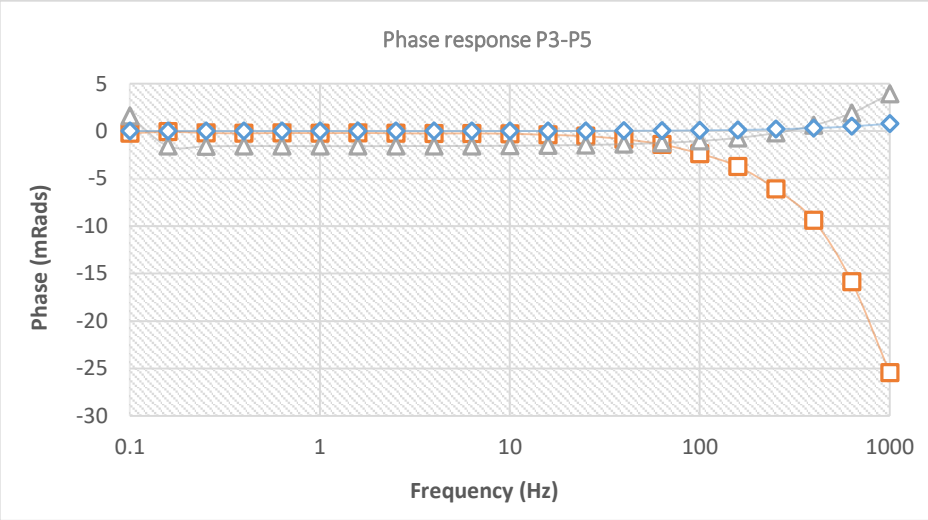
Phase response P3-P5
Phase (mRads)
5
0
-5
-10
-15
-20
-25
-30
0.1
1
10
100
1000
Frequency (Hz)

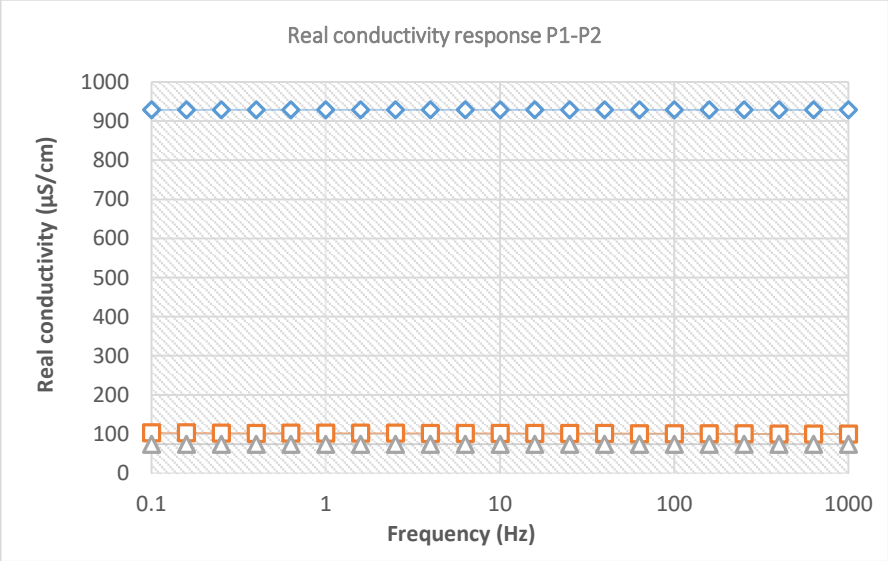
Real conductivity response P1-P2
Real conductivity (µS/cm)
1000
900
800
700
600
500
400
300
200
100
0
0.1
1
10
100
1000
Frequency (Hz)

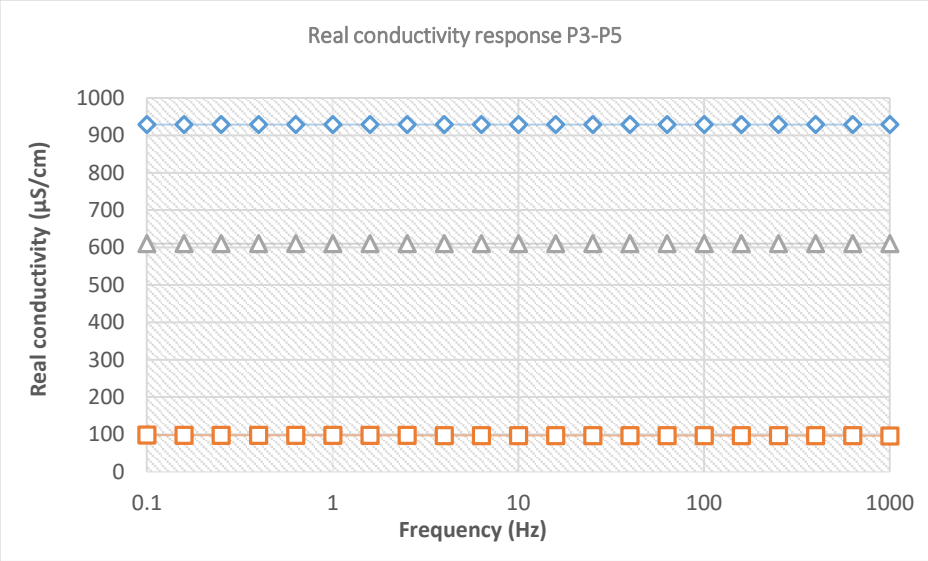
Real conductivity response P3-P5
Real conductivity (µS/cm)
1000
900
800
700
600
500
400
300
200
100
0
0.1
1
10
100
1000
Frequency (Hz)

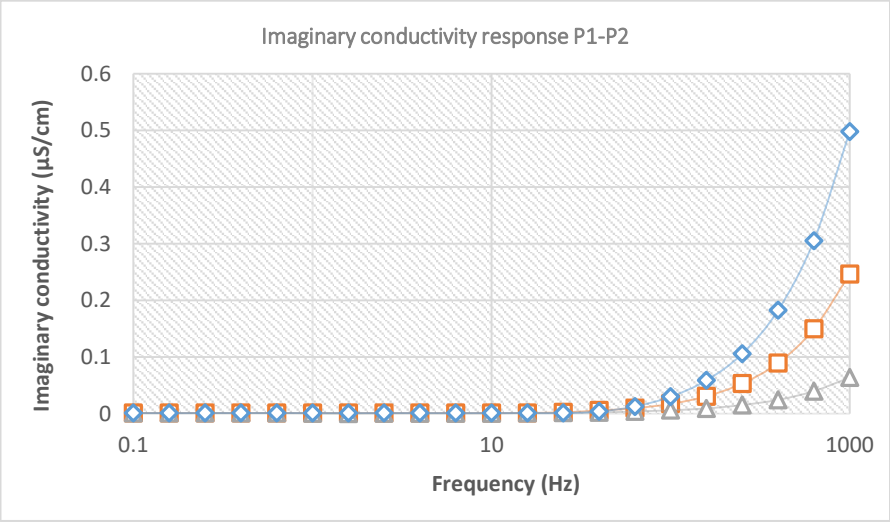
Imaginary conductivity response P1-P2
Imaginary conductivity (µS/cm)
0.6
0.5
0.4
0.3
0.2
0.1
0
0.1
10
1000
Frequency (Hz)

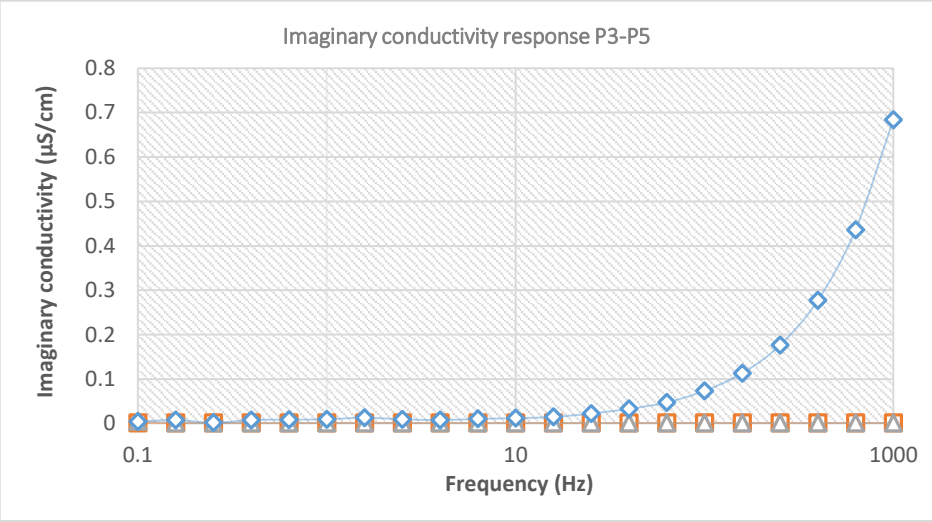
Imaginary conductivity response P3-P5
Imaginary conductivity (µS/cm)
0.8
0.7
0.6
0.5
0.4
0.3
0.2
0.1
0
0.1
10
1000
Frequency (Hz)

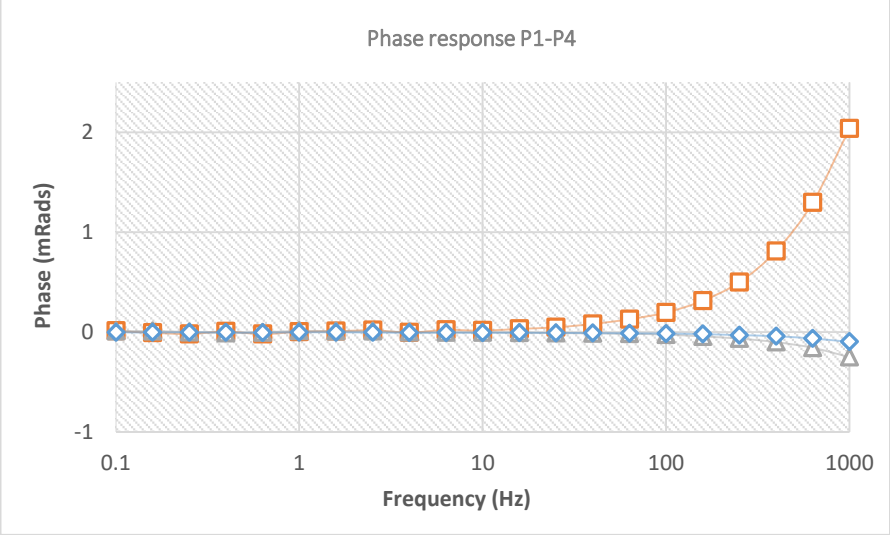
Phase response P1-P4
Phase (mRads)
2
1
0
-1
0.1
1
10
100
1000
Frequency (Hz)

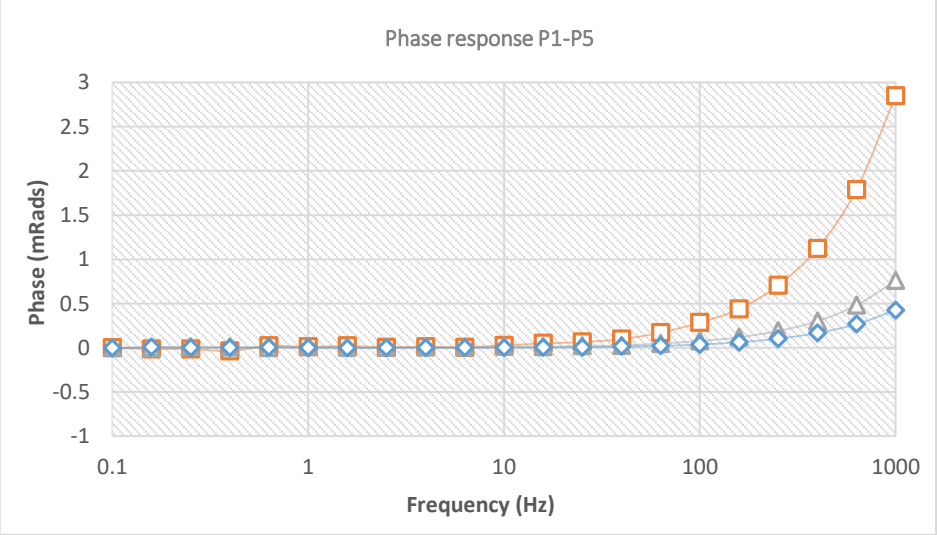
Phase response P1-P5
Phase (mRads)
3
2.5
2
1.5
1
0.5
0
-0.5
-1
0.1
1
10
100
1000
Frequency (Hz)

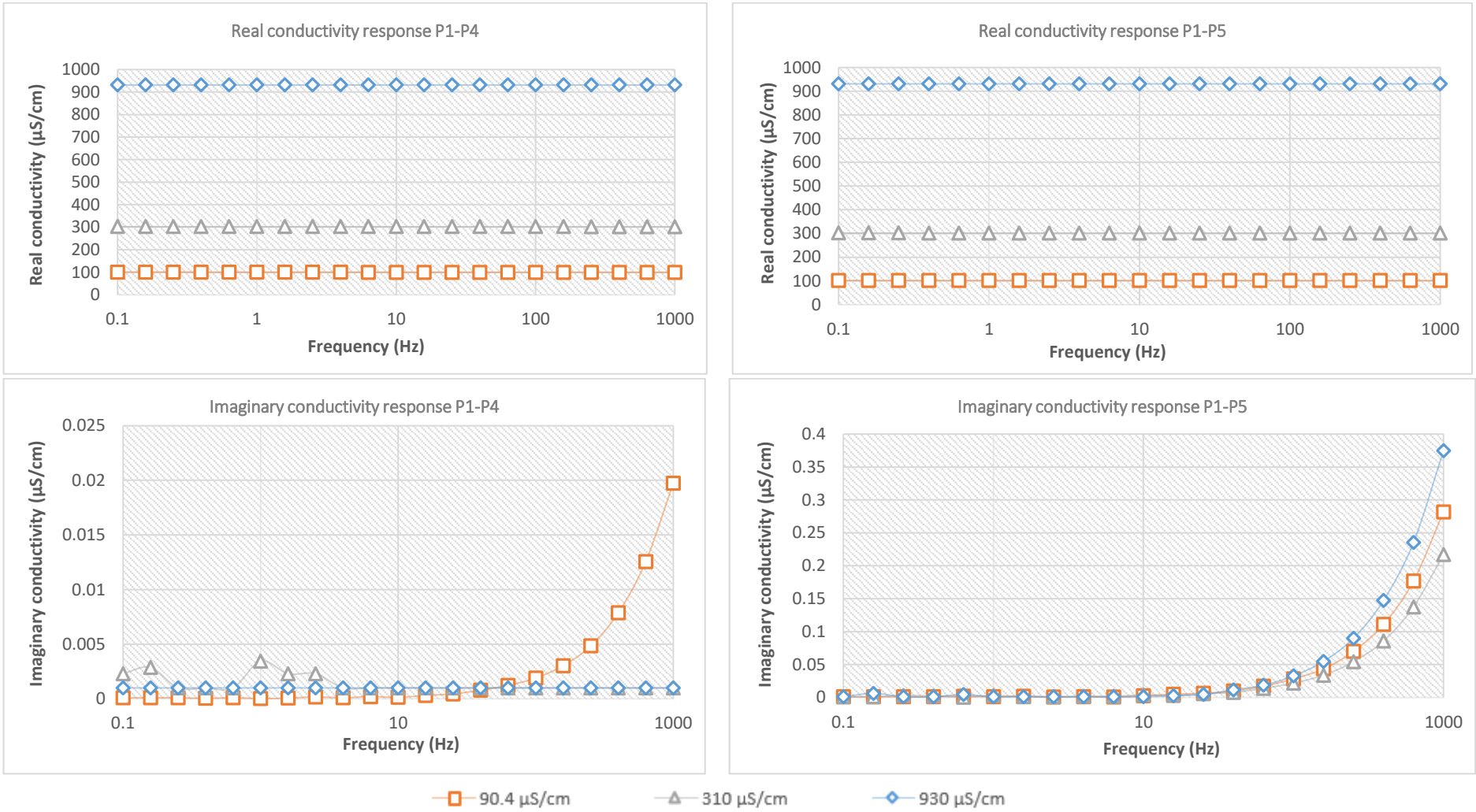

Figure B.5 Phase response and fluid conductivity (real and imaginary part) for column 4 during fluid tests after taking into account the K factor.

B.3 Grain size analysis

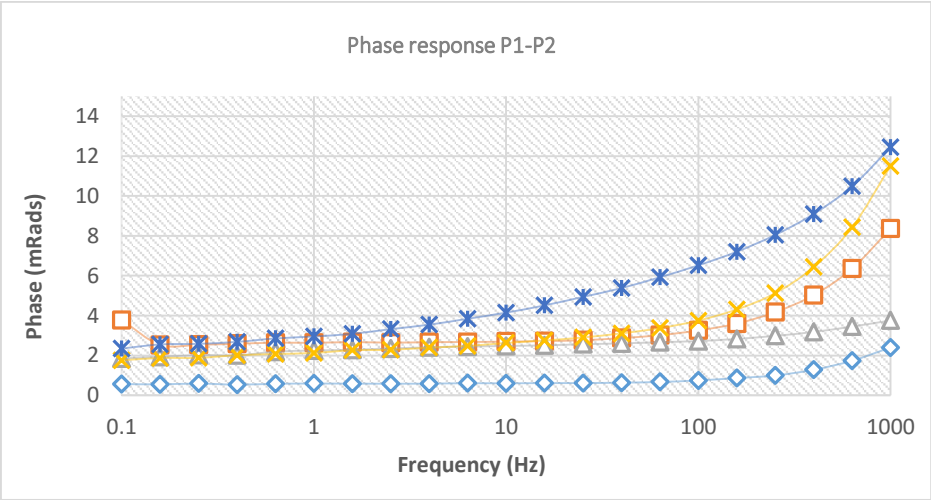

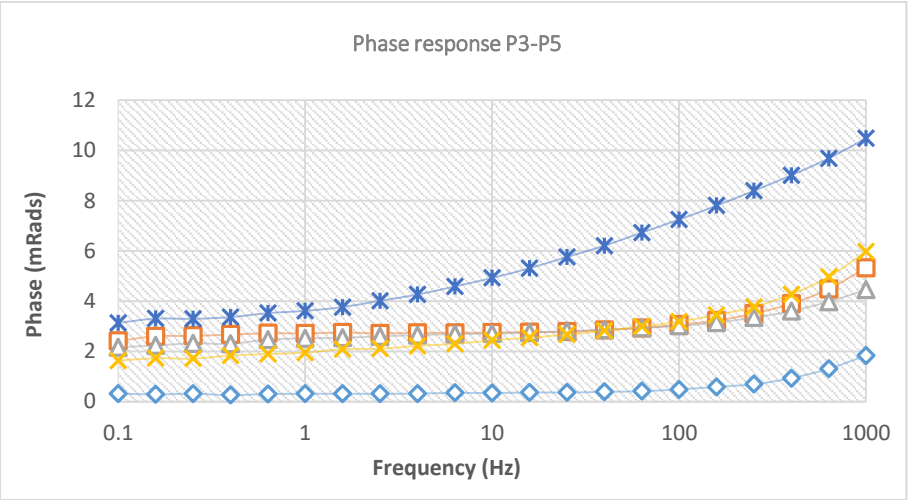

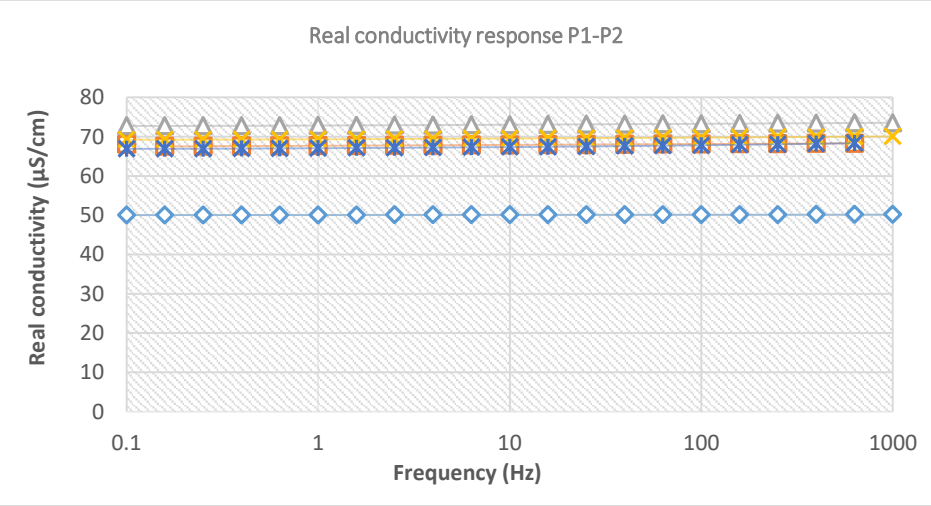

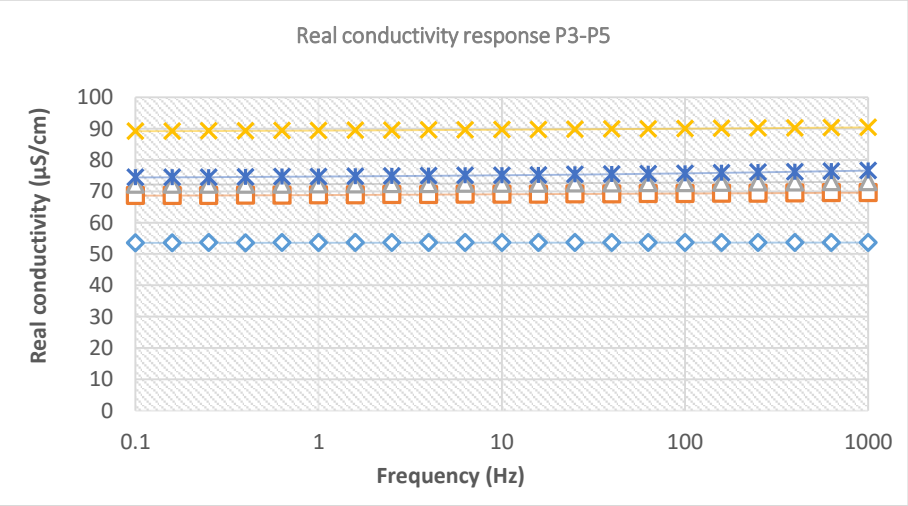

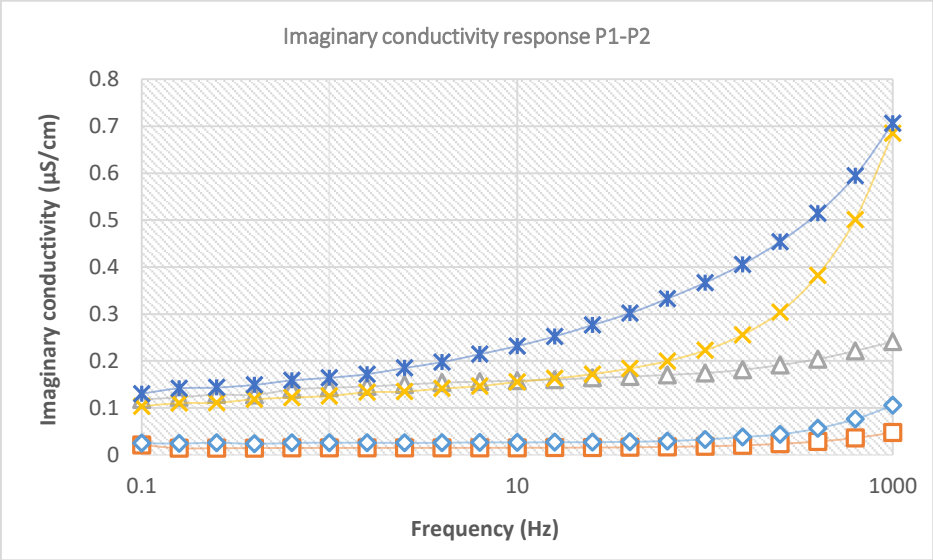
Imaginary conductivity response P1-P2
Imaginary conductivity (µS/cm)
0.8
0.7
0.6
0.5
0.4
0.3
0.2
0.1
0
0.1
10
1000
Frequency (Hz)

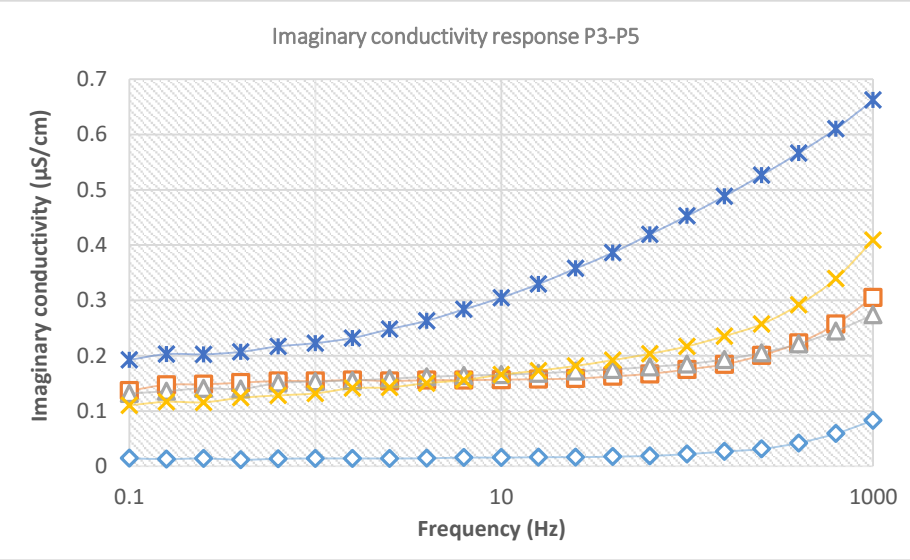
Imaginary conductivity response P3-P5
Imaginary conductivity (µS/cm)
0.7
0.6
0.5
0.4
0.3
0.2
0.1
0
0.1
10
1000
Frequency (Hz)

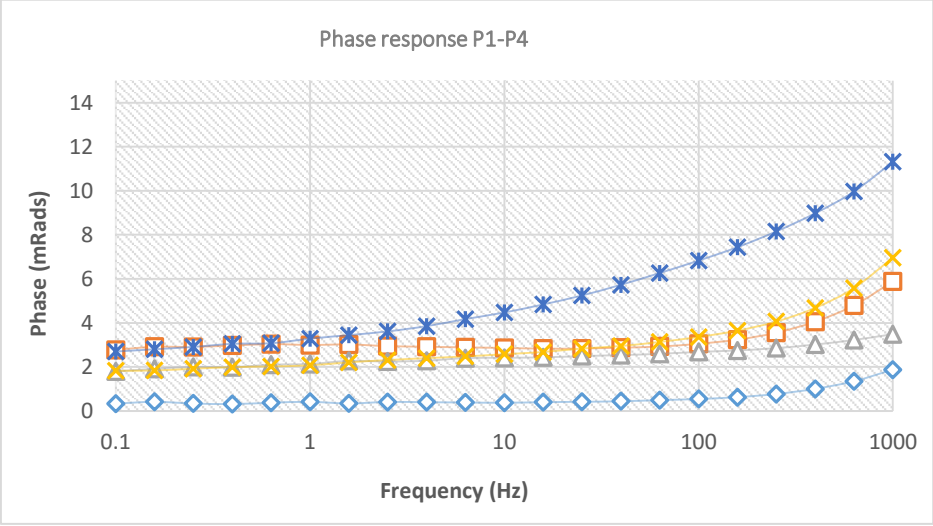
Phase response P1-P4
Phase (mRads)
14
12
10
8
6
4
2
0
0.1
1
10
100
1000
Frequency (Hz)

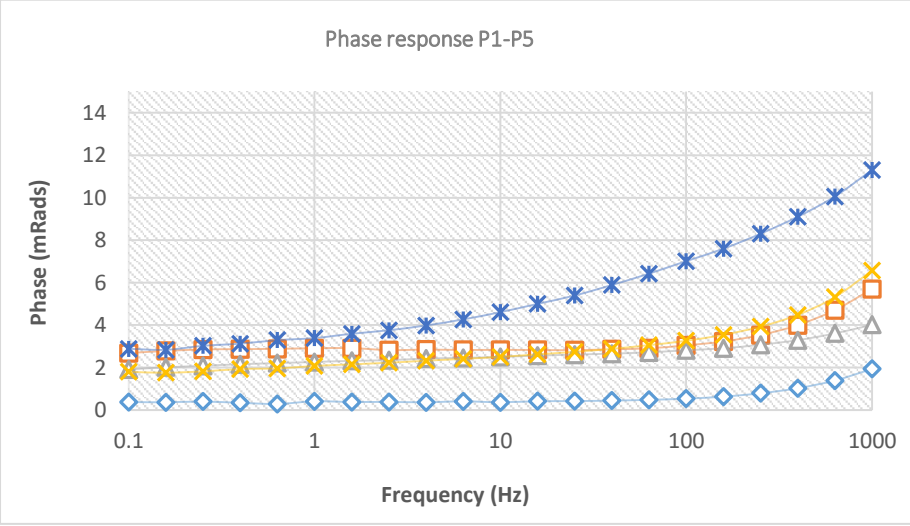
Phase response P1-P5
Phase (mRads)
14
12
10
8
6
4
2
0
0.1
1
10
100
1000
Frequency (Hz)

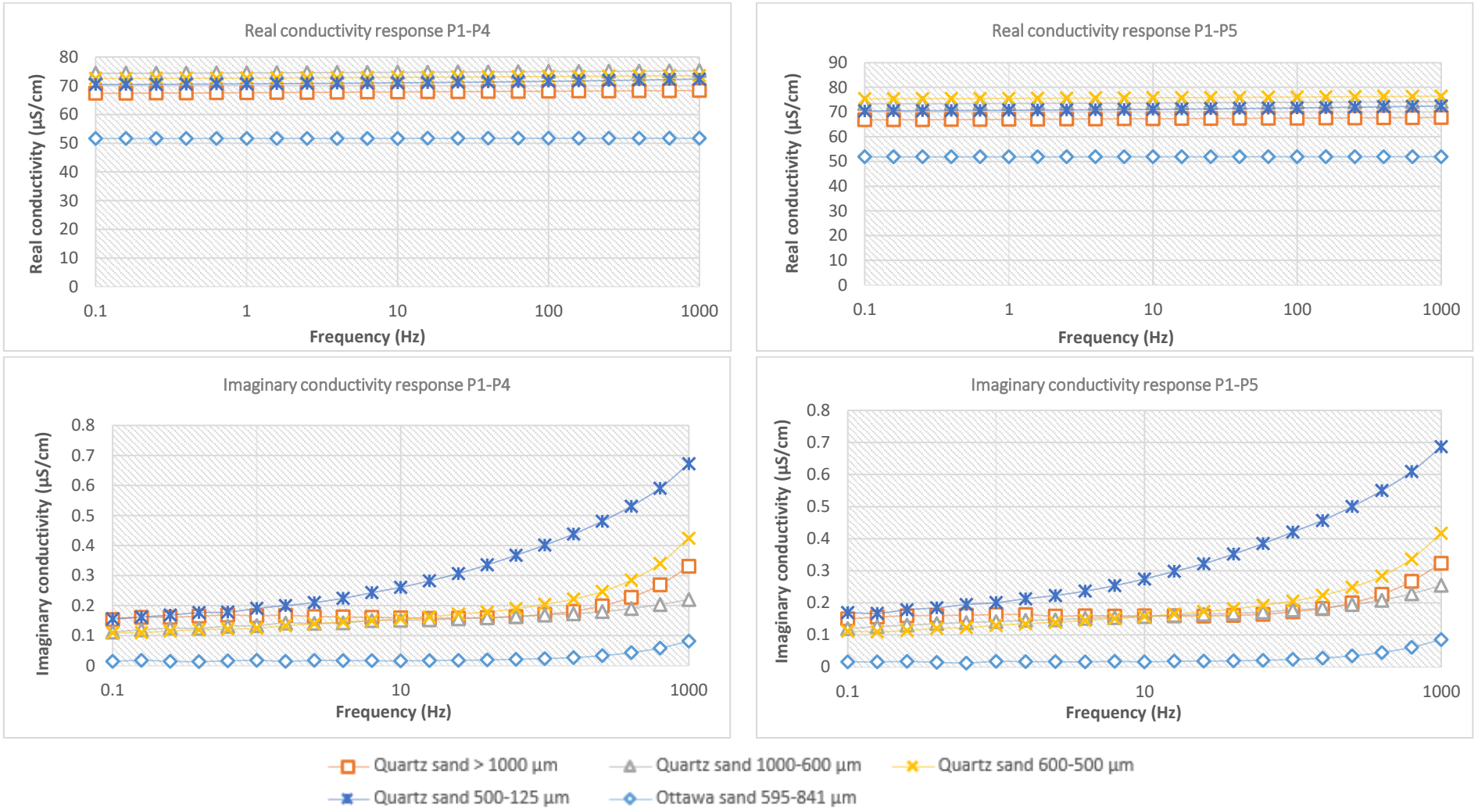

Figure B.6 Phase response and fluid conductivity (real and imaginary part) during the grain size analysis to 1000-0.1 Hz

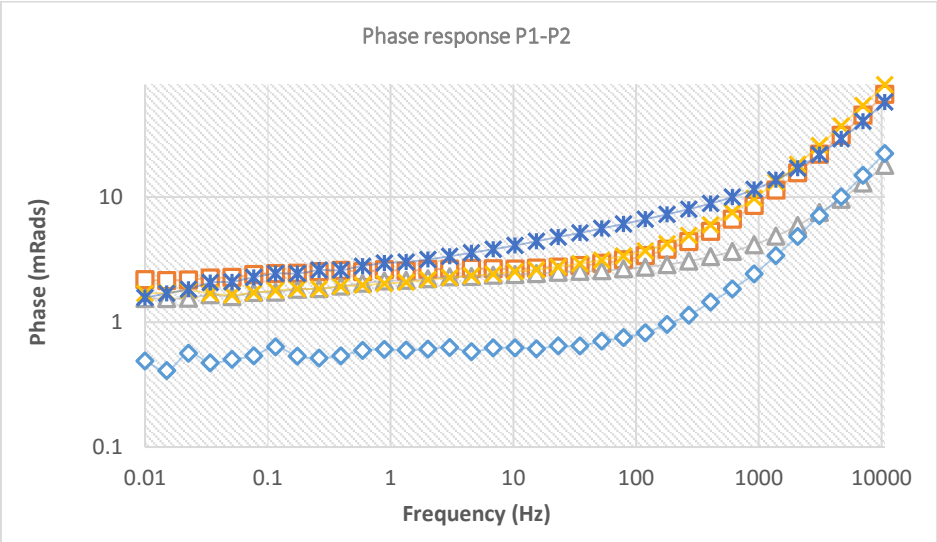
Phase response P1-P2
Phase (mRads)
10
1
0.1
0.01
0.1
1
10
100
1000
10000
Frequency (Hz)

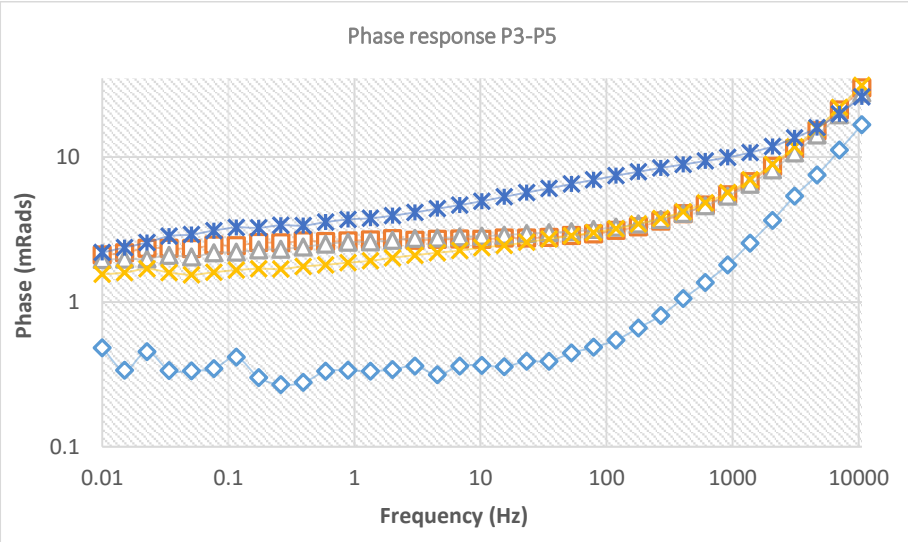
Phase response P3-P5
Phase (mRads)
10
1
0.1
0.01
0.1
1
10
100
1000
10000
Frequency (Hz)

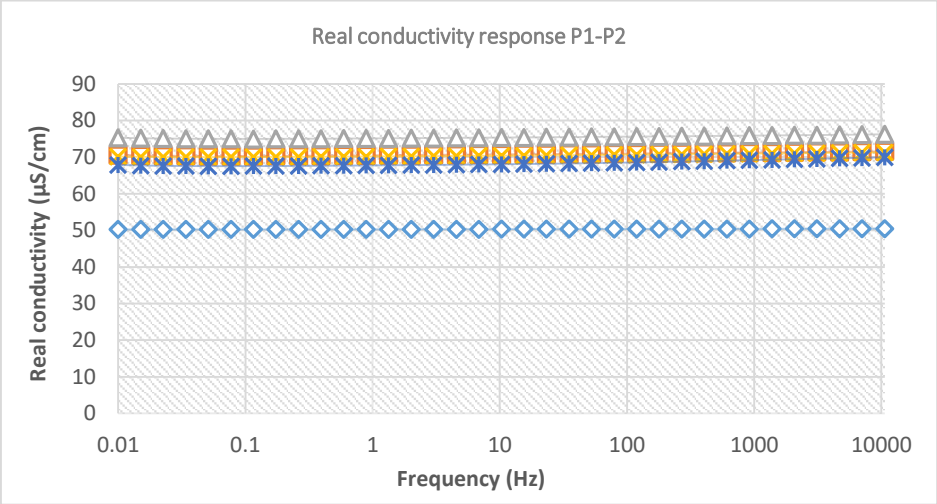
Real conductivity response P1-P2
Real conductivity (µS/cm)
90
80
70
60
50
40
30
20
10
0
0.01
0.1
1
10
100
1000
10000
Frequency (Hz)

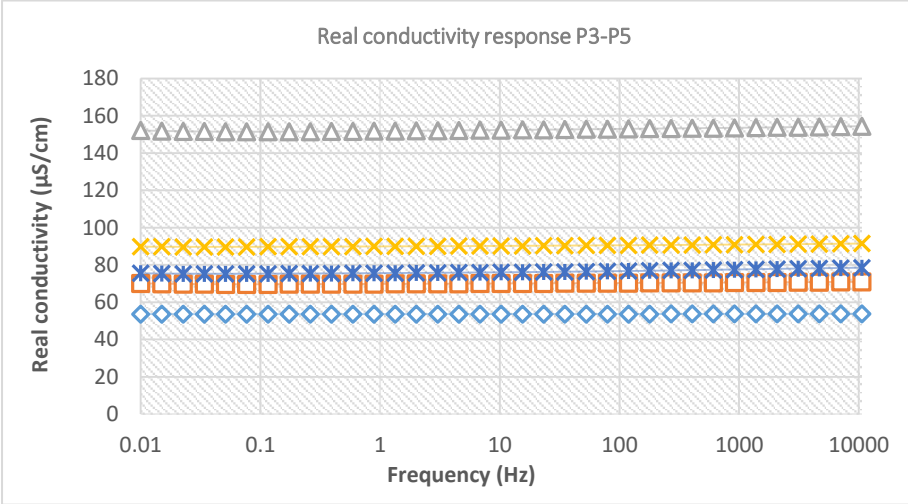
Real conductivity response P3-P5
Real conductivity (µS/cm)
180
160
140
120
100
80
60
40
20
0
0.01
0.1
1
10
100
1000
10000
Frequency (Hz)

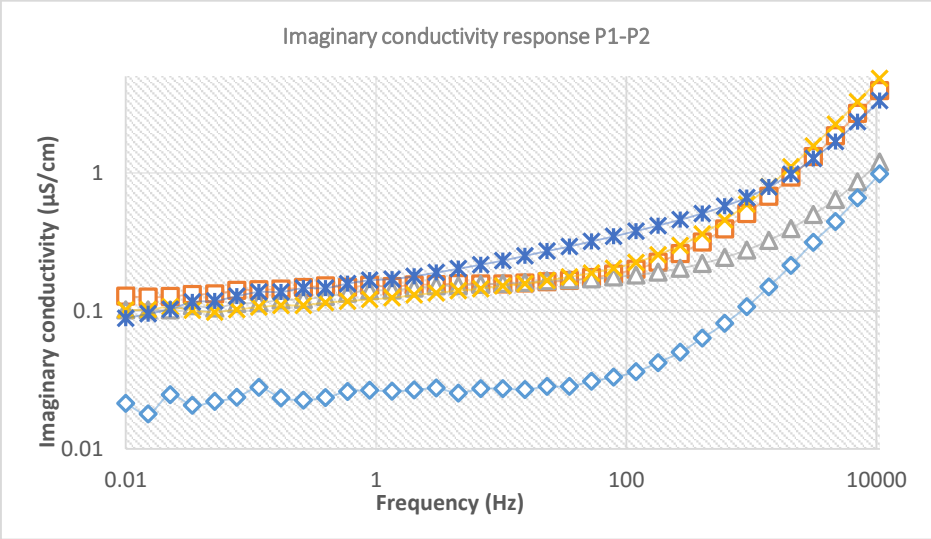
Imaginary conductivity response P1-P2
Imaginary conductivity (µS/cm)
1
0.1
0.01
0.01
1
100
10000
Frequency (Hz)

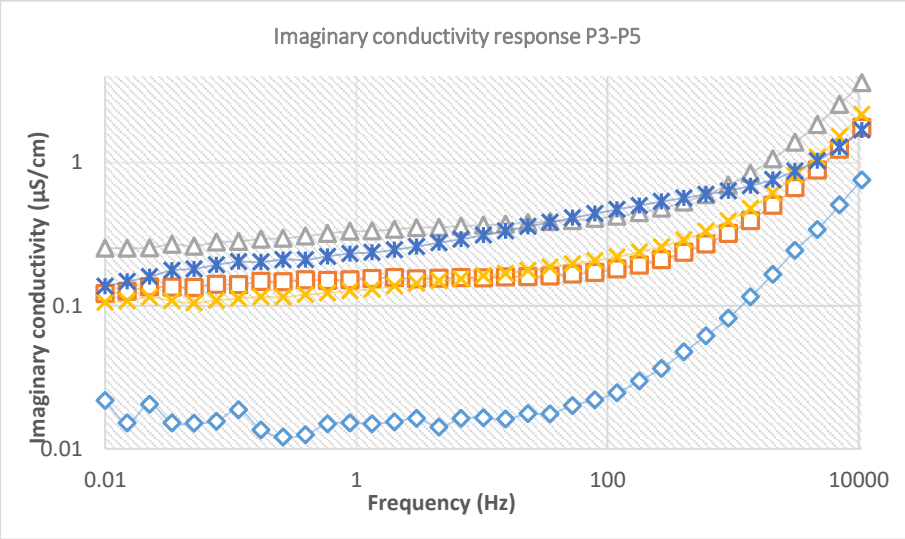
Imaginary conductivity response P3-P5
Imaginary conductivity (µS/cm)
1
0.1
0.01
0.01
1
100
10000
Frequency (Hz)

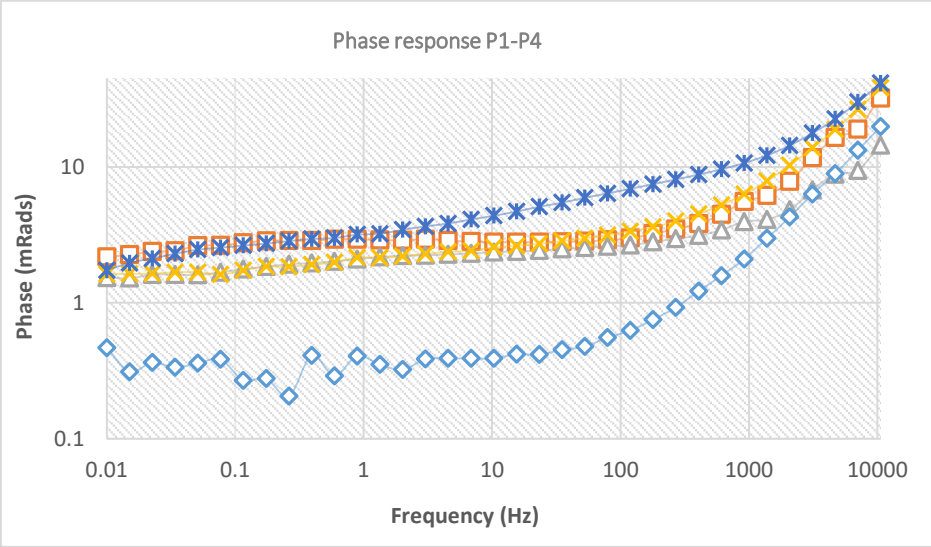
Phase response P1-P4
Phase (mRads)
10
1
0.1
0.01
0.1
1
10
100
1000
10000
Frequency (Hz)

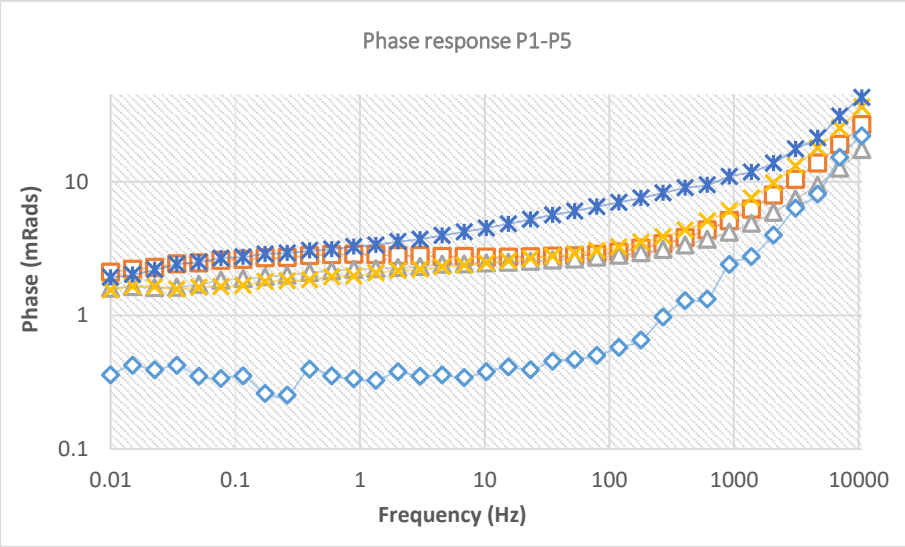
Phase response P1-P5
Phase (mRads)
10
1
0.1
0.01
0.1
1
10
100
1000
10000
Frequency (Hz)

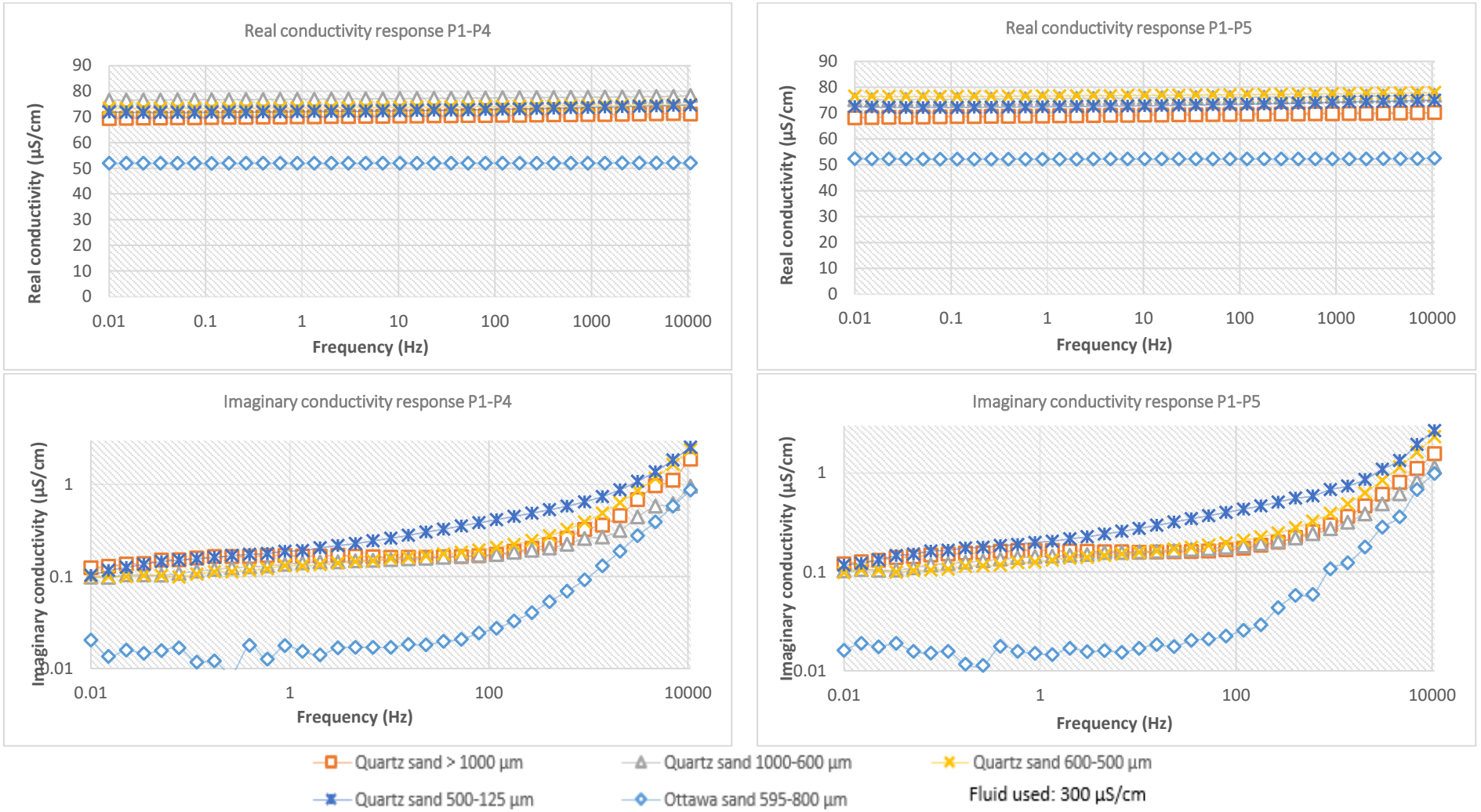

Figure B.7 Phase response and fluid conductivity (real and imaginary part) during the grain size analysis to 10000-0.01 Hz.

B.4 Different Concentrations

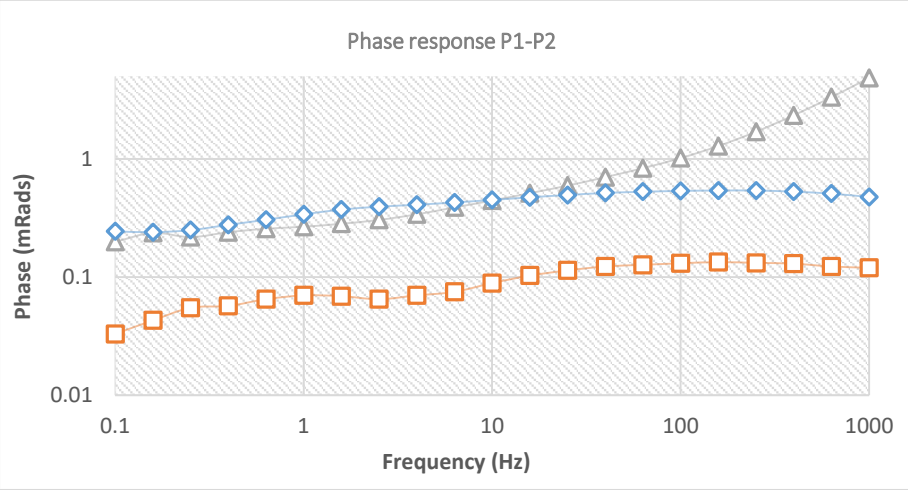

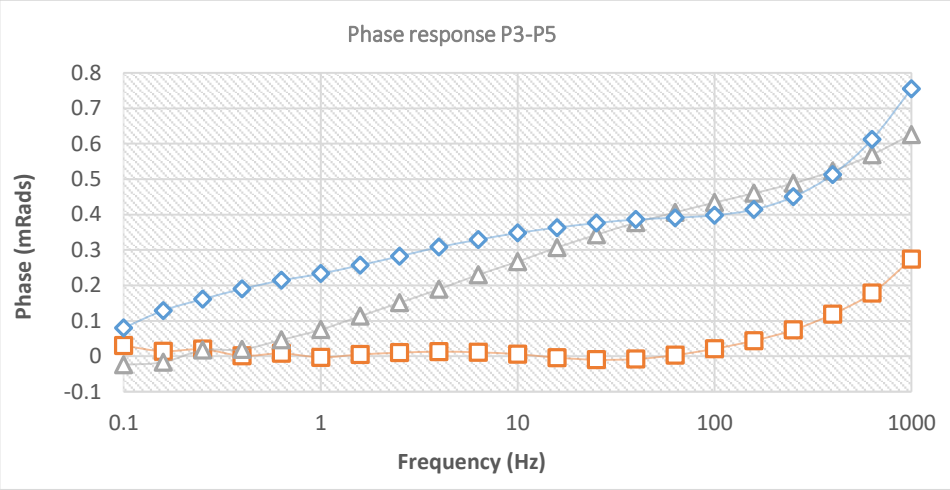

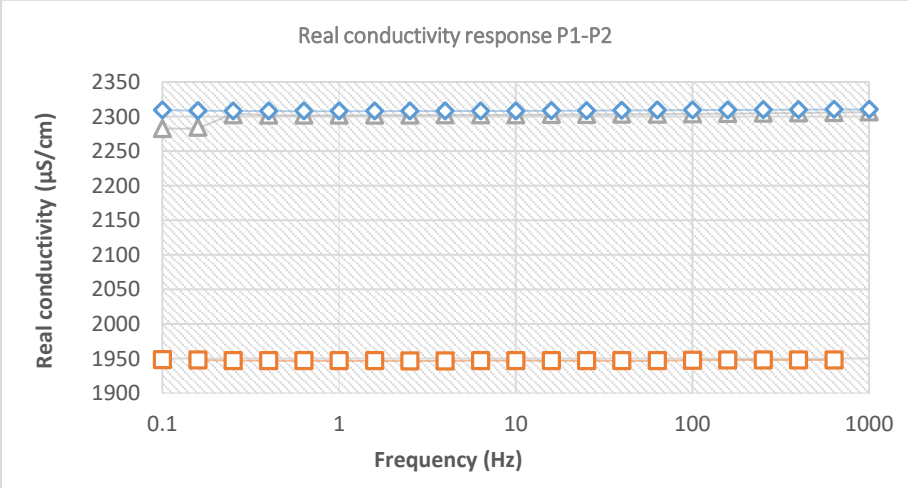

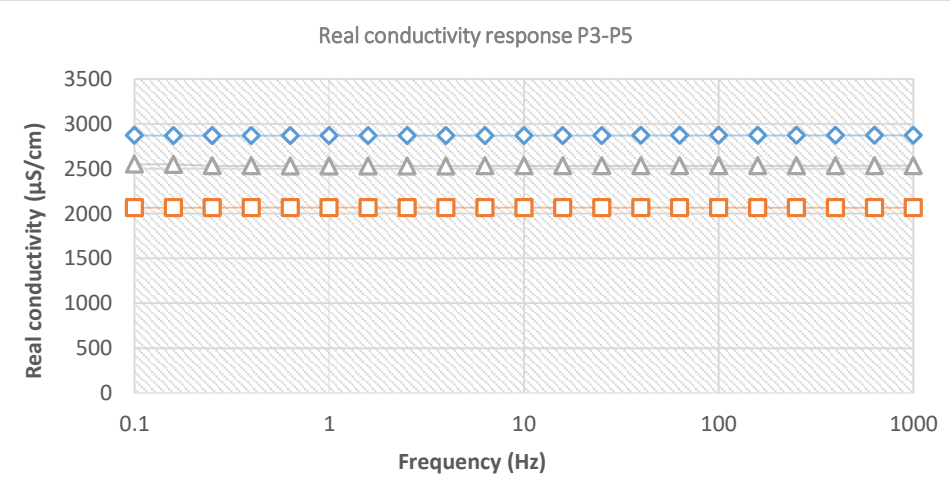

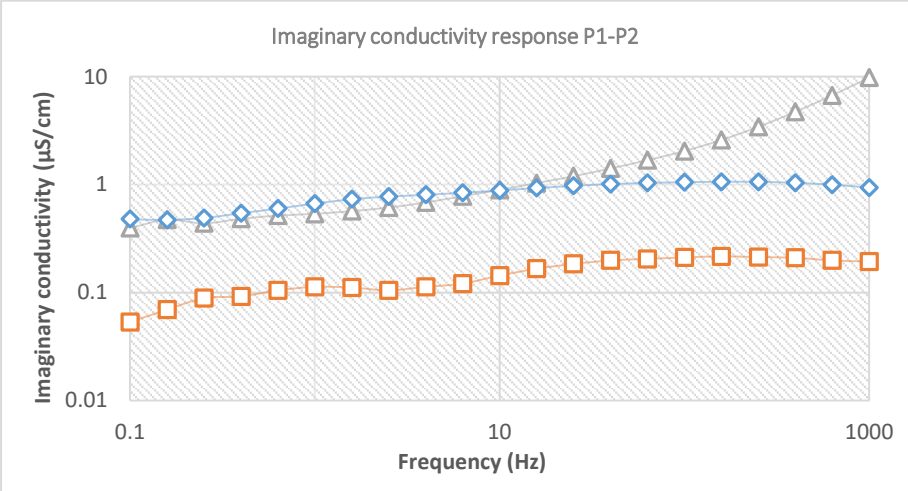
Imaginary conductivity response P1-P2
Imaginary conductivity (µS/cm)
10
1
0.1
0.01
0.1
10
1000
Frequency (Hz)

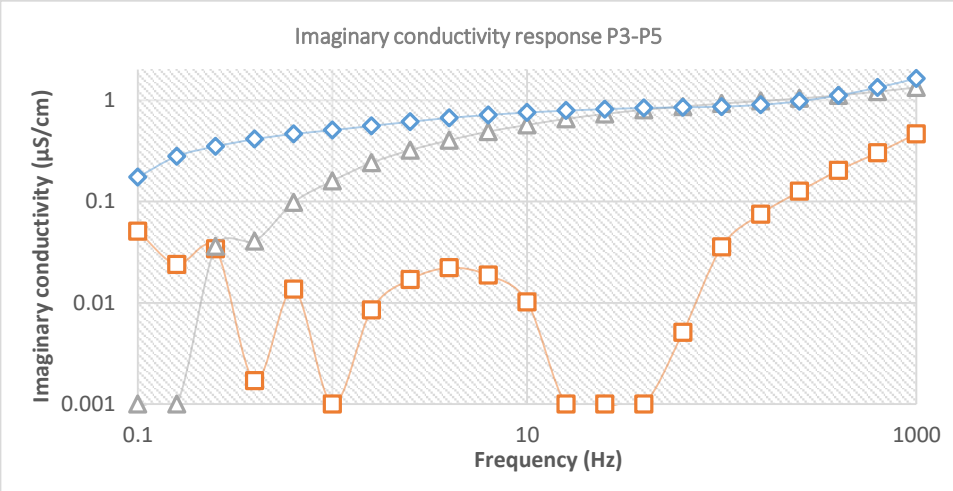
Imaginary conductivity response P3-P5
Imaginary conductivity (µS/cm)
1
0.1
0.01
0.001
0.1
10
1000
Frequency (Hz)

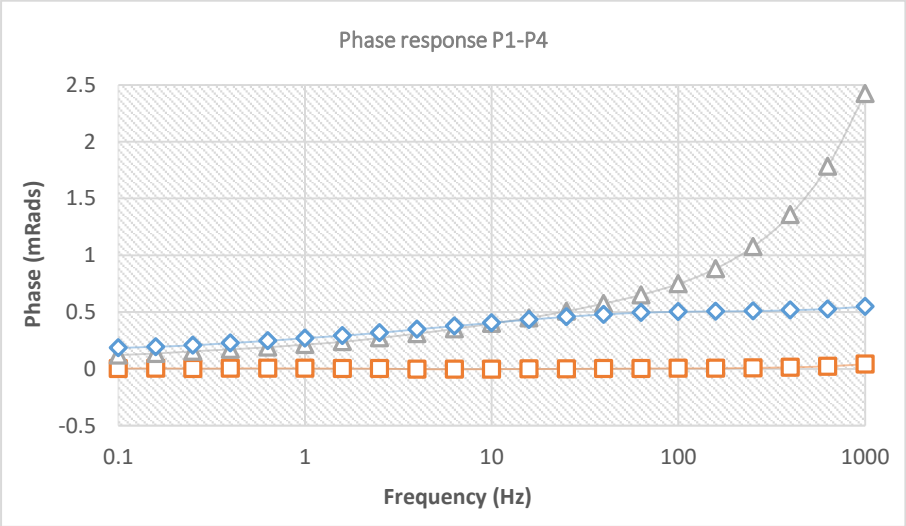
Phase response P1-P4
Phase (mRads)
2.5
2
1.5
1
0.5
0
-0.5
0.1
1
10
100
1000
Frequency (Hz)

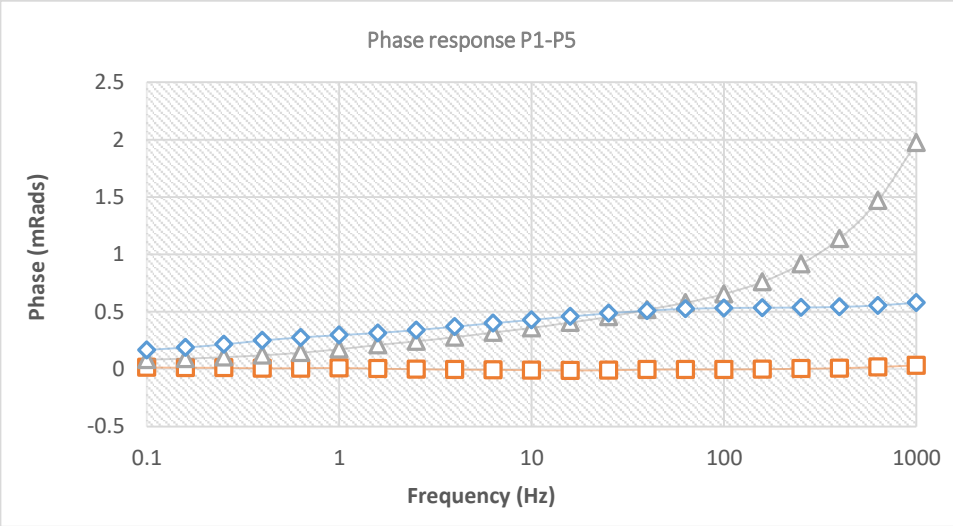
Phase response P1-P5
Phase (mRads)
2.5
2
1.5
1
0.5
0
-0.5
0.1
1
10
100
1000
Frequency (Hz)

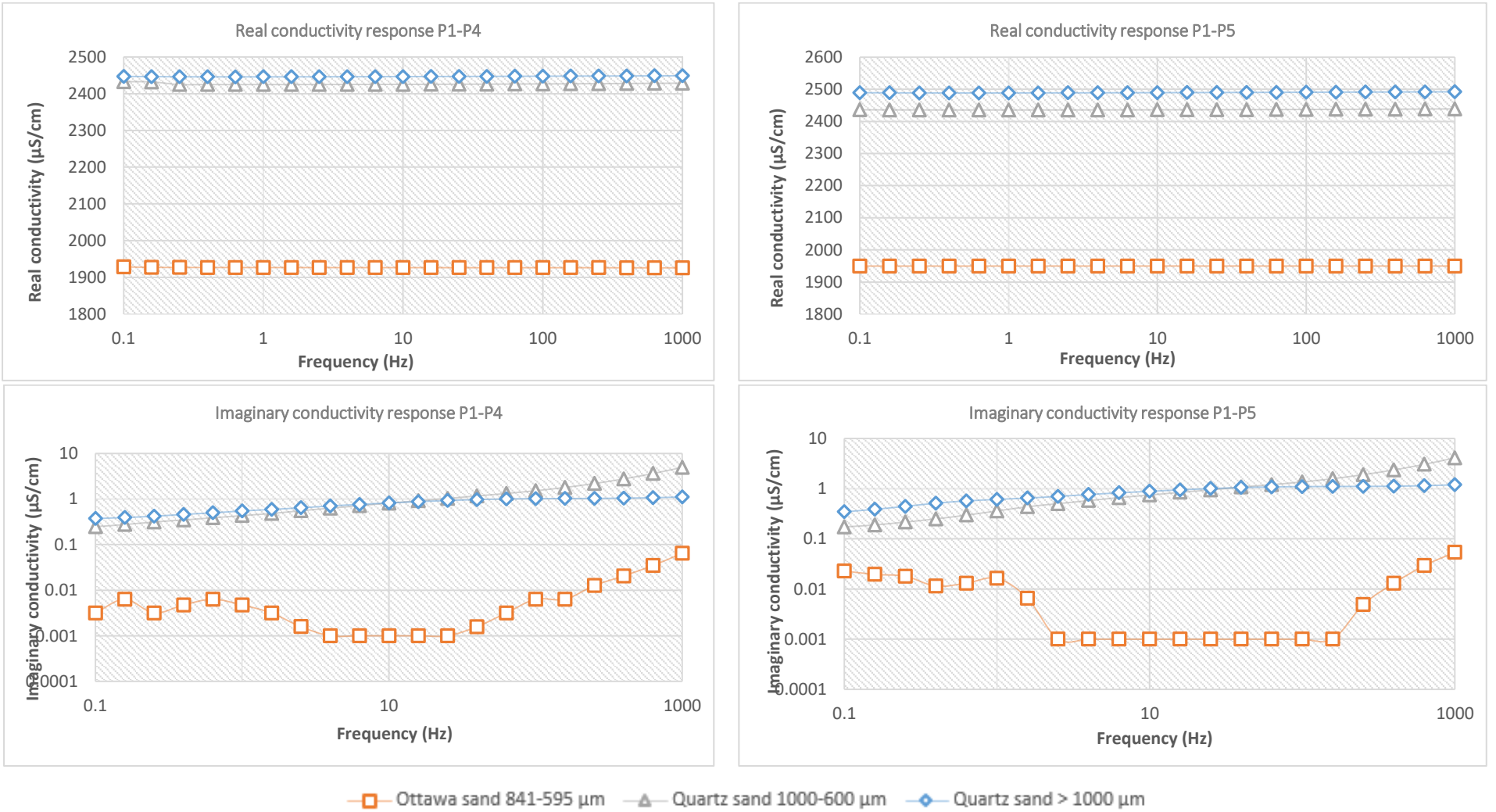

Figure B.8 Phase response and fluid conductivity during measurements with sands saturated with OMW (12090 µS/cm) to 1000-0.1 Hz.

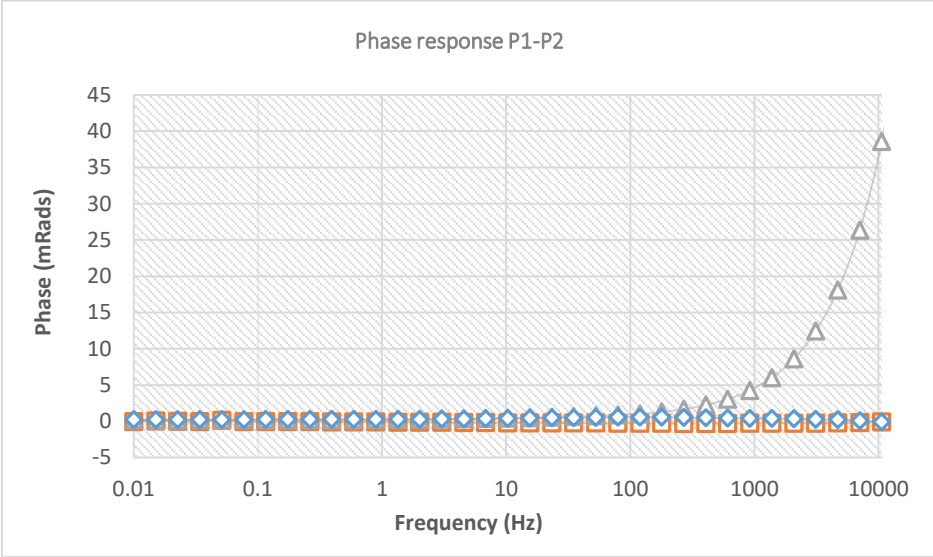
Phase response P1-P2
Phase (mRads)
45
40
35
30
25
20
15
10
5
0
-5
0.01
0.1
1
10
100
1000
10000
Frequency (Hz)

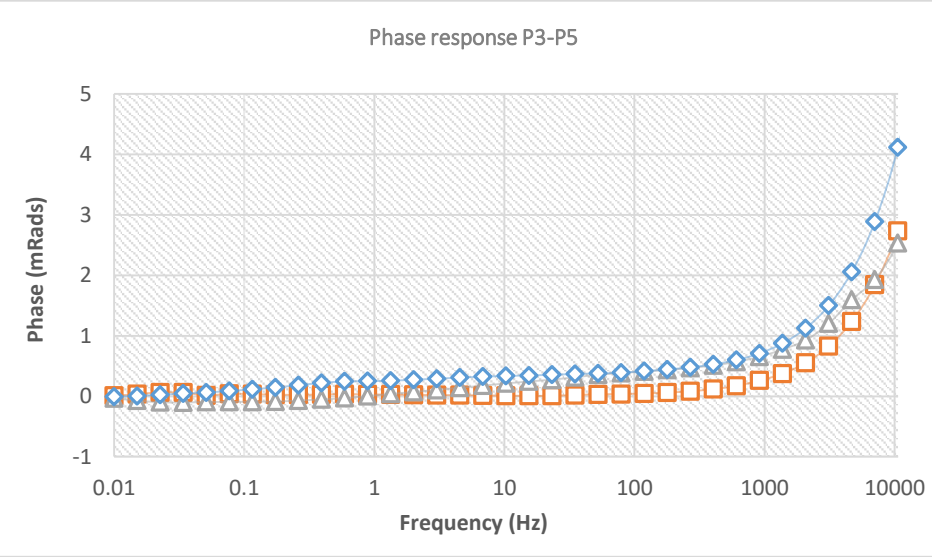
Phase response P3-P5
Phase (mRads)
5
4
3
2
1
0
-1
0.01
0.1
1
10
100
1000
10000
Frequency (Hz)

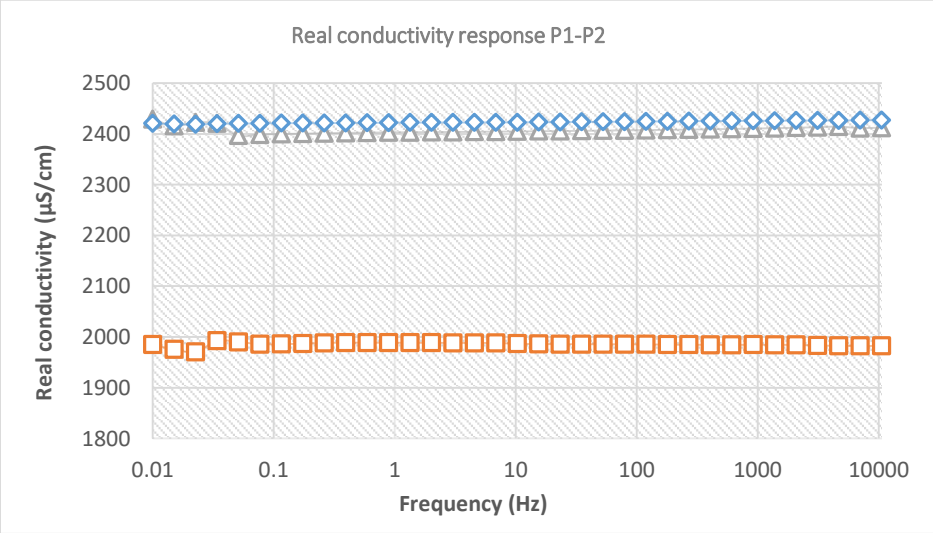
Real conductivity response P1-P2
Real conductivity (µS/cm)
2500
2400
2300
2200
2100
2000
1900
1800
0.01
0.1
1
10
100
1000
10000
Frequency (Hz)

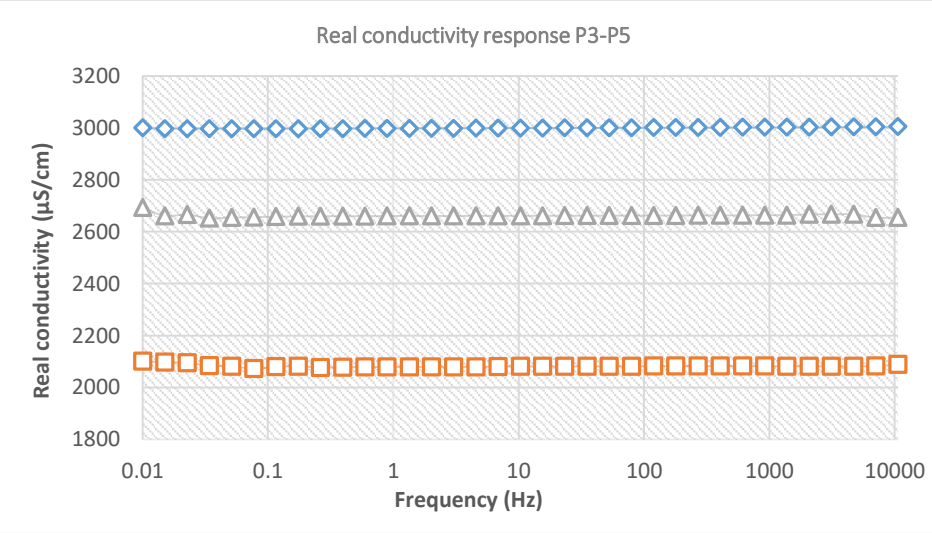
Real conductivity response P3-P5
Real conductivity (µS/cm)
3200
3000
2800
2600
2400
2200
2000
1800
0.01
0.1
1
10
100
1000
10000
Frequency (Hz)

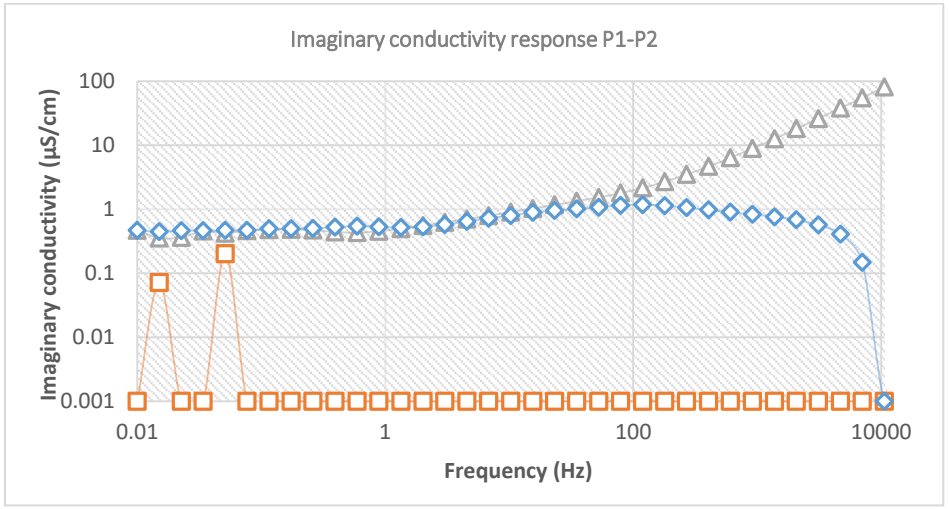
Imaginary conductivity response P1-P2
Imaginary conductivity (µS/cm)
100
10
1
0.1
0.01
0.001
0.01
1
100
10000
Frequency (Hz)

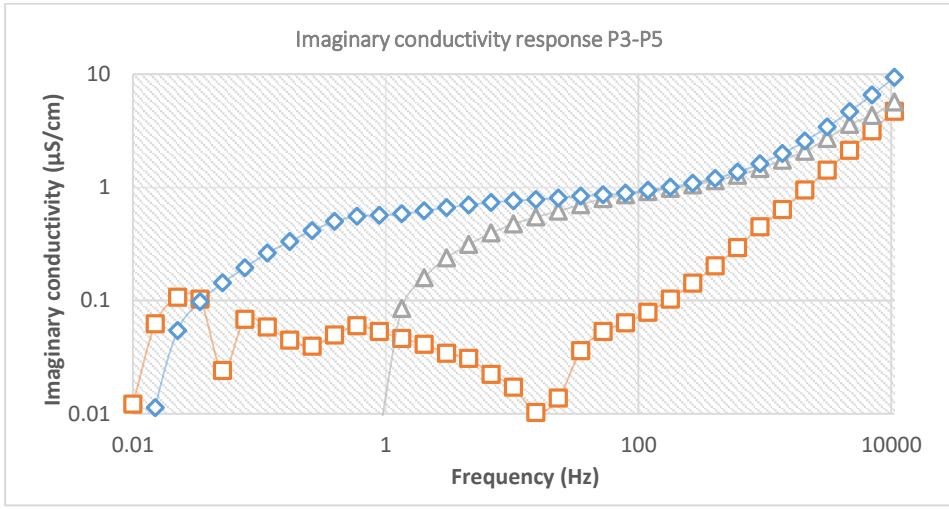
Imaginary conductivity response P3-P5
Imaginary conductivity (µS/cm)
10
1
0.1
0.01
0.01
1
100
10000
Frequency (Hz)

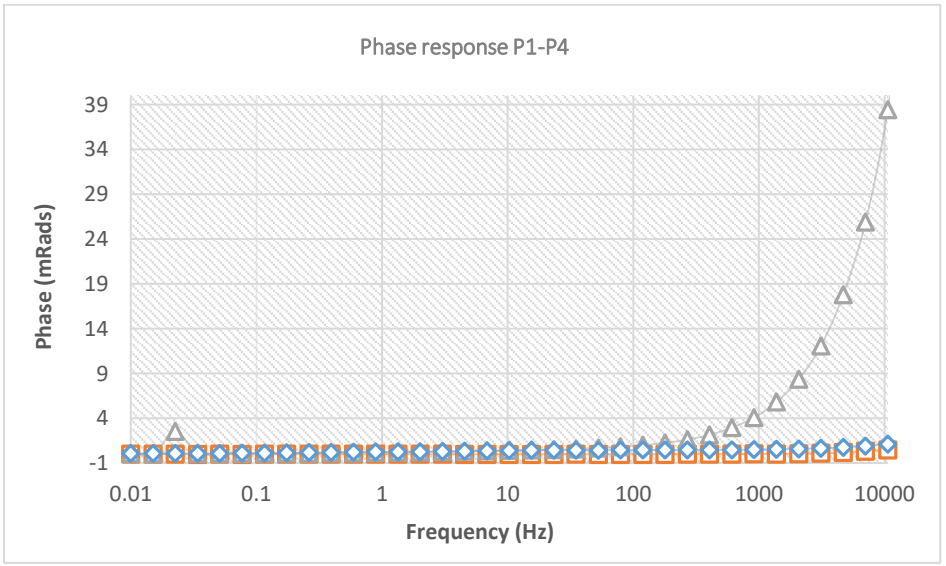
Phase response P1-P4
Phase (mRads)
39
34
29
24
19
14
9
4
-1
0.01
0.1
1
10
100
1000
10000
Frequency (Hz)

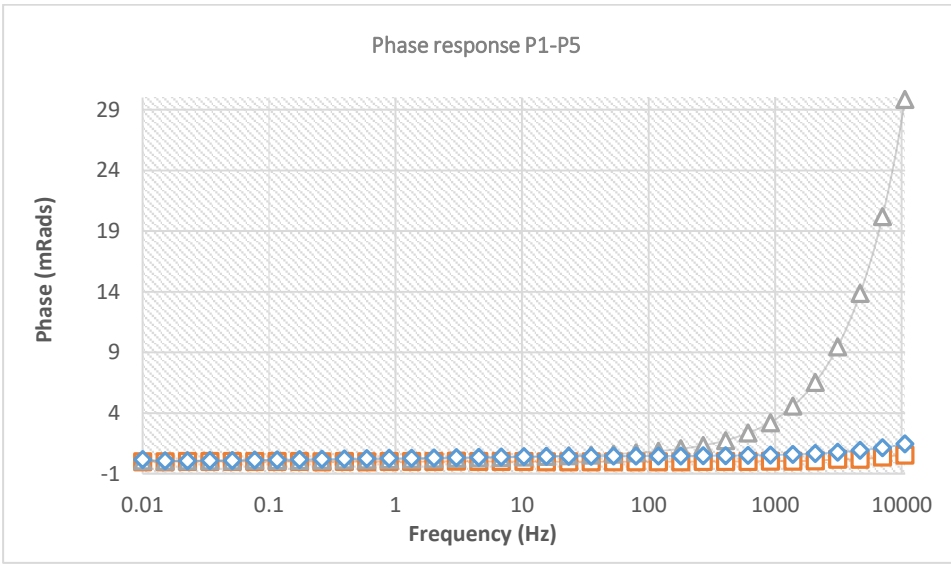
Phase response P1-P5
Phase (mRads)
29
24
19
14
9
4
-1
0.01
0.1
1
10
100
1000
10000
Frequency (Hz)

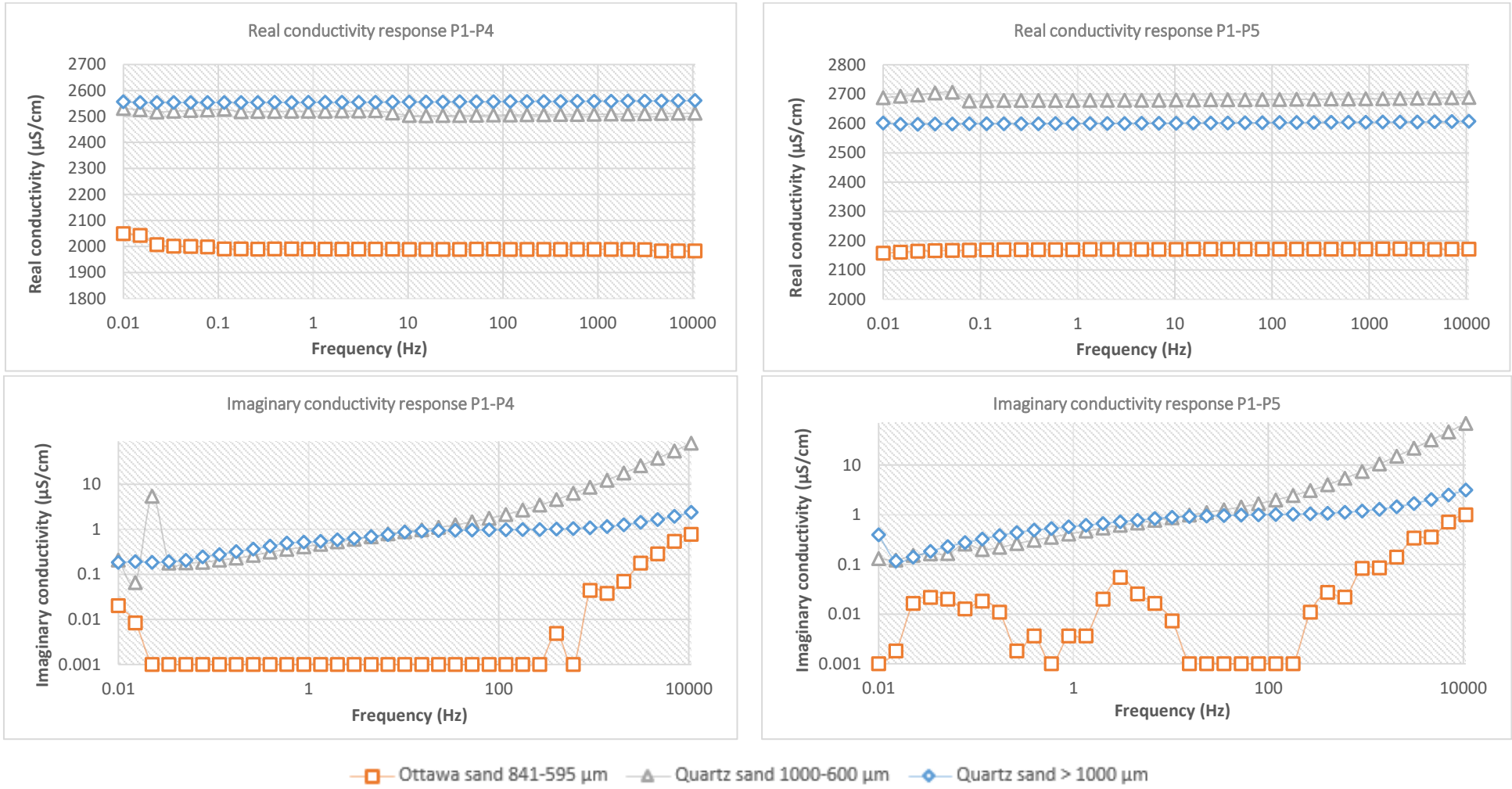

Figure B.9 Phase response and fluid conductivity during measurements with sands fully saturated with OOMW (12090 µS/cm) to 10000-0.01 Hz.

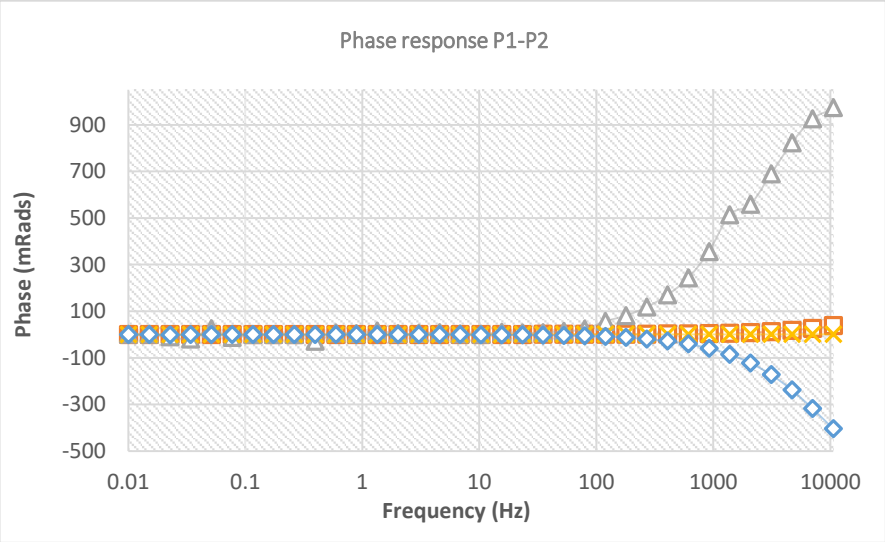
Phase response P1-P2
Phase (mRads)
900
700
500
300
100
-100
-300
-500
0.01
0.1
1
10
100
1000
10000
Frequency (Hz)

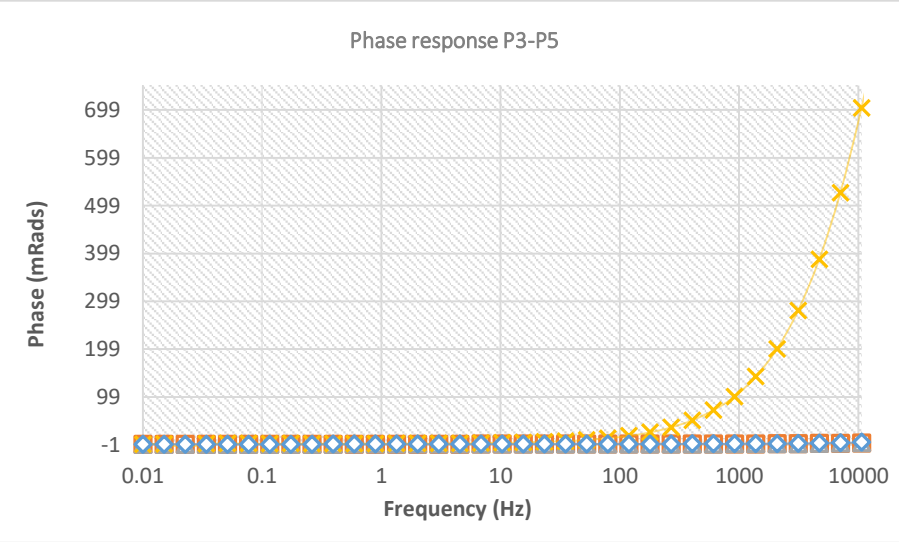
Phase response P3-P5
Phase (mRads)
699
599
499
399
299
199
99
-1
0.01
0.1
1
10
100
1000
10000
Frequency (Hz)

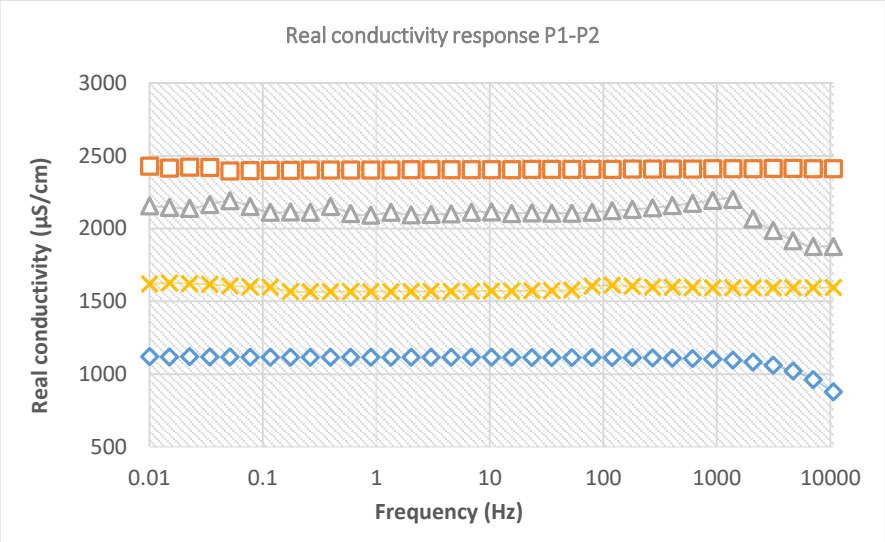
Real conductivity response P1-P2
Real conductivity (µS/cm)
3000
2500
2000
1500
1000
500
0.01
0.1
1
10
100
1000
10000
Frequency (Hz)

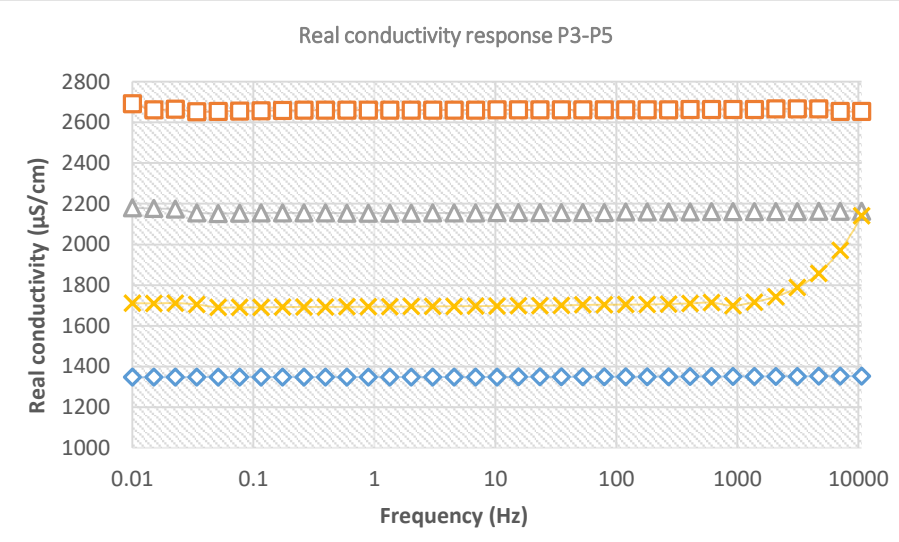
Real conductivity response P3-P5
Real conductivity (µS/cm)
2800
2600
2400
2200
2000
1800
1600
1400
1200
1000
0.01
0.1
1
10
100
1000
10000
Frequency (Hz)

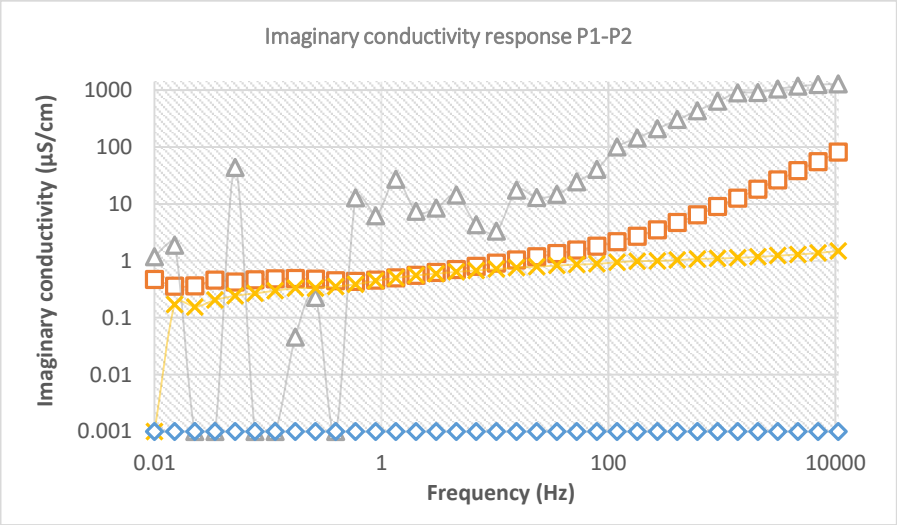
Imaginary conductivity response P1-P2
Imaginary conductivity (µS/cm)
1000
100
10
1
0.1
0.01
0.001
0.01
1
100
10000
Frequency (Hz)

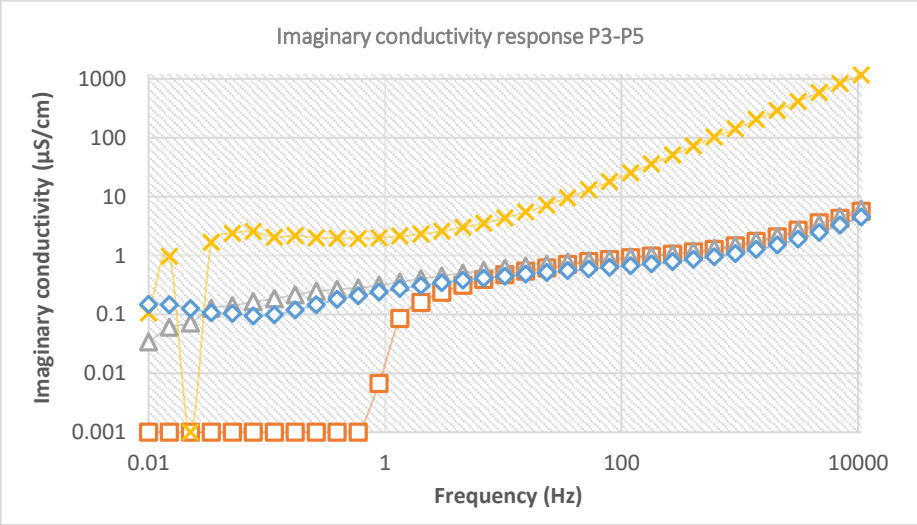
Imaginary conductivity response P3-P5
Imaginary conductivity (µS/cm)
1000
100
10
1
0.1
0.01
0.001
0.01
1
100
10000
Frequency (Hz)

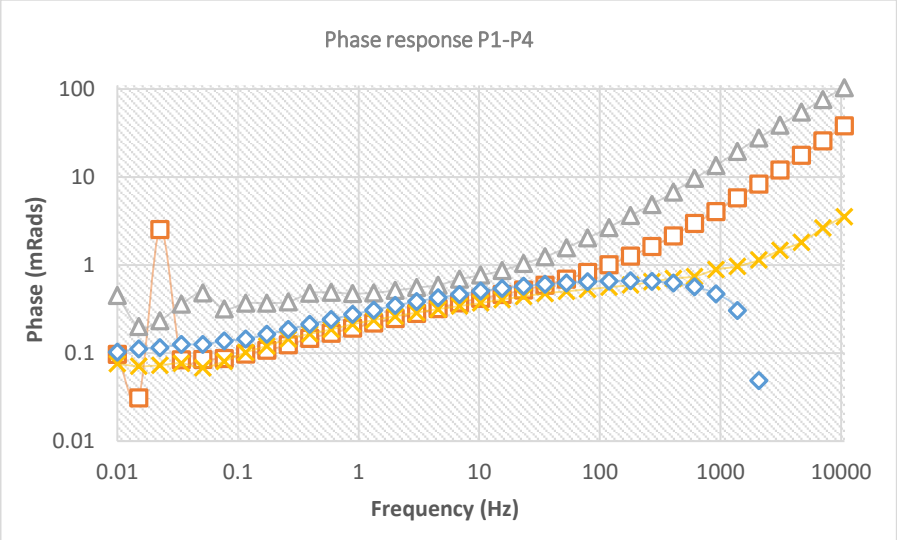
Phase response P1-P4
Phase (mRads)
100
10
1
0.1
0.01
0.01
0.1
1
10
100
1000
10000
Frequency (Hz)

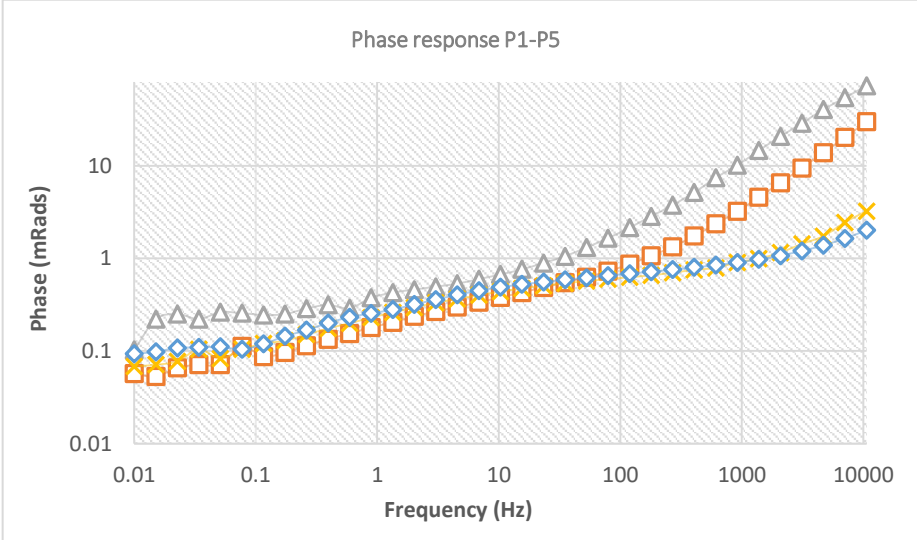
Phase response P1-P5
Phase (mRads)
10
1
0.1
0.01
0.01
0.1
1
10
100
1000
10000
Frequency (Hz)

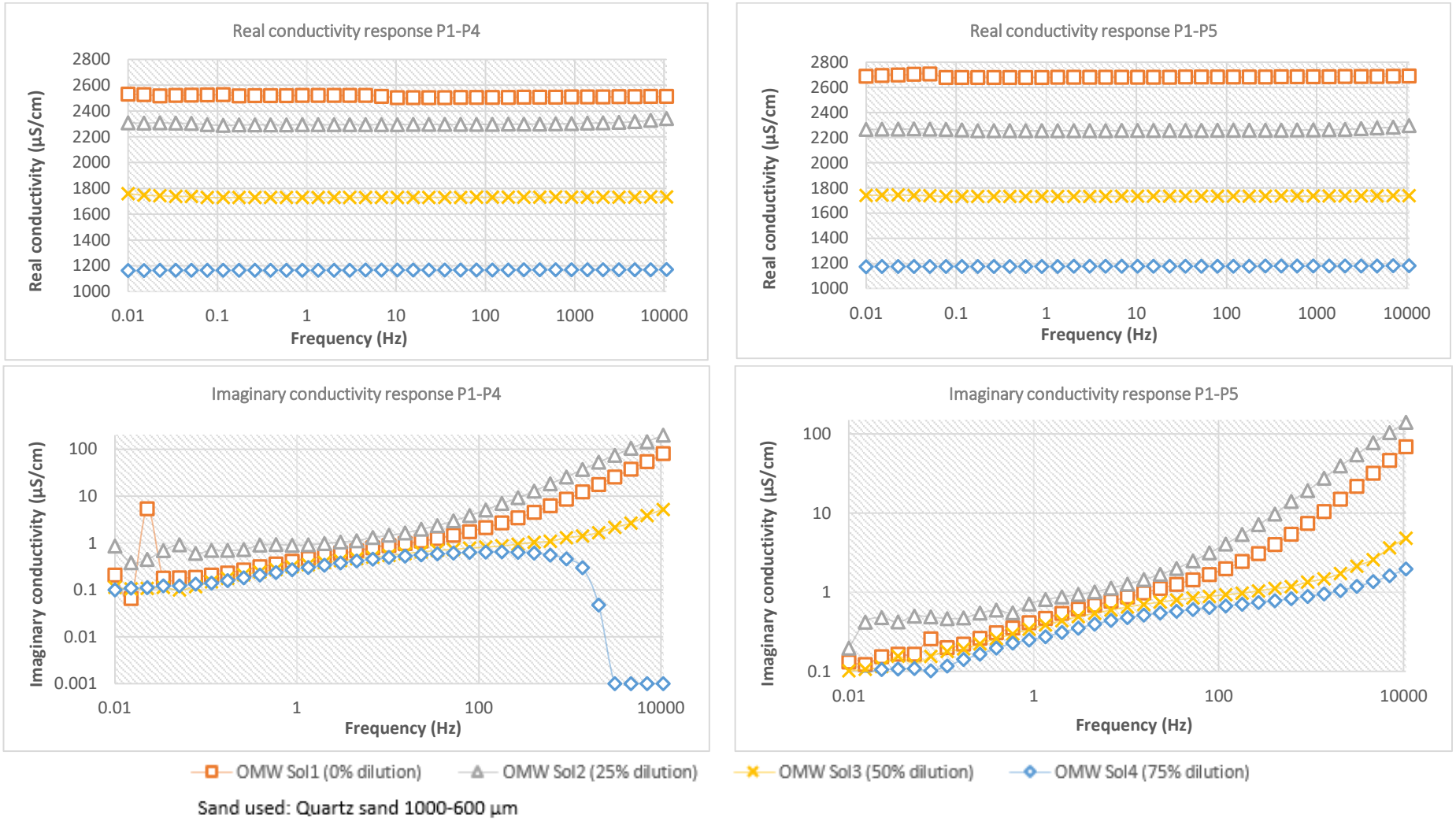

Figure B.10 Phase response and fluid conductivity during measurements with OMW solutions with different concentrations to 10000-0.01 Hz.

B.5 Phytoremediation

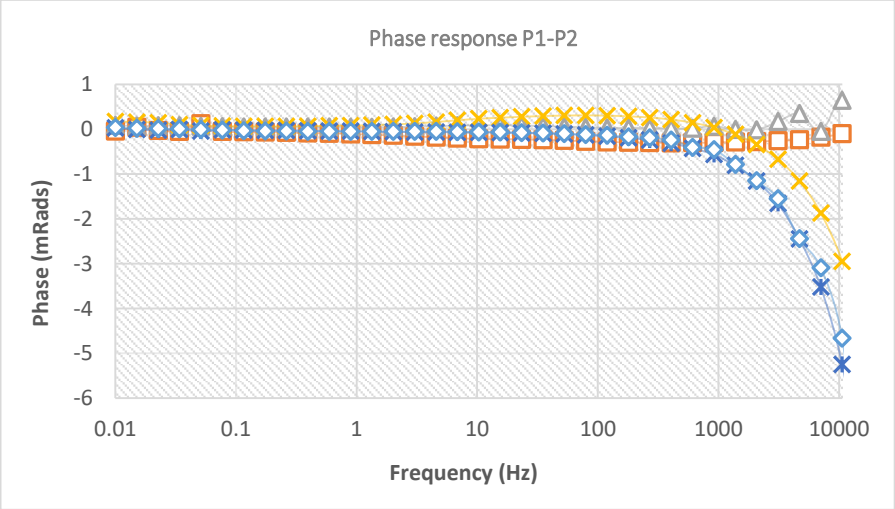

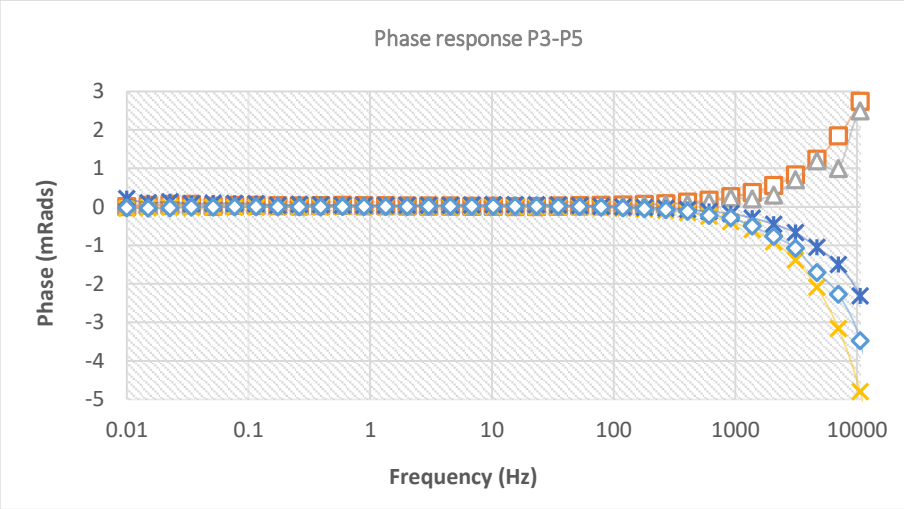

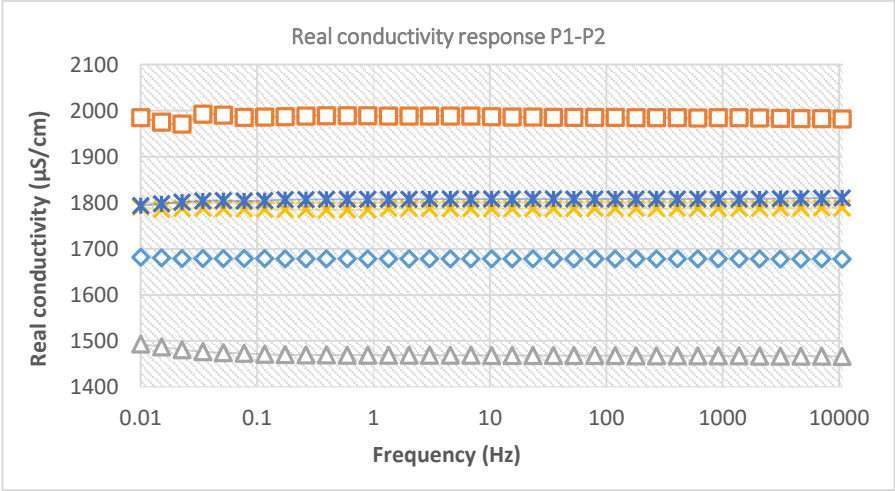

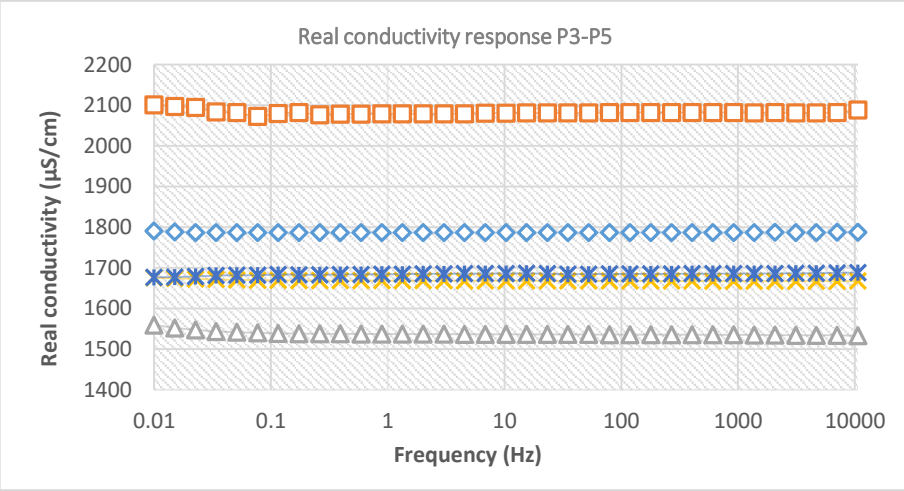

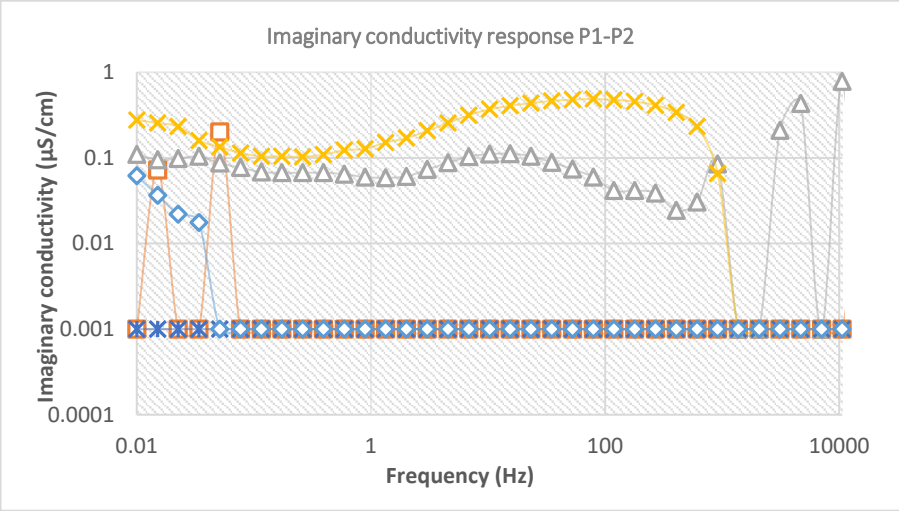
Imaginary conductivity response P1-P2
Imaginary conductivity (µS/cm)
1
0.1
0.01
0.001
0.0001
0.01
1
100
10000
Frequency (Hz)

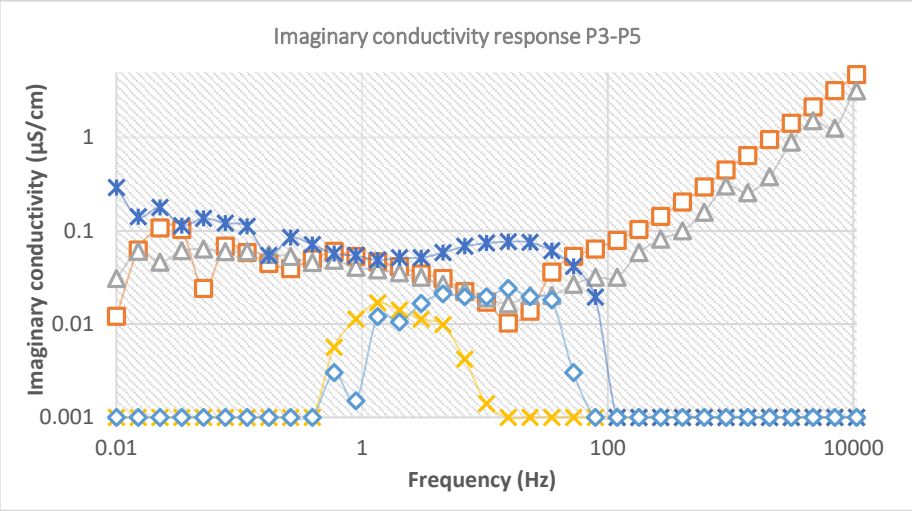
Imaginary conductivity response P3-P5
Imaginary conductivity (µS/cm)
1
0.1
0.01
0.001
0.01
1
100
10000
Frequency (Hz)

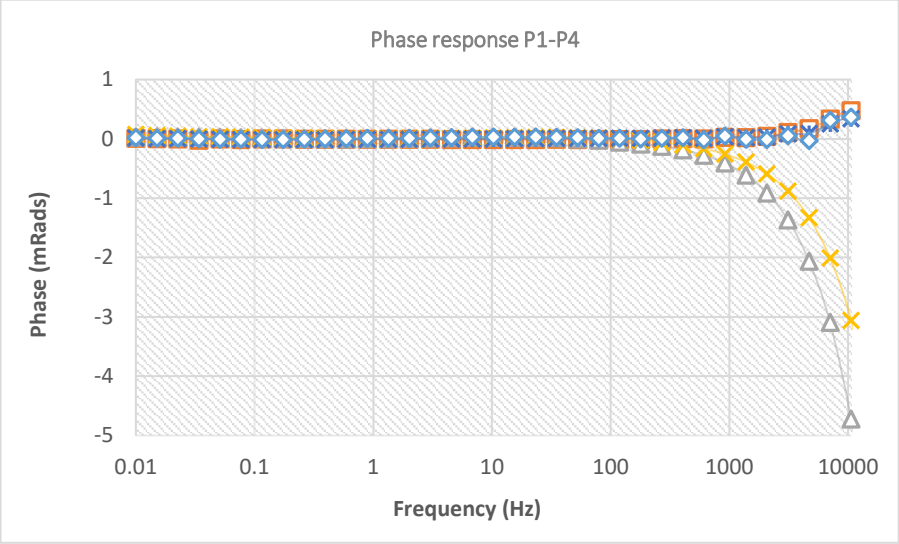
Phase response P1-P4
Phase (mRads)
1
0
-1
-2
-3
-4
-5
0.01
0.1
1
10
100
1000
10000
Frequency (Hz)

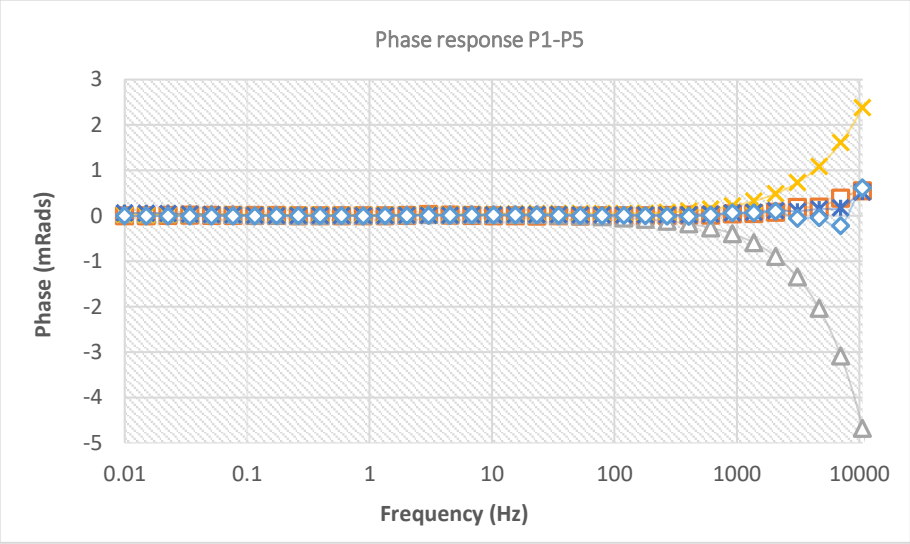
Phase response P1-P5
Phase (mRads)
3
2
1
0
-1
-2
-3
-4
-5
0.01
0.1
1
10
100
1000
10000
Frequency (Hz)

Figure B.11 Phase response and fluid conductivity measurements after phytoremediation treatment to 10000-0.01 Hz.

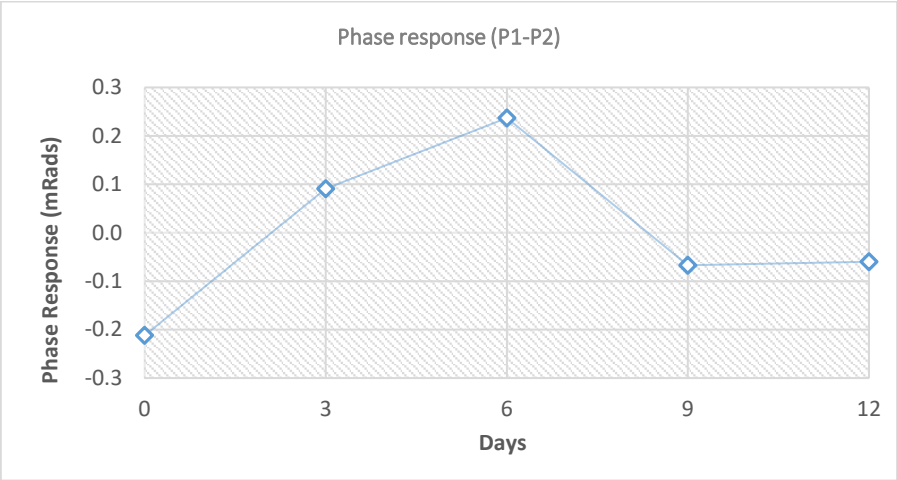
Phase response (P1-P2)
Phase Response (mRads)
0.3
0.2
0.1
0.0
-0.1
-0.2
-0.3
0
3
6
9
12
Days

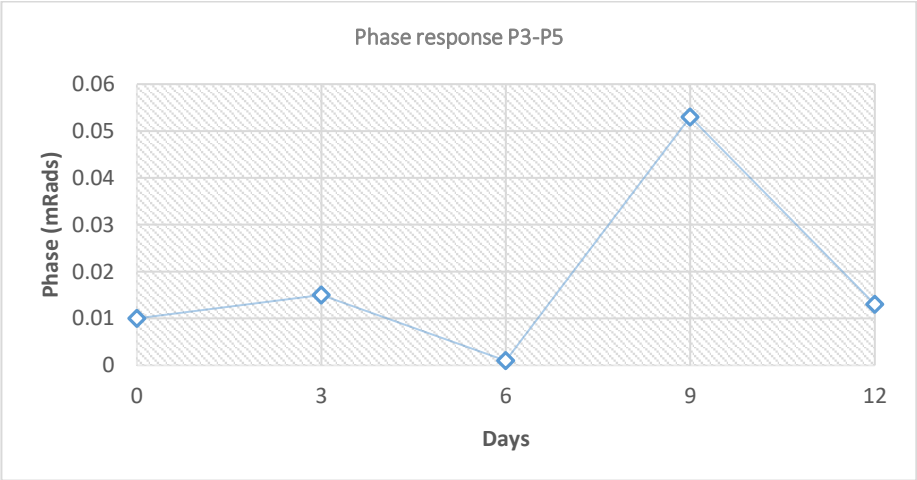
Phase response P3-P5
Phase (mRads)
0.06
0.05
0.04
0.03
0.02
0.01
0
0
3
6
9
12
Days

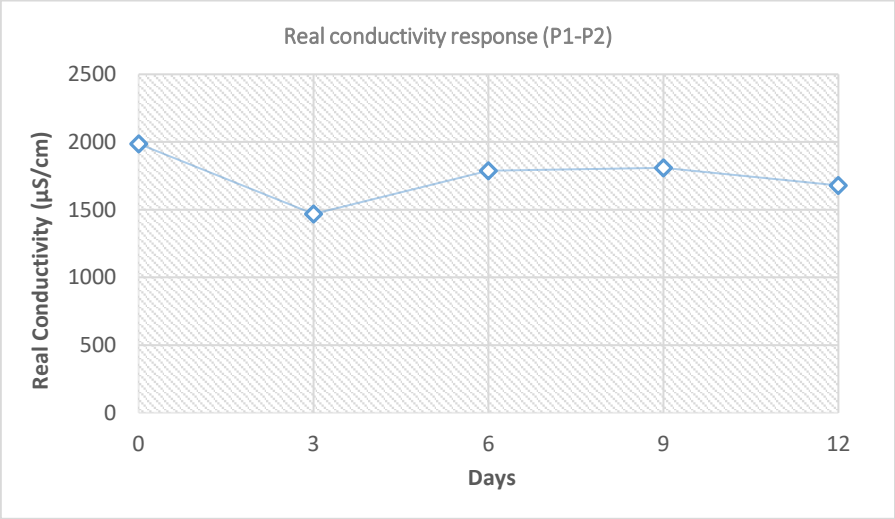
Real conductivity response (P1-P2)
Real Conductivity (µS/cm)
2500
2000
1500
1000
500
0
0
3
6
9
12
Days

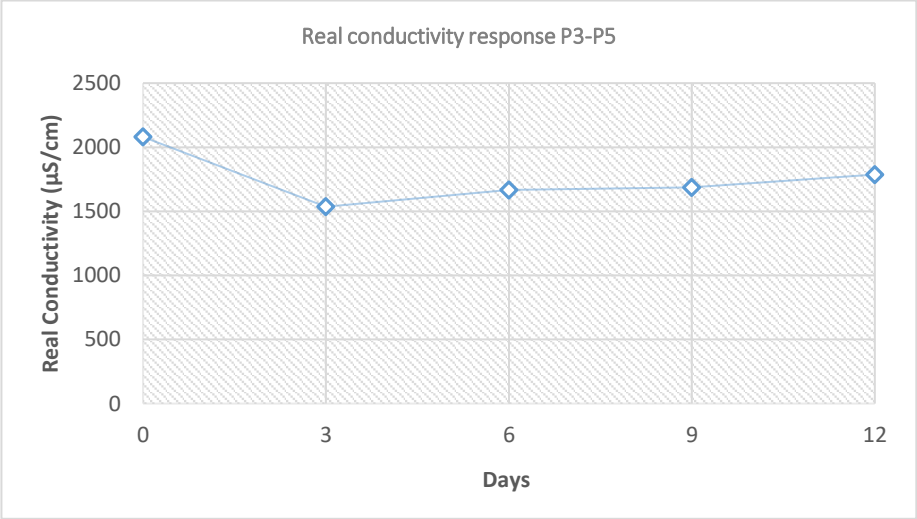
Real conductivity response P3-P5
Real Conductivity (µS/cm)
2500
2000
1500
1000
500
0
0
3
6
9
12
Days

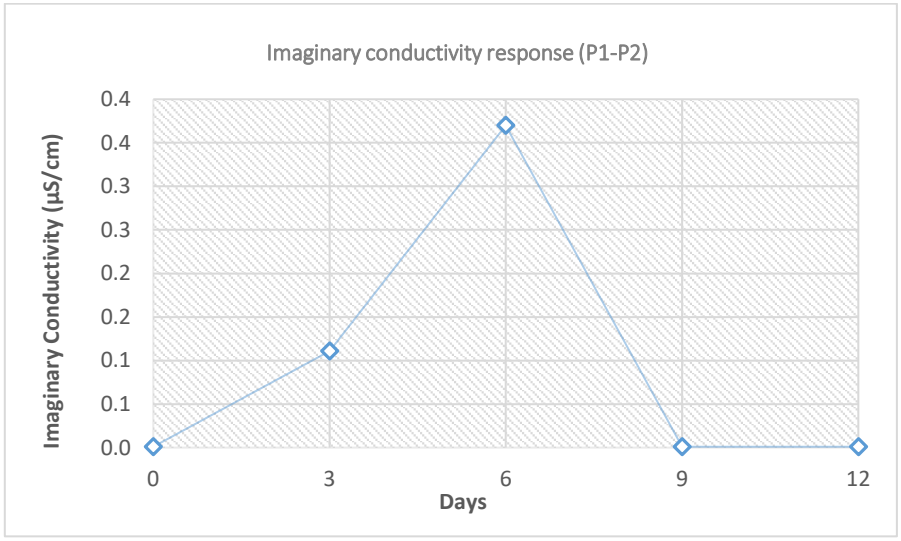
Imaginary conductivity response (P1-P2)
Imaginary Conductivity (µS/cm)
0.4
0.4
0.3
0.3
0.2
0.2
0.1
0.1
0.0
0
3
6
9
12
Days

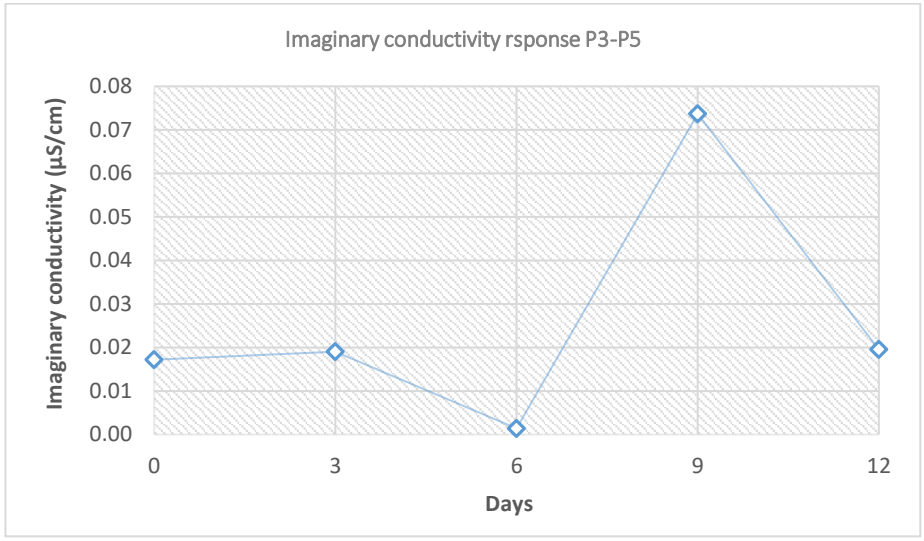
Imaginary conductivity rsponse P3-P5
Imaginary conductivity (µS/cm)
0.08
0.07
0.06
0.05
0.04
0.03
0.02
0.01
0.00
0
3
6
9
12
Days

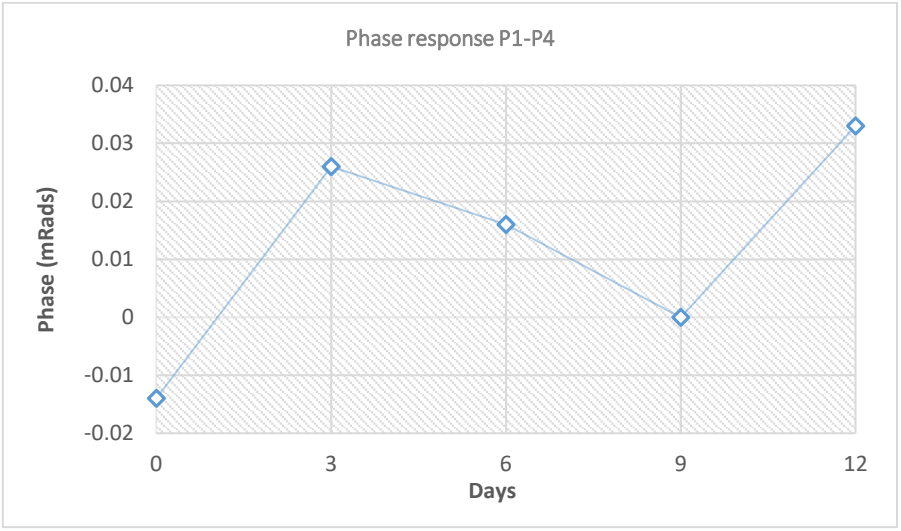
Phase response P1-P4
Phase (mRads)
0.04
0.03
0.02
0.01
0
-0.01
-0.02
0
3
6
9
12
Days

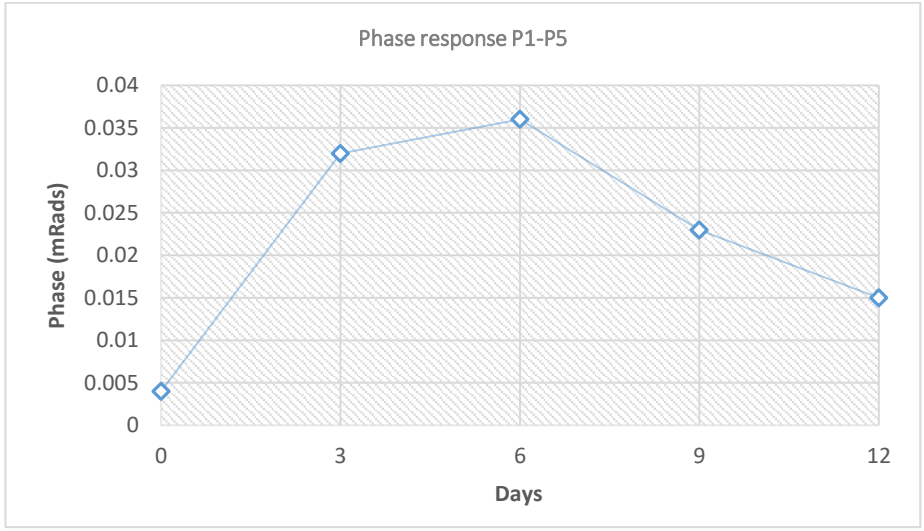
Phase response P1-P5
Phase (mRads)
0.04
0.035
0.03
0.025
0.02
0.015
0.01
0.005
0
0
3
6
9
12
Days

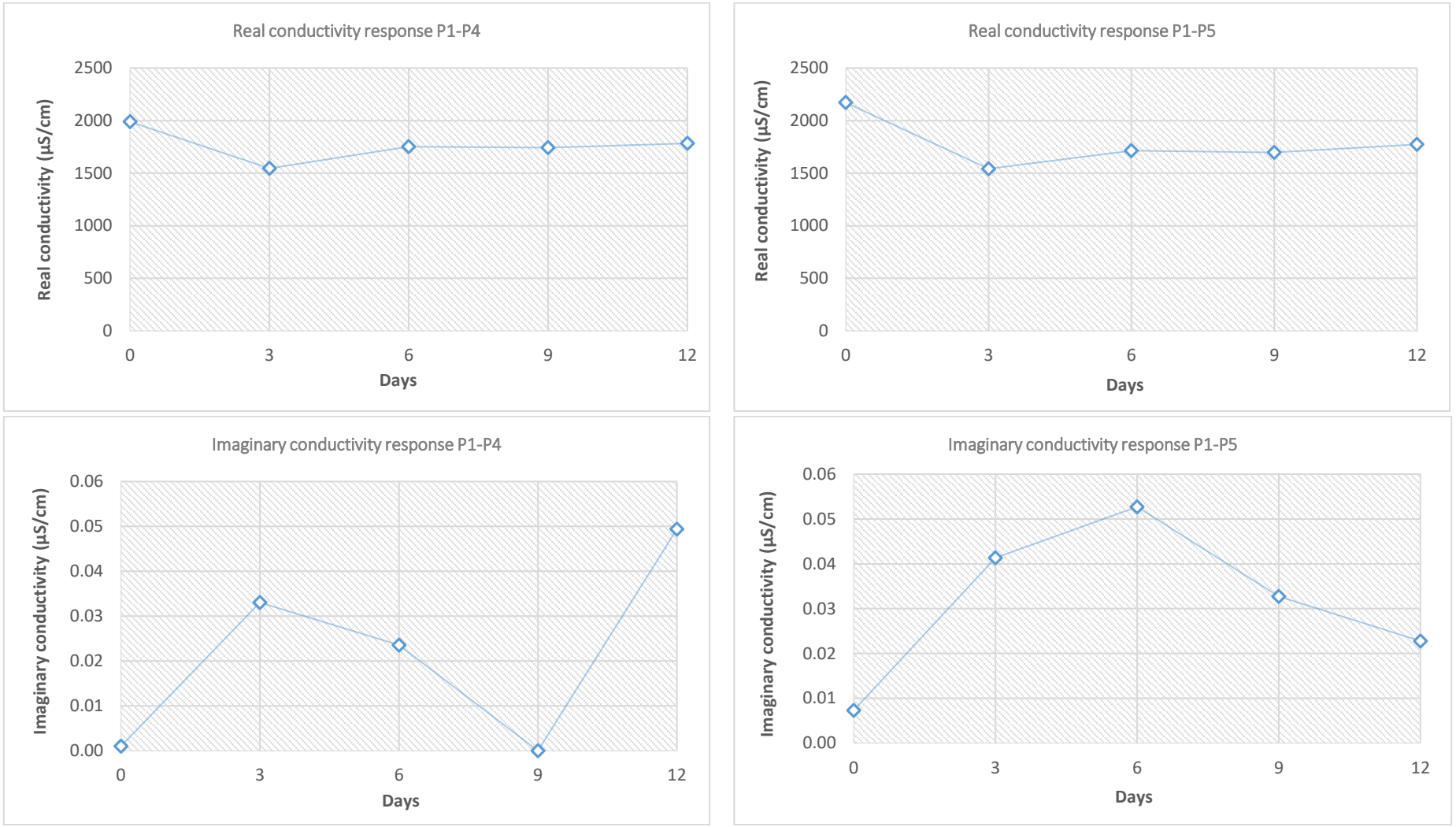

Figure B.12 Single frequency graphs after phytoremediation treatment to 10 Hz.

Table B.1 Time-lapse quantitative analysis of phytoremediation processes during the experimental process (T_0, … T_4 different experimental stages)

	Day	TDS (ppt)	COD (mg/L)	EC - Inflow (µS/cm)	EC (SIP) (µS/cm)	Ti/T0 (%)	Ti+1/Ti (%)
T0	0	6.2	49723	12400	2170	100.00%	71.01%
T1	3	3.75	10410	7500	1541	71.01%	111.10%
T2	6	4.3	13821	8700	1712	78.89%	99.07%
T3	9	3.91	12657	7840	1696	78.16%	104.60%
T4	12	3.8	8478	7740	1774	81.75%	

B.6 Biochar

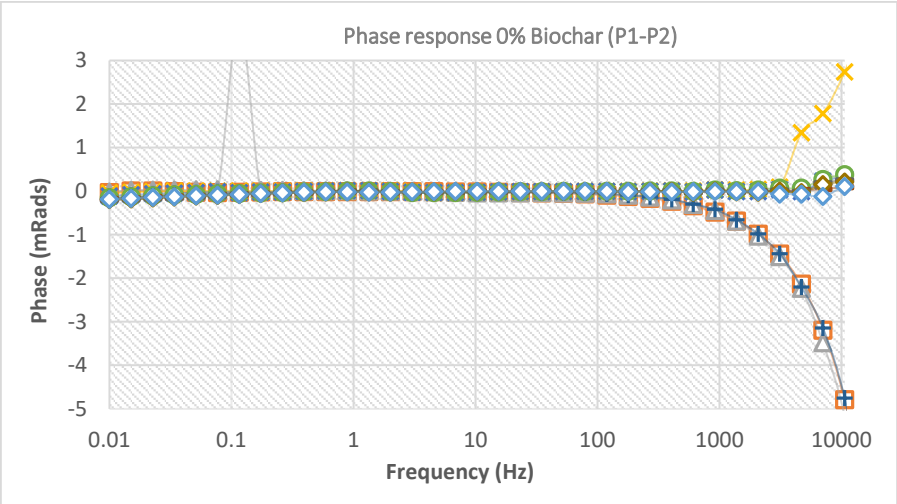
Phase response 0% Biochar (P1-P2)
Phase (mRads)
3
2
1
0
-1
-2
-3
-4
-5
0.01
0.1
1
10
100
1000
10000
Frequency (Hz)

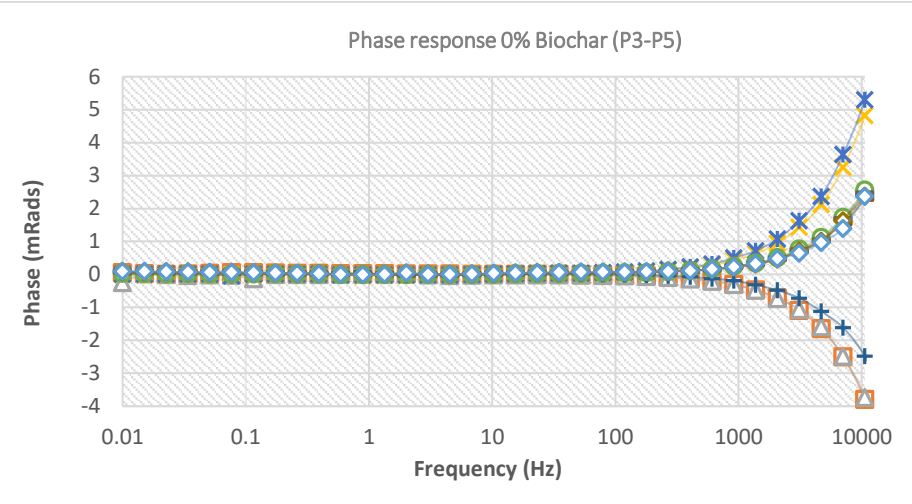
Phase response 0% Biochar (P3-P5)
Phase (mRads)
6
5
4
3
2
1
0
-1
-2
-3
-4
0.01
0.1
1
10
100
1000
10000
Frequency (Hz)

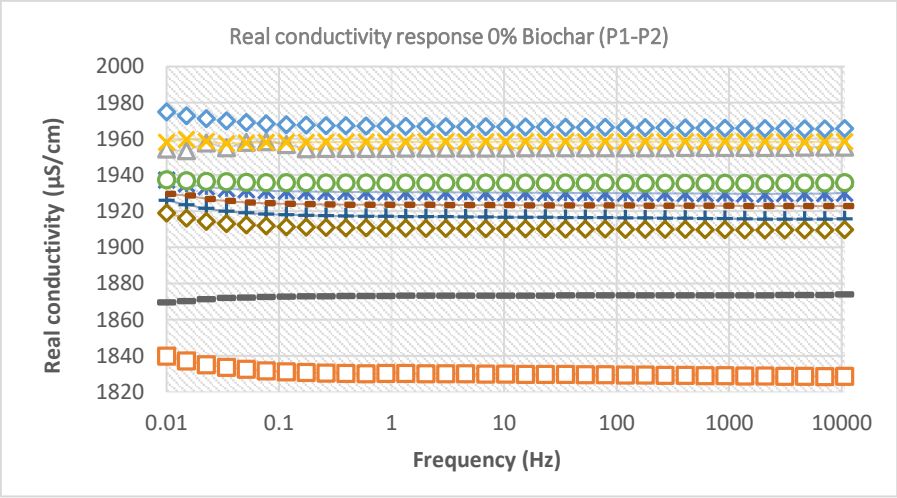
Real conductivity response 0% Biochar (P1-P2)
Real conductivity (µS/cm)
2000
1980
1960
1940
1920
1900
1880
1860
1840
1820
0.01
0.1
1
10
100
1000
10000
Frequency (Hz)

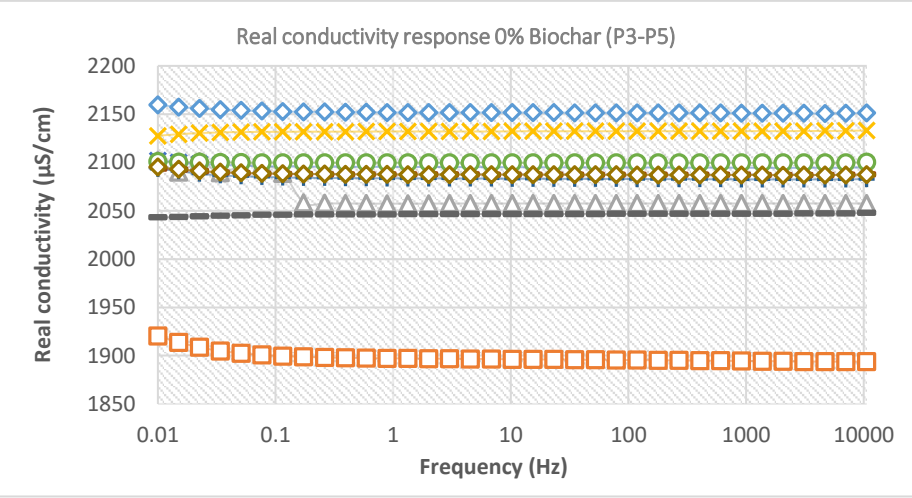
Real conductivity response 0% Biochar (P3-P5)
Real conductivity (µS/cm)
2200
2150
2100
2050
2000
1950
1900
1850
0.01
0.1
1
10
100
1000
10000
Frequency (Hz)

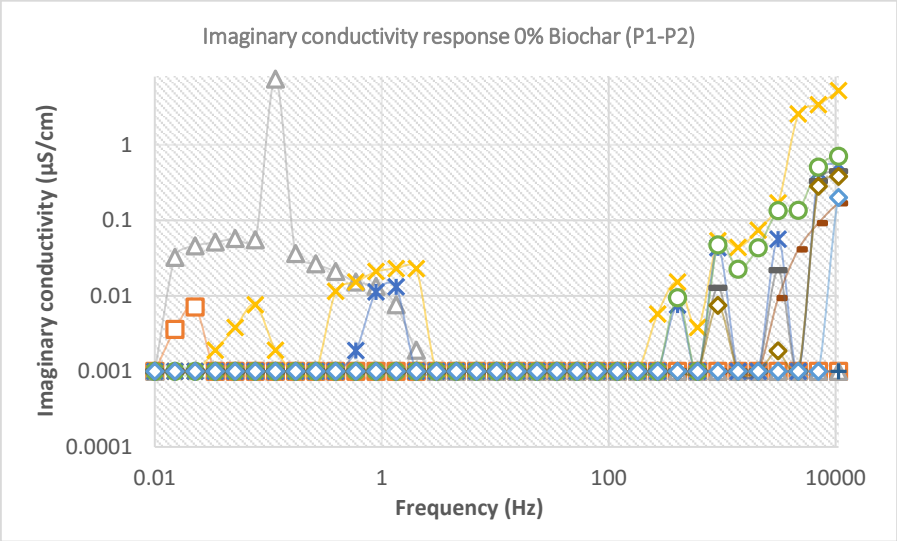
Imaginary conductivity response 0% Biochar (P1-P2)
Imaginary conductivity (µS/cm)
1
0.1
0.01
0.001
0.0001
0.01
1
100
10000
Frequency (Hz)

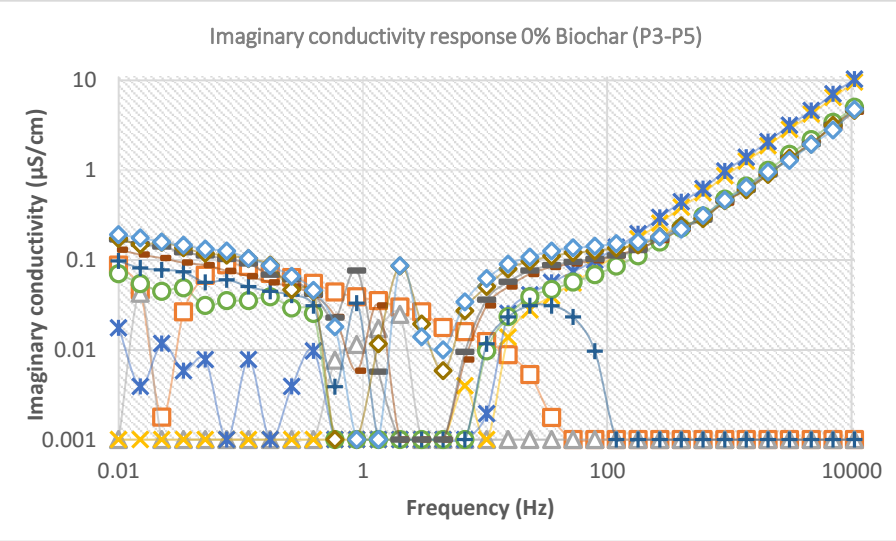
Imaginary conductivity response 0% Biochar (P3-P5)
Imaginary conductivity (µS/cm)
10
1
0.1
0.01
0.001
0.01
1
100
10000
Frequency (Hz)

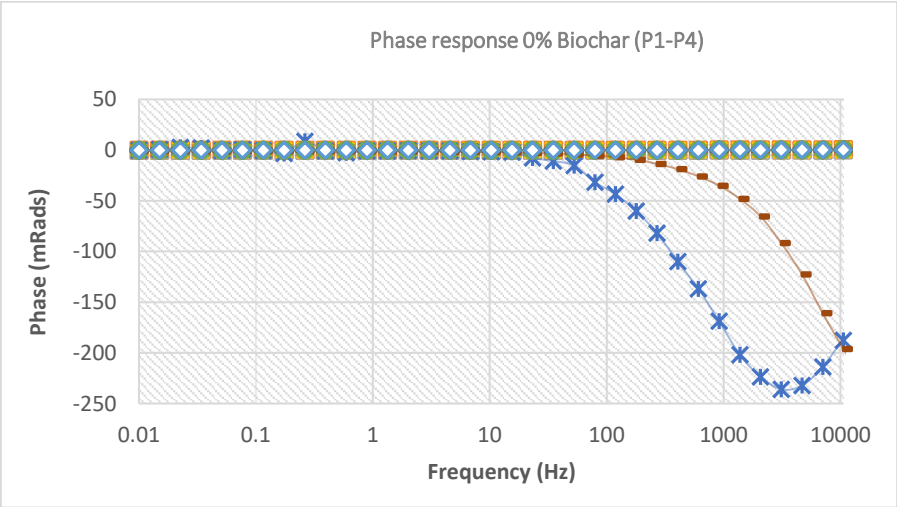
Phase response 0% Biochar (P1-P4)
Phase (mRads)
50
0
-50
-100
-150
-200
-250
0.01
0.1
1
10
100
1000
10000
Frequency (Hz)

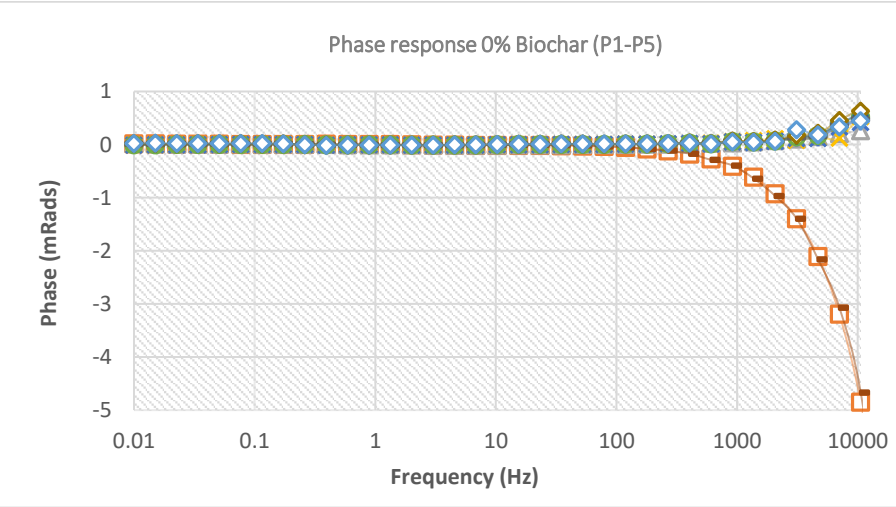
Phase response 0% Biochar (P1-P5)
Phase (mRads)
1
0
-1
-2
-3
-4
-5
0.01
0.1
1
10
100
1000
10000
Frequency (Hz)

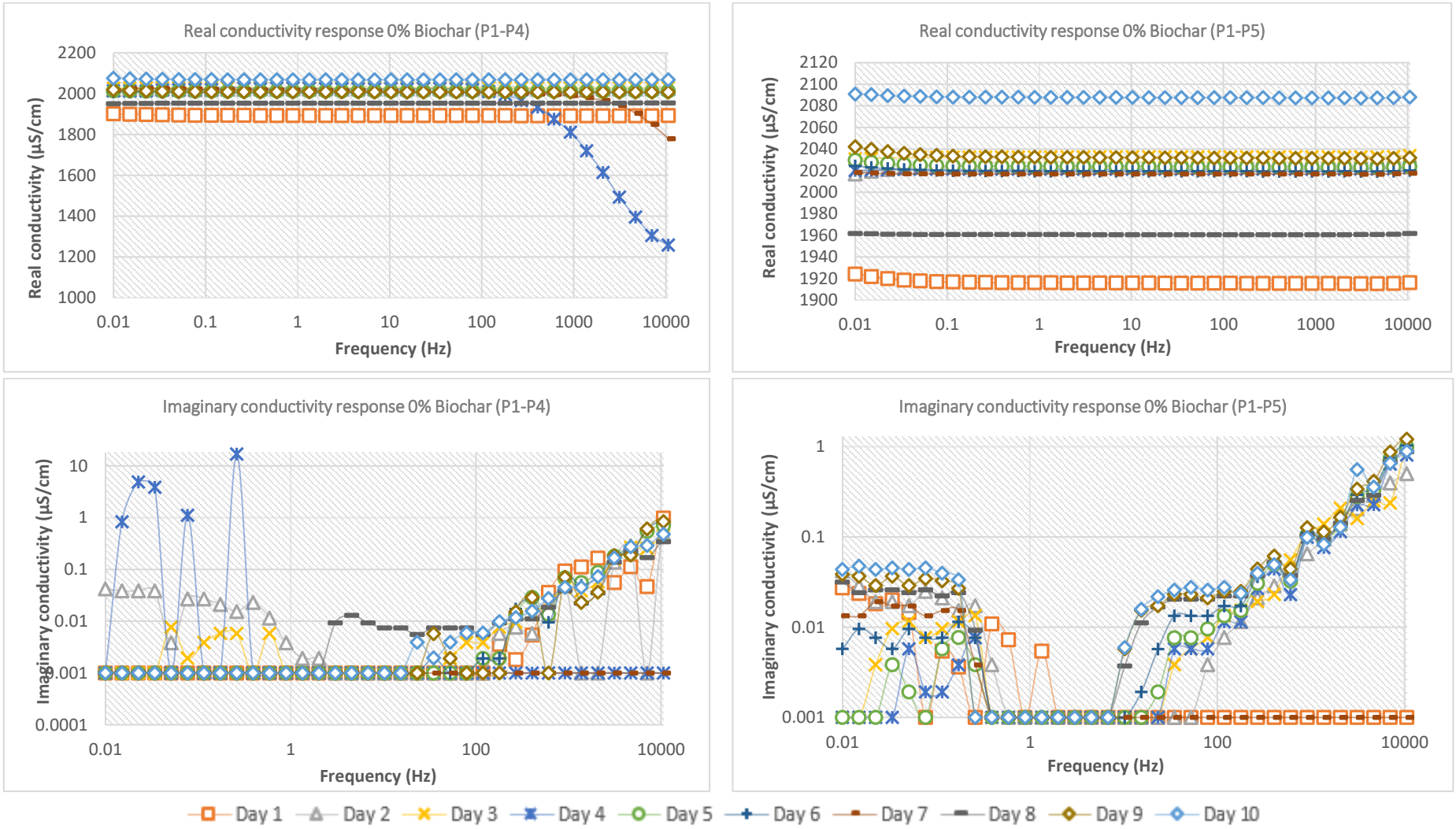

Figure B.13 Phase response and fluid conductivity measurements during 10 days with 0% w/w biochar to 10000-0.01 Hz.

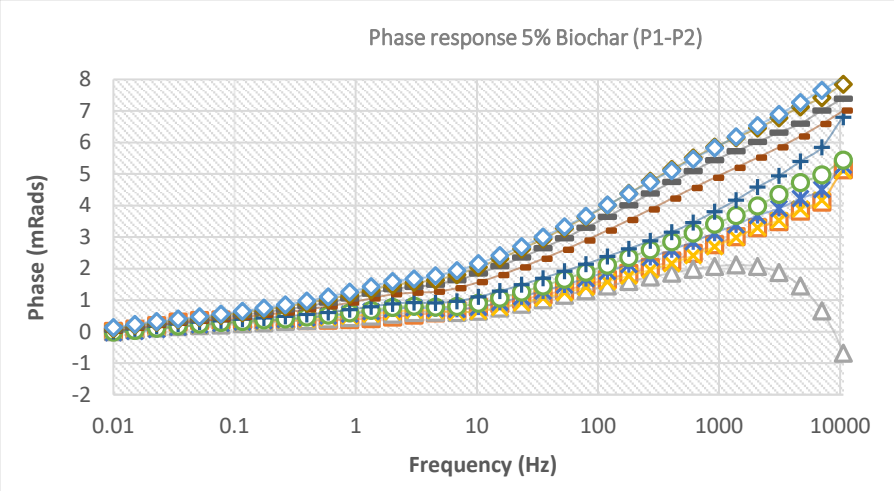
Phase response 5% Biochar (P1-P2)
Phase (mRads)
8
7
6
5
4
3
2
1
0
-1
-2
0.01
0.1
1
10
100
1000
10000
Frequency (Hz)

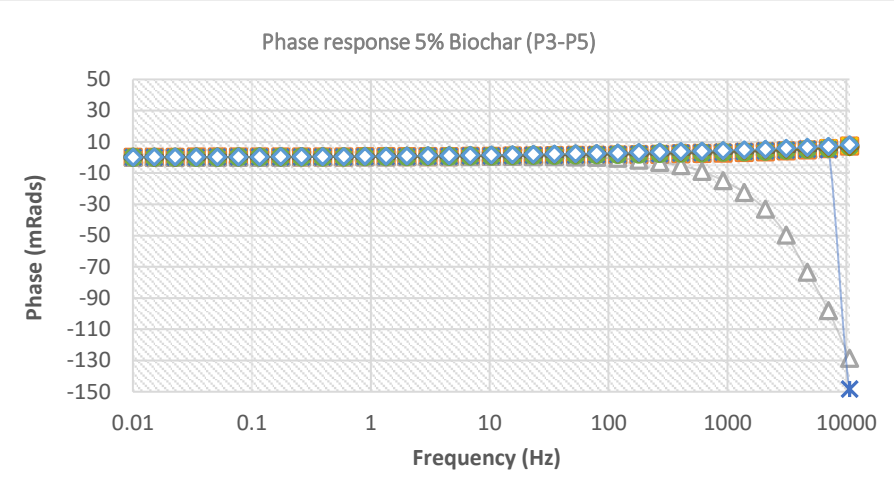
Phase response 5% Biochar (P3-P5)
Phase (mRads)
50
30
10
-10
-30
-50
-70
-90
-110
-130
-150
0.01
0.1
1
10
100
1000
10000
Frequency (Hz)

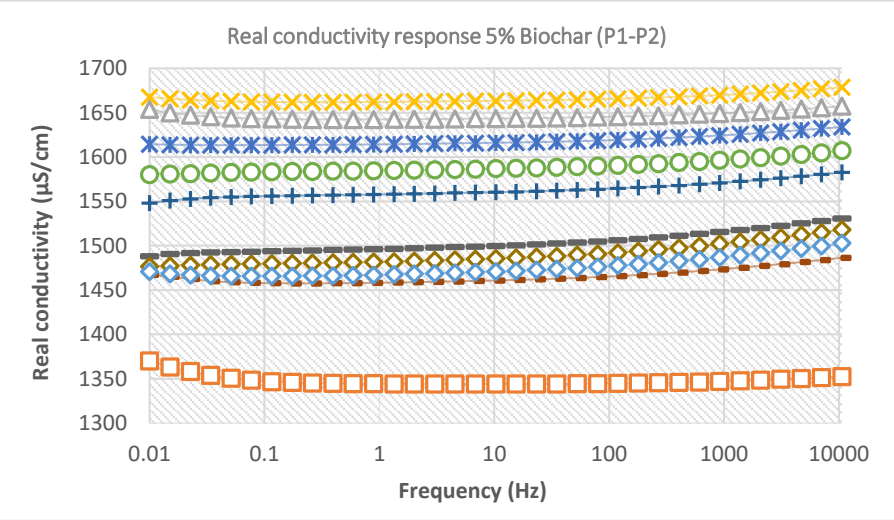
Real conductivity response 5% Biochar (P1-P2)
Real conductivity (µS/cm)
1700
1650
1600
1550
1500
1450
1400
1350
1300
0.01
0.1
1
10
100
1000
10000
Frequency (Hz)

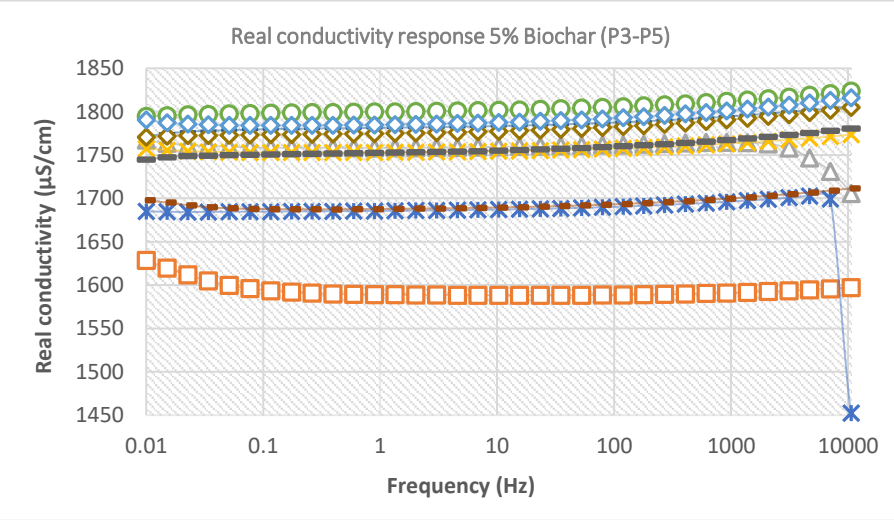
Real conductivity response 5% Biochar (P3-P5)
Real conductivity (µS/cm)
1850
1800
1750
1700
1650
1600
1550
1500
1450
0.01
0.1
1
10
100
1000
10000
Frequency (Hz)

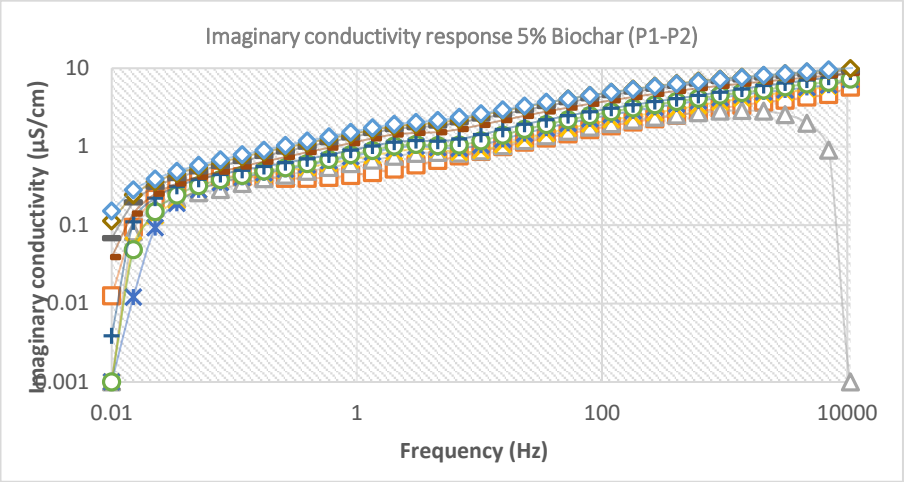
Imaginary conductivity response 5% Biochar (P1-P2)
Imaginary conductivity (µS/cm)
10
1
0.1
0.01
0.001
0.01
1
100
10000
Frequency (Hz)

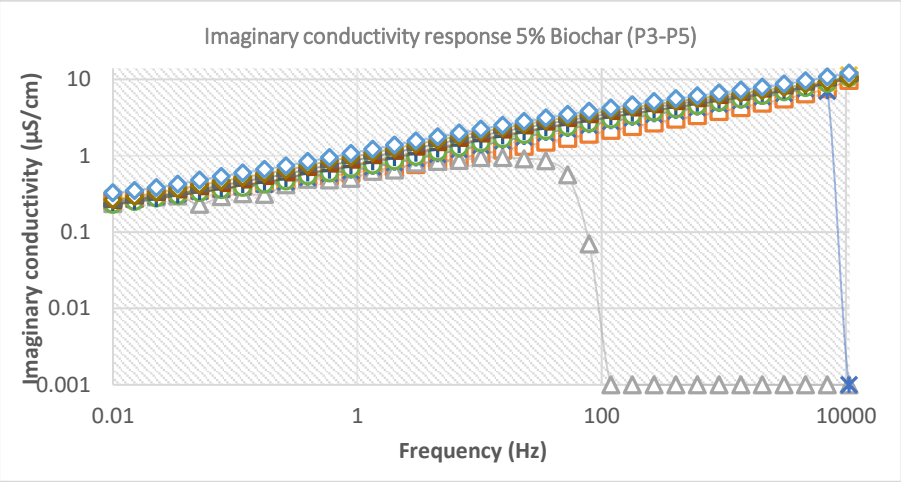
Imaginary conductivity response 5% Biochar (P3-P5)
Imaginary conductivity (µS/cm)
10
1
0.1
0.01
0.001
0.01
1
100
10000
Frequency (Hz)

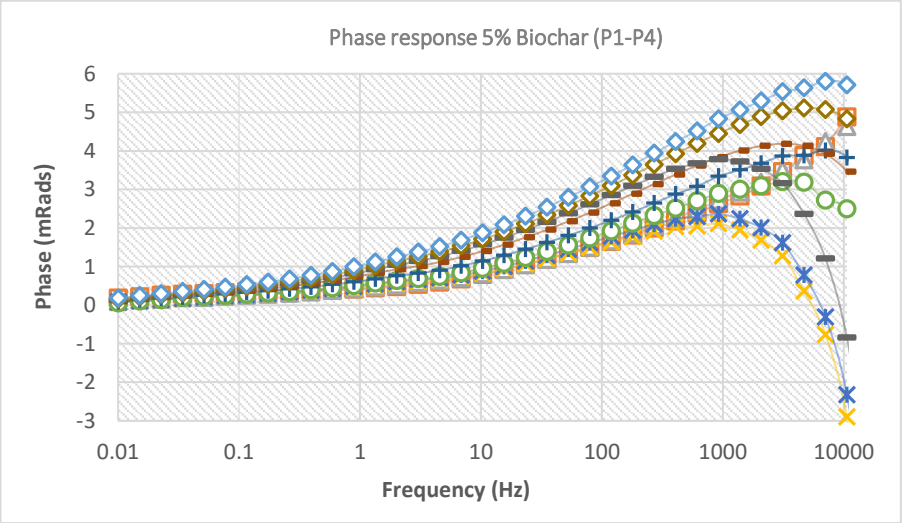
Phase response 5% Biochar (P1-P4)
Phase (mRads)
6
5
4
3
2
1
0
-1
-2
-3
0.01
0.1
1
10
100
1000
10000
Frequency (Hz)

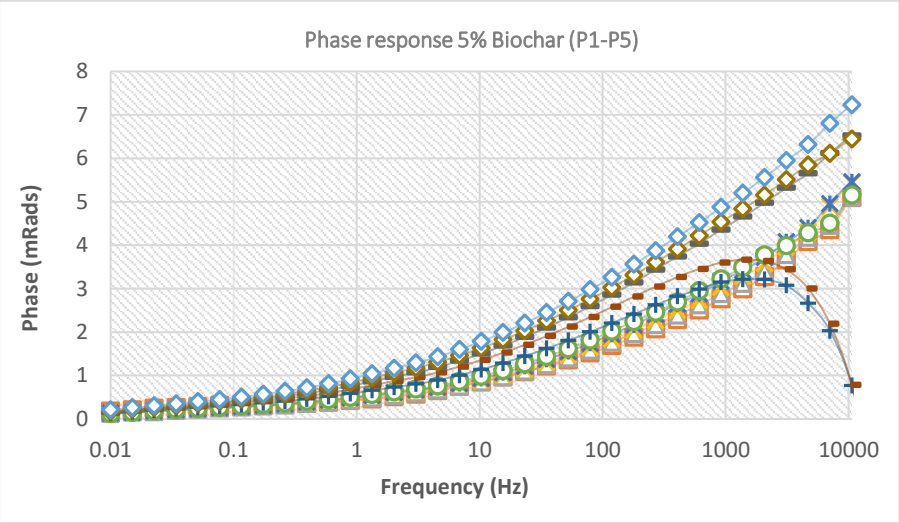
Phase response 5% Biochar (P1-P5)
Phase (mRads)
8
7
6
5
4
3
2
1
0
0.01
0.1
1
10
100
1000
10000
Frequency (Hz)

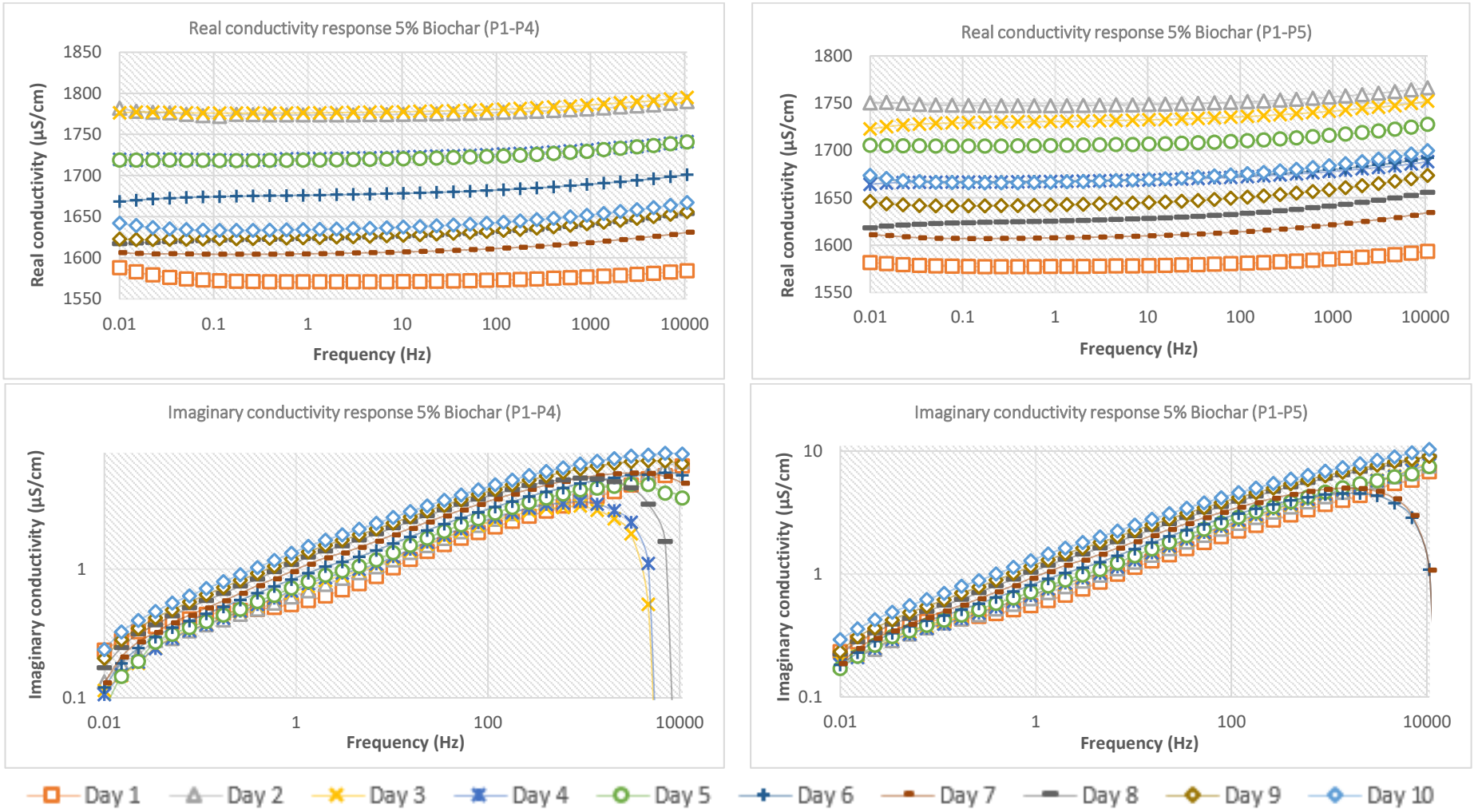

Figure B.14 Phase response and fluid conductivity measurements during 10 days treatment with 5% w/w biochar to 10000-0.01 Hz.

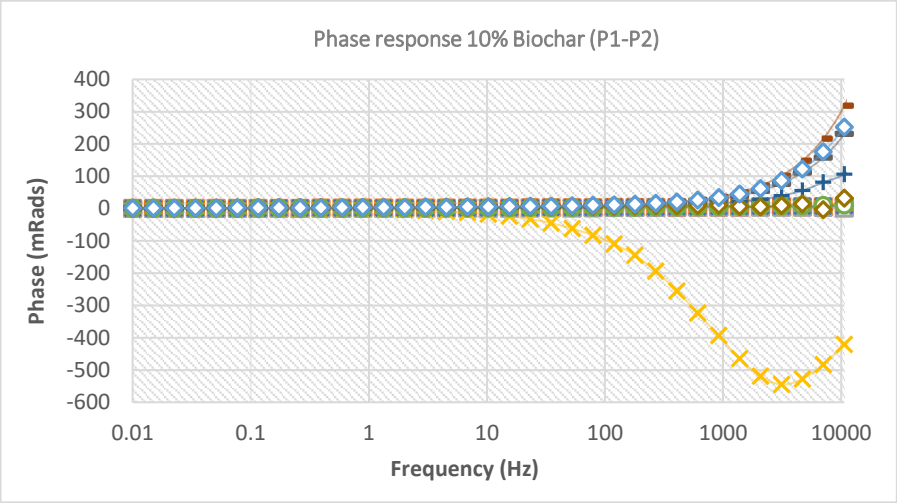
Phase response 10% Biochar (P1-P2)
Phase (mRads)
400
300
200
100
0
-100
-200
-300
-400
-500
-600
0.01
0.1
1
10
100
1000
10000
Frequency (Hz)

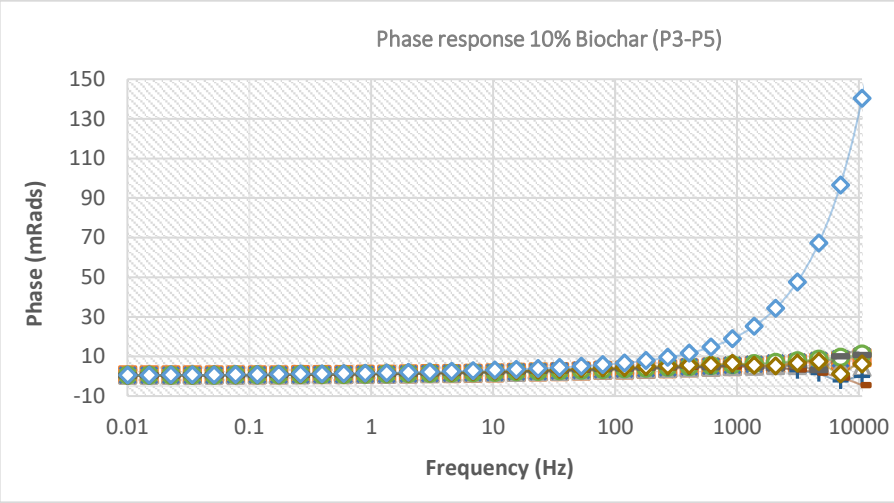
Phase response 10% Biochar (P3-P5)
Phase (mRads)
150
130
110
90
70
50
30
10
-10
0.01
0.1
1
10
100
1000
10000
Frequency (Hz)

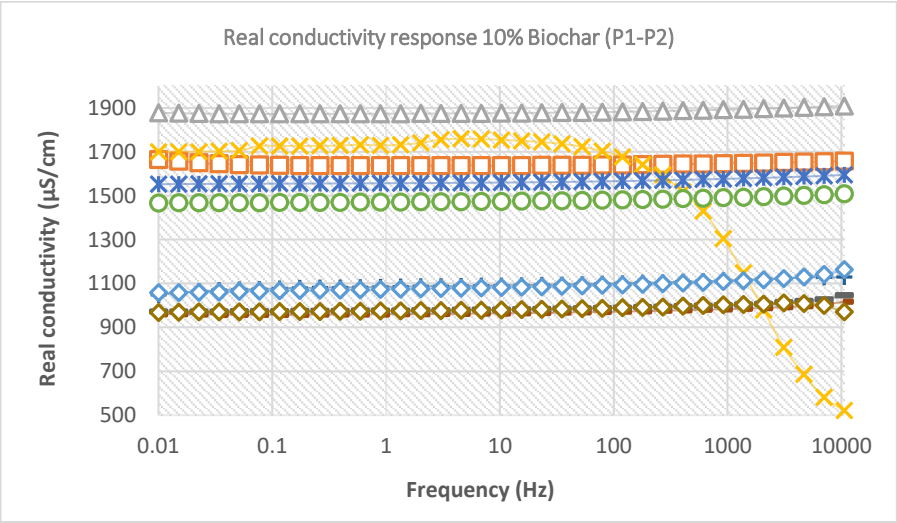
Real conductivity response 10% Biochar (P1-P2)
Real conductivity (µS/cm)
1900
1700
1500
1300
1100
900
700
500
0.01
0.1
1
10
100
1000
10000
Frequency (Hz)

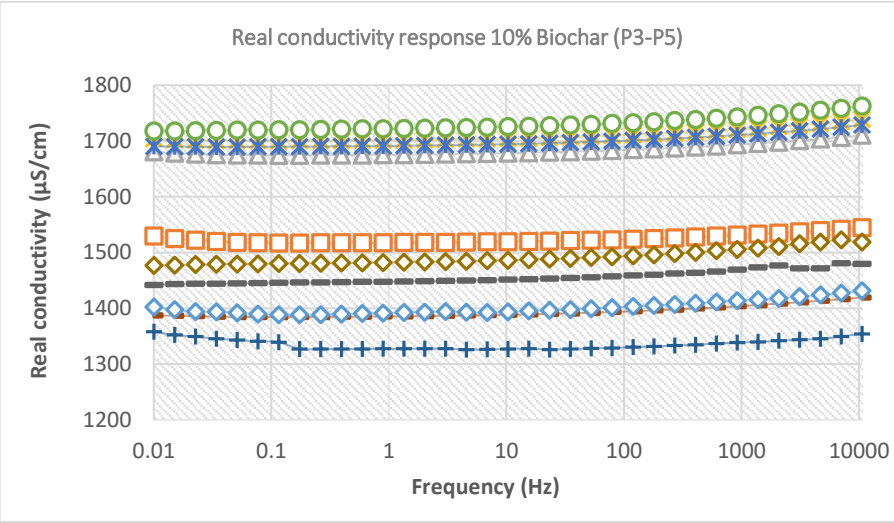
Real conductivity response 10% Biochar (P3-P5)
Real conductivity (µS/cm)
1800
1700
1600
1500
1400
1300
1200
0.01
0.1
1
10
100
1000
10000
Frequency (Hz)

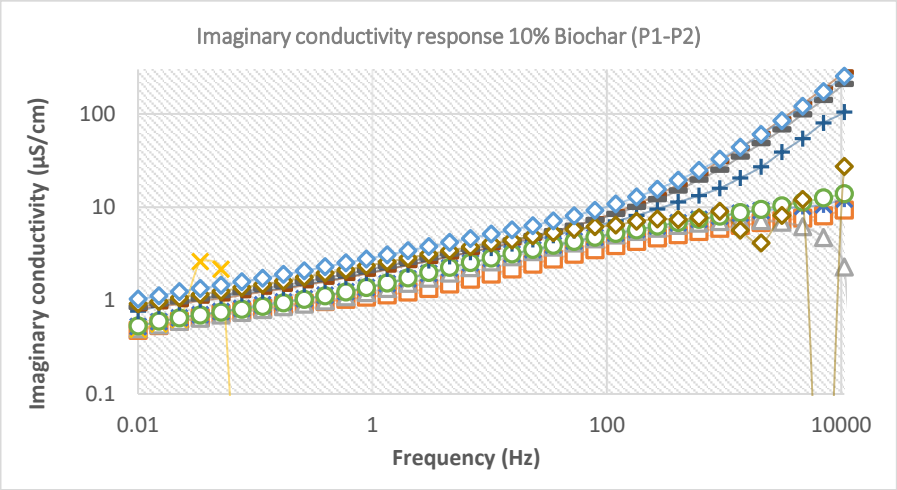
Imaginary conductivity response 10% Biochar (P1-P2)
Imaginary conductivity (µS/cm)
100
10
1
0.1
0.01
1
100
10000
Frequency (Hz)

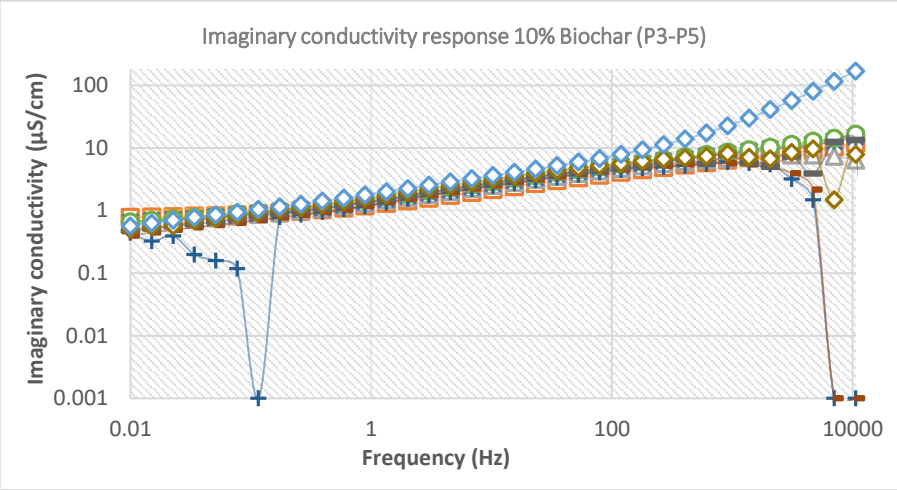
Imaginary conductivity response 10% Biochar (P3-P5)
Imaginary conductivity (µS/cm)
100
10
1
0.1
0.01
0.001
0.01
1
100
10000
Frequency (Hz)

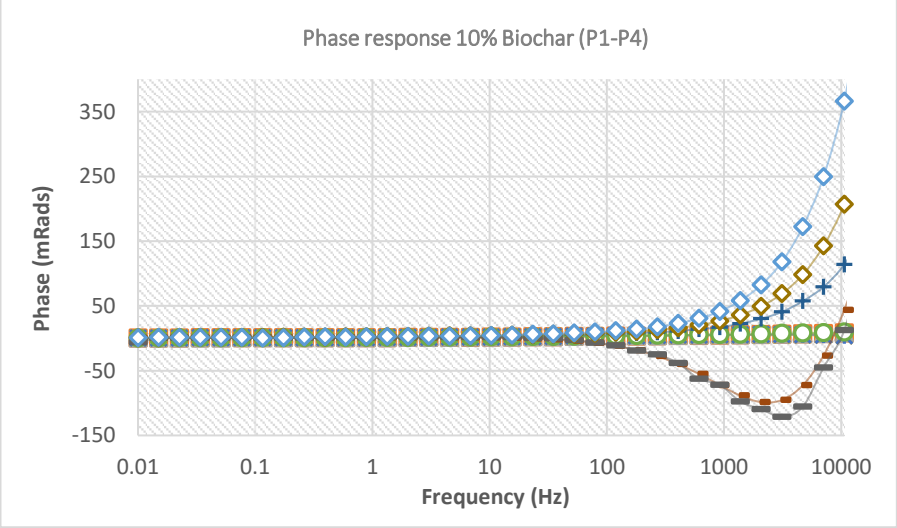
Phase response 10% Biochar (P1-P4)
Phase (mRads)
350
250
150
50
-50
-150
0.01
0.1
1
10
100
1000
10000
Frequency (Hz)

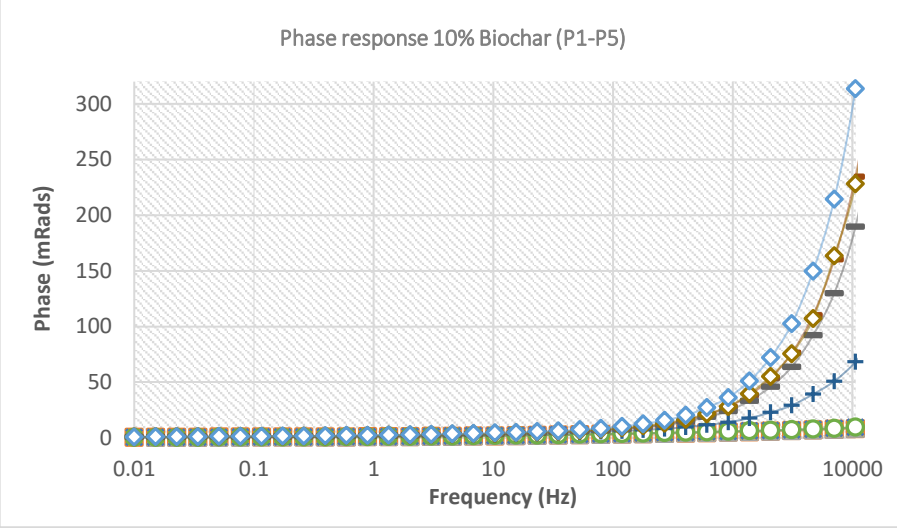
Phase response 10% Biochar (P1-P5)
Phase (mRads)
300
250
200
150
100
50
0
0.01
0.1
1
10
100
1000
10000
Frequency (Hz)

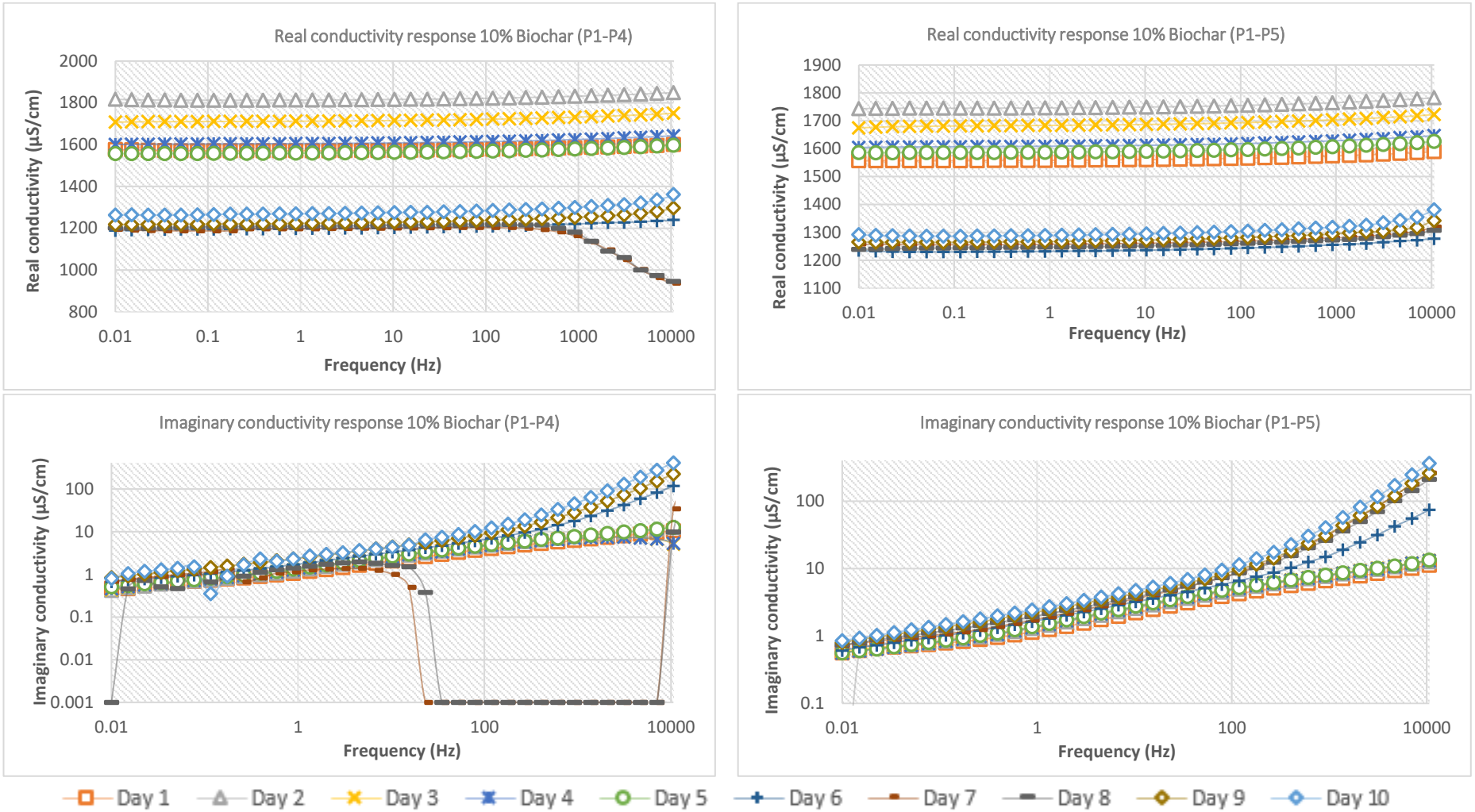

Figure B.15 Phase response and fluid conductivity measurements during 10 days treatment with 10% w/w biochar to 10000-0.01 Hz.

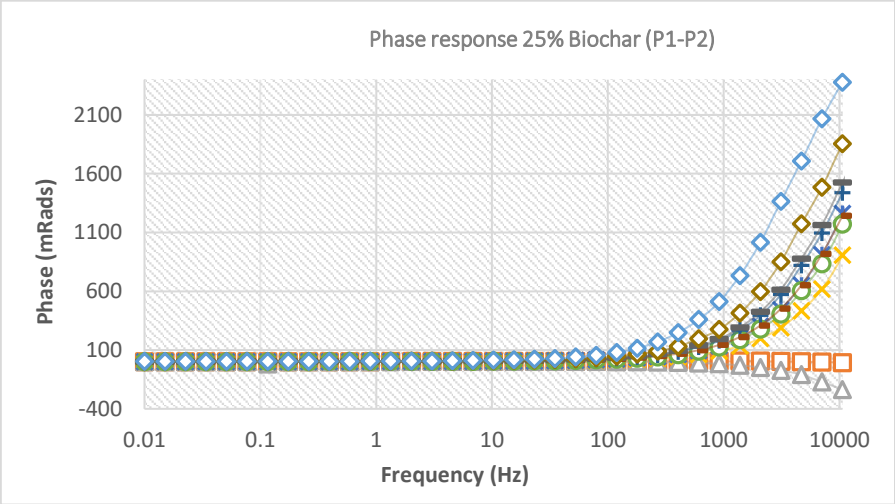
Phase response 25% Biochar (P1-P2)
Phase (mRads)
2100
1600
1100
600
100
-400
0.01
0.1
1
10
100
1000
10000
Frequency (Hz)

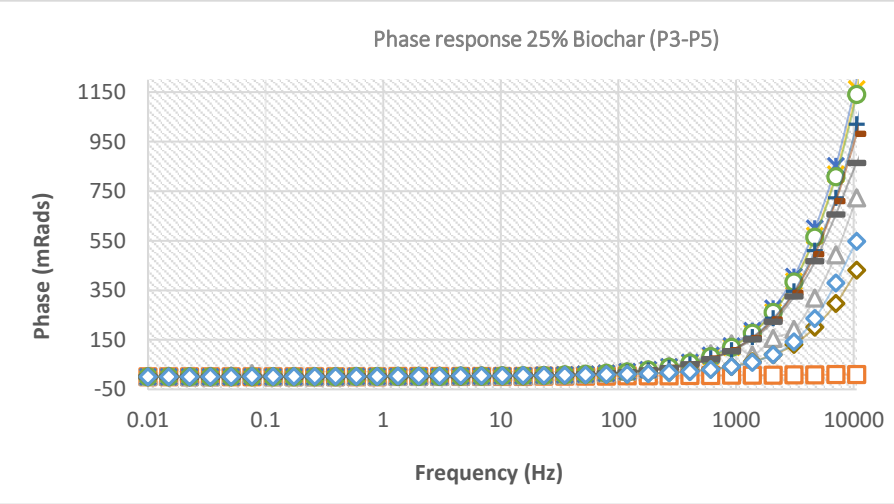
Phase response 25% Biochar (P3-P5)
Phase (mRads)
1150
950
750
550
350
150
-50
0.01
0.1
1
10
100
1000
10000
Frequency (Hz)

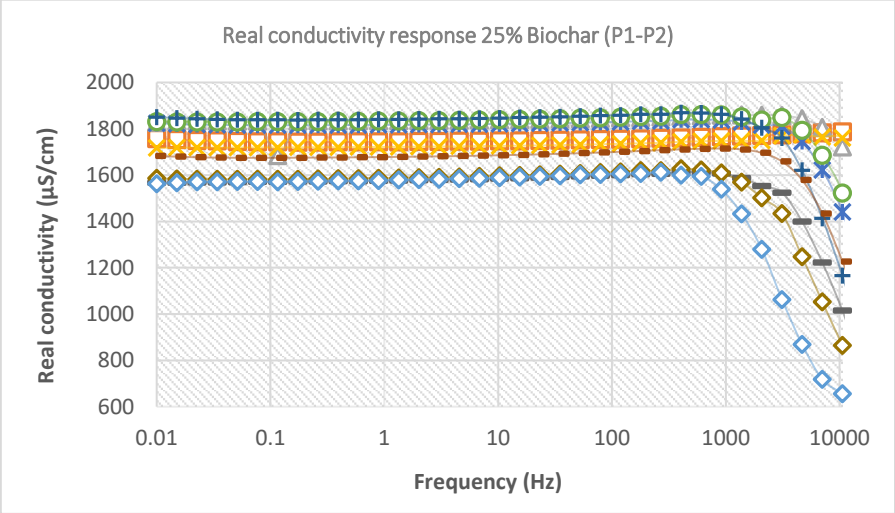
Real conductivity response 25% Biochar (P1-P2)
Real conductivity (µS/cm)
2000
1800
1600
1400
1200
1000
800
600
0.01
0.1
1
10
100
1000
10000
Frequency (Hz)

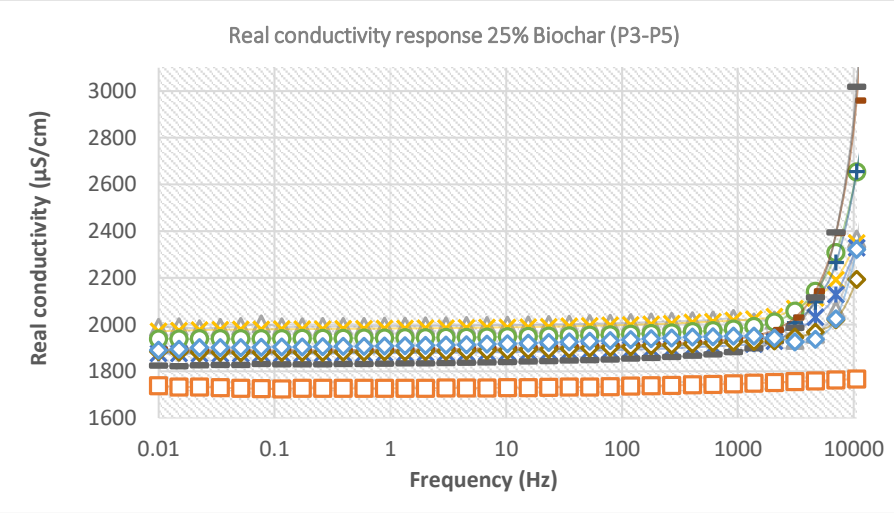
Real conductivity response 25% Biochar (P3-P5)
Real conductivity (µS/cm)
3000
2800
2600
2400
2200
2000
1800
1600
0.01
0.1
1
10
100
1000
10000
Frequency (Hz)

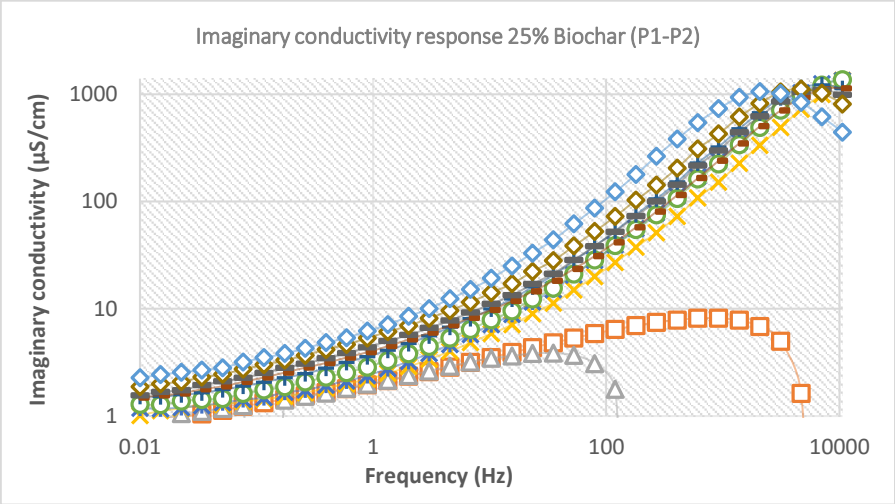
Imaginary conductivity response 25% Biochar (P1-P2)
Imaginary conductivity (µS/cm)
1000
100
10
1
0.01
1
100
10000
Frequency (Hz)

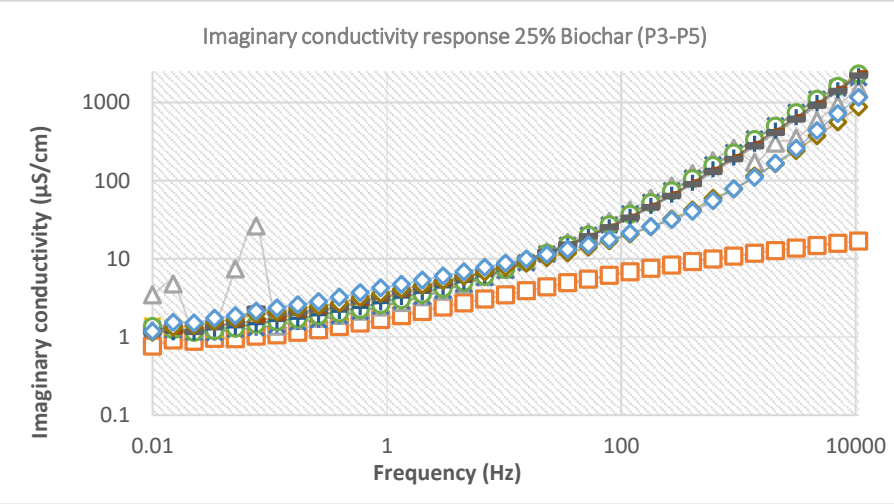
Imaginary conductivity response 25% Biochar (P3-P5)
Imaginary conductivity (µS/cm)
1000
100
10
1
0.1
0.01
1
100
10000
Frequency (Hz)

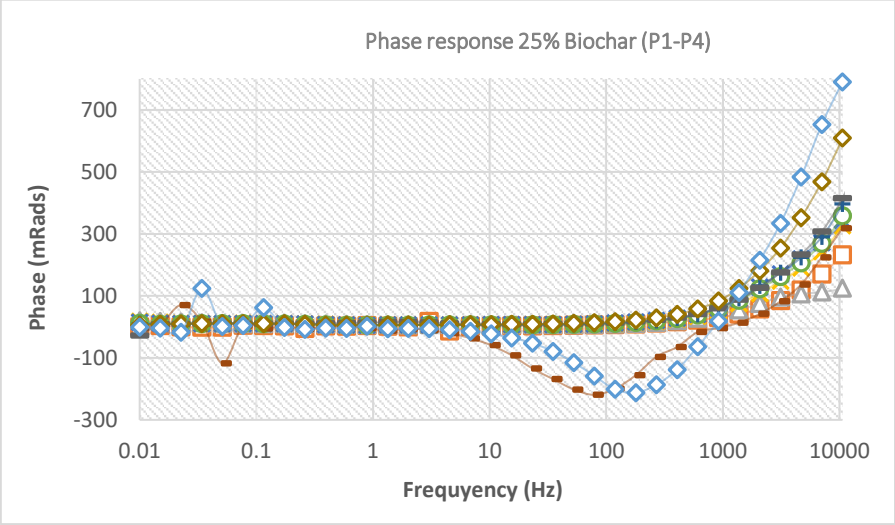
Phase response 25% Biochar (P1-P4)
Phase (mRads)
700
500
300
100
-100
-300
0.01
0.1
1
10
100
1000
10000
Frequyency (Hz)

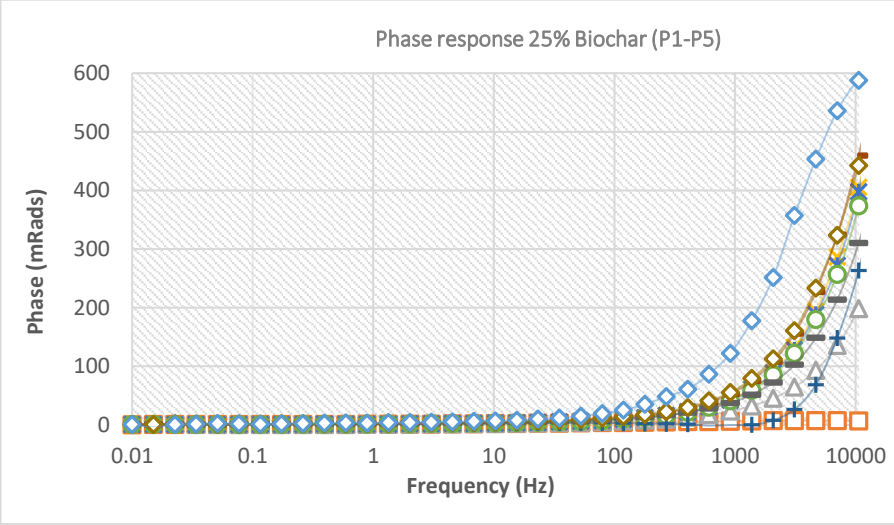
Phase response 25% Biochar (P1-P5)
Phase (mRads)
600
500
400
300
200
100
0
0.01
0.1
1
10
100
1000
10000
Frequency (Hz)

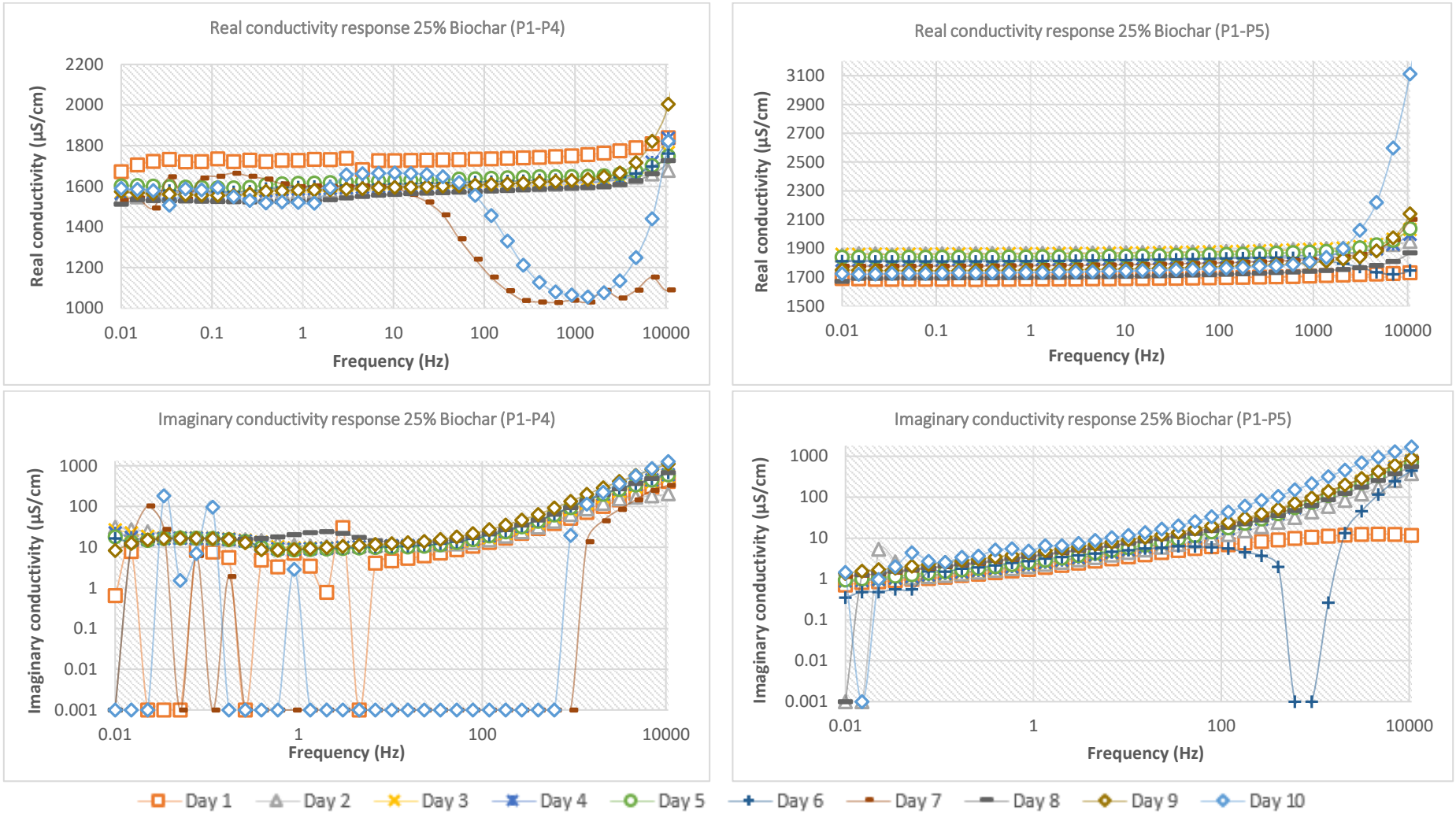

Figure B.16 Phase response and fluid conductivity measurements during 10 days treatment with 25% w/w biochar to 10000-0.01 Hz.

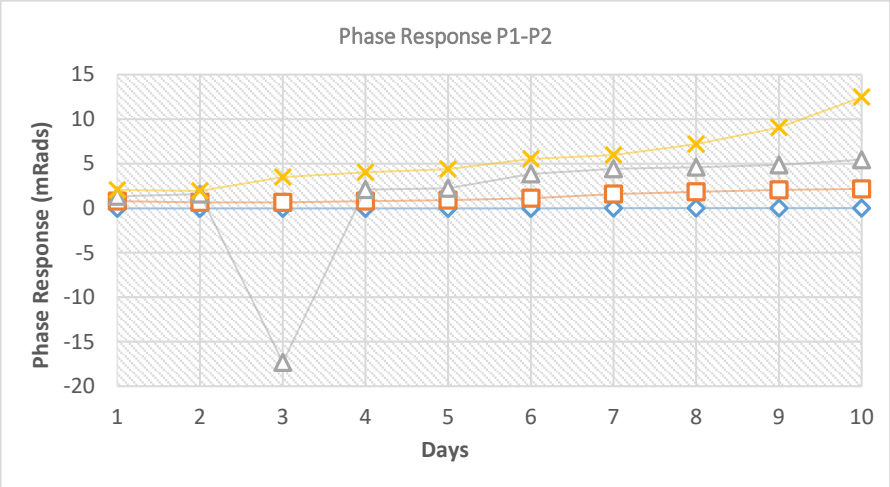
Phase Response P1-P2
Phase Response (mRads)
15
10
5
0
-5
-10
-15
-20
1
2
3
4
5
6
7
8
9
10
Days

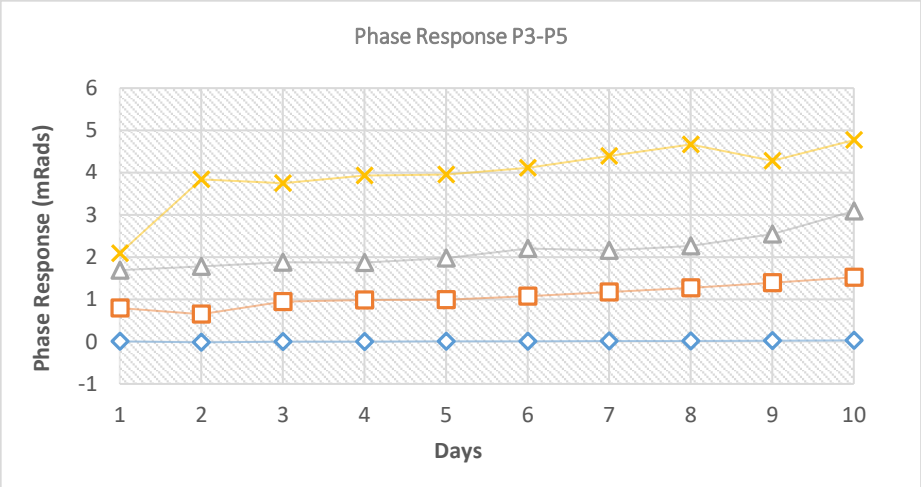
Phase Response P3-P5
Phase Response (mRads)
6
5
4
3
2
1
0
-1
1
2
3
4
5
6
7
8
9
10
Days

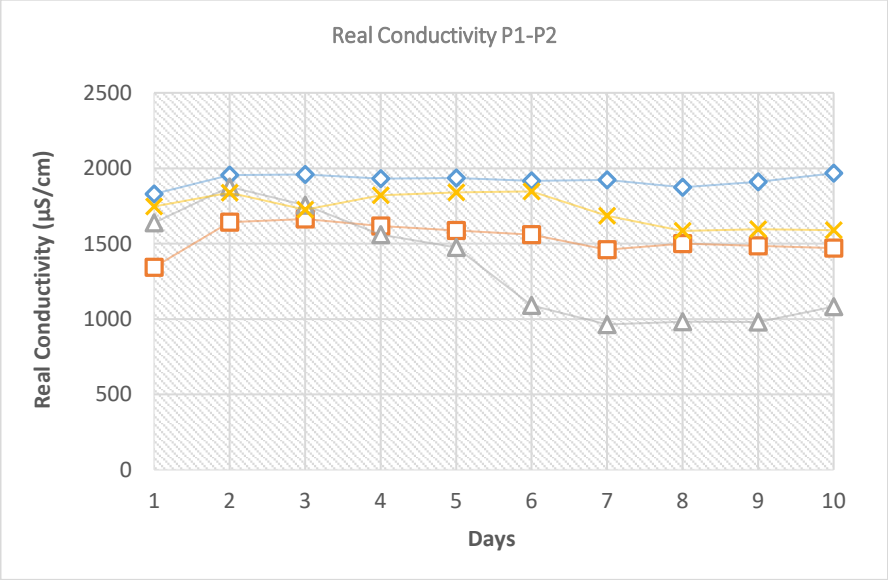
Real Conductivity P1-P2
Real Conductivity (µS/cm)
2500
2000
1500
1000
500
0
1
2
3
4
5
6
7
8
9
10
Days

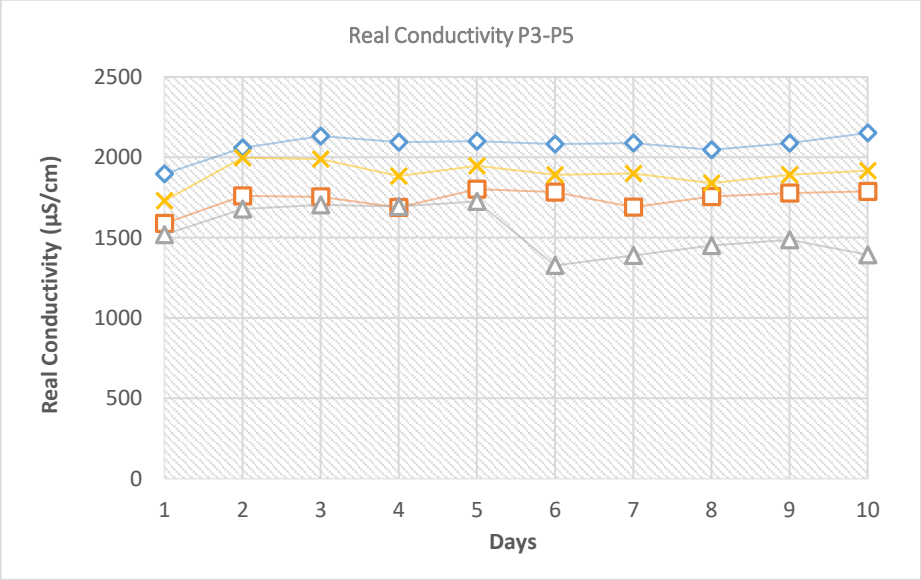
Real Conductivity P3-P5
Real Conductivity (µS/cm)
2500
2000
1500
1000
500
0
1
2
3
4
5
6
7
8
9
10
Days

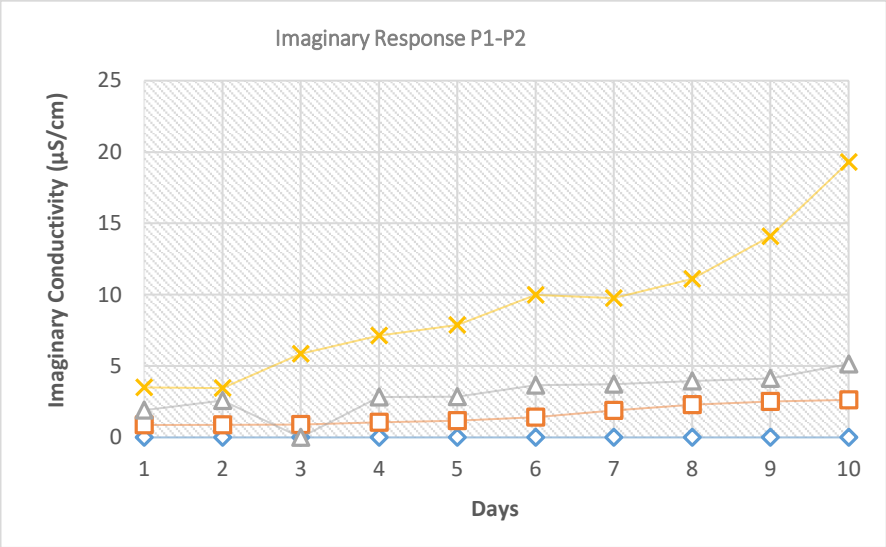
Imaginary Response P1-P2
Imaginary Conductivity (µS/cm)
25
20
15
10
5
0
1
2
3
4
5
6
7
8
9
10
Days

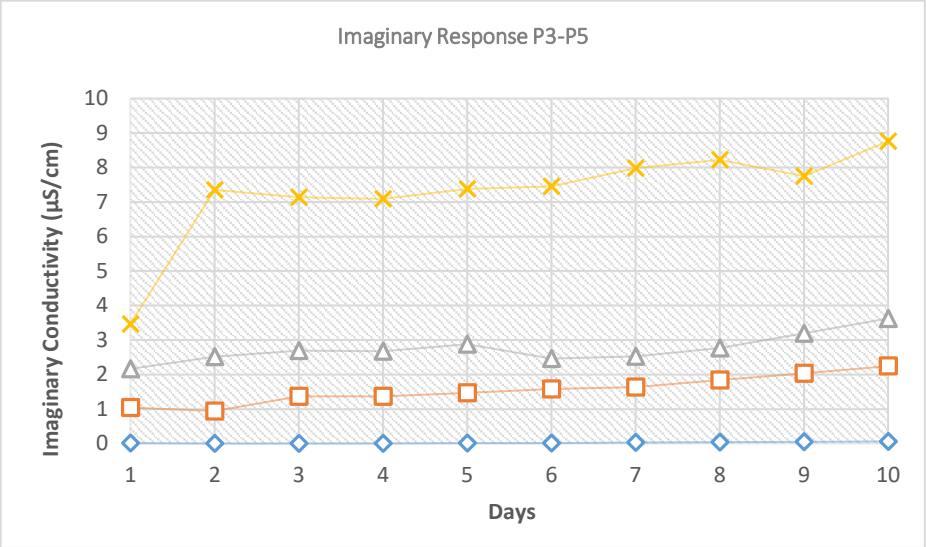
Imaginary Response P3-P5
Imaginary Conductivity (µS/cm)
10
9
8
7
6
5
4
3
2
1
0
1
2
3
4
5
6
7
8
9
10
Days

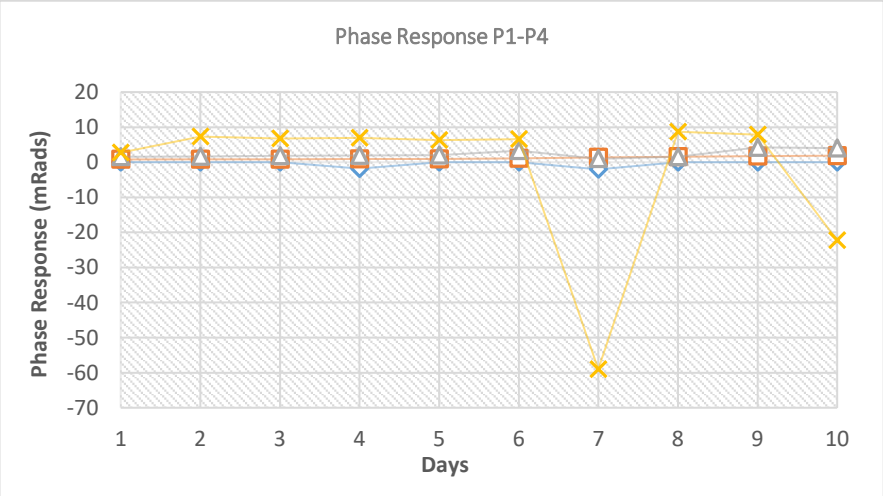
Phase Response P1-P4
Phase Response (mRads)
20
10
0
-10
-20
-30
-40
-50
-60
-70
1
2
3
4
5
6
7
8
9
10
Days

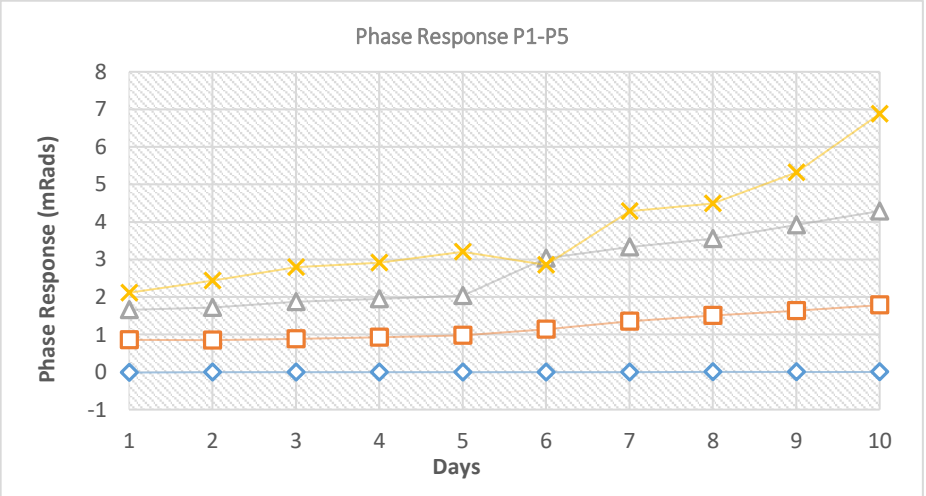
Phase Response P1-P5
Phase Response (mRads)
8
7
6
5
4
3
2
1
0
-1
1
2
3
4
5
6
7
8
9
10
Days

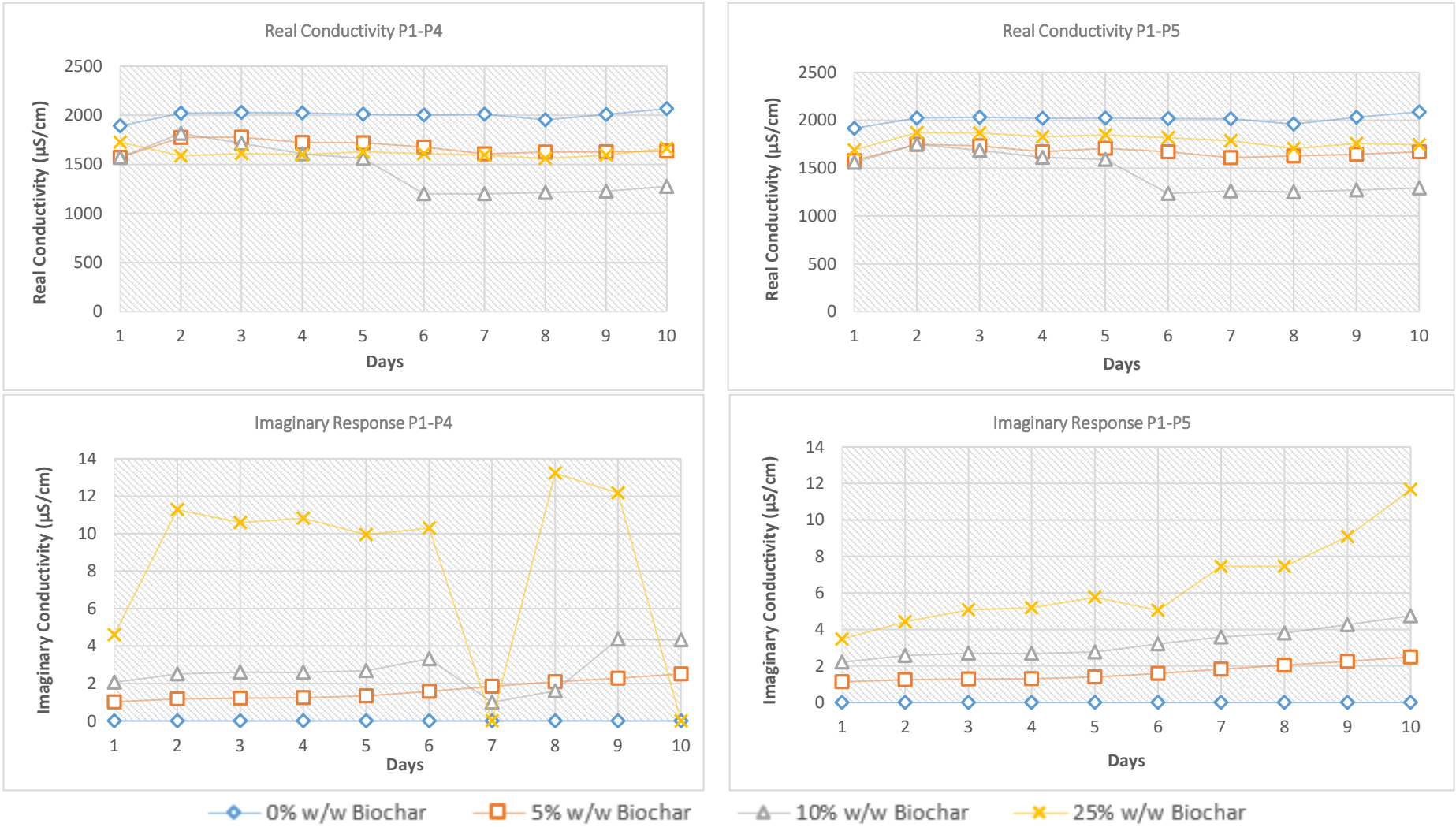

Figure B.17 Single frequency graphs during 10 days treatment with biochar to 10 Hz.